

# Adaptive heterogeneous multiscale models for the nonlinear simulation of concrete

(Adaptive heterogene Mehrskalenmodelle zur  
nichtlinearen Simulation von Beton)

## DISSERTATION

zur Erlangung des akademischen Grades  
Doktor-Ingenieur (Dr.-Ing.)  
an der Fakultät Bauingenieurwesen  
der  
Bauhaus-Universität Weimar

vorgelegt von  
Dipl.-Ing. Stefan Eckardt  
geboren am 11.03.1978 in Weimar

Weimar, Juli 2009

Mentor:

Prof. Dr.-Ing. habil. Carsten Könke, Bauhaus-Universität Weimar

Gutachter:

Prof. Dr. Ir. Lambertus Johannes Sluys, Delft University of Technology  
Prof. Dr.-Ing. Tom Schanz, Ruhr-Universität Bochum

Disputation am 22. November 2009

# Abstract

The nonlinear behavior of concrete can be attributed to the propagation of microcracks within the heterogeneous internal material structure. In this thesis, a mesoscale model is developed which allows for the explicit simulation of these microcracks. Consequently, the actual physical phenomena causing the complex nonlinear macroscopic behavior of concrete can be represented using rather simple material formulations.

On the mesoscale, the numerical model explicitly resolves the components of the internal material structure. For concrete, a three-phase model consisting of aggregates, mortar matrix and interfacial transition zone is proposed. Based on prescribed grading curves, an efficient algorithm for the generation of three-dimensional aggregate distributions using ellipsoids is presented. In the numerical model, tensile failure of the mortar matrix is described using a continuum damage approach. In order to reduce spurious mesh sensitivities, introduced by the softening behavior of the matrix material, nonlocal integral-type material formulations are applied. The propagation of cracks at the interface between aggregates and mortar matrix is represented in a discrete way using a cohesive crack approach. The iterative solution procedure is stabilized using a new path following constraint within the framework of load-displacement-constraint methods which allows for an efficient representation of snap-back phenomena. In several examples, the influence of the randomly generated heterogeneous material structure on the stochastic scatter of the results is analyzed. Furthermore, the ability of mesoscale models to represent size effects is investigated.

Mesoscale simulations require the discretization of the internal material structure. Compared to simulations on the macroscale, the numerical effort and the memory demand increases dramatically. Due to the complexity of the numerical model, mesoscale simulations are, in general, limited to small specimens. In this thesis, an adaptive heterogeneous multiscale approach is presented which allows for the incorporation of mesoscale models within nonlinear simulations of concrete structures. In heterogeneous multiscale models, only critical regions, i.e. regions in which damage develops, are resolved on the mesoscale, whereas undamaged or sparsely damage regions are modeled on the macroscale. A crucial point in simulations with heterogeneous multiscale models is the coupling of sub-domains discretized on different length scales. The sub-domains differ not only in the size of the finite elements but also in the constitutive description. In this thesis, different methods for the coupling of non-matching discretizations – constraint equations, the mortar method and the arlequin method – are investigated and the application to heterogeneous multiscale models is presented. Another important point is the detection of critical regions. An adaptive solution procedure allowing the transfer of macroscale sub-domains to the mesoscale is proposed. In this context, several indicators which trigger the model adaptation are introduced. Finally, the application of the proposed adaptive heterogeneous multiscale approach in nonlinear simulations of concrete structures is presented.

# Kurzfassung

Das nichtlineare Materialverhalten von Beton ist durch die Entwicklung von Mikrorissen innerhalb der heterogenen Materialstruktur gekennzeichnet. In dieser Arbeit wird ein Mesoskalenmodell entwickelt, welches die einzelnen Bestandteile der Materialstruktur explizit auflöst und somit die Simulation dieser Mikrorisse erlaubt. Dadurch können die wirklichen physikalischen Vorgänge, welche das komplexe nichtlineare Verhalten von Beton verursachen, durch relativ einfache Materialformulierungen abgebildet werden.

Für Beton wird auf der Mesoskala ein 3-Phasenmodell vorgeschlagen, bestehend aus groben Zuschlägen, Mörtelmatrix und Übergangszone zwischen Zuschlag und Matrix. In diesem Zusammenhang wird ein effizienter Algorithmus vorgestellt, welcher ausgehend von einer gegebenen Sieblinie dreidimensionale Kornstrukturen mittels Ellipsoiden simuliert. Im Mesoskalenmodell wird das Zugversagen der Mörtelmatrix durch einen Kontinuumsansatz beschrieben. Um Netzabhängigkeiten, welche durch das Entfestigungsverhalten des Materials hervorgerufen werden, zu reduzieren, kommen nichtlokale Materialformulierungen zum Einsatz. Risse innerhalb der Übergangszone zwischen Zuschlag und Matrix werden, basierend auf einem kohäsiven Modell, mittels eines diskreten Rissansatzes abgebildet. Die Verwendung einer neuen Nebenbedingung innerhalb der Last-Verschiebungs-Zwangsmethode führt zu einer Stabilisierung des iterativen Lösungsverfahrens, so dass eine effiziente Simulation von Snap-back Phänomenen möglich wird. Anhand von Beispielen wird gezeigt, dass Mesoskalenmodelle die stochastische Streuung von Ergebnissen und Maßstabeffekte abbilden können.

Da auf der Mesoskala die Diskretisierung der inneren Materialstruktur erforderlich ist, steigt im Vergleich zu Simulationen auf der Makroskala der numerische Aufwand erheblich. Aufgrund der Komplexität des numerischen Modells sind Mesoskalensimulationen in der Regel auf kleine Probekörper beschränkt. In dieser Arbeit wird ein adaptiver heterogener Mehrskalenansatz vorgestellt, welcher die Verwendung von Mesoskalenmodellen in nichtlinearen Simulationen von Betonstrukturen erlaubt. In heterogenen Mehrskalenmodellen werden nur kritische Bereiche auf der Mesoskala aufgelöst, während ungeschädigte Bereiche auf der Makroskala abgebildet werden. Ein wichtiger Aspekt in Simulationen mit heterogenen Mehrskalenmodellen ist die Kopplung der auf unterschiedlichen Längenskalen diskretisierten Teilgebiete. Diese unterscheiden sich nicht nur in der Größe der finiten Elemente sondern auch in der Beschreibung des Materials. Verschiedene Methoden zur Kopplung nicht übereinstimmender Vernetzungen – Kopplungsgleichungen, die Mortar-Methode und die Arlequin-Methode – werden untersucht und ihre Anwendung in heterogenen Mehrskalenmodellen wird gezeigt. Ein weiterer wichtiger Aspekt ist die Bestimmung kritischer Regionen. Eine adaptive Lösungsstrategie wird entwickelt, welche die Umwandlung von Makroskalengebieten auf die Mesoskala erlaubt. In diesem Zusammenhang werden Indikatoren vorgestellt, die eine Modellanpassung auslösen. Anhand nichtlinearer Simulationen von Betonstrukturen wird die Anwendung des vorgestellten adaptiven heterogenen Mehrskalenansatzes demonstriert.

# Vorwort

Die vorliegende Arbeit entstand während meiner Tätigkeit als wissenschaftlicher Mitarbeiter innerhalb des Sonderforschungsbereiches 524 „Werkstoffe und Konstruktionen für die Revitalisierung von Bauwerken“ und im Rahmen eines DFG-Einzelprojektes am Institut für Strukturmechanik an der Bauhaus-Universität Weimar. In diesem Zusammenhang möchte ich der Deutschen Forschungsgemeinschaft (DFG) für die finanzielle Unterstützung danken.

Mein besonderer Dank gilt Herrn Professor Carsten Könke für die Anregung und Förderung dieser Arbeit sowie für die sehr gute wissenschaftliche Betreuung. Die Kombination aus gewährter wissenschaftlicher Freiheit und geforderter zielgerichteter Projektarbeit hat wesentlich zum Gelingen dieser Arbeit beigetragen. Besonders wertvoll war seine frühzeitige Förderung der Teilnahme an internationalen Tagungen welche mich und diese Arbeit geprägt haben.

Besonders bedanken möchte ich mich auch bei Herrn Professor Bert Sluys und Herrn Professor Tom Schanz für die bereitwillige Übernahme der Gutachten, die wertvollen Anmerkungen und die sorgfältige Durchsicht meiner Arbeit.

Des weiteren möchte ich allen Mitarbeitern des Instituts für Strukturmechanik für die Unterstützung und die sehr angenehme und freundschaftliche Arbeitsatmosphäre danken. In diesem Zusammenhang möchte ich besonders meinen Studien- und Zimmerkollegen Dr. Jörg F. Unger hervorheben, der im Rahmen unzähliger Diskussionen in freundschaftlicher Atmosphäre durch stets kritische Fragen und fachliche Kompetenz entscheidend zum Gelingen dieser Arbeit beigetragen hat. Außerdem vielen Dank für die gewissenhafte Korrektur meiner Arbeit. Weiterhin möchte ich Dr. Thomas Most danken, der mich insbesondere in der Anfangszeit bei der numerischen Umsetzung und Implementation einiger Algorithmen in SLang unterstützt hat.

Ein ganz herzlicher Dank gebührt meinen Eltern für eine wunderschöne Kindheit und die Unterstützung und Förderung in den vergangenen Jahren. Von ganzen Herzen möchte ich mich bei meiner liebsten Ulrike für ihre kontinuierliche Unterstützung und ihr liebevolles Verständnis bedanken. Sie hat mich auch in schwierigen Phasen meiner Promotionszeit immer wieder motiviert und bot mir den bedingungslosen Rückhalt der zur Vollendung dieser Arbeit erforderlich war.

# Contents

<b>1</b>	<b>Introduction</b>	<b>1</b>
1.1	Motivation . . . . .	1
1.2	Aims and scope of the work . . . . .	3
1.3	Outline of the work . . . . .	4
<b>2</b>	<b>Finite Element Method</b>	<b>7</b>
2.1	Introduction . . . . .	7
2.2	Discretization by Finite Elements . . . . .	9
2.2.1	Interface Elements with Zero Thickness . . . . .	13
2.3	Material Nonlinearity . . . . .	17
2.4	Solution Strategies . . . . .	18
2.4.1	Load Control . . . . .	19
2.4.2	Direct Displacement Control . . . . .	20
2.4.3	Load-Displacement-Constraint Methods . . . . .	21
2.4.4	Line Search . . . . .	27
2.4.5	Step Size Adaptation . . . . .	30
<b>3</b>	<b>Continuum Damage Mechanics</b>	<b>32</b>
3.1	Introduction . . . . .	32
3.2	Regularization . . . . .	32
3.2.1	Crack-Band Theory . . . . .	33
3.2.2	Integral-Type Nonlocal Damage Models . . . . .	34
3.2.3	Nonlocal Averaging of the Displacement Field . . . . .	39
3.2.4	Gradient Enhanced Damage Models . . . . .	42
3.2.5	Discussion . . . . .	45
3.3	Isotropic Damage Model . . . . .	47
3.3.1	Local Formulation . . . . .	47
3.3.2	Nonlocal Formulation . . . . .	48
3.4	Rotating Crack Model . . . . .	52
3.4.1	Local Formulation . . . . .	53
3.4.2	Transition to Scalar Damage . . . . .	58
3.4.3	Nonlocal Formulation . . . . .	60
3.5	Microplane Damage Model . . . . .	61
3.5.1	Local Formulation . . . . .	62
3.5.2	Nonlocal Formulation . . . . .	66
3.5.3	Parameter Identification . . . . .	66
3.6	Interface Material Model . . . . .	68

<b>4</b>	<b>Mesoscale Modeling of Concrete</b>	<b>72</b>
4.1	Introduction . . . . .	72
4.2	Generation of the Internal Material Structure on the Mesoscale . . . . .	73
4.2.1	Simulation of the Aggregate Size Distribution (Take-Process) . . . . .	74
4.2.2	Simulation of the Spatial Aggregate Distribution (Place-Process) . . . . .	76
4.2.3	Example . . . . .	78
4.3	Numerical Model . . . . .	80
4.4	Examples . . . . .	83
4.4.1	Uniaxial Tension Test . . . . .	84
4.4.2	Size Effect . . . . .	94
4.4.3	Compression Test . . . . .	99
<b>5</b>	<b>Multiscale Modeling of Concrete</b>	<b>104</b>
5.1	Introduction . . . . .	104
5.1.1	Multiscale Approaches Based on Homogenization . . . . .	105
5.1.2	Hierarchical Multiscale Approaches . . . . .	109
5.2	Heterogeneous Multiscale Approach . . . . .	111
5.3	Coupling Conditions . . . . .	112
5.3.1	Constraint Equations . . . . .	114
5.3.2	Mortar Method . . . . .	117
5.3.3	Arlequin Method . . . . .	122
5.3.4	Example . . . . .	130
5.4	Model Adaptation from Macro- to Mesoscale . . . . .	135
5.5	Model Adaptation from Meso- to Macroscale . . . . .	138
5.6	Examples . . . . .	139
5.6.1	L-shaped Panel . . . . .	139
5.6.2	Size Effect . . . . .	146
<b>6</b>	<b>Conclusions</b>	<b>151</b>
	<b>Bibliography</b>	<b>155</b>
<b>A</b>	<b>Appendix</b>	<b>167</b>
A.1	Transformation and Projection of Stresses and Strains . . . . .	167
A.1.1	Orthogonal Transformation . . . . .	167
A.1.2	Projection . . . . .	168
A.2	Energies and Energy Derivatives . . . . .	169
A.3	Line Search for Load-Displacement-Constraint Methods . . . . .	170
A.4	Microplane Damage Model . . . . .	172
A.4.1	Numerical Integration of the Inverse Integrity Tensor . . . . .	172
A.4.2	Derivation of the Damage Effect Tensor . . . . .	173
A.4.3	Secant and Tangent Material Matrix (Plane Stress) . . . . .	175
A.5	Interface Material Model - Tangential Material Matrix . . . . .	177

# 1 Introduction

## 1.1 Motivation

Concrete is an artificial building material mainly composed of aggregates embedded in a matrix of hardened cement paste. Consequently, concrete is not a homogeneous material as it appears to be on structural level, but has a heterogeneous internal material structure. In general, the size of the material components is significantly smaller than the structural dimensions. The nonlinear behavior of concrete can be attributed to the initiation, propagation, accumulation and coalescence of microcracks within the internal material structure. Thus, failure of concrete structures is a multiscale phenomena – the material behavior of concrete on the macroscale, which corresponds to the structural level, is clearly influenced by the geometry, the spatial distribution and the material properties of the individual material constituents and their mutual interaction. A localization of these microcracks, which is also triggered by the heterogeneous internal material structure, leads to the formation of macroscopic cracks and is accompanied by a softening of the material. Other phenomena such as the stochastic scatter of the structural response or size effects can be, at least partially, attributed to the random heterogeneous microstructure of concrete.

In macroscale simulations of concrete structures, the heterogeneity of the material is, in general, neglected and concrete is assumed to be a homogeneous material. In these simulations, the material is represented in a homogenized way using effective material properties. The advantage of macroscale simulations is the numerical efficiency since the finite element discretization is predominantly defined by the geometry of the concrete structure. Consequently, the average element size is, in general, significantly larger than the dimension of the material components, which allows for a relatively coarse finite element mesh. One central problem in macroscale simulations is the formulation of material models, describing the overall (homogenized) response of concrete, and the determination of the corresponding effective material parameters. Especially in nonlinear simulations, complex constitutive models representing the physical effects inside the heterogeneous internal material structure in a phenomenological way are, in general, used to simulate the deterioration behavior of concrete. These models only allow for a homogenized interpretation of the individual processes such as the propagation of microcracks which occur on a smaller length scale than the structural length scale. Often, the internal parameters of these material models cannot be measured directly in physical experiments. As a result, the identification of these parameters is generally difficult.

In mesoscale simulations, the numerical model explicitly represents the individual components of the heterogeneous internal material structure of concrete, e.g. the shape and the spatial distribution of the aggregates. As a result, specific material models can be assigned

to each component of the mesoscale model. Since the physical effects such as the propagation of microcracks or failure of the interface between aggregates and matrix are considered separately in mesoscale simulations, rather simple material formulations can be used for each material phase to represent the complex macroscopic material behavior of concrete. Furthermore, these models also represent phenomena such as size effects on the nominal tensile strength, the stochastic scatter of the results in simulations with specimens with identical shape but different aggregate configurations or the localization of damage due to the heterogeneity of the material. Numerical simulations on the mesoscale require the discretization of the internal material structure. Compared to macroscale simulations, the numerical effort and the memory demand increases dramatically. Due to the complexity of the numerical model, mesoscale simulations are, in general, limited to small specimens.

In a multiscale approach, multiple numerical models describing the material behavior on different length scales are combined. On the macroscale, concrete is considered as a homogeneous material whereas on the mesoscale the heterogeneous internal material structure is explicitly resolved. It is to be noted that multiscale approaches are not limited to two scales. Additional finer scales can be employed in order to incorporate the influence of the internal material structure of the aggregates, the mortar matrix or the interfacial transition zone between aggregates and matrix, which also have a heterogeneous character, in numerical simulations. In multiscale approaches, the numerical model does not resolve the entire structure on the mesoscale. As a result, the numerical effort is reduced compared to full mesoscale simulations. In general, two different multiscale approaches can be distinguished. In the first approach, the entire structure is discretized on the macroscale. Using homogenization techniques, the constitutive relationship on the macroscale is derived from the structural response of a representative material sample which is modeled on the mesoscale. A general problem of such an approach is the definition of the size of the representative material sample, which becomes impossible in the case of localization phenomena. In the second approach, the structure is subdivided into sub-domains. Critical sub-domains, e.g. sub-domains in which microcracks propagate, are modeled on the mesoscale resolving explicitly the heterogeneous internal material structure. The remaining parts of the structure, which are still in the elastic domain, are represented on the macroscale using effective material properties and assuming a homogeneous material. Since the mesoscale sub-domain explicitly represents one part of the structure, this approach is also applicable if localization phenomena occur. One crucial point in multiscale simulations is the coupling between the scales, which requires the definition of a relationship between quantities calculated on the mesoscale, e.g. stresses, strains or displacements, and the corresponding counterparts on the macroscale. Due to the, in general, highly oscillating character of these mesoscale quantities, the coupling condition is, in most cases, only satisfied in an average (integral) sense.

The failure behavior of concrete is characterized by a softening of the material. Consequently, the load starts to decrease for increasing deformations after the maximum load is reached. In order to capture the post-peak behavior of concrete a displacement controlled loading strategy is required in experiments as well as in numerical simulations. Depending on the ratio between the specimen size and the size of the fracture process zone, the load-displacement curve may exhibit snap-backs, which cannot be represented using direct displacement control. In order to capture snap-back phenomena, a combined



load-displacement control has to be applied and the equilibrium state of the structure has to be characterized by an additional constraint, e.g. a predefined crack mouth opening displacement or a given amount of dissipated energy.

## 1.2 Aims and scope of the work

The principal goal of this thesis is to improve the accuracy of the damage representation in nonlinear simulations of concrete structures using mesoscale models. Within this context, several aspects have to be considered.

First of all, a mesoscale model describing the heterogeneous internal material structure of concrete is developed. On the mesoscale, three different phases can be distinguished – coarse aggregates, mortar matrix and the interfacial transition zone (ITZ) at the interface between aggregates and matrix. These components itself also have a heterogeneous character. The mortar matrix, for example, mainly consists of hardened cement paste, air voids and fine aggregates which are not explicitly considered as an individual phase in the model. In this thesis, the heterogeneity of the components is neglected. The material components are idealized as homogeneous materials and the material behavior is characterized by effective material properties. A crucial point in mesoscale simulations is an appropriate description of the internal material geometry. For concrete simulated on the mesoscale, the internal material structure is characterized by the shape, the size distribution and the spatial distribution of the aggregates. In this thesis, an efficient algorithm for the simulation of three-dimensional aggregate distributions with a large number of particles is developed. This algorithm directly takes into account grading curves used in the experiments. Based on these aggregate distributions a numerical model is generated which explicitly represents the heterogeneous internal material structure. In the numerical simulations presented in this thesis, only tensile failure within the mortar matrix and debonding of the interface between aggregates and matrix is considered. It is assumed that, due to the influence of the heterogeneous material structure, compressive failure on the macroscale can be reduced to tensile failure perpendicular to the direction of compressive stress on the mesoscale. Furthermore, assuming normal-strength concrete, the nonlinear behavior of the aggregates can be neglected. Another important aspect is the reliability of numerical simulations. A problem in numerical simulations of concrete is that the softening behavior of the material may lead to a spurious dependency of the results on the finite element discretization. In order to reduce spurious mesh sensitivities, due to softening and localization phenomena which are also observed on the mesoscale, appropriate regularized material formulations such as nonlocal formulations are applied. Furthermore, a solution strategy is developed which allows for an efficient simulation of softening and snap-back phenomena without a priori knowledge about the final failure zone.

Secondly, the mesoscale models are incorporated in nonlinear simulations of concrete structures. Due to the high numerical effort and memory demand of mesoscale simulations, it is, in general, not possible to simulate the full structure on the mesoscale with the computational power available nowadays. In order to reduce the numerical effort, a heterogeneous multiscale model is developed, in which only critical parts of the structure, e.g. regions

in which damage develops, are resolved on the mesoscale. A problem in simulations with heterogeneous multiscale models is the determination of the critical regions which are, in general, not known a priori. In this thesis, an adaptive solution strategy is introduced which automatically detects critical regions during the simulation. Consequently, based on the current loading situation, the numerical model is successively modified during the simulation – new mesoscale sub-domains are generated or existing mesoscale sub-domains are enlarged. In this context, indicators for a model adaptation are developed. Furthermore, an efficient procedure for the transfer of critical regions from the macroscale to the mesoscale is provided. Another problem in simulations with heterogeneous multiscale models is the coupling between sub-domains which are resolved on different length scales. On the common boundary between a macro- and a mesoscale sub-domain, the numerical model differs not only in the size of the finite elements but also in the representation of the material structure – homogeneous on the macroscale and heterogeneous on the mesoscale. In order to enforce compatibility between adjacent sub-domains special coupling conditions are applied.

All methods presented in this thesis are developed for the general three-dimensional case. Due to the complexity of three-dimensional mesoscale models and especially due to the limitation of the computational power, most examples are simulated using two-dimensional models. However, the application to three-dimensional simulations is, in general, straightforward.

## 1.3 Outline of the work

In Chapter 2, the displacement-based finite element method is briefly presented. Furthermore, the extension to nonlinear material behavior and the solution of the corresponding nonlinear global system of equations using the Newton-Raphson method is addressed. Special interest is focused on solution strategies which allow for the simulation of the softening behavior of concrete and the representation of snap-back phenomena. In the framework of load-displacement-constraint methods, a new path-following constraint based on the dissipation of the inelastic energy is developed. Since the constraint is based on the internal energy, the algorithm can be applied to any material formulation for which the inelastic energy can be defined. The proposed constraint is in particular advantageous in mesoscale simulations which are characterized by the propagation of multiple cracks, since no a priori knowledge of the final failure zone is required.

Chapter 3 deals with nonlinear material formulations which are based on the concept of continuum damage mechanics or on the smeared crack approach. In these material models, the softening behavior of concrete is described using a strain-softening continuum. In the first part of the chapter, the problem of spurious mesh dependency of the results due to localization is addressed. Different regularization techniques – the crack band theory, non-local integral-type models and gradient enhanced formulations – are discussed. Since the full Newton-Raphson scheme is applied in the solution of the generally nonlinear global system of equations, the derivation of the tangent stiffness matrix for the regularized material formulations is an important aspect. In the second part, different material formulations

are presented which can be used to describe the tensile failure of the mortar matrix. An isotropic damage model, a rotating crack model and a microplane based damage model are introduced. Several model specific aspects, such as failure surfaces, stress evaluation or parameter identification are addressed. Furthermore, the corresponding regularized formulations based on the nonlocal integral-type concept are presented for all material models. Finally, a cohesive zone model describing the nonlinear behavior of the interfacial transition zone is introduced.

In Chapter 4, a mesoscale model for concrete is proposed. One important aspect is an appropriate geometry description of the internal material structure. Based on the take-and-place method, an efficient algorithm for the simulation of three-dimensional aggregate distributions using ellipsoidal particles is developed. First of all, an algorithm for the random generation of the ellipsoids is derived, such that the aggregate size distribution observed in the simulation almost coincides with a prescribed grading curve. Secondly, the place process is presented. During the random placement of the ellipsoids separation checks have to be performed in order to avoid overlapping of the ellipsoids. Since a large number of ellipsoids have to be simulated, special interest is placed on the efficient application and combination of different inexact and exact separation checks. An example with approximately 300 000 ellipsoids is presented to illustrate the performance of the proposed algorithm. Another important aspect is the generation of the numerical model. Various discontinuous models and different continuum approaches are briefly discussed, and a continuum approach with an aligned discretization, in which the finite element mesh explicitly represents the surface of the aggregates, is proposed. In the last part of this chapter, the main features of the proposed mesoscale model are illustrated using several examples taken from literature. First of all, different material formulations for the mortar matrix and the interfacial transition zone, which were introduced in Chapter 3, are tested using two-dimensional simulations of tensile tests. In order to investigate the influence of the randomly generated heterogeneous material structure on the stochastic scatter of the results, simulations with varying aggregate configurations are performed. Furthermore, the ability of mesoscale models to represent size effects is analyzed. Finally, a three-dimensional mesoscale simulation of a compression test is presented. In the examples the application of the energy release control, which was proposed in Chapter 2, in nonlinear mesoscale simulations of concrete is illustrated.

Chapter 5 starts with a discussion on different multiscale approaches. Subsequently, a new heterogeneous multiscale model for concrete is developed and the major aspects of the implementation of such an approach are addressed. An important point is the coupling of sub-domains which are resolved on different length-scales. Three different coupling methods for non-matching finite element discretizations – constraint equations, the mortar method and the arlequin method – are presented. The application of these coupling techniques to heterogeneous multiscale models is illustrated using a two-dimensional linear elastic example. Another aspect is the model adaptation during the simulation. Several indicators triggering the conversion from macro- to mesoscale are proposed. Furthermore, an efficient adaptation procedure for the generation of new mesoscale sub-domains and the enlargement of existing mesoscale sub-domains is introduced and the application in the iterative solution procedure is presented. As an extension of the proposed multiscale approach, the conversion of mesoscale sub-domains back to the macroscale is briefly outlined.

Finally, two examples are presented to show the applicability of the adaptive heterogeneous multiscale approach to nonlinear simulations of concrete structures.

In Chapter 6, the main conclusions of this thesis are summarized. Furthermore, possible perspectives for future development of the proposed adaptive heterogeneous multiscale approach are shortly discussed.

# 2 Finite Element Method

## 2.1 Introduction

Assume a general three-dimensional body that occupies a domain  $\Omega \in R^3$  which is defined by a set of points  $\mathbf{x}$ . A body force  $\bar{\mathbf{b}}$  is prescribed inside the domain. Furthermore, surface tractions  $\bar{\mathbf{t}}$  and boundary displacements  $\bar{\mathbf{u}}$  are applied on the domain boundary surfaces  $\Gamma_t$  and  $\Gamma_u$ , with  $\Gamma_t \cup \Gamma_u = \Gamma$  and  $\Gamma_t \cap \Gamma_u = \emptyset$ , where  $\Gamma$  is the total domain boundary surface. The motion of this body with respect to the applied loading is expressed by the unknown displacement field  $\mathbf{u}$ . Assuming small displacements and a linear relationship between stresses  $\boldsymbol{\sigma}$  and strains  $\boldsymbol{\varepsilon}$  the governing differential equations can be written as

$$\sigma_{ij} = C_{ijkl}^e \varepsilon_{kl} \quad \forall \mathbf{x} \in \Omega \quad \dots \text{ constitutive equations} \quad (2.1)$$

$$\varepsilon_{ij} = \frac{1}{2} \left( \frac{\partial u_i}{\partial x_j} + \frac{\partial u_j}{\partial x_i} \right) \quad \forall \mathbf{x} \in \Omega \quad \dots \text{ kinematic equations} \quad (2.2)$$

$$\frac{\partial \sigma_{ij}}{\partial x_j} = \bar{b}_i \quad \forall \mathbf{x} \in \Omega \quad \dots \text{ static equations} \quad (2.3)$$

$$u_i = \bar{u}_i \quad \forall \mathbf{x} \in \Gamma_u \quad \dots \text{ essential boundary conditions} \quad (2.4)$$

$$\sigma_{ij} n_j = \bar{t}_i \quad \forall \mathbf{x} \in \Gamma_t \quad \dots \text{ natural boundary conditions} \quad (2.5)$$

where  $\mathbf{n}$  is a vector normal to the boundary surface. Considering an isotropic material, the linear elastic material tensor  $\mathbf{C}^e$  is given by

$$C_{ijkl}^e = \lambda \delta_{ij} \delta_{kl} + \mu (\delta_{ik} \delta_{jl} + \delta_{il} \delta_{jk}), \quad (2.6)$$

where  $\delta$  denotes the Kronecker delta which is defined as

$$\delta_{ij} = \begin{cases} 1 & \text{if } i = j \\ 0 & \text{if } i \neq j \end{cases}, \quad (2.7)$$

and  $\lambda$  and  $\mu$  are the Lamé's constants which can be expressed in terms of the Young's modulus  $E$  and the Poisson's ratio  $\nu$

$$\lambda = \frac{E\nu}{(1+\nu)(1-2\nu)} \quad \mu = \frac{E}{2(1+\nu)}. \quad (2.8)$$

It is to be noted that in this thesis Einstein's summation convention is used: whenever an index appears twice in a single term, summation over that index is performed.

As an alternative to the differential approach given in Eqs. (2.3) to (2.5), the equilibrium state can be expressed by the principle of virtual displacements (principle of virtual work)

$$\int_{\Omega} \sigma_{ij} \delta \varepsilon_{ij} \, d\Omega = \int_{\Omega} \bar{b}_i \delta u_i \, d\Omega + \int_{\Gamma_t} \bar{t}_i \delta u_i \, d\Gamma_t \quad \text{with } u_i = \bar{u}_i \text{ and } \delta u_i = 0 \quad \forall \mathbf{x} \in \Gamma_u. \quad (2.9)$$

This equality must hold for an arbitrary but kinematically compatible virtual displacement state  $(\delta \mathbf{u}, \delta \boldsymbol{\varepsilon})$ . In Bathe (1995), it is shown that both formulations are totally equivalent, if Eq. (2.9) is fulfilled for any kinematically compatible virtual displacement state.

In Eqs. (2.1) to (2.9) the tensor notation is used for the stresses and strains

$$\sigma_{ij} = \begin{bmatrix} \sigma_{11} & \sigma_{12} & \sigma_{13} \\ \sigma_{12} & \sigma_{22} & \sigma_{23} \\ \sigma_{13} & \sigma_{23} & \sigma_{33} \end{bmatrix} \quad \varepsilon_{ij} = \begin{bmatrix} \varepsilon_{11} & \varepsilon_{12} & \varepsilon_{13} \\ \varepsilon_{12} & \varepsilon_{22} & \varepsilon_{23} \\ \varepsilon_{13} & \varepsilon_{23} & \varepsilon_{33} \end{bmatrix}. \quad (2.10)$$

Due to the symmetry of these second order tensors, it is possible to store the stress and strain components in vectors

$$\boldsymbol{\sigma} = \begin{bmatrix} \sigma_{11} \\ \sigma_{22} \\ \sigma_{33} \\ \sigma_{12} \\ \sigma_{13} \\ \sigma_{23} \end{bmatrix} \quad \boldsymbol{\varepsilon} = \begin{bmatrix} \varepsilon_{11} \\ \varepsilon_{22} \\ \varepsilon_{33} \\ \gamma_{12} \\ \gamma_{13} \\ \gamma_{23} \end{bmatrix} = \begin{bmatrix} \varepsilon_{11} \\ \varepsilon_{22} \\ \varepsilon_{33} \\ 2\varepsilon_{12} \\ 2\varepsilon_{13} \\ 2\varepsilon_{23} \end{bmatrix}. \quad (2.11)$$

Furthermore, the fourth order material tensor can be written in matrix form. Assuming an isotropic linear elastic material behavior, the material matrix reads

$$\mathbf{C}^e = \frac{E}{(1+\nu)(1-2\nu)} \begin{bmatrix} 1-\nu & \nu & \nu & 0 & 0 & 0 \\ \nu & 1-\nu & \nu & 0 & 0 & 0 \\ \nu & \nu & 1-\nu & 0 & 0 & 0 \\ 0 & 0 & 0 & \frac{1-2\nu}{2} & 0 & 0 \\ 0 & 0 & 0 & 0 & \frac{1-2\nu}{2} & 0 \\ 0 & 0 & 0 & 0 & 0 & \frac{1-2\nu}{2} \end{bmatrix}. \quad (2.12)$$

Using vector notation, the constitutive equations, Eq. (2.1), can be rewritten as

$$\sigma_i = C_{ij}^e \varepsilon_j, \quad (2.13)$$

and the principle of virtual displacements given in Eq. (2.9) reads

$$\int_{\Omega} \sigma_i \delta \varepsilon_i \, d\Omega = \int_{\Omega} \bar{b}_i \delta u_i \, d\Omega + \int_{\Gamma_t} \bar{t}_i \delta u_i \, d\Gamma_t \quad \text{with } u_i = \bar{u}_i \text{ and } \delta u_i = 0 \quad \forall \mathbf{x} \in \Gamma_u. \quad (2.14)$$

As shown in appendix A.1, special attention must be paid to the transformation and projection of these vectors.

Closed-form solutions for the boundary value problem given in Eqs. (2.1) to (2.5) exist only for a small number of problems, usually those with simple geometry and loading. For most problems arising in engineering applications, the boundary value problem has to be solved in an approximate way using a numerical method. Today, the finite element method (FEM) is one of the most universal techniques applicable to problems with arbitrary geometry and boundary conditions. In the next section, the displacement based version of this method is briefly introduced. A detailed description can be found in one of the classical textbooks, e.g. Bathe (1995) or Zienkiewicz et al. (2005).

## 2.2 Discretization by Finite Elements

Using the finite element method, the entire body is subdivided into finite elements which are connected at a discrete number of nodes on the element boundaries. Each element is defined by a certain number of nodes. Within one element, the displacement field  $\mathbf{u}$  is approximated by linear combinations of so-called element shape functions  $N$ , which are weighted by nodal displacement values  $\hat{u}$ . One important property of the finite element shape functions is that the partition of unity is fulfilled in each point of the element

$$\sum_{k=1}^{n_N} N^{(k)}(\mathbf{x}) = 1 \quad \forall \mathbf{x} \in V_E, \quad (2.15)$$

where  $V_E$  is the element volume, and  $n_N$  is the number of nodes defining the element. Another typical property is that each shape function is associated to one of the element nodes and that the value of the  $i$ -th shape function is equal to one at node  $i$  and equal to zero at all other element nodes. As a result, the nodal displacement values are equal to the approximated displacement components calculated at the node coordinates. Assuming a displacement-based element with  $n_N$  nodes, the interpolation of the displacement components can be written as

$$\mathbf{u}(\mathbf{x}) = \sum_{k=1}^{n_N} N^{(k)}(\mathbf{x}) \hat{\mathbf{u}}^{(k)} \quad \forall \mathbf{x} \in V_E, \quad (2.16)$$

where  $\hat{\mathbf{u}}^{(k)}$  are the unknown displacement values of element node  $k$ . Substituting the displacement interpolation into the kinematic equations, given by Eq. (2.2), the approximation of the strain field is obtained

$$\varepsilon_{ij}(\mathbf{x}) = \frac{1}{2} \sum_{k=1}^{n_N} \left( \frac{\partial N^{(k)}}{\partial x_j}(\mathbf{x}) \hat{u}_i^{(k)} + \frac{\partial N^{(k)}}{\partial x_i}(\mathbf{x}) \hat{u}_j^{(k)} \right) \quad \forall \mathbf{x} \in V_E. \quad (2.17)$$

By storing the unknown nodal displacement values of one single element into a vector  $\mathbf{d}$  and

the associated element shape functions into a matrix  $\mathbf{N}$ , the displacement interpolation in Eq. (2.16) can be rewritten as

$$u_i(\mathbf{x}) = N_{ij}(\mathbf{x})d_j \quad (2.18)$$

with

$$\mathbf{N} = \begin{bmatrix} N^{(1)} & 0 & 0 & N^{(2)} & 0 & 0 & \dots & N^{(n)} & 0 & 0 \\ 0 & N^{(1)} & 0 & 0 & N^{(2)} & 0 & \dots & 0 & N^{(n)} & 0 \\ 0 & 0 & N^{(1)} & 0 & 0 & N^{(2)} & \dots & 0 & 0 & N^{(n)} \end{bmatrix} \quad (2.19)$$

$$\mathbf{d}^T = \begin{bmatrix} \hat{u}_1^{(1)} & \hat{u}_2^{(1)} & \hat{u}_3^{(1)} & \hat{u}_1^{(2)} & \hat{u}_2^{(2)} & \hat{u}_3^{(2)} & \dots & \hat{u}_1^{(n)} & \hat{u}_2^{(n)} & \hat{u}_3^{(n)} \end{bmatrix}. \quad (2.20)$$

Introducing vector notation for the strains, the relationship between strains and displacements, given by Eq. (2.17), reads

$$\varepsilon_i(\mathbf{x}) = B_{ij}(\mathbf{x})d_j, \quad (2.21)$$

where  $\mathbf{B}$  is the well known strain-displacement matrix (B-matrix), which is defined as

$$\mathbf{B} = \begin{bmatrix} \frac{\partial N^{(1)}}{\partial x_1} & 0 & 0 & \frac{\partial N^{(2)}}{\partial x_1} & 0 & 0 & \dots & \frac{\partial N^{(n)}}{\partial x_1} & 0 & 0 \\ 0 & \frac{\partial N^{(1)}}{\partial x_2} & 0 & 0 & \frac{\partial N^{(2)}}{\partial x_2} & 0 & \dots & 0 & \frac{\partial N^{(n)}}{\partial x_2} & 0 \\ 0 & 0 & \frac{\partial N^{(1)}}{\partial x_3} & 0 & 0 & \frac{\partial N^{(2)}}{\partial x_3} & \dots & 0 & 0 & \frac{\partial N^{(n)}}{\partial x_3} \\ \frac{\partial N^{(1)}}{\partial x_2} & \frac{\partial N^{(1)}}{\partial x_1} & 0 & \frac{\partial N^{(2)}}{\partial x_2} & \frac{\partial N^{(2)}}{\partial x_1} & 0 & \dots & \frac{\partial N^{(n)}}{\partial x_2} & \frac{\partial N^{(n)}}{\partial x_1} & 0 \\ \frac{\partial N^{(1)}}{\partial x_3} & 0 & \frac{\partial N^{(1)}}{\partial x_1} & \frac{\partial N^{(2)}}{\partial x_3} & 0 & \frac{\partial N^{(2)}}{\partial x_1} & \dots & \frac{\partial N^{(n)}}{\partial x_3} & 0 & \frac{\partial N^{(n)}}{\partial x_1} \\ 0 & \frac{\partial N^{(1)}}{\partial x_3} & \frac{\partial N^{(1)}}{\partial x_2} & 0 & \frac{\partial N^{(2)}}{\partial x_3} & \frac{\partial N^{(2)}}{\partial x_2} & \dots & 0 & \frac{\partial N^{(n)}}{\partial x_3} & \frac{\partial N^{(n)}}{\partial x_2} \end{bmatrix}. \quad (2.22)$$

By substituting Eq. (2.21) into Eq. (2.13), the approximation of the stress field is obtained

$$\sigma_i(\mathbf{x}) = C_{ij}^e(\mathbf{x})B_{jk}(\mathbf{x})d_k. \quad (2.23)$$

As a result, the constitutive equations, Eq. (2.1), and the kinematic equations, Eq. (2.2), are exactly satisfied. Due to the interpolation of the displacement field, which is now expressed as a function of a discrete number of nodal values, the static equations given in Eq. (2.3) cannot, in general, be satisfied exactly in every point of the body. By considering the approximations of displacements, strains and stresses in the principle of virtual displacements, Eq. (2.9), the weak form of the equilibrium equations is obtained

$$\int_V C_{ij}^e(\mathbf{x})B_{jk}(\mathbf{x})d_k \delta \varepsilon_i(\mathbf{x}) dV = \int_V \bar{b}_i(\mathbf{x})\delta u_i(\mathbf{x}) dV + \int_{\Gamma_t} \bar{t}_i(\mathbf{x})\delta u_i(\mathbf{x}) d\Gamma_t. \quad (2.24)$$



If this equality holds for an arbitrary but kinematically compatible virtual displacement and strain state, the equilibrium equations are satisfied, but only in an integral sense. Using the same approximation for the virtual displacement field as for the displacements

$$\delta u_i(\mathbf{x}) = N_{ij}(\mathbf{x})\delta d_j \quad (2.25)$$

and assuming that the virtual strain field satisfies the kinematic equations

$$\delta \varepsilon_i(\mathbf{x}) = B_{ij}(\mathbf{x})\delta d_j, \quad (2.26)$$

the discretized form of the principle of virtual displacements can be written as

$$\delta d_k \int_V B_{ik}(\mathbf{x})C_{ij}^e(\mathbf{x})B_{jl}(\mathbf{x}) dV d_l = \delta d_k \int_V N_{ik}(\mathbf{x})\bar{b}_i(\mathbf{x}) dV + \delta d_k \int_{\Gamma_t} N_{ik}(\mathbf{x})\bar{t}_i(\mathbf{x}) d\Gamma_t. \quad (2.27)$$

For an arbitrary virtual nodal displacement vector  $\delta \mathbf{d}$  this equation is only satisfied, if

$$K_{ij}d_j = f_{ext,i}, \quad (2.28)$$

where  $\mathbf{K}$  is the element stiffness matrix

$$K_{ij} = \int_V B_{ki}(\mathbf{x})C_{kl}^e(\mathbf{x})B_{lj}(\mathbf{x}) dV, \quad (2.29)$$

and  $\mathbf{f}_{ext}$  is the element equivalent external force vector

$$f_{ext,i} = \int_V N_{ki}(\mathbf{x})\bar{b}_k(\mathbf{x}) dV + \int_{\Gamma_t} N_{ki}(\mathbf{x})\bar{t}_k(\mathbf{x}) d\Gamma_t. \quad (2.30)$$

The discretized equations of equilibrium, Eq. (2.28), for the entire finite element mesh can be obtained by storing the unknown displacement values of all nodes in a global vector of nodal displacement values and by assembling the element stiffness matrices and the element external force vectors with respect to this vector. Due to the local character of the element shape functions, the global stiffness matrix is sparse and banded. This system of equations can then be solved for the unknown nodal displacement values.

For practical reasons, it is more convenient to derive shape functions for an element with a simple geometry defined in a local natural coordinate system  $\boldsymbol{\xi}$  and map this element and the corresponding element matrices and vectors into the global coordinate system  $\mathbf{x}$ . Assuming an isoparametric finite element, the same approximation for the displacement field and for the element geometry is used

$$u_i(\boldsymbol{\xi}) = \sum_{k=1}^{n_N} N^{(k)}(\boldsymbol{\xi}) \hat{u}_i^{(k)} \quad x_i(\boldsymbol{\xi}) = \sum_{k=1}^{n_N} N^{(k)}(\boldsymbol{\xi}) \hat{x}_i^{(k)}, \quad (2.31)$$

where  $\hat{\mathbf{x}}^{(k)}$  is the vector of global coordinates of node  $k$ . By applying the chain-rule, the

derivatives of the shape functions with respect to the global coordinates, required for the calculation of the strain-displacement matrix, can be obtained

$$\begin{bmatrix} \frac{\partial N^{(k)}}{\partial x_1} \\ \frac{\partial N^{(k)}}{\partial x_2} \\ \frac{\partial N^{(k)}}{\partial x_3} \end{bmatrix} = \underbrace{\begin{bmatrix} \frac{\partial \xi_1}{\partial x_1} & \frac{\partial \xi_2}{\partial x_1} & \frac{\partial \xi_3}{\partial x_1} \\ \frac{\partial \xi_1}{\partial x_2} & \frac{\partial \xi_2}{\partial x_2} & \frac{\partial \xi_3}{\partial x_2} \\ \frac{\partial \xi_1}{\partial x_3} & \frac{\partial \xi_2}{\partial x_3} & \frac{\partial \xi_3}{\partial x_3} \end{bmatrix}}_{\mathbf{J}^{-1}} \begin{bmatrix} \frac{\partial N^{(k)}}{\partial \xi_1} \\ \frac{\partial N^{(k)}}{\partial \xi_2} \\ \frac{\partial N^{(k)}}{\partial \xi_3} \end{bmatrix} = \underbrace{\begin{bmatrix} \frac{\partial x_1}{\partial \xi_1} & \frac{\partial x_2}{\partial \xi_1} & \frac{\partial x_3}{\partial \xi_1} \\ \frac{\partial x_1}{\partial \xi_2} & \frac{\partial x_2}{\partial \xi_2} & \frac{\partial x_3}{\partial \xi_2} \\ \frac{\partial x_1}{\partial \xi_3} & \frac{\partial x_2}{\partial \xi_3} & \frac{\partial x_3}{\partial \xi_3} \end{bmatrix}}_{\mathbf{J}} \begin{bmatrix} \frac{\partial N^{(k)}}{\partial x_1} \\ \frac{\partial N^{(k)}}{\partial x_2} \\ \frac{\partial N^{(k)}}{\partial x_3} \end{bmatrix}, \quad (2.32)$$

where  $\mathbf{J}$  is the Jacobian matrix. It is to be noted that in Eq. (2.32)  $N^{(k)}$  directly refers to the shape function of node  $k$  and should not be confused with the components of matrix  $\mathbf{N}$  given in Eq. (2.19). The integration of the element matrices and element vectors is performed in the local natural coordinate system. Using the substitution rule, the element stiffness matrix, given in Eq. (2.29), can be written as

$$K_{ij} = \iiint_{\xi} B_{ki}(\boldsymbol{\xi}) C_{kl}^e(\boldsymbol{\xi}) B_{lj}(\boldsymbol{\xi}) \det \mathbf{J}(\boldsymbol{\xi}) d\xi_1 d\xi_2 d\xi_3, \quad (2.33)$$

where  $\det \mathbf{J}$  is the determinant of the Jacobian matrix. Assuming that the boundary-surfaces with surface tractions can be described as a function of  $\xi_1$  and  $\xi_2$  and using integration by substitution, the element external force vector from Eq. (2.30) reads

$$\begin{aligned} f_{ext,i} &= \iiint_{\xi} N_{ki}(\boldsymbol{\xi}) \bar{b}_k(\boldsymbol{\xi}) \det J(\boldsymbol{\xi}) d\xi_1 d\xi_2 d\xi_3 \\ &+ \iint_{\xi_1 \xi_2} N_{ki}(\boldsymbol{\xi}) \bar{t}_k(\boldsymbol{\xi}) \sqrt{a_1(\boldsymbol{\xi}) a_2(\boldsymbol{\xi}) - a_3(\boldsymbol{\xi})^2} d\xi_1 d\xi_2, \end{aligned} \quad (2.34)$$

with

$$\begin{aligned} a_1 &= \left( \frac{\partial x_1}{\partial \xi_1} \right)^2 + \left( \frac{\partial x_2}{\partial \xi_1} \right)^2 + \left( \frac{\partial x_3}{\partial \xi_1} \right)^2 \\ a_2 &= \left( \frac{\partial x_1}{\partial \xi_2} \right)^2 + \left( \frac{\partial x_2}{\partial \xi_2} \right)^2 + \left( \frac{\partial x_3}{\partial \xi_2} \right)^2 \\ a_3 &= \frac{\partial x_1}{\partial \xi_1} \frac{\partial x_1}{\partial \xi_2} + \frac{\partial x_2}{\partial \xi_1} \frac{\partial x_2}{\partial \xi_2} + \frac{\partial x_3}{\partial \xi_1} \frac{\partial x_3}{\partial \xi_2}. \end{aligned} \quad (2.35)$$

It is to be noted that in the second term of Eq. (2.34) the surface area  $A$  of the element

boundary with surface tractions is expressed as

$$A = \iint_{\xi_1 \xi_2} \sqrt{a_1(\boldsymbol{\xi})a_2(\boldsymbol{\xi}) - a_3(\boldsymbol{\xi})^2} d\xi_1 d\xi_2, \quad (2.36)$$

cf. Bronstein et al. (1997). The analytical evaluation of the integrals in Eq. (2.33) and Eq. (2.34) is only possible in some special cases, e.g. for 4-node tetrahedral elements. In practice, the integration is performed numerically and the integrals are then replaced by sums

$$\mathbf{K} = \sum_{o=1}^{n_{IP}} w^{(o)} \mathbf{B}^T(\boldsymbol{\xi}^{(o)}) \mathbf{C}^e(\boldsymbol{\xi}^{(o)}) \mathbf{B}(\boldsymbol{\xi}^{(o)}) \det \mathbf{J}(\boldsymbol{\xi}^{(o)}) \quad (2.37)$$

$$\begin{aligned} \mathbf{f}_{ext} = & \sum_{o=1}^{n_{IP}} w^{(o)} \mathbf{N}^T(\boldsymbol{\xi}^{(o)}) \bar{\mathbf{b}}(\boldsymbol{\xi}^{(o)}) \det \mathbf{J}(\boldsymbol{\xi}^{(o)}) \\ & + \sum_{p=1}^{n_{TP}} w^{(p)} \mathbf{N}^T(\boldsymbol{\xi}^{(p)}) \bar{\mathbf{t}}(\boldsymbol{\xi}^{(p)}) \sqrt{a_1(\boldsymbol{\xi}^{(p)})a_2(\boldsymbol{\xi}^{(p)}) - a_3(\boldsymbol{\xi}^{(p)})^2}, \end{aligned} \quad (2.38)$$

where  $n_{IP}$  and  $n_{TP}$  are the number of integration points used for the numerical integration over the element volume and element boundary surface,  $\boldsymbol{\xi}^{(o)}$  and  $\boldsymbol{\xi}^{(p)}$  are the integration point coordinates in the local natural coordinate system and  $w^{(o)}$  and  $w^{(p)}$  are the corresponding weighting factors. Within the finite element method, Gauss quadrature is most commonly used for solid elements. Using an  $n$ -point Gauss quadrature rule exact results for polynomials with degree  $2n - 1$  can be obtained. For selected element types with different polynomial order, the position of the integration points and the corresponding weighting factors are given in Bathe (1995). Note that for elements with a complex geometry, e.g. curved surfaces, the elements of the stiffness matrix are no longer polynomials and an error due to the numerical integration with a Gauss quadrature is obtained. In most cases, this error is small and can be further reduced if the number of integration points is increased.

### 2.2.1 Interface Elements with Zero Thickness

Interface elements can be used to model displacement discontinuities, e.g. cohesive cracks, in a solid body. In finite element models, line interface elements in 2D, as illustrated in Fig. 2.1(a), or surface interface elements in 3D, as shown in Fig. 2.1(b), are used to connect two solid elements. The major difference compared to solid elements are the kinematic equations and the constitutive relations. For interface elements, the constitutive law describes the relationship between the relative displacements of the two interface sides and the tractions transferred through the interface. In this section, the concept of three-dimensional isoparametric interface elements is briefly introduced. A detailed description and the application to two-dimensional elements can be, for example, found in Gens et al. (1989); Mehlhorn and Kolleger (1995); Rots (1988).

For the twelve-node surface interface element, shown in Fig. 2.1(b), the geometry approx-

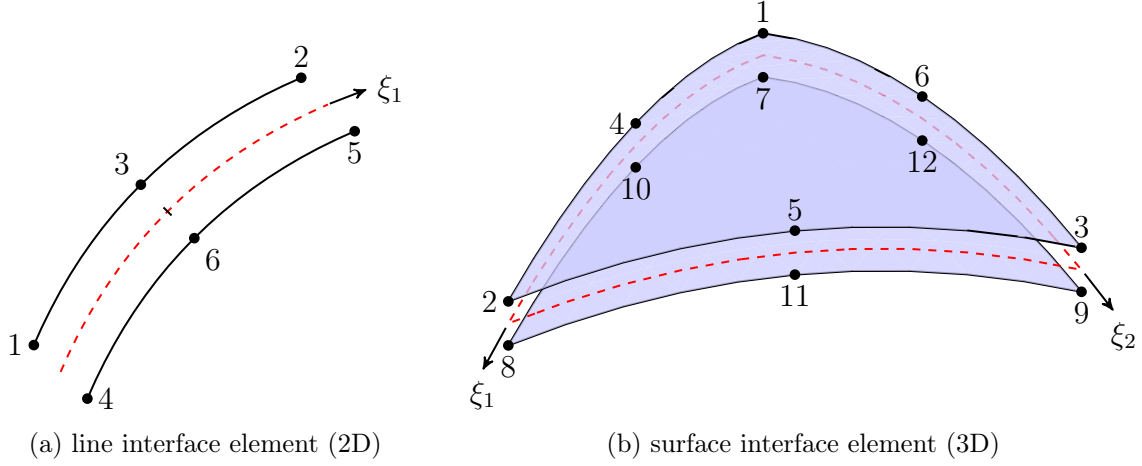


Figure 2.1: Continuous interface elements.

imation of the mid-surface is given by

$$\mathbf{x}(\boldsymbol{\xi}) = \sum_{i=1}^6 N^{(i)}(\boldsymbol{\xi}) \frac{\hat{\mathbf{x}}^{(i)} + \hat{\mathbf{x}}^{(i+6)}}{2} \quad (2.39)$$

and the displacement field of each surface is interpolated by

$$\mathbf{u}^{(u)}(\boldsymbol{\xi}) = \sum_{i=1}^6 N^{(i)}(\boldsymbol{\xi}) \hat{\mathbf{u}}^{(i)} \quad \mathbf{u}^{(l)}(\boldsymbol{\xi}) = \sum_{i=1}^6 N^{(i)}(\boldsymbol{\xi}) \hat{\mathbf{u}}^{(i+6)}, \quad (2.40)$$

where superscript  $u$  indicates the upper and superscript  $l$  the lower interface surface. In order to clearly identify the upper surface of an interface element with zero thickness, an additional reference node is introduced. This node must be located above the upper side of the interface. The kinematic equations can then be written as

$$\Delta \mathbf{u}^{(x)}(\boldsymbol{\xi}) = \mathbf{u}^{(u)}(\boldsymbol{\xi}) - \mathbf{u}^{(l)}(\boldsymbol{\xi}), \quad (2.41)$$

where  $\Delta \mathbf{u}^{(x)}$  is the relative displacement vector defined in the global coordinate system. Storing the unknown nodal displacement values in vector  $\mathbf{d}$ , this equation can be rewritten as

$$\Delta u_i^{(x)}(\boldsymbol{\xi}) = B_{ij}(\boldsymbol{\xi}) d_j \quad (2.42)$$

with

$$\mathbf{B} = \begin{bmatrix} N^{(1)} & 0 & 0 & \dots & N^{(6)} & 0 & 0 & -N^{(1)} & 0 & 0 & \dots & -N^{(6)} & 0 & 0 \\ 0 & N^{(1)} & 0 & \dots & 0 & N^{(6)} & 0 & 0 & -N^{(1)} & 0 & \dots & 0 & -N^{(6)} & 0 \\ 0 & 0 & N^{(1)} & \dots & 0 & 0 & N^{(6)} & 0 & 0 & -N^{(1)} & \dots & 0 & 0 & -N^{(6)} \end{bmatrix} \quad (2.43)$$

$$\mathbf{d}^T = \left[ \hat{u}_1^{(1)} \quad \hat{u}_2^{(1)} \quad \hat{u}_3^{(1)} \quad \hat{u}_1^{(2)} \quad \hat{u}_2^{(2)} \quad \hat{u}_3^{(2)} \quad \dots \quad \hat{u}_1^{(12)} \quad \hat{u}_2^{(12)} \quad \hat{u}_3^{(12)} \right]. \quad (2.44)$$

In general, the constitutive equations are given in the local element coordinate system, which is defined by the normal vector  $\mathbf{n}$  and two vectors  $\mathbf{t}_1$ ,  $\mathbf{t}_2$  tangential to the interface mid-surface. Assuming linear elastic behavior, the relationship between relative displacements  $\Delta \mathbf{u}$  and interface tractions  $\mathbf{t}$  in the local coordinate system reads

$$\begin{bmatrix} t_n \\ t_{t_1} \\ t_{t_2} \end{bmatrix} = \underbrace{\begin{bmatrix} K_{p,n} & 0 & 0 \\ 0 & K_{p,t} & 0 \\ 0 & 0 & K_{p,t} \end{bmatrix}}_{\mathbf{C}^e} \begin{bmatrix} \Delta u_n \\ \Delta u_{t_1} \\ \Delta u_{t_2} \end{bmatrix}, \quad (2.45)$$

where  $K_p$  is the so-called penalty stiffness. The transformation of relative displacements and interface tractions between the global and the local coordinate system can be written as

$$\begin{bmatrix} \Delta u_n \\ \Delta u_{t_1} \\ \Delta u_{t_2} \end{bmatrix} = \underbrace{\begin{bmatrix} n_1 & t_{1,1} & t_{2,1} \\ n_2 & t_{1,2} & t_{2,2} \\ n_3 & t_{1,3} & t_{2,3} \end{bmatrix}}_{\mathbf{T}} \begin{bmatrix} \Delta u_1 \\ \Delta u_2 \\ \Delta u_3 \end{bmatrix} \quad \begin{bmatrix} t_1 \\ t_2 \\ t_3 \end{bmatrix} = \underbrace{\begin{bmatrix} n_1 & n_2 & n_3 \\ t_{1,1} & t_{1,2} & t_{1,3} \\ t_{2,1} & t_{2,2} & t_{2,3} \end{bmatrix}}_{\mathbf{T}^T = \mathbf{T}^{-1}} \begin{bmatrix} t_n \\ t_{t_1} \\ t_{t_2} \end{bmatrix}, \quad (2.46)$$

where  $\mathbf{T}$  is a transformation matrix describing a pure rotation (the normal and tangential vectors are orthogonal and normalized). Using Eqs. (2.45) and (2.46), the constitutive equations in the global coordinate system can be written as

$$\begin{bmatrix} t_1 \\ t_2 \\ t_3 \end{bmatrix} = \begin{bmatrix} n_1 & n_2 & n_3 \\ t_{1,1} & t_{1,2} & t_{1,3} \\ t_{2,1} & t_{2,2} & t_{2,3} \end{bmatrix} \begin{bmatrix} K_{p,n} & 0 & 0 \\ 0 & K_{p,t} & 0 \\ 0 & 0 & K_{p,t} \end{bmatrix} \begin{bmatrix} n_1 & t_{1,1} & t_{2,1} \\ n_2 & t_{1,2} & t_{2,2} \\ n_3 & t_{1,3} & t_{2,3} \end{bmatrix} \begin{bmatrix} \Delta u_1 \\ \Delta u_2 \\ \Delta u_3 \end{bmatrix}. \quad (2.47)$$

By substituting Eqs. (2.42) and (2.47) into the principle of virtual displacements, the element stiffness matrix is obtained

$$K_{ij} = \iint_{\xi_1 \xi_2} B_{ki}(\boldsymbol{\xi}) T_{mk}(\boldsymbol{\xi}) C_{mn}^e(\boldsymbol{\xi}) T_{nl}(\boldsymbol{\xi}) B_{lj}(\boldsymbol{\xi}) \sqrt{a_1(\boldsymbol{\xi}) a_2(\boldsymbol{\xi}) - a_3(\boldsymbol{\xi})^2} d\xi_1 d\xi_2, \quad (2.48)$$

where the parameters  $a_1$ ,  $a_2$  and  $a_3$  are given by Eq. (2.35). Using a numerical integration scheme Eq. (2.48) reads

$$\mathbf{K} = \sum_{o=1}^{n_{IP}} w^{(o)} \mathbf{B}^T(\boldsymbol{\xi}^{(o)}) \mathbf{T}^T(\boldsymbol{\xi}^{(o)}) \mathbf{C}^e(\boldsymbol{\xi}^{(o)}) \mathbf{T}(\boldsymbol{\xi}^{(o)}) \mathbf{B}(\boldsymbol{\xi}^{(o)}) \sqrt{a_1(\boldsymbol{\xi}^{(o)}) a_2(\boldsymbol{\xi}^{(o)}) - a_3(\boldsymbol{\xi}^{(o)})^2}, \quad (2.49)$$

where  $n_{IP}$  is the number of integration points,  $\boldsymbol{\xi}^{(o)}$  are the coordinates of integration point  $o$  in the local natural coordinate system and  $w^{(o)}$  is the corresponding weighting factor.

Based on Schellekens and de Borst (1993), the performance of two different integration schemes - Gaussian quadrature and Newton-Cotes formulas - for line interface elements is investigated using two-dimensional, linear elastic simulations of a notched four-point

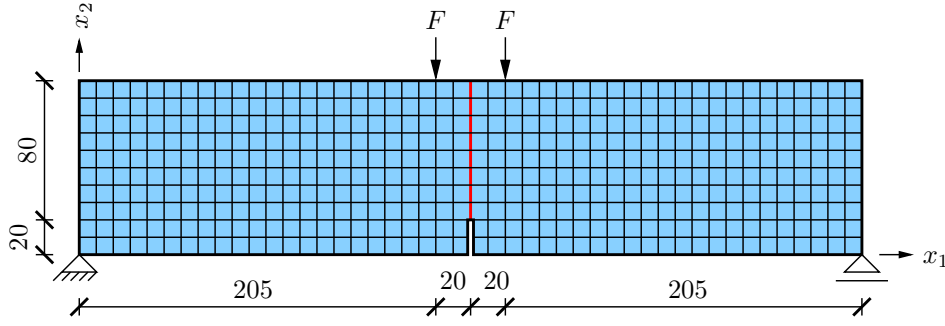


Figure 2.2: Finite element mesh for linear elastic analysis of notched 4-point bending beam with line interface elements above the notch (dimensions in  $mm$ , thickness:  $100\text{ mm}$ ).

bending beam. Figure 2.2 shows the specimen geometry with boundary conditions and loading conditions. The beam is discretized by rectangular plane elements with an average element size of  $10\text{ mm}$ . A Young's modulus  $E = 20\,000\text{ N/mm}^2$  and a Poisson's ratio  $\nu = 0.2$  is used for these continuum elements. Line interface elements (highlighted by the red line in Fig. 2.2) are introduced in front of the notch to simulate the potential development of a discrete crack. In order to approximate a closed crack during the linear elastic analysis, the penalty stiffness normal and tangential to the interface is chosen as  $K_{p,n} = K_{p,t} = 100\,000\text{ N/mm}^3$ . The diagrams in Fig. 2.3 show the distribution of the normal interface tractions for finite elements with linear and quadratic interpolation functions. Using Gauss quadrature, which is exact for the interface elements, oscillations in the normal tractions are observed, which are caused by the high displacement gradient in the first interface element in front of the notch. This effect can be significantly reduced if Newton-Cotes quadrature with the same number of integration points as for the Gauss quadrature is applied. In one-dimensional problems, Gauss quadrature with  $n$  integration points allows for the exact integration of a polynomial with degree  $2n - 1$ , whereas an

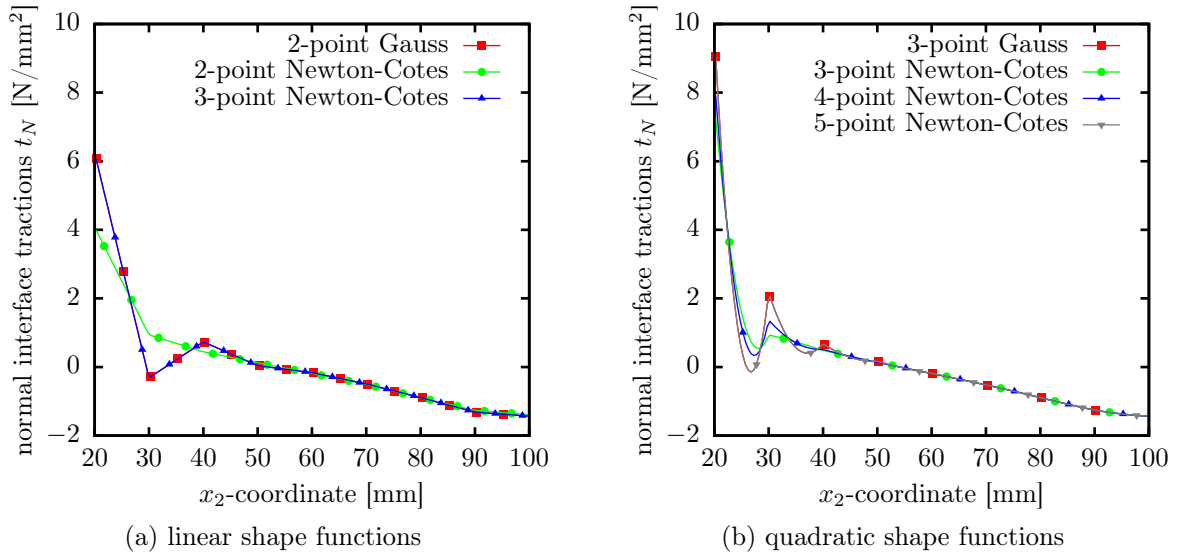


Figure 2.3: Normal interface tractions in front of the notch of the 4-point bending beam.

$n$ -point Newton-Cotes quadrature is only exact for a polynomial up to degree  $n - 1$ . As a result, the numerical integration with the proposed Newton-Cotes quadrature is inexact even for interface elements with straight boundary lines. If higher order Newton-Cotes rules are used which result in an exact integration of the interface (3-point rule for linear interpolation functions and 5-point rule for quadratic shape functions), the same results as for simulations with a Gauss quadrature are obtained.

In this thesis, a three-point Gauss rule is used for the 12-node surface interface element and a three-point Newton-Cotes rule is applied for the numerical integration of the 6-node line interface element.

## 2.3 Material Nonlinearity

In the previous sections, a linear relationship between stresses and strains has been assumed. Consequently, the material properties are constant and independent from the deformation state of the structure. In real materials, this assumption is, in general, valid until a certain deformation is reached. If the loading is further increased, changes within the material micro- or nano-structure result in modified macroscopic material parameters. As a consequence, the constitutive equations, representing the relationship between stresses and strains, become nonlinear. Furthermore, the stresses may depend not only on the current deformation state, but also on the deformation history of the material. Using the finite element method with a nonlinear stress strain relationship, the weak form of the equilibrium can be written as

$$\delta d_i \int_V B_{ji}(\mathbf{x}) \sigma_j(\boldsymbol{\varepsilon}(\mathbf{x})) dV = \delta d_i \int_V N_{ji}(\mathbf{x}) \bar{b}_j(\mathbf{x}) dV + \delta d_i \int_{\Gamma_t} N_{ji}(\mathbf{x}) \bar{t}_j(\mathbf{x}) d\Gamma_t. \quad (2.50)$$

The final system of equations, representing the equilibrium of the discretized system, is given by

$$\mathbf{f}_{int}(\mathbf{d}) = \mathbf{f}_{ext}, \quad (2.51)$$

where  $\mathbf{f}_{ext}$  is the external force vector

$$f_{ext,i} = \int_V N_{ji}(\mathbf{x}) \bar{b}_j(\mathbf{x}) dV + \int_{\Gamma_t} N_{ji}(\mathbf{x}) \bar{t}_j(\mathbf{x}) d\Gamma_t, \quad (2.52)$$

and  $\mathbf{f}_{int}$  is the vector of internal forces

$$f_{int,i}(\mathbf{d}) = \int_V B_{ji}(\mathbf{x}) \sigma_j(\boldsymbol{\varepsilon}(\mathbf{x})) dV, \quad (2.53)$$

which depends on the unknown nodal displacement values in a nonlinear way. The concept of linearization can be used for the numerical solution of this nonlinear system of equations.

Starting from a strain state  $\bar{\boldsymbol{\varepsilon}}$  for which the stresses are known, the constitutive equations in the vicinity of  $\bar{\boldsymbol{\varepsilon}}$  can be approximated by a truncated Taylor series

$$\sigma_i(\bar{\boldsymbol{\varepsilon}} + \boldsymbol{\delta\varepsilon}) = \sigma_i(\bar{\boldsymbol{\varepsilon}}) + \frac{\partial\sigma_i}{\partial\varepsilon_j}(\bar{\boldsymbol{\varepsilon}}) \delta\varepsilon_j = \sigma_i(\bar{\boldsymbol{\varepsilon}}) + C_{ij}(\bar{\boldsymbol{\varepsilon}}) \delta\varepsilon_j, \quad (2.54)$$

where  $C_{ij} = \partial\sigma_i/\partial\varepsilon_j$  is the tangent material matrix. By substituting the linearized constitutive equations into Eq. (2.53), and by considering the kinematic equations in Eq. (2.2), an approximation for the internal forces can be obtained

$$f_{int,i}(\bar{\boldsymbol{d}} + \boldsymbol{\delta d}) = \int_V B_{ji}(\boldsymbol{x}) \sigma_j(\bar{\boldsymbol{\varepsilon}}(\boldsymbol{x})) dV + \int_V B_{ji}(\boldsymbol{x}) C_{jk}(\bar{\boldsymbol{\varepsilon}}(\boldsymbol{x})) \delta\varepsilon_k(\boldsymbol{x}) dV \quad (2.55)$$

$$= f_{int,i}(\bar{\boldsymbol{d}}) + \int_V B_{ji}(\boldsymbol{x}) C_{jk}(\bar{\boldsymbol{\varepsilon}}(\boldsymbol{x})) B_{kl}(\boldsymbol{x}) dV \delta d_l \quad (2.56)$$

$$= f_{int,i}(\bar{\boldsymbol{d}}) + K_{il}(\bar{\boldsymbol{d}}) \delta d_l, \quad (2.57)$$

where  $\bar{\boldsymbol{d}}$  is the vector of nodal displacement values representing the deformation state for which the stresses and internal forces are known, and  $K_{ij} = \partial f_{int,i}/\partial d_j$  is the tangential stiffness matrix. In the implementation, a numerical integration scheme is used for the evaluation of the element internal forces and the tangent element stiffness matrix

$$\boldsymbol{f}_{int}(\bar{\boldsymbol{d}}) = \sum_{o=1}^{n_{IP}} w^{(o)} \boldsymbol{B}^T(\boldsymbol{\xi}^{(o)}) \boldsymbol{\sigma}(\bar{\boldsymbol{\varepsilon}}(\boldsymbol{\xi}^{(o)})) \det \boldsymbol{J}(\boldsymbol{\xi}^{(o)}) \quad (2.58)$$

$$\boldsymbol{K}(\bar{\boldsymbol{d}}) = \sum_{o=1}^{n_{IP}} w^{(o)} \boldsymbol{B}^T(\boldsymbol{\xi}^{(o)}) \boldsymbol{C}(\bar{\boldsymbol{\varepsilon}}(\boldsymbol{\xi}^{(o)})) \boldsymbol{B}(\boldsymbol{\xi}^{(o)}) \det \boldsymbol{J}(\boldsymbol{\xi}^{(o)}), \quad (2.59)$$

with

$$\bar{\boldsymbol{\varepsilon}}(\boldsymbol{\xi}^{(o)}) = \boldsymbol{B}(\boldsymbol{\xi}^{(o)}) \bar{\boldsymbol{d}} \quad (2.60)$$

where  $n_{IP}$  is the number of integration points,  $\boldsymbol{\xi}^{(o)}$  are the coordinates of integration point  $o$  in the local natural coordinate system and  $w^{(o)}$  is the corresponding weighting factor. The global vector of internal forces and the global tangent stiffness matrix is assembled from the element contributions.

## 2.4 Solution Strategies

The nonlinear behavior of structures can be characterized by load-displacement curves, as for example illustrated in Fig. 2.4. Each point on this curve represents an admissible equilibrium state of the structure in terms of a monitored displacement value and the corresponding external force. Additionally, the equilibrium state can be characterized by the opening displacement of a crack or by the amount of dissipated energy. In order to obtain the equilibrium path of a structure by numerical simulations, the load path is



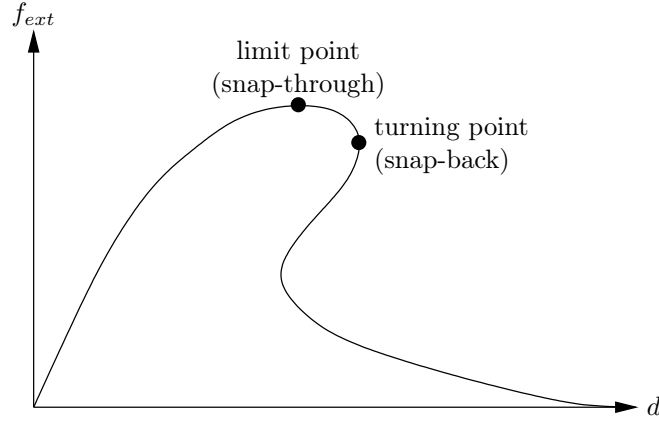


Figure 2.4: Load-displacement curve of a softening material, including snap-back.

subdivided into several load increments and the structural response after each load step is computed using the equilibrium equations given in Eq. (2.51). In this section, several step size control techniques are introduced. In all of these techniques, Newton's method is applied to iteratively solve the generally nonlinear system of equations for each load increment.

### 2.4.1 Load Control

Using direct load control, the load increment  $n$  is characterized by the vector of external forces  $\mathbf{f}_{ext}^{(n)}$  that acts on the structure at the end of that load step. Consequently, the load-path is then described by a sequence  $\mathbf{f}_{ext}^{(1)}, \mathbf{f}_{ext}^{(2)}, \dots, \mathbf{f}_{ext}^{(n_L)}$  and the aim of the nonlinear simulation is to find the corresponding deformations  $\mathbf{d}^{(1)}, \mathbf{d}^{(2)}, \dots, \mathbf{d}^{(n_L)}$ , such that the equilibrium equation

$$\mathbf{f}_{int}^{(n)} = \mathbf{f}_{ext}^{(n)} \quad n = 1, 2, 3, \dots, n_L \quad (2.61)$$

is satisfied, where  $n_L$  is the number of load increments, and  $\mathbf{f}_{int}^{(n)} = \mathbf{f}_{int}(\mathbf{d}^{(n)})$  is the vector of internal forces, given in Eq. (2.53). By applying Newton's method, an iterative solution procedure for the unknown nodal displacement values is obtained. In the  $i$ -th iteration step of the  $n$ -th load increment, the linearized system of equations reads

$$\left. \begin{aligned} \mathbf{K}^{(n,i-1)} \delta \mathbf{d}^{(n,i)} &= \mathbf{r}^{(n,i-1)} \\ \mathbf{d}^{(n,i)} &= \mathbf{d}^{(n,i-1)} + \delta \mathbf{d}^{(n,i)} \end{aligned} \right\} \quad i = 1, 2, 3, \dots \quad (2.62)$$

where  $\mathbf{K}^{(n,i)} = \mathbf{K}(\mathbf{d}^{(n,i)})$  is the tangential stiffness matrix,  $\mathbf{r}^{(n,i)} = \mathbf{f}_{ext}^{(n)} - \mathbf{f}_{int}(\mathbf{d}^{(n,i)})$  is the residual vector, which is also known as vector of out-of-balance forces, and  $\delta \mathbf{d}^{(n,i+1)}$  is the correction of the displacement vector. The displacement values obtained for the previous load increment are used as the starting vector  $\mathbf{d}^{(n,0)} = \mathbf{d}^{(n-1)}$  of the Newton iteration. It is to be noted that in each iteration step a new (consistent) tangent stiffness matrix is calculated. The iterative procedure given in Eq. (2.62) is repeated until a certain

convergence criterion is satisfied. In this thesis, two different convergence criteria are used. The first criterion is based on the correction of the displacement vector

$$\|\delta \mathbf{d}^{(n,i)}\|_2 \leq \epsilon_r \|\mathbf{d}^{(n,i)}\|_2 + \epsilon_a, \quad (2.63)$$

where  $\|\dots\|_2$  denotes the  $L_2$ -norm of a vector,  $\epsilon_r$  is the relative tolerance and  $\epsilon_a$  is the absolute tolerance. As a result, the iteration is stopped if the correction of the displacement vector becomes small. In some situations, the obtained displacement approximation does not satisfy the equilibrium equations in Eq. (2.61) with sufficient accuracy. This motivates a second convergence criterion which is based on the out-of-balance forces

$$\|\mathbf{r}^{(n,i)}\|_2 = \|\mathbf{f}_{ext}^{(n)} - \mathbf{f}_{int}^{(n,i)}\|_2 \leq \epsilon_r \|\mathbf{f}_{ext}^{(n)} - \mathbf{f}_{ext}^{(n-1)}\|_2 + \epsilon_a. \quad (2.64)$$

Newton's method converges if the initial guess is sufficiently close to the desired solution. If the iteration diverges, i.e. a predefined number of iteration steps is reached without convergence or the  $L_2$ -norm of the out-of-balance force vector exceeds a certain value, the load increment is reduced and the iteration is restarted from the last converged load increment. Since in standard load-control the external forces are successively increased, this solution strategy fails if the load-carrying capacity of the structure is reached. Consequently, only the nonlinear structural response up to the limit point of the load-displacement curve, shown in Fig. 2.4, can be simulated by using load control. More advanced solution strategies, such as direct displacement control or load-displacement-constraint methods are required to simulate the post-peak behavior of the structure.

## 2.4.2 Direct Displacement Control

Using direct displacement control, the nodal degrees of freedom  $\mathbf{d}^{(n)}$  of load step  $n$  can be subdivided into two groups  $[\mathbf{d}_1^{(n)}, \mathbf{d}_2^{(n)}]^T$ . Unknown nodal displacement values belong to the first group. The second group are nodal degrees of freedom for which the displacement values are prescribed. According to this subdivision, the vectors of internal and external forces are partitioned into  $[\mathbf{f}_{int,1}^{(n)}, \mathbf{f}_{int,2}^{(n)}]^T$  and  $[\mathbf{f}_{ext,1}^{(n)}, \mathbf{f}_{ext,2}^{(n)}]^T$ , respectively. Consequently, the equilibrium equations, given in Eq. (2.51) can be rewritten as

$$\mathbf{f}_{int,1}^{(n)} = \mathbf{f}_{int,1}(\mathbf{d}_1^{(n)}, \mathbf{d}_2^{(n)}) = \mathbf{f}_{ext,1}^{(n)} \quad (2.65)$$

$$\mathbf{f}_{int,2}^{(n)} = \mathbf{f}_{int,2}(\mathbf{d}_1^{(n)}, \mathbf{d}_2^{(n)}) = \mathbf{f}_{ext,2}^{(n)}. \quad (2.66)$$

By using the concept of linearization, this, in general, nonlinear system of equations is replaced by a linear system of equations, which reads in the first iteration step ( $i = 1$ ) of the  $n$ -th load increment

$$\mathbf{f}_{int,1}^{(n,0)} + \mathbf{K}_{11}^{(n,0)} \delta \mathbf{d}_1^{(n,1)} + \mathbf{K}_{12}^{(n,0)} \delta \mathbf{d}_2^{(n,1)} = \mathbf{f}_{ext,1}^{(n)} \quad (2.67)$$

$$\mathbf{f}_{int,2}^{(n,0)} + \mathbf{K}_{21}^{(n,0)} \delta \mathbf{d}_1^{(n,1)} + \mathbf{K}_{22}^{(n,0)} \delta \mathbf{d}_2^{(n,1)} = \mathbf{f}_{ext,2}^{(n)}, \quad (2.68)$$

where  $\mathbf{K}^{(n,i)} = \mathbf{K}(\mathbf{d}_1^{(n)}, \mathbf{d}_2^{(n)})$  is the corresponding partitioned tangent stiffness matrix which is defined as

$$\mathbf{K} = \frac{\partial \mathbf{f}_{int}}{\partial \mathbf{d}} = \begin{bmatrix} \frac{\partial \mathbf{f}_{int,1}}{\partial \mathbf{d}_1} & \frac{\partial \mathbf{f}_{int,1}}{\partial \mathbf{d}_2} \\ \frac{\partial \mathbf{f}_{int,2}}{\partial \mathbf{d}_1} & \frac{\partial \mathbf{f}_{int,2}}{\partial \mathbf{d}_2} \end{bmatrix} = \begin{bmatrix} \mathbf{K}_{11} & \mathbf{K}_{12} \\ \mathbf{K}_{21} & \mathbf{K}_{22} \end{bmatrix}. \quad (2.69)$$

Since the displacement increment  $\delta \mathbf{d}_2^{(n,1)} = \mathbf{d}_2^{(n)} - \mathbf{d}_2^{(n-1)}$  is known from the prescribed displacement values, Eq. (2.67) can be rewritten as

$$\mathbf{K}_{11}^{(n,0)} \delta \mathbf{d}_1^{(n,1)} = \mathbf{f}_{ext,1}^{(n)} - \mathbf{f}_{int,1}^{(n,0)} - \mathbf{K}_{12}^{(n,0)} \delta \mathbf{d}_2^{(n,1)}. \quad (2.70)$$

This system of equations can be solved for the correction of the unknown displacement vector  $\delta \mathbf{d}_1^{(n,1)}$  independently from Eq. (2.68). Assuming that the start vectors are defined as  $\mathbf{d}_1^{(n,0)} = \mathbf{d}_1^{(n-1)}$  and  $\mathbf{d}_2^{(n,0)} = \mathbf{d}_2^{(n-1)}$ , the first approximation of the displacement vectors can be obtained

$$\mathbf{d}_1^{(n,1)} = \mathbf{d}_1^{(n,0)} + \delta \mathbf{d}_1^{(n,1)} \quad (2.71)$$

$$\mathbf{d}_2^{(n,1)} = \mathbf{d}_2^{(n,0)} + \delta \mathbf{d}_2^{(n,1)}. \quad (2.72)$$

After the first iteration step the displacement vector  $\mathbf{d}_2^{(n,1)} = \mathbf{d}_2^{(n)}$  satisfies the prescribed displacement values. Consequently, in the following iteration steps the iterative solution procedure for the unknown displacements  $\mathbf{d}_1^{(n)}$  can be simplified to

$$\left. \begin{aligned} \mathbf{K}_{11}^{(n,i-1)} \delta \mathbf{d}_1^{(n,i)} &= \mathbf{r}_1^{(n,i-1)} \\ \mathbf{d}_1^{(n,i)} &= \mathbf{d}_1^{(n,i-1)} + \delta \mathbf{d}_1^{(n,i)} \end{aligned} \right\} \quad i = 2, 3, 4, \dots, \quad (2.73)$$

where  $\mathbf{r}_1^{(n,i)} = \mathbf{f}_{ext,1}^{(n)} - \mathbf{f}_{int,1}^{(n,i)}$  is the vector of out-of-balance forces that corresponds to the unknown nodal displacement values. This iteration is repeated until the convergence criterion, given by Eq. (2.63) or Eq. (2.64), is satisfied. Direct displacement control fails, if, for the controlled nodal degree of freedom, the corresponding load displacement-curve exhibits a snap-back, as illustrated in Fig. 2.4. If the turning point is reached, the iteration diverges independently from the chosen load-step size since the displacement increment of the controlled nodal degree of freedom is successively increased. Alternatively, advanced incrementation control techniques such as load-displacement-constraint methods can be used for very brittle failure, which is characterized by a snap-back in the global load-displacement curve.

### 2.4.3 Load-Displacement-Constraint Methods

In load-displacement-constraint methods, the values of the external forces or the displacements at the supports after each load-step are not prescribed in advance. Instead, the

external load vector is parametrized by a scalar load factor  $\mu$

$$\mathbf{f}_{ext} = \mathbf{f}_0 + \mu \hat{\mathbf{f}}, \quad (2.74)$$

where  $\mathbf{f}_0$  is a vector of constant loads, e.g. the dead load of the structure, and  $\hat{\mathbf{f}}$  is a given reference load vector. Assuming a constant load factor in each load step, standard load control is obtained. If the load factor is considered as an unknown during the iteration process, the equilibrium equation, Eq. (2.51), is enhanced by an additional constraint equation  $l$

$$\mathbf{f}_{int}^{(n)} = \mathbf{f}_{int}(\mathbf{d}^{(n)}) = \mathbf{f}_0 + \mu^{(n)} \hat{\mathbf{f}} \quad (2.75)$$

$$l^{(n)} = l(\mathbf{d}^{(n)}, \mu^{(n)}) = 0. \quad (2.76)$$

Linearization of Eq. (2.75) in the  $i$ -th iteration of load increment  $n$  leads to

$$\mathbf{K}^{(n,i-1)} \delta \mathbf{d}^{(n,i)} = \mathbf{f}_0 + \mu^{(n,i-1)} \hat{\mathbf{f}} - \mathbf{f}_{int}^{(n,i-1)} + \delta \mu^{(n,i)} \hat{\mathbf{f}}, \quad i = 1, 2, 3, \dots, \quad (2.77)$$

where  $\delta \mu^{(n,i)}$  is the unknown correction of the load factor. Using the indirect solution procedure proposed by Ramm (1980) and Crisfield (1982), the unknown displacement correction is decomposed into two parts

$$\delta \mathbf{d}^{(n,i)} = \delta \mathbf{d}_0^{(n,i)} + \delta \mu^{(n,i)} \delta \mathbf{d}_f^{(n,i)}. \quad (2.78)$$

The first part, vector  $\delta \mathbf{d}_0^{(n,i)}$ , corresponds to the first three terms on the right hand side of Eq. (2.77) which are known

$$\mathbf{K}^{(n,i-1)} \delta \mathbf{d}_0^{(n,i)} = \mathbf{r}^{(n,i-1)} = \mathbf{f}_0 + \mu^{(n,i-1)} \hat{\mathbf{f}} - \mathbf{f}_{int}^{(n,i-1)}. \quad (2.79)$$

The second part of the displacement correction, vector  $\delta \mathbf{d}_f^{(n,i)}$ , is obtained from the reference load vector

$$\mathbf{K}^{(n,i-1)} \delta \mathbf{d}_f^{(n,i)} = \hat{\mathbf{f}}. \quad (2.80)$$

Consequently, the correction of the displacement vector can be expressed as function of the unknown correction of the load factor. By substitution of Eq. (2.78) into the constraint equation, Eq. (2.76), the correction of the load factor can be calculated.

Direct displacement control can be obtained by assuming a constant displacement value  $d_{const}$  for a single nodal degree of freedom  $d_k$ . The corresponding constraint equation reads

$$d_k^{(n,i-1)} + \delta d_k^{(n,i)} - d_{const} = 0. \quad (2.81)$$

By substituting Eq. (2.78) into Eq. (2.81), a linear equation is obtained which can be

solved for the correction of the load factor

$$\delta\mu^{(n,i)} = \frac{d_{const} - d_k^{(n,i-1)} - \delta d_{0,k}^{(n,i)}}{\delta d_{f,k}^{(n,i)}}. \quad (2.82)$$

More advanced definitions of the constraint equation such as arc-length, indirect displacement control or energy release control, which allow for more complex load paths and the simulation of structures for which the global load-displacement curve exhibits snap-through and snap-back, are introduced in the next paragraphs.

### Arc-Length

The most popular load-displacement-constraint method is the arc-length method introduced by Wempner (1971) and Riks (1972). In this method, the size of the load increment is represented by the geometrical distance between the initial and the final state in the global load-displacement space – the so-called arc-length. According to Crisfield (1983), the constraint equation for the spherical arc-length method can be written as

$$\Delta\mathbf{d}^{(n)T} \Delta\mathbf{d}^{(n)} + b \Delta\mu^{(n)2} \hat{\mathbf{f}}^T \hat{\mathbf{f}} - \Delta l^2 = 0 \quad (2.83)$$

where  $\Delta l$  is the prescribed arc-length, and  $b$  is a scaling parameter that weights the relative contribution of loads and displacements. In the  $i$ -th iteration of the  $n$ -th load increment this constraint equation reads

$$\left( \Delta\mathbf{d}^{(n,i-1)} + \delta\mathbf{d}^{(n,i)} \right)^T \left( \Delta\mathbf{d}^{(n,i-1)} + \delta\mathbf{d}^{(n,i)} \right) + b \left( \Delta\mu^{(n,i-1)} + \delta\mu^{(n,i)} \right)^2 \hat{\mathbf{f}}^T \hat{\mathbf{f}} - \Delta l^2 = 0, \quad (2.84)$$

where  $\Delta\mathbf{d}^{(n,i)}$  are the accumulated corrections of the displacement vector

$$\Delta\mathbf{d}^{(n,i)} = \sum_{k=1}^i \delta\mathbf{d}^{(n,k)} \quad \Delta\mathbf{d}^{(n,0)} = 0 \quad (2.85)$$

and  $\Delta\mu^{(n,i)}$  are the accumulated corrections of the load factor

$$\Delta\mu^{(n,i)} = \sum_{k=1}^i \delta\mu^{(n,k)} \quad \Delta\mu^{(n,0)} = 0. \quad (2.86)$$

Substitution of Eq. (2.78) into Eq. (2.84) yields a quadratic equation

$$a_1 \delta\mu^{(n,i)2} + 2 a_2 \delta\mu^{(n,i)} + a_3 = 0, \quad (2.87)$$

with

$$\begin{aligned}
 a_1 &= \delta \mathbf{d}_f^{(n,i)T} \delta \mathbf{d}_f^{(n,i)} + b \hat{\mathbf{f}}^T \hat{\mathbf{f}} \\
 a_2 &= \delta \mathbf{d}_f^{(n,i)T} \left( \Delta \mathbf{d}^{(n,i-1)} + \delta \mathbf{d}_0^{(n,i)} \right) + b \Delta \mu^{(n,i-1)} \hat{\mathbf{f}}^T \hat{\mathbf{f}} \\
 a_3 &= \left( \Delta \mathbf{d}^{(n,i-1)} + \delta \mathbf{d}_0^{(n,i)} \right)^T \left( \Delta \mathbf{d}^{(n,i-1)} + \delta \mathbf{d}_0^{(n,i)} \right) + b \Delta \mu^{(n,i-1)^2} \hat{\mathbf{f}}^T \hat{\mathbf{f}} - \Delta l^2
 \end{aligned} \tag{2.88}$$

which can be solved for the correction of the load factor  $\delta \mu^{(n,i)}$ . In general, Eq. (2.87) has two real solutions  $\delta \mu_1^{(n,i)}$  and  $\delta \mu_2^{(n,i)}$ , which correspond to two trial states

$$\Delta \mathbf{d}_1^{(n,i)} = \Delta \mathbf{d}^{(n,i-1)} + \delta \mathbf{d}_0^{(n,i)} + \delta \mu_1^{(n,i)} \delta \mathbf{d}_f^{(n,i)} \quad \Delta \mu_1^{(n,i)} = \Delta \mu^{(n,i-1)} + \delta \mu_1^{(n,i)} \tag{2.89}$$

$$\Delta \mathbf{d}_2^{(n,i)} = \Delta \mathbf{d}^{(n,i-1)} + \delta \mathbf{d}_0^{(n,i)} + \delta \mu_2^{(n,i)} \delta \mathbf{d}_f^{(n,i)} \quad \Delta \mu_2^{(n,i)} = \Delta \mu^{(n,i-1)} + \delta \mu_2^{(n,i)} \tag{2.90}$$

with distance  $\Delta l$  from the last equilibrium state  $(\mathbf{d}^{(n-1)}, \mu^{(n-1)})$ . One crucial point in nonlinear simulations using the arc-length method is the selection of the right solution. In this thesis, the cylindrical arc-length method which can be derived from Eq. (2.83) by setting  $b = 0$  is used. For this method, Crisfield (1991) proposes to select  $\Delta \mu^{(n,i)}$  such that the smallest angle between the trial displacement increment,  $\Delta \mathbf{d}_1^{(n,i)}$  or  $\Delta \mathbf{d}_2^{(n,i)}$ , and the previous displacement increment,  $\Delta \mathbf{d}^{(n,i)}$ , is obtained

$$\max \left( \frac{\Delta \mathbf{d}^{(n,i-1)T} \Delta \mathbf{d}_1^{(n,i)}}{\Delta l^2}; \frac{\Delta \mathbf{d}^{(n,i-1)T} \Delta \mathbf{d}_2^{(n,i)}}{\Delta l^2} \right). \tag{2.91}$$

In Hellweg and Crisfield (1998) it is shown that this criterion may fail for sharp snap-backs and the authors propose a criterion based on the out-of-balance loads. In this approach, the solution with minimum residual is selected

$$\min \left( \|\mathbf{r}_1^{(n,i)}\|_2; \|\mathbf{r}_2^{(n,i)}\|_2 \right), \tag{2.92}$$

with

$$\mathbf{r}_k^{(n,i)} = \mathbf{f}_0 + \left( \mu^{(n-1)} + \Delta \mu_k^{(n,i)} \right) \hat{\mathbf{f}} - \mathbf{f}_{int} \left( \mathbf{d}^{(n-1)} + \Delta \mathbf{d}_k^{(n,i)} \right) \quad k = 1, 2. \tag{2.93}$$

## Indirect Displacement Control

The indirect displacement control can be motivated by the fact that the global load-displacement-curve of a brittle structure may exhibit snap-back but the opening of the dominant macroscopic crack monotonically increases during the failure process. Consequently, the crack mouth opening displacement can be used as control parameter in numerical simulations as well as in experiments. In general, it is sufficient to use a linear combination of displacement values, that increases monotonically during the entire failure process, as control parameter in numerical simulations. The corresponding constraint equation can

then be written as

$$\mathbf{c}^T \Delta \mathbf{d}^{(n)} - \Delta l = 0, \quad (2.94)$$

in which the vector  $\mathbf{c}$  contains the coefficients of the selected linear combination. In the  $i$ -th iteration of the  $n$ -th load step, this constraint equation can be rewritten as

$$\mathbf{c}^T \left( \Delta \mathbf{d}^{(n,i-1)} + \delta \mathbf{d}^{(n,i)} \right) - \Delta l = 0. \quad (2.95)$$

By substituting Eq. (2.78) into Eq. (2.95), a linear equation is obtained, which can be solved for the correction of the load factor

$$\delta \mu^{(n,i+1)} = \frac{\Delta l - \mathbf{c}^T \left( \Delta \mathbf{d}^{(n,i)} + \delta \mathbf{d}_0^{(n,i+1)} \right)}{\mathbf{c}^T \delta \mathbf{d}_f^{(n,i+1)}}. \quad (2.96)$$

Compared to the arc-length method, this approach is much simpler, since the constraint equation has only one solution. The performance of indirect displacement control techniques depends on the choice of the linear combination of displacement values. In general, this requires knowledge about the final failure mechanism. Especially in simulations with multiple cracks, the choice of the right linear combination may become difficult.

## Energy Release Control

Gutiérrez (2004) proposes a path-following constraint which is based on the energy release rate. In contrast to indirect displacement control, this approach is also applicable to nonlinear simulations for which the failure behavior of the structure is not known a priori. In numerical simulations using continuum damage models to represent the nonlinear material behavior, the energy  $\Delta \mathcal{G}$  released in load increment  $n$  can be written as

$$\Delta \mathcal{G} = \frac{1}{2} \left[ \mu^{(n-1)} \Delta \mathbf{d}^{(n)} - \Delta \mu^{(n)} \mathbf{d}^{(n-1)} \right]^T \hat{\mathbf{f}}. \quad (2.97)$$

Assuming that the energy released during a load increment is constant, the constraint equation can be obtained. In the  $i$ -th equilibrium iteration step this constraint equation reads

$$\frac{1}{2} \left[ \mu^{(n-1)} \left( \Delta \mathbf{d}^{(n,i-1)} + \delta \mathbf{d}^{(n,i)} \right) - \left( \Delta \mu^{(n,i-1)} + \delta \mu^{(n,i)} \right) \mathbf{d}^{(n-1)} \right]^T \hat{\mathbf{f}} - \Delta \mathcal{G} = 0. \quad (2.98)$$

Substituting Eq. (2.78) into Eq. (2.98), the unknown correction of the load factor can be obtained

$$\delta \mu^{(n,i)} = \frac{2 \Delta \mathcal{G} - \left[ \mu^{(n-1)} \left( \Delta \mathbf{d}^{(n,i-1)} + \delta \mathbf{d}_0^{(n,i)} \right) - \Delta \mu^{(n,i-1)} \mathbf{d}^{(n-1)} \right]^T \hat{\mathbf{f}}}{\left[ \mu^{(n-1)} \delta \mathbf{d}_f^{(n,i)} - \mathbf{d}^{(n-1)} \right]^T \hat{\mathbf{f}}}. \quad (2.99)$$

Due to the limitation to continuum damage models, the constraint equation can be defined only as a function of external variables: load-factor, reference load vector and displacement vector. This allows for a very fast evaluation of the constraint equation independently from the chosen continuum damage formulation.

In this thesis, a more general approach which is directly based on the dissipated (inelastic) energy is introduced. In general, the inelastic energy can be defined as

$$U_{inel} = U_{tot} - U_{el}, \quad (2.100)$$

where  $U_{tot}$  is the total energy and  $U_{el}$  is the elastic energy. Assuming that a predefined amount of energy  $\Delta\mathcal{G}$  should be dissipated in each load increment  $n$ , the corresponding constraint equation can be written as

$$U_{inel}^{(n)} - U_{inel}^{(n-1)} - \Delta\mathcal{G} = 0, \quad (2.101)$$

with  $U_{inel}^{(n)} = U_{inel}(\mathbf{d}^{(n)})$  and  $U_{inel}^{(n-1)} = U_{inel}(\mathbf{d}^{(n-1)})$ . Approximating the unknown energy dissipation by a truncated Taylor series, the constraint equation in the  $i$ -th iteration step reads

$$U_{inel}^{(n,i-1)} + \left[ \frac{\partial U_{inel}^{(n,i-1)}}{\partial \mathbf{d}} \right]^T \delta \mathbf{d}^{(n,i)} - U_{inel}^{(n-1)} - \Delta\mathcal{G} = 0. \quad (2.102)$$

Using Eq. (2.78), this linear equation can be solved for the unknown correction of the load factor

$$\delta \mu^{(n,i)} = \frac{\Delta\mathcal{G} + U_{inel}^{(n-1)} - U_{inel}^{(n,i-1)} - \left[ \frac{\partial U_{inel}^{(n,i-1)}}{\partial \mathbf{d}} \right]^T \delta \mathbf{d}_0^{(n,i)}}{\left[ \frac{\partial U_{inel}^{(n,i-1)}}{\partial \mathbf{d}} \right]^T \delta \mathbf{d}_f^{(n,i)}}. \quad (2.103)$$

A detailed description of the calculation of the dissipated energy and the corresponding derivatives is given in appendix A.2. Assuming nonlinear simulations with continuum damage material models, the second approach in Eq. (2.103) is totally equivalent to Eq. (2.99). Compared to the first approach, a higher numerical effort is required since the derivative of the inelastic energy with respect to the displacements, which involves the computation of the tangent material matrix, must be calculated for each element. Furthermore, an assembling of the corresponding element contributions in the global vector of energy derivatives must be performed. Due to the usage of the inelastic energy this approach is not limited to continuum damage models. It is also applicable to plasticity and combined damage-plasticity models.

Both constraint equations can only be used if damage or plasticity is evolving during the load step. In general, this is not the case at the beginning of the loading process. As long as the structure is in the elastic regime, the simulation is performed with load control and the dissipated energy is calculated in each iteration step using Eq. (2.97) or (2.101). If



damage or plasticity initiates and inelastic energy starts to dissipate, the load control is replaced by an energy release control.

### 2.4.4 Line Search

In nonlinear finite element simulations, line searches can be applied to improve the global convergence of the iterative solution procedure, see for instance Matthies and Strang (1979); Crisfield (1982). In each iteration step, an optimum line search parameter  $\eta$  is determined which scales the correction of the displacement vector. Using line searches with load control or direct displacement control, the update of the displacement vector is given by

$$\mathbf{d}^{(n,i)}(\eta) = \mathbf{d}^{(n,i-1)} + \eta \delta \mathbf{d}^{(n,i)} \quad (2.104)$$

and the residual is defined as

$$\mathbf{r}^{(n,i)}(\eta) = \mathbf{f}_{ext}^{(n)} - \mathbf{f}_{int}(\mathbf{d}^{(n,i)}(\eta)). \quad (2.105)$$

According to Schweizerhof (1993), the line search in simulations using load-displacement-constrained methods is performed in the direction of  $\delta \mathbf{d}_0^{(n,i)}$  and then corrected by the load term  $\delta \mu^{(n,i)} \delta \mathbf{d}_f^{(n,i)}$ . Consequently, the parameter  $\eta$  not only affects the correction of the displacement vector

$$\delta \mathbf{d}^{(n,i)}(\eta) = \mathbf{d}^{(n,i-1)} + \eta \delta \mathbf{d}_0^{(n,i)} + \delta \mu^{(n,i)}(\eta) \delta \mathbf{d}_f^{(n,i)}, \quad (2.106)$$

but also the correction of the load factor  $\delta \mu^{(n,i)}$ . The corresponding out-of-balance forces are given by

$$\mathbf{r}^{(n,i)}(\eta) = \mathbf{f}_0 + (\mu^{(n,i-1)} + \delta \mu^{(n,i)}(\eta)) \hat{\mathbf{f}} - \mathbf{f}_{int}(\mathbf{d}^{(n,i-1)} + \delta \mathbf{d}^{(n,i)}(\eta)). \quad (2.107)$$

In order to assure convergence of the applied solution procedure, the calculated iteration step length must result in a sufficient improvement of the displacement approximation. In the next paragraphs, two different approaches for the determination of the line search parameter  $\eta$ , based on the total potential and on the residuals are presented.

#### Total Potential Line Search

Alternatively to the differential approach and the principle of virtual displacements, presented in Sect. 2.1, the equilibrium state of a body can be expressed for certain problems as an optimization problem, see for instance Bathe (1995),

$$\Pi_{tot}(\mathbf{d}) \rightarrow \min \quad \Rightarrow \quad \frac{\partial \Pi_{tot}}{\partial \mathbf{d}}(\mathbf{d}) = \mathbf{r}(\mathbf{d}) = 0, \quad (2.108)$$

where  $\Pi_{tot}$  is the total potential and  $\mathbf{r}$  are the out-of-balance forces. Crisfield (1991) and Schweizerhof (1993) propose a line search which is based on the total potential. During

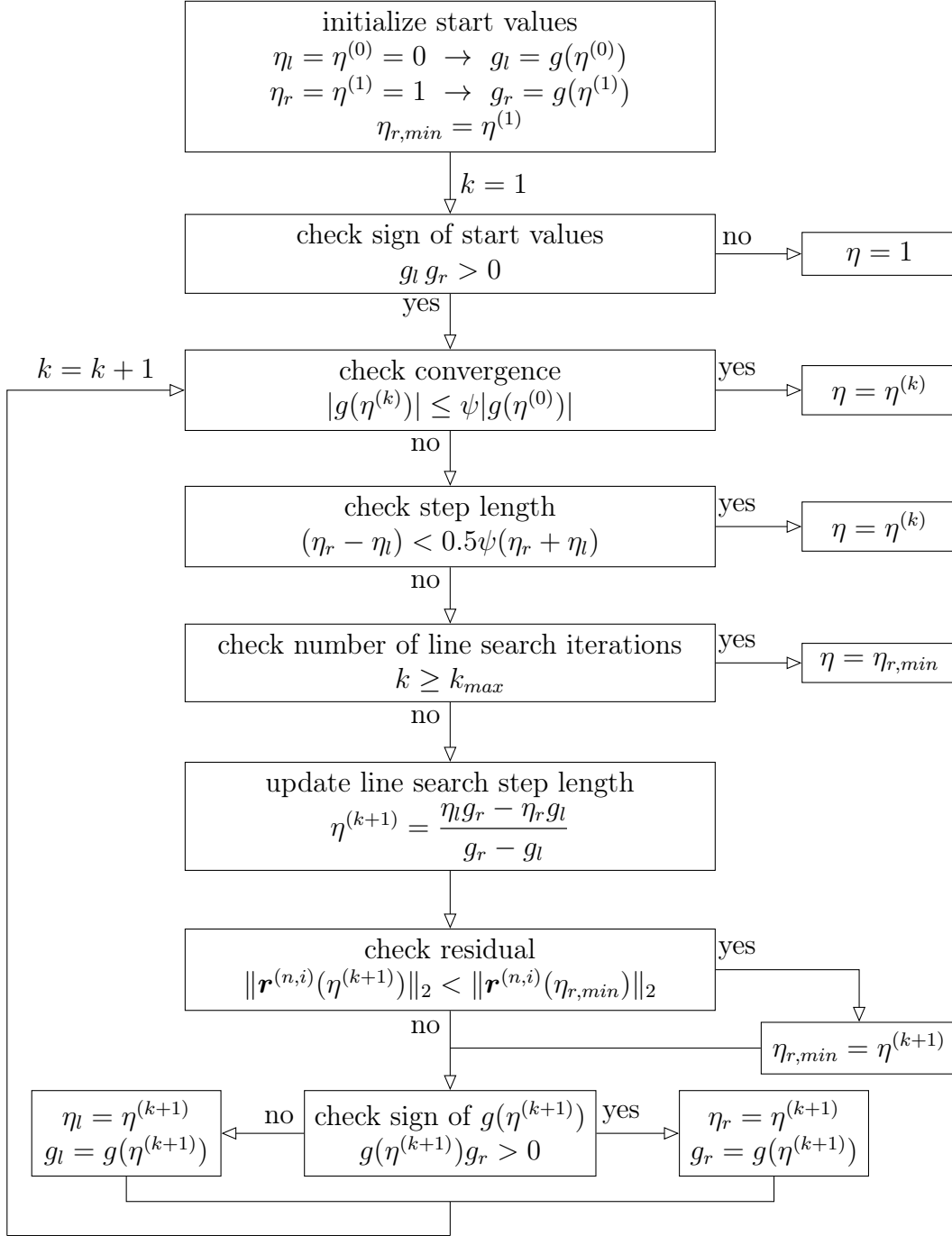


Figure 2.5: Energy based line search – flowchart for calculating the line search step length.

the line search, the direction of the displacement correction,  $\delta \mathbf{d}^{(n,i)}$  or  $\delta \mathbf{d}_0^{(n,i)}$  and  $\delta \mathbf{d}_f^{(n,i)}$ , is fixed and the minimization is performed with respect to the line search parameter  $\eta$

$$\Pi_{tot}(\eta) \rightarrow \min \quad \Rightarrow \quad \frac{\partial \Pi_{tot}}{\partial \eta} = \left( \frac{\partial \Pi_{tot}}{\partial \mathbf{d}} \right)^T \frac{\partial \mathbf{d}}{\partial \eta} = \mathbf{r}^T \frac{\partial \mathbf{d}}{\partial \eta} = 0. \quad (2.109)$$

This equation is solved iteratively using the regula falsi method. Figure 2.5 shows the

algorithm for the calculation of the line search parameter. In this algorithm the parameter  $\psi$  is the so-called line search tolerance. According to Schweizerhof (1993) this parameter is chosen in the interval between 0.5 and 0.8. As a result, an inexact line search is performed. Using standard load control or direct displacement control, the gradient  $g$  of the total potential with respect to the line-search parameter  $\eta$  can be written as

$$g(\eta^{(k)}) = (\mathbf{r}^{(n,i)}(\eta^{(k)}))^T \delta \mathbf{d}^{(n,i)}. \quad (2.110)$$

In each iteration step  $k$ , a new displacement vector is calculated using Eq. (2.104) and the out-of-balance force vector given in Eq. (2.105) is updated. Using load-displacement-constrained methods, the gradient of the total potential reads

$$g(\eta^{(k)}) = (\mathbf{r}^{(n,i)}(\eta^{(k)}))^T \left( \delta \mathbf{d}_0^{(n,i)} + \frac{\partial \delta \mu^{(n,i)}}{\partial \eta}(\eta^{(k)}) \delta \mathbf{d}_f^{(n,i)} \right). \quad (2.111)$$

In addition to the update of the displacement vector, Eq. (2.106), and the out-of-balance forces, Eq. (2.107), a new correction of the load factor, Eqs. (A.23) to (A.29) in appendix A.3, and the corresponding derivative of the load factor correction with respect to the line search parameter, Eqs. (A.30) to (A.35), is calculated in each line search iteration step.

## Residual Line Search

One criterion for the convergence of an iterative solution procedure in finite element simulations is based on the norm of the out-of-balance forces, which describes the difference between internal forces and external loads. The algorithm converges if in each iteration step a sufficiently large decrease of the out-of-balance forces is obtained with the applied step length. Using the Armijo-Goldstein condition, see for instance Nocedal and Wright (2006), a sufficiently large decrease is achieved, if the step length factor  $\eta$  satisfies

$$f(\mathbf{d}^{(n,i-1)} + \eta \delta \mathbf{d}^{(n,i)}) \leq f(\mathbf{d}^{(n,i-1)}) + \epsilon \eta \left( \nabla f(\mathbf{d}^{(n,i-1)}) \right)^T \delta \mathbf{d}^{(n,i)}, \quad 0 < \epsilon < 1, \quad (2.112)$$

where  $f$  is the objective function, defined as

$$f(\mathbf{d}^{(n,i)}) = \|\mathbf{r}^{(n,i)}\|_2 = \sqrt{\mathbf{r}^{(n,i)T} \mathbf{r}^{(n,i)}}, \quad (2.113)$$

and  $\nabla f$  is the corresponding gradient, which can be written as

$$\nabla f(\mathbf{d}^{(n,i)}) = \frac{\partial f}{\partial \mathbf{d}}(\mathbf{d}^{(n,i)}) = \frac{-2}{2 \|\mathbf{r}^{(n,i)}\|_2} \left( \frac{\partial \mathbf{f}_{int}^{(n,i)}}{\partial \mathbf{d}} \right)^T \mathbf{r}^{(n,i)} = -\frac{\mathbf{K}^{(n,i)T} \mathbf{r}^{(n,i)}}{\|\mathbf{r}^{(n,i)}\|_2}. \quad (2.114)$$

By substituting Eqs. (2.113) and (2.114) into Eq. (2.112) and by considering Eq. (2.62), this condition can be rewritten as

$$\|\mathbf{r}^{(n,i)}(\eta)\|_2 \leq \|\mathbf{r}^{(n,i-1)}\|_2 - \epsilon \eta \|\mathbf{r}^{(n,i-1)}\|_2. \quad (2.115)$$

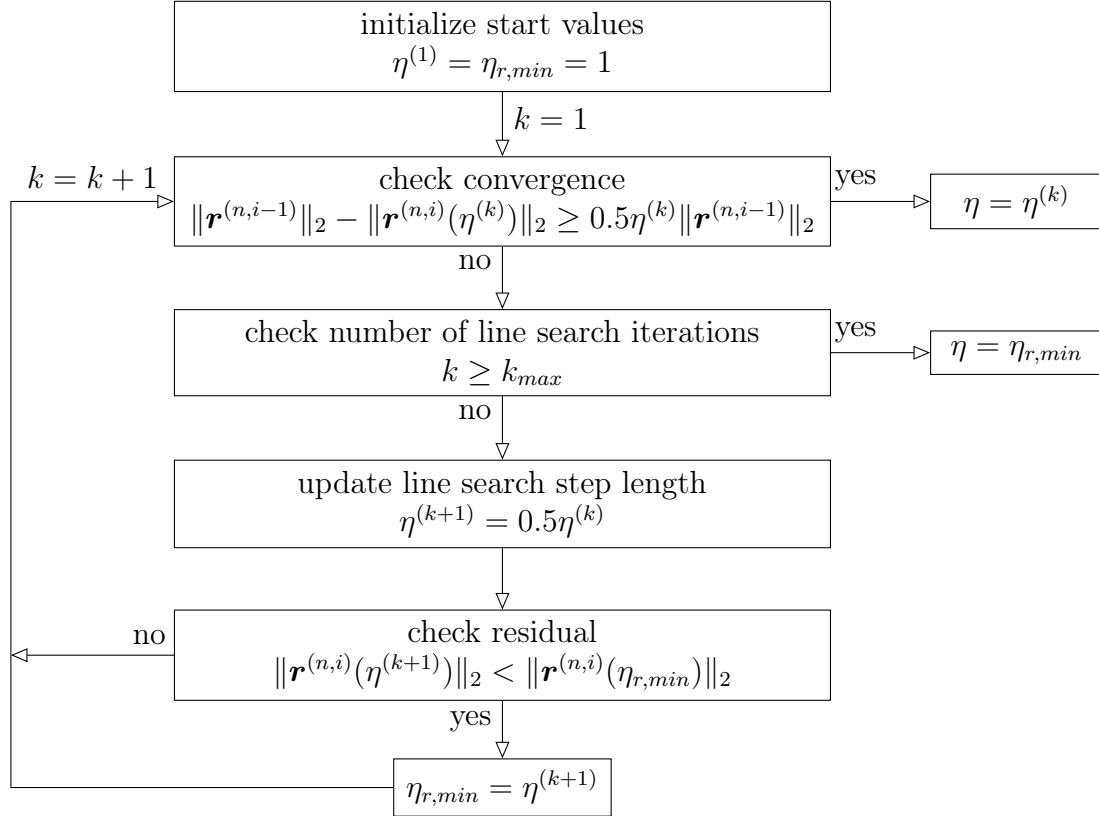


Figure 2.6: Residual based line search – flowchart for calculating the line search step length.

The parameter  $\epsilon$  controls the required reduction of the out of balance forces. According to the user's guide of the MATLAB PDE Toolbox (2008),  $\epsilon$  is chosen to 0.5 and the Armijo-Goldstein condition, given in Eq. (2.112), is slightly modified

$$\|\mathbf{r}^{(n,i-1)}\|_2 - \|\mathbf{r}^{(n,i)}(\eta)\|_2 \geq 0.5 \eta \|\mathbf{r}^{(n,i-1)}\|_2. \quad (2.116)$$

This condition is not too stringent, since, in general, quadratic convergence is obtained for nonlinear simulations using the Newton-Raphson method with the consistent tangent stiffness matrix, if the start vector is sufficiently close to the desired solution. Consequently, the line search is only performed if the Newton-Raphson method does not converge. The iterative procedure for the determination of the step length factor  $\eta$  is summarized in Fig. 2.6. Starting with a value of 1, the step length factor is successively halved until either Eq. (2.116) is satisfied or the number of line search iterations exceeds a certain limit. If the maximum number of line search iterations is reached, the step length factor with the smallest residual is chosen. In this case, the residual may increase compared to the previous equilibrium iteration step.

### 2.4.5 Step Size Adaptation

In order to reduce the computing time for nonlinear analyses, the step size is adapted during the simulation. According to Ramm (1980), the step size is related to the number

of iterations,  $n_i^{(n-1)}$ , required in the previous load increment

$$\Delta l^{(n)} = \sqrt{\frac{\bar{n}_i}{n_i^{(n-1)}}} \Delta l^{(n-1)} \quad n > 1, \quad (2.117)$$

where  $\bar{n}_i$  is a desired number of iterations, and  $\Delta l$  represents the step length. Consequently, the step size is either increased or decreased depending in the number of iterations required for convergence. If the number of iterations in the current load-step exceeds a certain limit, which indicates divergence of the solution, the step-size is halved and the equilibrium iteration is restarted from the last converged solution.

# 3 Continuum Damage Mechanics

## 3.1 Introduction

According to Kachanov (1986), damage is a, in general, irreversible process of accumulation of microstructural changes, e.g. the initiation and propagation of microcracks or microvoids, leading to a progressive degradation of the material. This effect is caused by stress concentrations at material interfaces within the heterogeneous material microstructure or in the vicinity of initial microdefects or by atomic debonding at the nanolevel. In the theory of continuum damage mechanics, introduced by Kachanov in 1958 for creep rupture, damage is described phenomenologically by a set of continuous damage variables representing the microstructural defects in a material. The value of a damage variable in a given point is a measure of the amount of microdefects in the vicinity of this point. A comprehensive study on the definition of damage variables in terms of physical quantities can be found in Lemaitre and Chaboche (1990) or Krajcinovic (1996). In elasticity based damage models, it is assumed that the material behavior is linear elastic if damage does not grow. Furthermore, viscous effects and plastic deformations are neglected. Consequently, the evolution of microdefects is the primary deterioration mechanism, which is typical for quasi-brittle materials such as concrete. The initiation, evolution and coalescence of microcracks results in a gradual decrease of the initial elastic material parameters. Furthermore, it is assumed that in the initial state the material is undamaged. Initial material defects, which always exist in real materials, are included in the elastic material properties. In this thesis, elasticity based continuum damage models are used to describe the deterioration behavior of the mortar matrix.

## 3.2 Regularization

Tension tests of concrete show that the material starts to soften after the fracture strength is reached. Consequently, the specimen does not collapse promptly but the stress decreases gradually for increasing deformation. This phenomenon, termed softening, is characterized by a high degree of microstructural changes. According to Sluys (1992) and Hofstetter and Mang (1995), at about 60% of the maximum load, microcracks arise at the interface between aggregates and mortar matrix. If the load is further increased, the interface cracks propagate into the mortar matrix and additional microcracks initiate within the mortar matrix. At maximum load level, the microcracks start to interact and to coalesce which results in a localization of deformation in macroscopic failure zones. At the same time, the surrounding material starts to unload. The width of these failure bands, which depends on

the material microstructure, cf. Bažant and Pijaudier-Cabot (1989), is, in general, much smaller compared to the region in which microdefects have been developed.

In numerical simulations, damaged concrete can be modeled as a strain-softening continuum using continuum damage models. In these material formulations, the softening is explicitly considered within the stress-strain relationship, which results in a negative slope of the stress-strain curve. From the mathematical point of view, a negative tangent modulus results in the so-called loss of ellipticity of the governing differential equations and the boundary value problem becomes ill-posed. Assuming the academical case of uniform material properties and stresses, an infinite number of solutions exist for the equilibrium problem, see for instance Jirásek and Bažant (2001). If imperfections of the material and the geometry are taken into account the material properties and the stresses become inhomogeneous. As a result, softening starts not in the entire structure simultaneously but only in one cross-section. At the same time the surrounding material starts unloading. Consequently, damage localizes in the weakened cross-section. Since the softening region becomes infinitely small, the energy dissipated during the failure process is zero and the load-displacement curve always exhibits snap-back, Bažant (1976). In finite element simulations, ill-posedness results in a pathological sensitivity of the results to the element size, see for instance Pietruszczak and Mróz (1981) or de Vree et al. (1995). Damage tends to localize in a single layer of finite elements if a standard local continuum damage model is used. Consequently, the numerical solution does not converge to a physically meaningful solution upon mesh refinement. Furthermore, as shown in Sluys (1992); Jirásek and Zimmermann (1998a); Jirásek and Grassl (2008), the direction in which damage develops may depend on the finite element shape and orientation. In the next subsections regularization methods for continuum material models are introduced which can be used to improve the objectivity of the numerical results with respect to the finite element discretization.

### 3.2.1 Crack-Band Theory

In order to avoid the sensitivity of the constitutive models with respect to the size of the finite elements, for shear failure of elasto-plastic materials Pietruszczak and Mróz (1981) introduce a characteristic thickness of the shear band. The post-peak behavior of the material, represented by the softening modulus, is adjusted using the ratio of this additional material parameter and the finite element size. As a result, the obtained load-displacement curves become almost independent from the element size. A similar approach, the so-called crack-band theory, was proposed by Bažant and Oh (1983a) for smeared crack models of concrete. In these models, it is assumed that fracture can be modeled as a band of parallel, densely distributed microcracks. Furthermore, the softening behavior of the material is expressed as function of the fracture energy  $G_f$ , which is defined as the energy dissipated during the fracture process related to the area of the crack surface. Assuming one single macroscopic crack, this parameter can be determined from experiments as the area under the load-displacement curve divided by the area of the crack surface. Note that the width of the fracture process zone is not considered in this parameter. Since in the numerical model the inelastic energy is dissipated over the damaged volume, this area specific material parameter must be related to the width of the localization zone.

Therefore, on element level, the standard fracture energy is replaced by a volume specific fracture energy  $g_f$  which is defined as

$$g_f = \frac{G_f}{l_{eq}}, \quad (3.1)$$

where  $l_{eq}$  is the so-called equivalent element length representing the width of the localization zone within the numerical model. In Mančevski (1998), this parameter is connected to the element size

$$l_{eq} = \begin{cases} l^e & \text{line elements} \\ \sqrt{A^e} & \text{plane elements} \\ \sqrt[3]{V^e} & \text{volume elements} \end{cases} \quad (3.2)$$

in which  $l^e$ ,  $A^e$  and  $V^e$  denote the length, area and volume of the element, respectively. More sophisticated approaches, which additionally take into account the element shape, the integration scheme or the crack orientation can be found in Rots (1988), Oliver (1989) or Červenka and Pukl (1994). Even though the crack-band concept was originally developed for smeared crack models, this approach can be similarly applied to classical damage models, cf. Jirásek and Grassl (2008).

Using the crack band approach, fracture still localizes in a single layer of elements. Consequently, the numerical model does not represent the actual width of the fracture process zone, but it preserves the correct amount of energy dissipated during the fracture process. It is to be noted that the orientation of the localization zone is still influenced by the finite element mesh, Jirásek and Zimmermann (1998b); Jirásek and Grassl (2008).

### 3.2.2 Integral-Type Nonlocal Damage Models

Another class of approaches allowing to reduce spurious mesh sensitivities is based on localization limiters. In contrast to the crack band approach, in which the width of the localization zone varies with the size of the finite elements, the introduction of a localization limiter into the constitutive model enforces a realistic and mesh independent size of the numerically simulated fracture process zone. The width of the fracture process zone is specified by an additional material parameter, the so-called characteristic length. This approach can be motivated by experimental results which indicate that the fracture process zone has a finite width. For example, Bažant and Pijaudier-Cabot (1989) investigate for tensile specimens of concrete that the characteristic length is approximately 2.7 times the maximum aggregate size.

A wide class of localization limiters is based on a nonlocal continuum, which was originally developed for elasticity, e.g. Eringen (1966); Kröner (1967). Pijaudier-Cabot and Bažant (1987) extend this approach to strain softening materials leading to the nonlocal damage theory, in which the nonlocal concept is applied only to those variables that control strain softening, whereas the elastic part of the model remains local. By replacing a certain state



variable  $\mathbf{g}$  by its nonlocal counterpart  $\bar{\mathbf{g}}$ , the corresponding stress-strain relationship can be written as

$$\sigma_i(\mathbf{x}) = \sigma_i(\boldsymbol{\varepsilon}(\mathbf{x}), \bar{\mathbf{g}}(\mathbf{x})) = C_{ij}^s(\bar{\mathbf{g}}(\mathbf{x})) \varepsilon_j(\mathbf{x}) \quad (3.3)$$

where  $\mathbf{C}^s$  is the secant material matrix. There exist several possibilities of choosing the nonlocal variable, e.g. the damage energy release rate (Pijaudier-Cabot and Bažant (1987)), the damage variable (Bažant and Pijaudier-Cabot (1988)), strain components (Bažant and Lin (1988)) or the equivalent strain (de Vree et al. (1995)). A comprehensive study of the different approaches can be found in Jirásek (1998b).

In integral-type nonlocal damage models, Jirásek and Bažant (1994), the nonlocal quantity at point  $\mathbf{x}$  is defined as the weighted average which is evaluated over the spatial neighborhood of that point

$$\bar{\mathbf{g}}(\mathbf{x}) = \int_V \alpha(\mathbf{x}, \boldsymbol{\xi}) \mathbf{g}(\boldsymbol{\xi}) \, d\boldsymbol{\xi}, \quad (3.4)$$

where  $\alpha(\mathbf{x}, \boldsymbol{\xi})$  is a given weight function. As a result, the constitutive model does not longer satisfy the principle of local action. The stresses at a given point depend not only on the deformations and the deformation history in this point itself but also on the deformations and the deformation history in its vicinity. This results in a smoothing of the numerically simulated deformation field and the corresponding damage distribution. Physically, the nonlocal averaging represents in a homogenized way the influence of the material microlevel on the macroscopic damage evolution. This interrelationship can be justified by micromechanical considerations. According to Bažant (1991, 1994); Bažant and Jirásek (2002), nonlocality is caused by the heterogeneity of the material microstructure, by the fact that the growth of a microcrack depends on the overall energy release in the vicinity of that microcrack, and by interactions between microcracks. As shown in Jirásek and Bažant (1994), the consideration of long-range interactions between microcracks requires a different type of nonlocal formulation, which is not used in this work. Short-range effects are taken into account by standard nonlocal models, Eq. (3.4), with isotropic averaging function. In order to guarantee that the nonlocal averaging does not alter a uniform field and in order to avoid boundary effects, the weight function must satisfy the following normalizing condition

$$\int_V \alpha(\mathbf{x}, \boldsymbol{\xi}) \, d\boldsymbol{\xi} = 1. \quad (3.5)$$

This can be achieved by modifying the weight function  $\alpha$

$$\alpha(\mathbf{x}, \boldsymbol{\xi}) = \frac{\alpha_0(\|\mathbf{x} - \boldsymbol{\xi}\|)}{\int_V \alpha_0(\|\mathbf{x} - \boldsymbol{\eta}\|) \, d\boldsymbol{\eta}}, \quad (3.6)$$

where  $\alpha_0$  is a monotonically decreasing nonnegative function of the distance between two

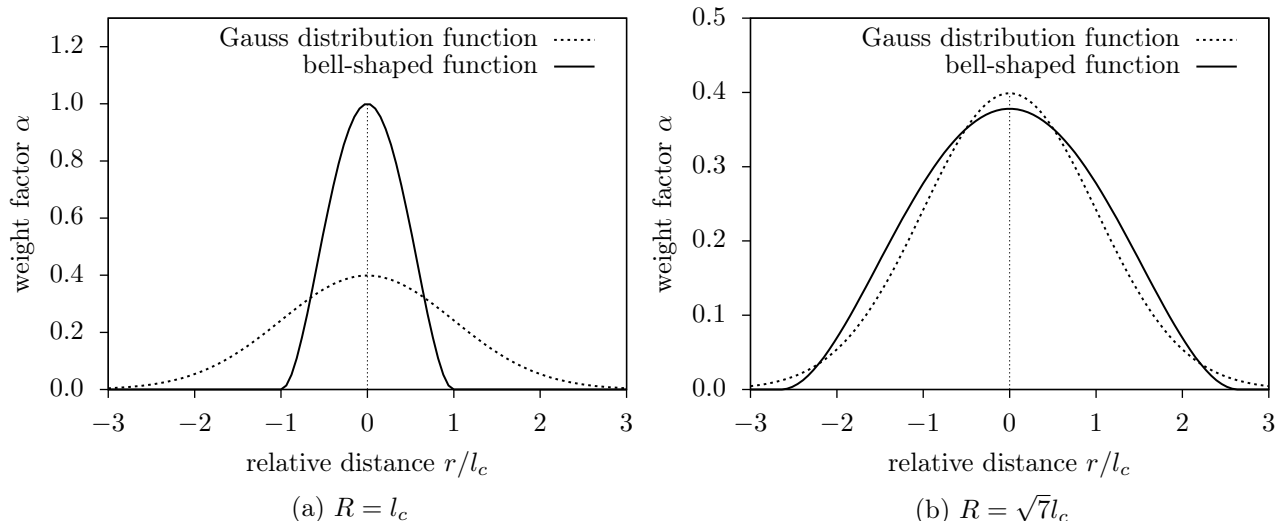


Figure 3.1: Nonlocal weight functions.

points, and  $\mathbf{x}$ ,  $\boldsymbol{\xi}$  and  $\boldsymbol{\eta}$  are the coordinates of these points. Due to this modification, the weight function becomes non-symmetric with respect to the arguments  $\mathbf{x}$  and  $\boldsymbol{\xi}$ . Borino et al. (2003) propose another modification of the weight function which preserves symmetry and satisfies the normalizing condition, given by Eq. (3.5). Since the tangential stiffness matrix of continuum damage models may become already in local formulations non-symmetric, this approach is not further investigated in this work. Several functions  $\alpha_0$  can be found in literature. For instance, Askes and Sluys (2000) use the Gauss distribution function

$$\alpha_0(r) = \exp\left(-\frac{r^2}{2l_c^2}\right), \quad (3.7)$$

in which  $l_c$  denotes the internal (characteristic) length of the nonlocal continuum. The Gaussian function has an unbounded support which would imply that the nonlocal averaging is performed over the entire body. This can be avoided by truncating the weight function if the radius exceeds a certain value. As a result, the nonlocal influence of each point is restricted to its vicinity. Another possible choice for  $\alpha_0$ , introduced by Bažant and Ožbolt (1990) and used in this work, is a bell-shaped function with bounded support

$$\alpha_0(r) = \begin{cases} 0.0 & r > R \\ \left[1 - \frac{r^2}{R^2}\right]^2 & r \leq R \end{cases}, \quad (3.8)$$

where  $R$  is the so-called nonlocal interaction radius which is related, but not equal, to the characteristic length. The different meaning of these two parameters is illustrated in Fig. 3.1(a) which shows the corresponding normalized weight function  $\alpha$ . In this plot, the characteristic length  $l_c$  is set equal to the nonlocal interaction radius  $R$ . According to Jirásek (1998a), a comparable length scale is imposed by both weight functions if  $R = \sqrt{7}l_c$ , cf. Fig. 3.1(b).

## Finite Element Implementation

In general, the nonlocal quantity can be a scalar, a vector or a tensor. For the sake of simplicity, it is assumed that a scalar value, e.g. the equivalent strain, is used for nonlocal averaging. The extension to a vector or a tensor is straightforward. In finite element implementations of nonlocal material laws, the integrals given in Eqs. (3.4) and (3.6) are, in general, evaluated numerically using the integration points of the finite elements. In the discretized form, the nonlocal averaging in Eq. (3.4) reads

$$\bar{g}(\mathbf{x}) = \sum_{q=1}^{n_E} \sum_{r \in \mathcal{I}^{(q)}} w^{(r)} \det \mathbf{J}^{(q)}(\mathbf{x}^{(r)}) \alpha(\mathbf{x}, \mathbf{x}^{(r)}) g^{(q)}(\mathbf{x}^{(r)}) \quad (3.9)$$

where  $n_E$  is the number of elements,  $\mathcal{I}^{(q)}$  is the set of integration points of element  $q$ ,  $\det \mathbf{J}^{(q)}$  is the determinant of the Jacobian of element  $q$ , and  $\mathbf{x}^{(r)}$  and  $w^{(r)}$  are the coordinates and the weight factor of integration point  $r$ . The normalized nonlocal weight factor  $\alpha$  is given by

$$\alpha(\mathbf{x}, \boldsymbol{\xi}) = \frac{\alpha_0(\|\mathbf{x} - \boldsymbol{\xi}\|)}{\sum_{m=1}^{n_E} \sum_{n \in \mathcal{I}^{(m)}} w^{(n)} \det \mathbf{J}^{(m)}(\mathbf{x}^{(n)}) \alpha_0(\|\mathbf{x} - \mathbf{x}^{(n)}\|)}. \quad (3.10)$$

In the implementation, only those integration points with the same material are used for nonlocal averaging. The calculation of the nonlocal weight factors starts with the determination of the nonlocal elements of each integration point. Nonlocal elements of a given integration point are all elements which are not completely outside the domain of nonlocal influence of that point, which is represented by a sphere of radius  $R$  around that point. The determination of the nonlocal elements is done in an iterative procedure. Starting with the element to which the integration point belongs, the neighboring elements are determined. This procedure is successively repeated for each neighboring element, which is not completely outside the domain of nonlocal influence. Note that an element is neighbor of another element if both elements have a common surface. If the nonlocal elements of the integration point are known, the summation in the nonlocal averaging procedure, Eq. (3.9), can be performed only over the integration points of the nonlocal elements. For computational efficiency, the nonlocal elements of each integration point and the corresponding nonlocal weight factors are evaluated and stored at the beginning of an simulation. In order to save memory, the nonlocal elements are not stored at the integration points itself, but the union of the nonlocal elements for all integration points of an element is determined and stored at that element. Only the vector of nonlocal weight factors are stored at the integration point level. As a result, the number of vanishing weight factors saved at each integration point might slightly increase.

Due to the integral-type nonlocal formulation, the internal forces of an element, Eq. (2.53), depend not only on the nodal displacements of the element itself but also on the nodal values of the neighboring elements. As a consequence, the bandwidth of the tangential stiffness matrix increases during the simulation depending on the evolution of damage,

Jirásek and Patzák (2002). The tangential stiffness matrix of an element is stored as block matrix. Each block of this matrix is defined as the derivative of the internal load vector  $\mathbf{f}_{int}^{(o)}$  of element  $o$  with respect to the displacement vector  $\mathbf{d}^{(q)}$  of element  $q$

$$K_{ij}^{(o,q)} = \frac{\partial f_{int,i}^{(o)}}{\partial d_j^{(q)}} = \frac{\partial}{\partial d_j^{(q)}} \int_{V^{(o)}} B_{ki}^{(o)}(\mathbf{x}) \sigma_k^{(o)}(\mathbf{x}) \, dV \quad (3.11)$$

$$= \int_{V^{(o)}} B_{ki}^{(o)}(\mathbf{x}) \sum_{r \in \mathcal{I}^{(q)}} \frac{\partial \sigma_k^{(o)}(\mathbf{x})}{\partial \varepsilon_l^{(q)}(\mathbf{x}^{(r)})} \frac{\partial \varepsilon_l^{(q)}(\mathbf{x}^{(r)})}{\partial d_j^{(q)}} \, dV \quad (3.12)$$

$$= \int_{V^{(o)}} B_{ki}^{(o)}(\mathbf{x}) \sum_{r \in \mathcal{I}^{(q)}} \frac{\partial \sigma_k^{(o)}(\mathbf{x})}{\partial \varepsilon_l^{(q)}(\mathbf{x}^{(r)})} B_{lj}^{(q)}(\mathbf{x}^{(r)}) \, dV, \quad (3.13)$$

where  $V^{(o)}$  is the element volume and  $\mathbf{B}^{(o)}$  is the well known strain-displacement matrix. Using numerical integration, Eq. (3.13) is rewritten as

$$K_{ij}^{(o,q)} = \sum_{p \in \mathcal{I}^{(o)}} w^{(p)} \det \mathbf{J}^{(o)}(\mathbf{x}^{(p)}) B_{ki}^{(o)}(\mathbf{x}^{(p)}) \sum_{r \in \mathcal{I}^{(q)}} \frac{\partial \sigma_k^{(o)}(\mathbf{x}^{(p)})}{\partial \varepsilon_l^{(q)}(\mathbf{x}^{(r)})} B_{lj}^{(q)}(\mathbf{x}^{(r)}). \quad (3.14)$$

The corresponding tangential material matrix, which is also stored as block matrix, is given by

$$\frac{\partial \sigma_k^{(o)}(\mathbf{x}^{(p)})}{\partial \varepsilon_l^{(q)}(\mathbf{x}^{(r)})} = \frac{\partial \sigma_k^{(o)}(\mathbf{x}^{(p)})}{\partial \bar{g}^{(o)}(\mathbf{x}^{(p)})} \frac{\partial \bar{g}^{(o)}(\mathbf{x}^{(p)})}{\partial g^{(q)}(\mathbf{x}^{(r)})} \frac{\partial g^{(q)}(\mathbf{x}^{(r)})}{\partial \varepsilon_l^{(q)}(\mathbf{x}^{(r)})} + \delta_{oq} \delta_{pr} \bar{C}_{ij}^{s(o)}(\mathbf{x}^{(p)}), \quad (3.15)$$

where  $\delta$  is the Kronecker delta, and  $\bar{\mathbf{C}}^s$  is the secant (unloading) material matrix of the nonlocal model. The derivative of the nonlocal quantity, given by Eq. (3.9), with respect to its local counterpart reads

$$\frac{\partial \bar{g}^{(o)}(\mathbf{x}^{(p)})}{\partial g^{(q)}(\mathbf{x}^{(r)})} = w^{(r)} \det \mathbf{J}^{(q)}(\mathbf{x}^{(r)}) \alpha(\mathbf{x}^{(p)}, \mathbf{x}^{(r)}). \quad (3.16)$$

By substituting Eq. (3.16) into Eq. (3.15) the tangential material matrix can be rewritten as

$$\begin{aligned} \frac{\partial \sigma_k^{(o)}(\mathbf{x}^{(p)})}{\partial \varepsilon_l^{(q)}(\mathbf{x}^{(r)})} &= w^{(r)} \det \mathbf{J}^{(q)}(\mathbf{x}^{(r)}) \alpha(\mathbf{x}^{(p)}, \mathbf{x}^{(r)}) \frac{\partial \sigma_k^{(o)}(\mathbf{x}^{(p)})}{\partial \bar{g}^{(o)}(\mathbf{x}^{(p)})} \frac{\partial g^{(q)}(\mathbf{x}^{(r)})}{\partial \varepsilon_l^{(q)}(\mathbf{x}^{(r)})} \\ &+ \delta_{oq} \delta_{pr} \bar{C}_{ij}^{s(o)}(\mathbf{x}^{(p)}). \end{aligned} \quad (3.17)$$

Due to the storage of the element stiffness matrix as block matrices, only minor changes are required in the global assembling procedure which is performed for each block matrix separately. During the assembling of block matrix  $\mathbf{K}^{(o,q)}$ , it must be considered that the global degrees of freedom of the nodes of element  $o$  are associated with the rows and that the columns are specified by the global degrees of freedom of the nodes of element  $q$ .

### 3.2.3 Nonlocal Averaging of the Displacement Field

Jirásek and Marfia (2005) have demonstrated that the averaging of strain like variables, presented in Sect. 3.2.2, may result in stress oscillations in certain regions of the fracture process zone. Furthermore, it is shown that by using a nonlocal damage model based on displacement averaging these stress oscillations can be substantially reduced. In the material model presented in Jirásek and Marfia (2005), the evolution of damage is driven by the nonlocal strain tensor  $\bar{\boldsymbol{\varepsilon}}$  which is defined as the symmetric gradient of the nonlocal displacement field

$$\bar{\varepsilon}_{ij}(\mathbf{x}) = \frac{1}{2} \left[ \frac{\partial \bar{u}_i}{\partial x_j}(\mathbf{x}) + \frac{\partial \bar{u}_j}{\partial x_i}(\mathbf{x}) \right]. \quad (3.18)$$

Using an integral-type approach, the nonlocal displacements  $\bar{\mathbf{u}}$  are derived as the weighted average of the local displacement field  $\mathbf{u}$

$$\bar{\mathbf{u}}(\mathbf{x}) = \int_V \alpha(\mathbf{x}, \boldsymbol{\xi}) \mathbf{u}(\boldsymbol{\xi}) d\boldsymbol{\xi}. \quad (3.19)$$

In order to avoid artificially induced damage at the specimen boundaries due to rigid body rotations the nonlocal averaging has to preserve not only a constant field but also a linear field. Consequently, the nonlocal weight function  $\alpha$  must satisfy an additional normalizing condition

$$\int_V (\boldsymbol{\xi} - \mathbf{x}) \alpha(\mathbf{x}, \boldsymbol{\xi}) d\boldsymbol{\xi} = \mathbf{0}. \quad (3.20)$$

This requires a further modification of the nonlocal weight function, which can be written as

$$\alpha(\mathbf{x}, \boldsymbol{\xi}) = \left[ p_0(\mathbf{x}) + (\boldsymbol{\xi} - \mathbf{x})^T \mathbf{p}_1(\mathbf{x}) \right] \alpha_0(\|\mathbf{x} - \boldsymbol{\xi}\|), \quad (3.21)$$

where  $p_0$  and  $\mathbf{p}_1$  are unknown parameters which can be determined from the normalizing conditions. Substituting the modified weight function, Eq. (3.21) into the normalizing conditions, Eqs. (3.5) and (3.20), a linear system of equations, which can be solved for the parameters  $p_0$  and  $\mathbf{p}_1$ , is obtained

$$\begin{bmatrix} r_{00} & \mathbf{r}_{10}^T \\ \mathbf{r}_{10} & \mathbf{R}_{11} \end{bmatrix} \begin{bmatrix} p_0 \\ \mathbf{p}_1 \end{bmatrix} = \begin{bmatrix} 1 \\ \mathbf{0} \end{bmatrix} \quad (3.22)$$

where

$$r_{00}(\mathbf{x}) = \int_V \alpha_0(\|\mathbf{x} - \boldsymbol{\xi}\|) d\boldsymbol{\xi} \quad (3.23)$$

$$\mathbf{r}_{10}(\mathbf{x}) = \int_V (\boldsymbol{\xi} - \mathbf{x}) \alpha_0(\|\mathbf{x} - \boldsymbol{\xi}\|) d\boldsymbol{\xi} \quad (3.24)$$

$$\mathbf{R}_{11}(\mathbf{x}) = \int_V (\boldsymbol{\xi} - \mathbf{x})(\boldsymbol{\xi} - \mathbf{x})^T \alpha_0(\|\mathbf{x} - \boldsymbol{\xi}\|) d\boldsymbol{\xi}. \quad (3.25)$$

It is to be noted, that the size of vector  $\mathbf{p}_1$  is equal to the number of spatial dimensions.

### Finite Element Implementation

Using the finite element method, it is convenient to approximate the nonlocal displacement field  $\bar{\mathbf{u}}$  in each element by standard finite element shape functions

$$\bar{u}_i^{(o)}(\mathbf{x}) = \sum_{p \in \mathcal{N}^{(o)}} N^{(o,p)}(\mathbf{x}) \bar{u}_i^{(p)}, \quad (3.26)$$

where  $\mathcal{N}^{(o)}$  is the set of nodes of element  $o$ ,  $\bar{\mathbf{u}}^{(p)}$  are the nonlocal nodal displacement values of node  $p$  and  $N^{(o,p)}$  is the corresponding element shape function. Using a numerical integration scheme, the nonlocal nodal displacements values, given by Eq. (3.19), can be written as

$$\bar{u}_i^{(p)} = \bar{u}_i(\hat{\mathbf{x}}^{(p)}) \quad (3.27)$$

$$= \sum_{q=1}^{n_E} \sum_{r \in \mathcal{I}^{(q)}} w^{(r)} \det \mathbf{J}^{(q)}(\mathbf{x}^{(r)}) \alpha(\hat{\mathbf{x}}^{(p)}, \mathbf{x}^{(r)}) u_i^{(q)}(\mathbf{x}^{(r)}), \quad (3.28)$$

where  $n_E$  is the number of elements,  $\det \mathbf{J}^{(q)}$  is determinant of the Jacobian of element  $q$ ,  $\mathcal{I}^{(q)}$  represents the set of integration points of element  $q$ ,  $\mathbf{x}^{(r)}$  and  $w^{(r)}$  are the coordinates and the weight of integration point  $r$ , and  $\hat{\mathbf{x}}^{(p)}$  are the coordinates of node  $p$ . Substituting the interpolation of the local displacement field, given by Eq. (2.16), into Eq. (3.28) the nonlocal nodal displacement values  $\bar{\mathbf{u}}$  can be expressed as function of the local nodal displacement values  $\hat{\mathbf{u}}$

$$\bar{u}_i^{(p)} = \sum_{q=1}^{n_E} \sum_{r \in \mathcal{I}^{(q)}} w^{(r)} \det \mathbf{J}^{(q)}(\mathbf{x}^{(r)}) \alpha(\hat{\mathbf{x}}^{(p)}, \mathbf{x}^{(r)}) \sum_{s \in \mathcal{N}^{(q)}} N^{(q,s)}(\mathbf{x}^{(r)}) \hat{u}_i^{(s)}. \quad (3.29)$$

The approximation of the nonlocal strain field is obtained by substituting Eq. (3.26) into Eq. (3.18). Using vector notation, the nonlocal strain components can be written as

$$\bar{\varepsilon}_i^{(o)}(\mathbf{x}) = \sum_{p \in \mathcal{N}^{(o)}} \tilde{B}_{ij}^{(o,p)}(\mathbf{x}) \bar{u}_j^{(p)}, \quad (3.30)$$

where  $\tilde{\mathbf{B}}^{(o,p)}$  is that part of the B-matrix, which defines the relationship between the strains of element  $o$  and the nodal displacement values of node  $p$

$$\tilde{\mathbf{B}}^{(o,p)}(\mathbf{x}) = \begin{bmatrix} \frac{\partial N^{(o,p)}}{\partial x_1}(\mathbf{x}) & 0 & 0 \\ 0 & \frac{\partial N^{(o,p)}}{\partial x_2}(\mathbf{x}) & 0 \\ 0 & 0 & \frac{\partial N^{(o,p)}}{\partial x_3}(\mathbf{x}) \\ \frac{\partial N^{(o,p)}}{\partial x_2}(\mathbf{x}) & \frac{\partial N^{(o,p)}}{\partial x_1}(\mathbf{x}) & 0 \\ \frac{\partial N^{(o,p)}}{\partial x_3}(\mathbf{x}) & 0 & \frac{\partial N^{(o,p)}}{\partial x_1}(\mathbf{x}) \\ 0 & \frac{\partial N^{(o,p)}}{\partial x_3}(\mathbf{x}) & \frac{\partial N^{(o,p)}}{\partial x_2}(\mathbf{x}) \end{bmatrix}. \quad (3.31)$$

The corresponding constitutive relationship of element  $o$  is given by

$$\sigma_i^{(o)}(\mathbf{x}) = \sigma_i^{(o)}(\boldsymbol{\varepsilon}^{(o)}(\mathbf{x}), \bar{\boldsymbol{\varepsilon}}^{(o)}(\mathbf{x})) = C_{ij}^{s(o)}(\bar{\boldsymbol{\varepsilon}}^{(o)}(\mathbf{x})) \varepsilon_j^{(o)}(\mathbf{x}) \quad (3.32)$$

where  $\mathbf{C}^s$  is the secant material matrix.

In Eq. (3.29), the nonlocal displacements are calculated as sum over elements and integration points. According to Jirásek and Marfia (2005), the efficiency of the nonlocal model can be increased if this double sum is replaced by a sum over nodes

$$\tilde{u}_i^{(p)} = \sum_{m=1}^{n_N} \tilde{\alpha}^{(m)}(\hat{\mathbf{x}}^{(p)}) \hat{u}_i^{(m)}, \quad (3.33)$$

where  $n_N$  is the number of nodes,  $\hat{\mathbf{u}}^{(m)}$  are the local nodal displacement values of global node  $m$ , and  $\hat{\mathbf{x}}^{(p)}$  are the coordinates of node  $p$ . Using Eq. (3.29), the factor  $\tilde{\alpha}^{(m)}$ , representing the influence of the local displacements of node  $m$  on the nonlocal displacement field, can be defined as

$$\tilde{\alpha}^{(m)}(\mathbf{x}) = \sum_{q \in \mathcal{E}^{(m)}} \sum_{r \in \mathcal{I}^{(r)}} w^{(r)} \det \mathbf{J}^{(q)}(\mathbf{x}^{(r)}) \alpha(\mathbf{x}, \mathbf{x}^{(r)}) N^{(q,m)}(\mathbf{x}^{(r)}), \quad (3.34)$$

where  $\mathcal{E}^{(m)}$  is the set of elements connected to node  $m$ . Since the interaction between two nodes vanishes if the distance exceeds a certain value, the sum in Eq. (3.33) can be limited to the so-called nonlocal nodes. These are nodes for which the nonlocal weight factor does not vanish. For computational efficiency, the nonlocal nodes and the corresponding nonlocal weight factors of a node are determined and stored at the beginning of the simulation.

The tangential element stiffness matrix, representing the derivative of the internal load vector  $\mathbf{f}_{int}^{(o)}$  of element  $o$  with respect to the local nodal displacement values  $\hat{\mathbf{u}}^{(q)}$  of global

node  $q$  is given by

$$K_{ij}^{(o,q)} = \frac{\partial f_{int,i}^{(o)}}{\partial \hat{u}_j^{(q)}} = \frac{\partial}{\partial \hat{u}_j^{(q)}} \int_{V^{(o)}} B_{ki}^{(o)}(\mathbf{x}) \sigma_k^{(o)}(\mathbf{x}) \, dV \quad (3.35)$$

$$\begin{aligned} &= \int_{V^{(o)}} B_{ki}^{(o)}(\mathbf{x}) \frac{\partial \sigma_k^{(o)}}{\partial \bar{\varepsilon}_l^{(o)}}(\mathbf{x}) \sum_{p \in \mathcal{N}^{(o)}} \frac{\partial \bar{\varepsilon}_l^{(o)}(\mathbf{x})}{\partial \bar{u}_j^{(p)}} \frac{\partial \bar{u}_j^{(p)}}{\partial \hat{u}_j^{(q)}} \\ &\quad + B_{ki}^{(o)}(\mathbf{x}) \frac{\partial \sigma_k^{(o)}}{\partial \varepsilon_l^{(o)}}(\mathbf{x}) \frac{\partial \varepsilon_l^{(o)}(\mathbf{x})}{\partial \hat{u}_j^{(q)}} \, dV \end{aligned} \quad (3.36)$$

$$\begin{aligned} &= \int_{V^{(o)}} B_{ki}^{(o)}(\mathbf{x}) \frac{\partial \sigma_k^{(o)}}{\partial \bar{\varepsilon}_l^{(o)}}(\mathbf{x}) \sum_{p \in \mathcal{N}^{(o)}} \tilde{B}_{lj}^{(o,p)}(\mathbf{x}) \tilde{\alpha}^{(q)}(\hat{\mathbf{x}}^{(p)}) \, dV \\ &\quad + \begin{cases} \int_{V^{(o)}} B_{ki}^{(o)}(\mathbf{x}) \bar{C}_{kl}^{s(o)}(\mathbf{x}) \tilde{B}_{lj}^{(o,q)}(\mathbf{x}) \, dV & q \in \mathcal{N}^{(o)} \\ 0 & q \notin \mathcal{N}^{(o)} \end{cases} \end{aligned} \quad (3.37)$$

By applying a numerical integration scheme, Eq. (3.37) reads

$$\begin{aligned} K_{ij}^{(o,q)} &= \sum_{r \in \mathcal{I}^{(o)}} w^{(r)} \det \mathbf{J}^{(o)}(\mathbf{x}^{(r)}) B_{ki}^{(o)}(\mathbf{x}^{(r)}) \frac{\partial \sigma_k^{(o)}}{\partial \bar{\varepsilon}_l^{(o)}}(\mathbf{x}^{(r)}) \sum_{p \in \mathcal{N}^{(o)}} \tilde{B}_{lj}^{(o,p)}(\mathbf{x}^{(r)}) \tilde{\alpha}^{(q)}(\hat{\mathbf{x}}^{(p)}) \\ &\quad + \begin{cases} \sum_{r \in \mathcal{I}^{(o)}} w^{(r)} \det \mathbf{J}^{(o)}(\mathbf{x}^{(r)}) B_{ki}^{(o)}(\mathbf{x}^{(r)}) \bar{C}_{kl}^{s(o)}(\mathbf{x}^{(r)}) \tilde{B}_{lj}^{(o,q)}(\mathbf{x}^{(r)}) & q \in \mathcal{N}^{(o)} \\ 0 & q \notin \mathcal{N}^{(o)} \end{cases} \end{aligned} \quad (3.38)$$

Since the element stiffness matrix is stored in this way, the same procedure for the assembling of the global stiffness matrix as for standard local material formulations can be used. The only modification required is that the column index in the global stiffness matrix is not specified by the global degrees of freedom of the element nodes but by the global degrees of freedom of the nonlocal nodes of that element.

### 3.2.4 Gradient Enhanced Damage Models

In an alternative approach, which can be derived as approximation of the nonlocal formulation given by Eq. (3.4), cf. Bažant (1984a); Lasry and Belytschko (1988), nonlocality is introduced into the constitutive relations by higher-order deformation gradients. Peerlings et al. (1996) propose for an isotropic damage model the following partial differential equation for the nonlocal equivalent strain  $\bar{\varepsilon}_{eq}$ :

$$\bar{\varepsilon}_{eq}(\mathbf{x}) - c \nabla^2 \bar{\varepsilon}_{eq}(\mathbf{x}) = \varepsilon_{eq}(\mathbf{x}) \quad \forall \mathbf{x} \in \Omega \quad (3.39)$$



where  $\varepsilon_{eq}$  is the corresponding local equivalent strain,  $\nabla^2$  is the Laplacian, and  $c$  is a parameter which is related to the internal length scale. Peerlings (1999) has shown that due to the correlation between gradient enhanced models and nonlocal integral-type models,  $c$  can be related to the free parameters  $l$  and  $R$  of the nonlocal weight functions, given by Eqs. (3.7) or (3.8),

$$c = \frac{l^2}{2} = \frac{R^2}{14}. \quad (3.40)$$

A unique solution of Eq. (3.39) requires the definition of additional boundary conditions for the nonlocal equivalent strain. According to Peerlings (1999), the natural boundary condition

$$\frac{\partial \bar{\varepsilon}_{eq}}{\partial x_i}(\mathbf{x}) n_i(\mathbf{x}) = 0 \quad \forall \mathbf{x} \in \Gamma, \quad (3.41)$$

in which  $\mathbf{n}$  denotes the outward unit vector normal to the boundary  $\Gamma$ , is used in this work. Assuming a homogeneous strain field, this boundary condition results in a nonlocal equivalent strain field which is identical to its local counterpart.

### Finite Element Implementation

In order to solve this partial differential equation, the nonlocal field is approximated by a linear combination of  $n_{\bar{N}}$  linearly independent trial functions  $\bar{N}$

$$\bar{\varepsilon}_{eq}(\mathbf{x}) \approx \sum_{i=1}^{n_{\bar{N}}} \bar{N}_i(\mathbf{x}) \bar{e}_i, \quad (3.42)$$

where  $\bar{e}_i$  are unknown coefficients. In general, this approximation does not exactly satisfy Eq. (3.39) and an error or residual can be defined. By applying the method of weighted residuals, the coefficients are determined such that the weighted average of the error between the approximation and the actual solution vanishes. This leads to a system of  $n_{\bar{N}}$  equations for the unknown coefficients

$$\int_{\Omega} \bar{W}_i(\mathbf{x}) (\varepsilon_{eq}(\mathbf{x}) - \bar{\varepsilon}_{eq}(\mathbf{x})) d\Omega + c \int_{\Omega} \bar{W}_i(\mathbf{x}) \nabla^2 \bar{\varepsilon}_{eq}(\mathbf{x}) d\Omega = 0 \quad i = 1, 2, \dots, n_{\bar{N}}, \quad (3.43)$$

in which  $\bar{W}_i$  denote the weight functions. Using integration by parts and applying the divergence theorem, the second term of Eq. (3.43) can be rewritten as

$$\int_{\Omega} \bar{W}_i(\mathbf{x}) \nabla^2 \bar{\varepsilon}_{eq}(\mathbf{x}) d\Omega = \int_{\Gamma} \bar{W}_i(\mathbf{x}) \frac{\partial \bar{\varepsilon}_{eq}}{\partial x_j}(\mathbf{x}) n_j(\mathbf{x}) d\Gamma - \int_{\Omega} \frac{\partial \bar{W}_i}{\partial x_j}(\mathbf{x}) \frac{\partial \bar{\varepsilon}_{eq}}{\partial x_j}(\mathbf{x}) d\Omega. \quad (3.44)$$

Substituting Eq. (3.44) into Eq. (3.43) and considering the natural boundary conditions, Eq. (3.41), the weak form of Eq. (3.39) is obtained

$$\int_{\Omega} \bar{W}_i(\mathbf{x}) \bar{\varepsilon}_{eq}(\mathbf{x}) + c \frac{\partial \bar{W}_i}{\partial x_j}(\mathbf{x}) \frac{\partial \bar{\varepsilon}_{eq}}{\partial x_j}(\mathbf{x}) \, d\Omega = \int_{\Omega} \bar{W}_i(\mathbf{x}) \varepsilon_{eq}(\mathbf{x}) \, d\Omega. \quad (3.45)$$

By using the Galerkin approach, in which the weight functions  $\bar{W}_i$  are chosen to be identical to the trial functions  $\bar{N}$ , and by substituting the approximation of the nonlocal equivalent strain field, Eq. (3.42), into Eq. (3.45), the weak form can be rewritten as

$$\underbrace{\int_{\Omega} \bar{N}_i(\mathbf{x}) \bar{N}_j(\mathbf{x}) + c \bar{B}_{ik}(\mathbf{x}) \bar{B}_{jk}(\mathbf{x}) \, d\Omega}_{K_{ij}^{\bar{e}\bar{e}}} \bar{e}_j = \underbrace{\int_{\Omega} \bar{N}_i(\mathbf{x}) \varepsilon_{eq}(\mathbf{x}) \, d\Omega}_{f_i^{\bar{e}}} \quad i, j = 1, 2, \dots, n_{\bar{N}}, \quad (3.46)$$

in which the matrix  $\bar{\mathbf{B}}$  is defined as

$$\bar{B}_{ij}(\mathbf{x}) = \frac{\partial \bar{N}_i}{\partial x_j}(\mathbf{x}). \quad (3.47)$$

In the presented approach, the nonlocal variable is interpolated by standard finite element shape functions using the same spatial discretization as for the local displacement field. In general, the interpolation functions for both fields can be defined independently. Peerlings (1999) has shown that for the presented model the usage of interpolation polynomials of the same order for both fields may result in stress oscillations. In order to avoid these stress oscillations, Peerlings (1999) proposes to use for the displacements an interpolation of one order higher than that for the nonlocal equivalent strains.

In an equilibrium state, finite element models with gradient enhanced damage formulations must satisfy both, the weak form of the standard equilibrium equations, Eq. (2.50), and the weak form of the partial differential equation for the nonlocal equivalent strain, Eq. (3.45). This leads to a coupled, two field problem which is represented by a generally nonlinear system of equations. Using Newton's method, the unknown nodal values (displacements  $\mathbf{d}$  and nonlocal equivalent strains  $\bar{\mathbf{e}}$ ) can be determined in an iterative way. In the  $i$ -th iteration step, the linearized equations are given by

$$\begin{bmatrix} \mathbf{K}^{dd^{(i-1)}} & \mathbf{K}^{d\bar{e}^{(i-1)}} \\ \mathbf{K}^{\bar{e}d^{(i-1)}} & \mathbf{K}^{\bar{e}\bar{e}} \end{bmatrix} \begin{bmatrix} \Delta \mathbf{d}^{(i)} \\ \Delta \bar{\mathbf{e}}^{(i)} \end{bmatrix} = \begin{bmatrix} \mathbf{f}_{ext} - \mathbf{f}_{int}^{(i-1)} \\ \mathbf{f}^{\bar{e}^{(i-1)}} - \mathbf{K}^{\bar{e}\bar{e}} \bar{\mathbf{e}}^{(i-1)} \end{bmatrix} \quad i = 1, 2, \dots \quad (3.48)$$

in which the sub-matrices and sub-vectors are defined as

$$K_{kl}^{dd^{(i-1)}} = \int_{\Omega} B_{mk}(\mathbf{x}) \frac{\partial \sigma_m}{\partial \varepsilon_n}(\mathbf{u}^{(i-1)}(\mathbf{x}), \bar{\varepsilon}_{eq}^{(i-1)}(\mathbf{x})) B_{nl}(\mathbf{x}) \, d\Omega \quad (3.49)$$

$$K_{kl}^{d\bar{e}^{(i-1)}} = \int_{\Omega} B_{mk}(\mathbf{x}) \frac{\partial \sigma_m}{\partial \bar{\varepsilon}_{eq}}(\mathbf{u}^{(i-1)}(\mathbf{x}), \bar{\varepsilon}_{eq}^{(i-1)}(\mathbf{x})) \bar{N}_k(\mathbf{x}) \, d\Omega \quad (3.50)$$

$$K_{kl}^{\bar{e}d(i-1)} = \int_{\Omega} \bar{N}_k(\mathbf{x}) \frac{\partial \varepsilon_{eq}}{\partial \varepsilon_m}(\mathbf{u}^{(i-1)}(\mathbf{x})) B_{ml}(\mathbf{x}) d\Omega \quad (3.51)$$

$$K_{kl}^{\bar{e}\bar{e}} = \int_{\Omega} \bar{N}_k(\mathbf{x}) \bar{N}_l(\mathbf{x}) + c \bar{B}_{km}(\mathbf{x}) \bar{B}_{lm}(\mathbf{x}) d\Omega \quad (3.52)$$

$$f_{int,k}^{(i-1)} = \int_{\Omega} B_{mk}(\mathbf{x}) \sigma_m(\mathbf{u}^{(i-1)}(\mathbf{x}), \bar{\varepsilon}_{eq}^{(i-1)}(\mathbf{x})) d\Omega \quad (3.53)$$

$$f_k^{\bar{e}(i-1)} = \int_{\Omega} \bar{N}_k(\mathbf{x}) \varepsilon_{eq}(\mathbf{u}^{(i-1)}(\mathbf{x})) d\Omega. \quad (3.54)$$

By solving this linear system of equations, an improved approximation of the unknown nodal degrees of freedom is obtained

$$d_j^{(i)} = d_j^{(i-1)} + \Delta d_j^{(i)} \quad (3.55)$$

$$\bar{e}_j^{(i)} = \bar{e}_j^{(i-1)} + \Delta \bar{e}_j^{(i)}. \quad (3.56)$$

The successive update of the unknown nodal values is repeated until a predefined convergence criterion is satisfied. Due to the different physical meaning of the two fields, the system of equations given by Eq. (3.48) may become ill-conditioned even if the material is still linear elastic. The condition number of the coefficient matrix can be improved by scaling the partial differential equation for the nonlocal equivalent strain, Eq. (3.39), by the Young's modulus  $E$  of the undamaged material. Then, the modified equation reads

$$E(\bar{\varepsilon}_{eq}(\mathbf{x}) - c \nabla^2 \bar{\varepsilon}_{eq}(\mathbf{x})) = E \varepsilon_{eq}(\mathbf{x}) \quad \forall \mathbf{x} \in \Omega. \quad (3.57)$$

Since Eq. (3.57) is multiplied by the Young's modulus on both sides, only the sub-matrices and sub-vectors in the second row of the coefficient matrix and the right-hand-side vector in Eq. (3.48) are modified, whereas the correction of the unknown nodal values of the nonlocal variable remain unchanged.

### 3.2.5 Discussion

In the preceding subsections, three different methods – the crack band approach, the nonlocal integral type approach and the nonlocal gradient approach – for the regularization of damage material formulations are presented. In this thesis, the crack band approach and the nonlocal integral type approach with averaging of strain like variables as well as averaging of the displacement field are used for the regularization of continuum damage models and smeared crack models, introduced in Sects. 3.3 to 3.5.

The adjustment of the fracture energy with respect to the element size, as proposed in the crack band approach (Sect. 3.2.1), is easy to understand and to implement in existing finite element codes. Using Eq. (3.2), the obtained equivalent element size gives, in general, an improper approximation of the actual width of the numerically simulated fracture process

zone, especially for irregular finite element meshes. More sophisticated approaches taking into account the orientation of the fracture process zone require a substantial higher computational effort. Furthermore, damage still localizes in a single layer of elements. Consequently, the orientation of the simulated fracture process zone may depend on the orientation and shape of the finite elements. On the mesoscale, the evolution of multiple microcracks, involving crack branching and crack coalescence, must be represented by the numerical model. In general, these effects cannot be properly simulated using local material formulations even with the crack band approach, cf. Eckardt et al. (2004). As a result, the application of local material formulations to mesoscale simulations of concrete is not further investigated in this thesis.

By using nonlocal material formulations, pathological sensitivities of the numerical results with respect to mesh refinement and mesh orientation can be reduced. Patzák and Jirásek (2004) show that in simulations using nonlocal material formulations an average mesh size smaller than the nonlocal interaction radius, which is, in general, related to the actual size of the fracture process zone, is required to obtain a smooth representation of the damage distribution. Compared to simulations with local material formulations using the crack band approach, which explicitly assume that the element size is larger than the actual size of the fracture process zone, the total number of finite elements increases significantly. In this thesis, the nonlocal integral type approach with averaging of strain like variables, Sect. 3.2.2, as well as averaging of the displacement field, Sect. 3.2.3, is used for damage simulations due to the objectivity of the obtained numerical results. The implementation of integral type nonlocal models in existing finite element codes is relatively straightforward, since major modifications, e.g. the evaluation of the nonlocal quantity, are mostly limited to element routines. Due to the different storage of the element stiffness matrix, an additional minor modification is required within the global assembling procedure. Since in each iteration step the nonlocal quantity must be calculated for each integration point, the computational effort increases if a nonlocal integral type model is used. Furthermore, the storage of nonlocal weight factors, nonlocal elements or nonlocal nodes require additional memory. The numerical effort and the memory demand for the solution of the global system of equations is affected by the increasing bandwidth and the additional loss of symmetry of the tangential stiffness matrix. Compared to simulations with local material formulations, the analysis with a nonlocal material models show, in general, a significantly better convergence behavior.

Using a gradient enhanced damage model, additional nodal degrees of freedom are introduced into the numerical model. As a result, the size of the global system of equations, which must be solved in each iteration step for the unknown nodal displacements and the nonlocal quantities, increases significantly, even if the material is still in the linear elastic range. Consequently, the gradient enhanced damage approach is not used in this thesis for mesoscale simulations of concrete. It is to be noted that, from a mathematical point of view, the gradient formulation is still local, since stresses in a given point depend only on values (deformations and nonlocal variables) in this point itself. As a result, this approach is, in contrast to integral type nonlocal models, well suited for parallel applications based on domain decomposition, since no further communication between sub-domains is required for the calculation of the nonlocal value.

## 3.3 Isotropic Damage Model

### 3.3.1 Local Formulation

The simplest version of a continuum damage model is the isotropic damage model. In this model, only a scalar parameter  $\omega$  characterizes the density and orientation of microdefects. This implies the assumption that the orientation of these microdefects is distributed uniformly in all directions, Lemaitre and Chaboche (1990). Consequently, the damage state of the material can be characterized by the amount of microdefects on a cross-section with arbitrary orientation in the body under consideration. According to Kachanov (1986), the damage parameter can be defined by relating the damaged part  $A_D$  of the cross-section area, to the initial area  $A_0$  of this cross-section

$$\omega = \frac{A_D}{A_0}. \quad (3.58)$$

As a result, the damage parameter monotonically increases, due to the initiation and propagation of microdefects, from zero, representing the undamaged or virgin material, to unity, which corresponds to a completely damaged material. By introducing the concept of effective stresses, Kachanov (1986), and by using the principle of strain-equivalence, Lemaitre (1984), the constitutive equations can be written as

$$\sigma_i = (1 - \omega)\sigma_{eff,i} = (1 - \omega)C_{ij}^e \varepsilon_j = C_{ij}^s \varepsilon_j, \quad (3.59)$$

where  $\boldsymbol{\sigma}$  is the nominal stress vector,  $\boldsymbol{\sigma}_{eff}$  is the effective stress vector,  $\mathbf{C}^e$  is the linear elastic material matrix,  $\mathbf{C}^s$  is the secant material matrix, and  $\boldsymbol{\varepsilon}$  is the vector of total strains. The nominal stress is, in general, used in the macroscopic equilibrium equations, while the effective stress can be interpreted as the stress acting on the material microstructure. It is to be noted that the assumption of isotropic stiffness degradation represented by the evolution of one scalar parameter  $\omega$  implies that the Poisson's ratio is constant during the failure process.

In general, the evolution of the damage parameter is driven by a so-called equivalent strain,  $\varepsilon_{eq}$ , which is a scalar measure of the deformation state. The definition of the equivalent strain directly affects the shape of the failure surface, which represents the boundary of the elastic domain. In this thesis, the Rankine criterion is used to describe the tensile failure of the mortar matrix. The corresponding equivalent strain is defined as

$$\varepsilon_{eq} = \frac{1}{E} \max_{i=1,2,3} \langle s_{eff,i} \rangle, \quad (3.60)$$

where  $s_{eff,i}$  is the  $i$ -th eigenvalue of the effective stress tensor. The brackets  $\langle \dots \rangle$  denote that only positive eigenvalues are considered in the definition of the equivalent strain. Assuming that the elastic limit is defined by the tensile strength  $f_t$ , damage initiates if the largest eigenvalue of the effective stress tensor reaches this value. The normalization by the Young's modulus  $E$  is introduced to obtain a strain like quantity. In order to avoid numerical problems due to identical eigenvalues, the original definition of the equivalent

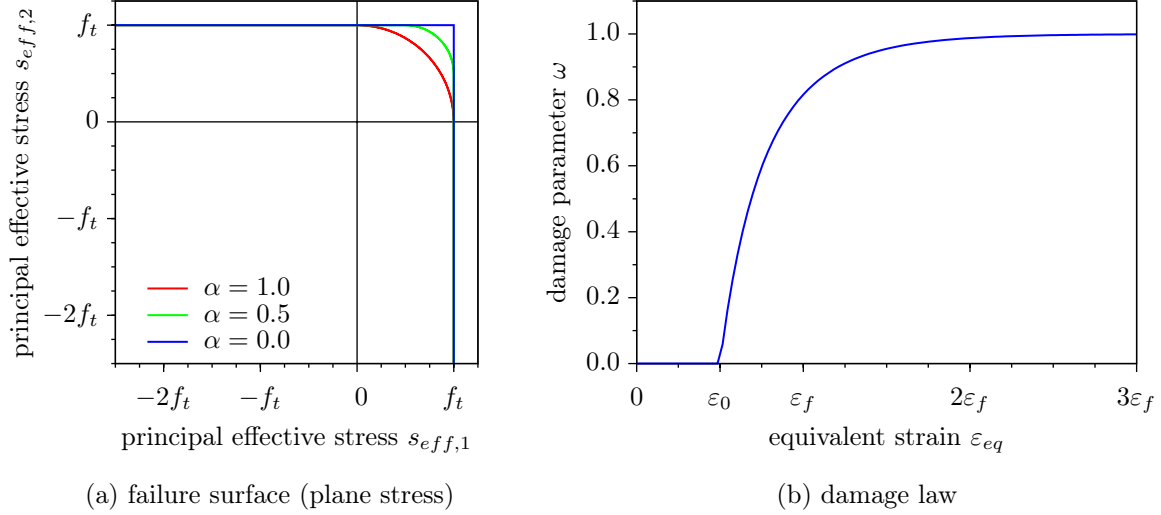


Figure 3.2: Isotropic damage model – failure surface and damage law.

strain is rewritten as

$$\varepsilon_{eq} = \frac{1}{E} \left( \sqrt{\sum_{i=1}^3 \langle s_{eff,i} - \alpha f_t \rangle^2} + \alpha f_t \right), \quad (3.61)$$

where  $\alpha$  is a dimensionless parameter ranging from zero, which corresponds to the original Rankine criterion, to unity. Assuming  $\alpha = 1$ , the corners in the octants with more than one positive eigenvalue are rounded. The diagram in Fig. 3.2(a) shows the corresponding failure surface for varying values of  $\alpha$ .

The evolution of the damage parameter  $\omega$  is defined by an exponential damage law, Fig. 3.2(b). This implies that the damage variable approaches unity only asymptotically. In order to guarantee that the damage parameter monotonically increases, a history variable  $\varepsilon_{eq,max}$  is introduced, characterizing the maximum equivalent strain ever reached in material history, and the damage law is expressed as function of this variable

$$\omega(\varepsilon_{eq,max}) = \begin{cases} 0.0 & \varepsilon_{eq,max} < \varepsilon_0 \\ 1.0 - \frac{\varepsilon_0}{\varepsilon_{eq,max}} \exp\left(-\frac{\varepsilon_{eq,max} - \varepsilon_0}{\varepsilon_f - \varepsilon_0}\right) & \varepsilon_{eq,max} \geq \varepsilon_0 \end{cases}, \quad (3.62)$$

where  $\varepsilon_0 = f_t/E$  is the elastic limit,  $\varepsilon_f = 2g_f/f_t$  is a parameter controlling the ductility of the material. Assuming a local material formulation and using the crack band approach, the volume specific fracture energy  $g_f$  is defined by Eq. (3.1).

### 3.3.2 Nonlocal Formulation

A nonlocal version of the isotropic damage model is presented in Patzák and Jirásek (2004). In this model, the equivalent strain is calculated from the nonlocal strain vector  $\bar{\varepsilon}$ , which

is defined either as weighted average of the local strain field, Eq. (3.4), or as function of the nonlocal displacement field, Eq. (3.18). The corresponding stress-strain relationship can be written as

$$\sigma_i = (1 - \omega(\varepsilon_{eq}(\bar{\varepsilon}))) C_{ij}^e \varepsilon_j. \quad (3.63)$$

A comparison of alternative nonlocal formulations of the isotropic damage model can be found in Jirásek (1998b). Depending on the chosen nonlocal formulation, the tangential stiffness matrix is given either by Eq. (3.13) or Eq. (3.37). The corresponding derivative of the stresses with respect to the components of the nonlocal strain vector can be written as

$$\frac{\partial \sigma_i}{\partial \bar{\varepsilon}_j} = - \frac{\partial \omega}{\partial \bar{\varepsilon}_j} C_{ik}^e \varepsilon_k = - \frac{\partial \omega}{\partial \varepsilon_{eq}} \frac{\partial \varepsilon_{eq}}{\partial \bar{\varepsilon}_j} C_{ik}^e \varepsilon_k. \quad (3.64)$$

### Determination of the Volume Specific Fracture Energy

In the isotropic damage model presented above, the evolution of damage is characterized by the Mode I fracture energy. This material parameter is defined as the energy dissipated during the fracture process divided by the area of the final crack surface. Consequently, the width of the fracture process zone perpendicular to the crack surface is not included in this parameter. Using a nonlocal material formulation, the width of the fracture process zone is introduced as an additional material parameter into the material model. Depending on the chosen nonlocal weight function, the width is either represented by the characteristic length  $l_c$ , Eq. (3.7), or the nonlocal interaction radius  $R$ , Eq. (3.8). In general, the actual width of the fracture process zone in concrete cannot be properly determined by experiments. Therefore, the significance of the nonlocal radius as material property is neglected in this thesis and the nonlocal interaction radius is considered as a numerical parameter. As shown in Patzák and Jirásek (2004), a minimum number of integration points and finite elements is required inside the fracture process zone in order to represent the nonlocal field sufficiently smooth. Consequently, the maximum allowable mesh size inside the fracture process zone is related to the nonlocal interaction radius. By considering the nonlocal radius as numerical parameter – and not as material property – the nonlocal radius can be chosen with respect to the present mesh size. Since the numerical effort for calculating the nonlocal quantity and the memory demand for storing the tangential matrix increases significantly with increasing ratio between the nonlocal radius and average finite element size, this approach is especially advantageous for finite element simulations in which a very fine finite element mesh is required for an appropriate representation of the geometry or the stress and strain field.

In the isotropic damage model, the damage evolution is described as a function of the volume specific fracture energy  $g_f$ . In order to ensure that the dissipation of inelastic energy is identical in experiments and numerical simulations, the area specific fracture energy  $G_f$ , measured in the experiments, has to be related to the width of the fracture process zone observed in the numerical simulation. Since in nonlocal material formulations the size of the fracture process zone depends on the nonlocal radius  $R$ , the volume specific

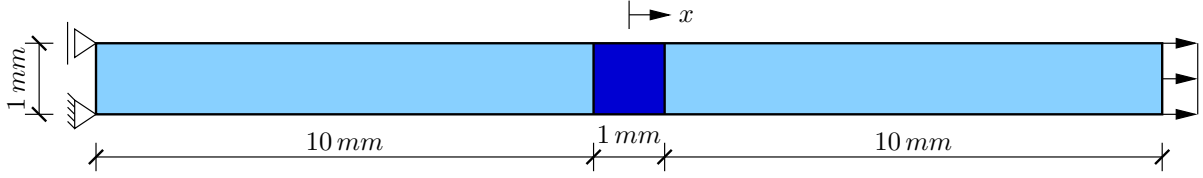


Figure 3.3: Geometry and loading setup of the bar in uniaxial tension (the dark blue color indicates the weakened domain).

fracture energy is defined as

$$g_f = \frac{G_f}{\beta R}, \quad (3.65)$$

where  $\beta$  is a scalar parameter representing the damage distribution in the fracture process zone. The value of this parameter depends on the nonlocal material formulation, the nonlocal quantity and the nonlocal weight function. It is to be noted, that this approach implies the assumption that in numerical simulations the damage profile perpendicular to the fracture process zone is a typical property of the material model. Furthermore, it is assumed that the fracture process zone is completely developed. This is not the case if damage evolves along an material interface. Since the fracture process zone is bounded by the interface, the volume in which inelastic energy is dissipated decreases. Assuming a constant volume specific fracture energy, a lower amount of energy would be dissipated during the fracture process.

The numerical simulation of a uniaxial tension test of a concrete specimen, shown in Fig. 3.3, is used to determine the parameter  $\beta$  for the nonlocal isotropic damage model presented above. The corresponding material parameters are summarized in Table 3.1. In order to ensure that damage localizes during the simulation, the tensile strength is reduced to 90 % in the middle of the specimen. In Fig. 3.3 the weakened region is plotted in dark blue. The specimen geometry is discretized by two-dimensional 9-node plane elements assuming plane stress conditions. Simulations with varying element sizes are performed to investigate the sensitivity of the numerical results with respect to the element size. The diagrams in Fig. 3.4 show the damage profile perpendicular to the final crack, the corresponding distribution of the equivalent strain and the distribution of the inelastic energy density for different mesh sizes and for both nonlocal formulations. In all simulations, almost the same width of the damage zone is observed. Consequently, due to the nonlocal formulation of the material law the size of the fracture process zone becomes independent of the mesh size. In simulations with the coarse mesh, with equal element size and non-

Table 3.1: Material parameters of the nonlocal isotropic damage model.

Young's modulus	$E$	$[N/mm^2]$	30 000
Poisson's ratio	$\nu$	$[-]$	0.2
Tensile strength	$f_t$	$[N/mm^2]$	3.0
Fracture energy	$G_f$	$[Nmm/mm^2]$	0.1
Nonlocal radius	$R$	$[mm]$	1.0



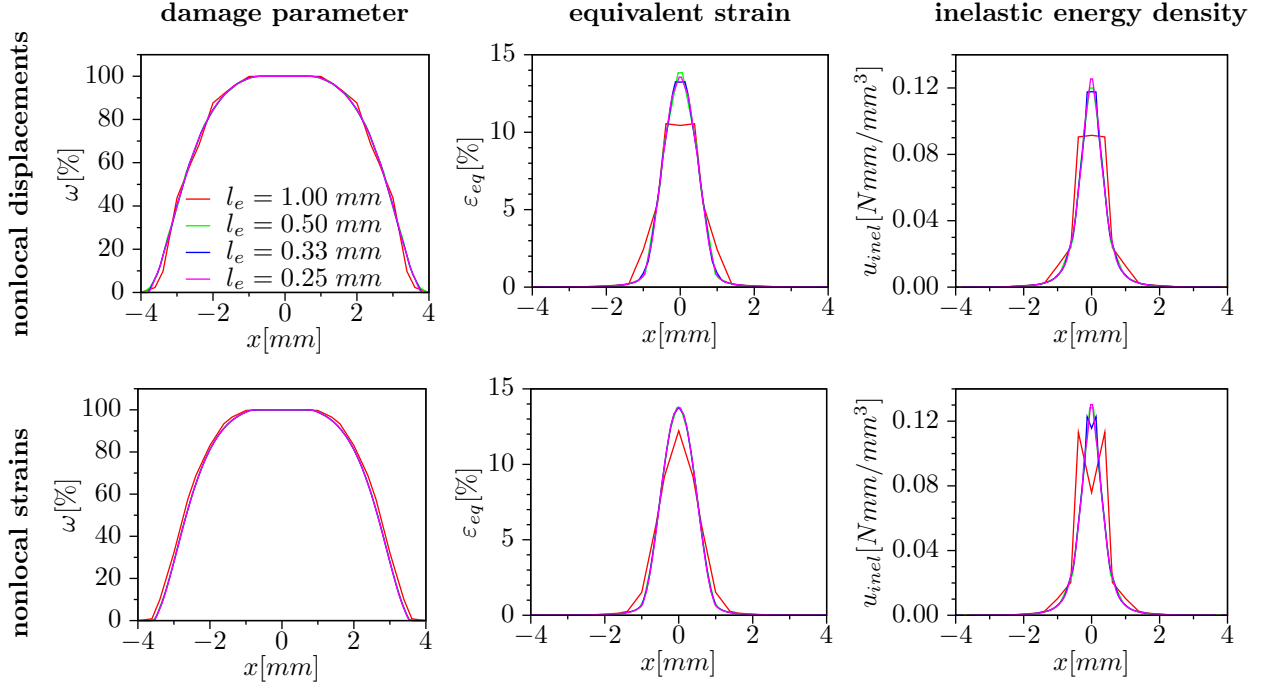


Figure 3.4: Final distribution of the damage variable, the equivalent strain and the inelastic energy density for the nonlocal isotropic damage model with averaging of the displacement field and of the strain field.

local radius, a good approximation of the damage profile is already obtained, but major variations compared to the finer meshes are noticeable in the distribution of the equivalent strain and the inelastic energy density. Using a ratio of 0.5 or smaller between element size and nonlocal radius the differences in the equivalent strain and in the inelastic energy density become negligible.

The 9-node plane element uses a 3x3 Gauss rule for the numerical integration of the element contributions. As shown in Fig. 3.4, a local minimum in the inelastic energy density is observed in the specimen center for the nonlocal model with averaging of the strain field if integration points are located on the axis of symmetry. Due to the symmetry, a constant local strain field is observed in the center element. In these points, a maximum is obtained in the equivalent strain which is calculated from the nonlocal strains and in the damage parameter. As a consequence of the higher damage parameter, lower nominal stress values are obtained in the integration points on the axis of symmetry. Since the stresses decrease faster in these points, a lower amount of inelastic energy is dissipated. This phenomena is not observed for the isotropic damage model with nonlocal displacement averaging. Due to symmetry an almost constant nonlocal equivalent strain field is obtained for this model in the center element. As a result the damage parameter, the nominal stresses and the inelastic energy density are also almost constant.

The parameter  $\beta$  required for the calculation of the volume specific Mode I fracture energy, Eq. (3.65), is determined from numerical simulations with the finest mesh. In order to evaluate the inelastic energy dissipated during the fracture process, the nonlinear sim-

ulation is performed until the final crack becomes almost stress free. Consequently, the entire load-displacement curve including the softening branch is obtained. At first, the numerical simulation is performed assuming  $\beta = 1.0$ . Then, the total amount of dissipated energy is calculated either from the final distribution of the inelastic energy density or from the global load-displacement curve. By relating the dissipated energy to the area of the specimen cross section the fracture energy is obtained. It is to be noted, that this approach implies the assumption of a single crack. Finally, the parameter  $\beta$  is calculated as the ratio between the fracture energy obtained in the numerical simulation with  $\beta = 1.0$  and the actual fracture energy of the material, which is used as input parameter. For both nonlocal formulations, nonlocal strains and nonlocal displacements, a value of  $\beta = 1.7$  is obtained.

### 3.4 Rotating Crack Model

A special class of constitutive models developed for tensile failure of quasi-brittle materials, such as concrete, is based on the smeared crack approach, which was introduced by Rashid (1968). In contrast to the discrete crack concept, in which the crack is modeled as geometrical discontinuity, the smeared crack approach represents the cracked solid as continuum. By modifying the components of the elastic material stiffness or compliance matrix as a function of the crack orientation, e.g. Rashid (1968), or by introducing cracking strains normal and tangential to the crack surface, e.g. Bažant and Gambarova (1980), the crack is “smeared” over a finite volume. As a result, initial isotropic material behavior becomes orthotropic as soon as first cracks develop. Smeared crack concepts can be classified into fixed and rotating crack approaches. With the fixed crack approach, e.g. Rashid (1968); Bažant and Oh (1983a), the crack orientation, specified by the crack initiation criterion, remains constant during the simulation. Using the Rankine criterion for crack initiation, the crack direction coincides with the direction of the principal stress. During the simulation, the assumption of a fixed crack direction may result in a misalignment between the axes of material orthotropy, representing the crack, and the principal axes of stresses. As consequence of this misalignment, the evolution of the crack opening is controlled by the stresses and strains along the axes of material orthotropy and not, as induced by the Rankine criterion, by the principal stresses and strains of the current state, cf. Willam et al. (1987). By using the fixed multi-directional crack concept, as proposed by de Borst and Nauta (1985) for non-orthogonal cracks, this defect of the fixed single-crack concept can be avoided. Whenever the misalignment between the crack direction and the direction of principal stress exceeds a certain angle, a new crack is initiated. In an alternative approach, proposed by Cope et al. (1980), the axes of material orthotropy co-rotate with the axes of principal strains. In these initial versions of a rotating crack model, the direction of principal stresses may deviate from the direction of principal strains due to the developing material orthotropy which was criticized by Bažant (1983). As a result, Bažant (1983) outlined an additional condition for these kind of models that enforces coaxiality between principal stress and strains. The first true rotating crack formulation, proposed by Gupta and Akbar (1984), is free of this shortcoming. A comprehensive study of both concepts – fixed and rotating cracks – can be found in Rots (1988).

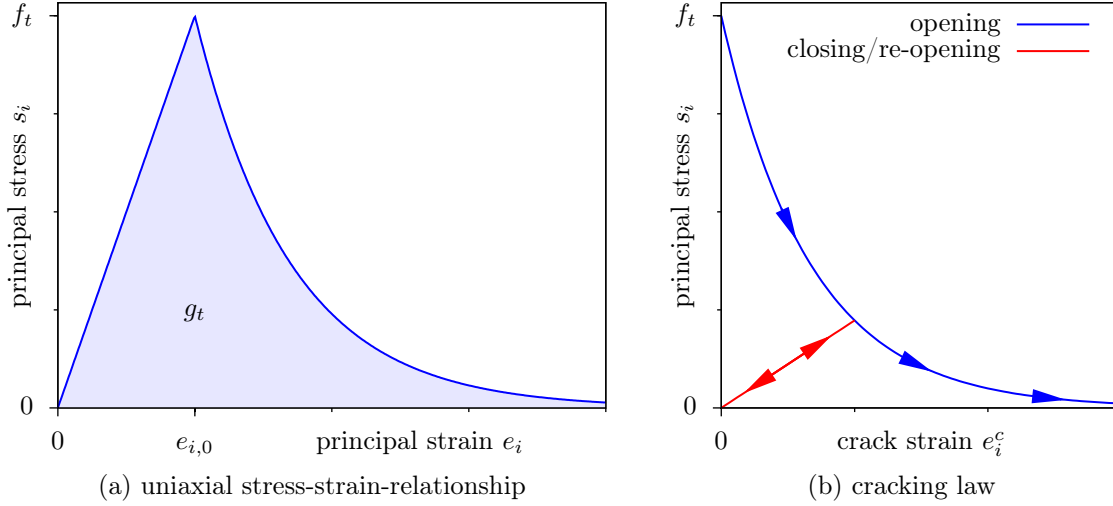


Figure 3.5: Uniaxial stress-strain-relationship and damage law of the rotating crack model.

### 3.4.1 Local Formulation

In the present work, the rotating crack model (RCM) developed by Jirásek and Zimmermann (1998a) is used. In this model, the total strain vector  $\boldsymbol{\varepsilon}$  is decomposed into an elastic part  $\boldsymbol{\varepsilon}^e$ , representing the strains in the undamaged material between the cracks, and an inelastic part  $\boldsymbol{\varepsilon}^c$  due to cracking

$$\varepsilon_i = \varepsilon_i^e + \varepsilon_i^c. \quad (3.66)$$

For the material between the cracks the constitutive equations are given by

$$\sigma_i = C_{ij}^e \varepsilon_j^e = C_{ij}^e (\varepsilon_j - \varepsilon_j^c) = C_{ij}^s \varepsilon_j, \quad (3.67)$$

where  $\mathbf{C}^e$  is the linear elastic material matrix and  $\mathbf{C}^s$  is the secant material matrix. In the general three-dimensional case up to three orthogonal cracks, which are aligned with the principal direction of stresses and strains, may develop independently in a single material point. The initiation of each crack is defined by the Rankine criterion

$$s_i \leq f_t. \quad (3.68)$$

A crack is initiated if the corresponding principal stress  $s_i$  reaches the tensile strength  $f_t$ . After crack initiation, the relationship between the inelastic strain  $e_i^c$  normal to the crack and the corresponding principal stress value representing the stress which is still transferred through the crack, is given by the cracking law. Assuming that the crack opens, the constitutive equation of the crack is defined by an exponential function

$$s_i(e_i^c) = f_t \exp\left(-\frac{e_i^c}{\gamma_t}\right), \quad (3.69)$$

where  $\gamma_t$  is a material parameter which can be derived from the uniaxial stress strain relationship of crack  $i$  shown in the diagram in Fig. 3.5(a). Using this uniaxial relationship, the inelastic energy dissipated at infinite strains, which must be equal to the volume specific fracture energy  $g_t$ , Eq. (3.1), can be written as

$$\begin{aligned} g_t &= \int_{e_i=0}^{\infty} s_i(e_i) de_i = \int_{e_i=0}^{e_{i,0}} E e_i de_i + \int_{e_i=e_{i,0}}^{\infty} f_t \exp\left(-\frac{e_i - e_{i,0}}{\gamma_t}\right) de_i \\ &= \frac{E}{2} e_i^2 \Big|_0^{e_{i,0}} - \gamma_t f_t \exp\left(-\frac{e_i - e_{i,0}}{\gamma_t}\right) \Big|_{e_{i,0}}^{\infty} = \frac{E}{2} e_{i,0}^2 + \gamma_t f_t \end{aligned} \quad (3.70)$$

where  $e_{i,0}$  indicates the elastic limit,  $f_t$  is the tensile strength, and  $E$  is the Young's modulus of the undamaged material. By substituting  $e_{i,0} = f_t/E$  into Eq. (3.70) and by rearranging, the parameter  $\gamma_t$  is obtained

$$\gamma_t = \frac{g_t}{f_t} - \frac{f_t}{2E}. \quad (3.71)$$

If the crack is in a closing situation, an unloading to the origin is performed and the corresponding cracking law reads

$$s_i(e_i^c) = \frac{s_i(e_{i,max}^c)}{e_{i,max}^c} e_i^c \quad e_i^c < e_{i,max}^c \quad (3.72)$$

where  $e_{i,max}^c$  is the maximum inelastic strain ever reached for this crack in the material history. This relationship is also applied if the crack re-opens. The diagram, Fig. 3.5(b), illustrates the complete cracking law for a single crack.

## Evaluation of Stresses and Inelastic Strains

In the rotating crack model, the evolution of the inelastic strains, representing the damage state of the material, is a function of the current stress state, which is also unknown. As a result, the implementation of the rotating crack model requires an algorithm that evaluates the crack configuration characterized by the corresponding stresses  $\boldsymbol{\sigma}^{(n)}$  and inelastic strains  $\boldsymbol{\epsilon}^{(n)}$  for a prescribed strain state  $\boldsymbol{\epsilon}^{(n)}$  at the material point. At the beginning of this algorithm, it is assumed that the crack configuration obtained for the previous equilibrium state is known. This includes for each crack  $i$  the inelastic strains  $e_i^{c(n-1)}$ , the maximum inelastic strains  $e_{i,max}^{c(n-1)}$ , the crack direction and the crack status. In a first step, the principal strain values  $e_i^{(n)}$  and the corresponding principal directions  $\mathbf{n}_i$  are calculated. In order to guarantee that a crack is assigned to the right principal strain, the principal strains are sorted in the way that for each crack the smallest angle between previous crack direction and current principal direction is obtained. Rewriting Eq. (3.67) in terms of the principal components and by considering the maximum inelastic strains in

this equation, a trial stress state in principal directions can be obtained

$$s_i^{trial} = \tilde{C}_{ij}^e \left( e_j^{(n)} - e_{j,max}^{c(n-1)} \right), \quad (3.73)$$

where  $\tilde{C}^e$  is the reduced linear elastic material matrix, defined as

$$\tilde{C}^e = \frac{E}{(1+\nu)(1-2\nu)} \begin{bmatrix} 1-\nu & \nu & \nu \\ \nu & 1-\nu & \nu \\ \nu & \nu & 1-\nu \end{bmatrix}. \quad (3.74)$$

By comparing the trial stresses with the stresses which would be transferred through the crack under the assumption that the inelastic strains are equal to the maximum inelastic strains, the current crack status can be determined

$$\text{status of crack } i = \begin{cases} \text{opening} & \text{if } s_i^{trial} \geq f_t \text{ or } s_i^{trial} \geq s_i(e_{i,max}^{c(n-1)}) \\ \text{closing/re-opening} & \text{if } e_{i,max}^{c(n-1)} > 0 \text{ and } s_i^{trial} < s_i(e_{i,max}^{c(n-1)}) \\ \text{no crack} & \text{if } s_i^{trial} < f_t \text{ and } e_{i,max}^{c(n-1)} = 0 \end{cases}. \quad (3.75)$$

In a second step, the inelastic strains are calculated. For each crack  $i$ , the following equality must be satisfied

$$s_i \left( e_i^{c(n)} \right) = \tilde{C}_{ij}^e \left( e_j^{(n)} - e_j^{c(n)} \right), \quad (3.76)$$

which implies that the stress transferred through the crack, Eq. (3.69), must be identical to the corresponding principal stress value. By using Newton's method, with the inelastic strains of the last converged load step as starting values, this, in general, nonlinear system of equations can be solved iteratively for the unknown inelastic strains. Linearization of Eq. (3.76) leads to

$$\left. \begin{aligned} \left[ \frac{\partial s_i}{\partial e_k^c} \left( e_i^{c(n,p-1)} \right) + \tilde{C}_{ik}^e \right] \delta e_k^{c(n,p)} &= \tilde{C}_{ij}^e \left( e_j^{(n)} - e_j^{c(n,p-1)} \right) - s_i \left( e_i^{c(n,p-1)} \right) \\ e_i^{c(n,p)} &= e_i^{c(n,p-1)} + \delta e_i^{c(n,p)} \end{aligned} \right\} p = 1, 2, \dots \quad (3.77)$$

where  $\delta e^{c(n,p)}$  is the correction of the inelastic strains in the  $p$ -th iteration of load step  $n$ . After convergence of this procedure, the status of each crack is determined again

$$\text{status of crack } i = \begin{cases} \text{closing} & \text{if old status is opening and } e_i^{c(n)} < e_i^{c(n-1)} \\ \text{opening} & \text{if old status is re-opening and } e_i^{c(n)} > e_{i,max}^{c(n-1)} \\ \text{old status} & \text{otherwise} \end{cases}. \quad (3.78)$$

If the status of a crack is changed, the iterative procedure for the calculation of the inelastic strains is repeated. Otherwise, the corresponding principal stress values  $\mathbf{s}^{(n)}$  are calculated.

As a last step, the transformation of the principal stresses back to the initial coordinate system is performed

$$\begin{bmatrix} \sigma_{11} \\ \sigma_{22} \\ \sigma_{33} \\ \sigma_{12} \\ \sigma_{13} \\ \sigma_{23} \end{bmatrix} = \begin{bmatrix} n_{1,1}n_{1,1} & n_{2,1}n_{2,1} & n_{3,1}n_{3,1} \\ n_{1,2}n_{1,2} & n_{2,2}n_{2,2} & n_{3,2}n_{3,2} \\ n_{1,3}n_{1,3} & n_{2,3}n_{2,3} & n_{3,3}n_{3,3} \\ n_{1,1}n_{1,2} & n_{2,1}n_{2,2} & n_{3,1}n_{3,2} \\ n_{1,1}n_{1,3} & n_{2,1}n_{2,3} & n_{3,1}n_{3,3} \\ n_{1,2}n_{1,3} & n_{2,2}n_{2,3} & n_{3,2}n_{3,3} \end{bmatrix} \begin{bmatrix} s_1 \\ s_2 \\ s_3 \end{bmatrix}, \quad (3.79)$$

where  $\mathbf{n}_i$  is the  $i$ -th eigenvector of the strain tensor and the stress tensor.

### Tangential Material Matrix

The compliance form of the constitutive equations in principal direction can be written as

$$e_i = \tilde{D}_{n,ij}^e s_j + e_i^c, \quad (3.80)$$

where  $\tilde{D}_n^e$  is the reduced linear elastic compliance matrix defined as

$$\tilde{D}_n^e = \frac{1}{E} \begin{bmatrix} 1 & -\nu & -\nu \\ -\nu & 1 & -\nu \\ -\nu & -\nu & 1 \end{bmatrix}. \quad (3.81)$$

Differentiating Eq. (3.80) with respect to the principal strains yields

$$\frac{\partial e_i}{\partial e_k} = \delta_{ik} = \tilde{D}_{n,ij}^e \frac{\partial s_j}{\partial e_k} + \frac{\partial e_i^c}{\partial e_k} = \underbrace{\left[ \tilde{D}_{n,ij}^e + \frac{\partial e_i^c}{\partial s_j} \right]}_{\tilde{D}_{n,ij}} \frac{\partial s_j}{\partial e_k}, \quad (3.82)$$

where  $\tilde{D}_n$  is the reduced tangential compliance matrix in principal directions. According to the cracking law, Eq. (3.69) or Eq. (3.72), the stress transferred through the crack is only a function of a single inelastic strain component. As a result, the reduced tangential compliance matrix can be rewritten as

$$\tilde{D}_{n,ij} = \tilde{D}_{n,ij}^e + \delta_{ij} \left( \frac{\partial s_i}{\partial e_i^c} \right)^{-1}. \quad (3.83)$$

Willam et al. (1987) have shown that the full tangent material matrix in principal directions can be written as

$$\tilde{C} = \begin{bmatrix} \tilde{C}_n & \mathbf{0} \\ \mathbf{0} & \tilde{C}_s \end{bmatrix}, \quad (3.84)$$

where the sub-matrix  $\tilde{\mathbf{C}}_n$ , which corresponds to the normal components, is given by

$$\tilde{\mathbf{C}}_n = \tilde{\mathbf{D}}_n^{-1}. \quad (3.85)$$

In order to satisfy the condition of coaxiality between principal stresses and principal strains, the sub-matrix  $\tilde{\mathbf{C}}_s$ , which corresponds to the shear components, is, according to Bažant (1983), defined as

$$\tilde{\mathbf{C}}_s = \begin{bmatrix} \frac{s_1 - s_2}{2(e_1 - e_2)} & 0 & 0 \\ 0 & \frac{s_1 - s_3}{2(e_1 - e_3)} & 0 \\ 0 & 0 & \frac{s_2 - s_3}{2(e_2 - e_3)} \end{bmatrix}. \quad (3.86)$$

This equation illustrates one weak point of rotating crack formulations, since the shear coefficients are defined only if the corresponding principal strain components are different. Jirásek and Zimmermann (1998a) have shown that for the special case of identical principal strains and history variables, i.e. identical inelastic strains and maximum inelastic strains, the corresponding shear coefficient can be expressed as a function of the normal components. Assuming that the principal directions 1 and 2 are identical, the undefined value

$$\frac{s_1 - s_2}{2(e_1 - e_2)} = \frac{0}{0} \quad (3.87)$$

of the shear component  $\tilde{C}_{44}$  is replaced by

$$\tilde{C}_{44} = \frac{\tilde{C}_{11} - \tilde{C}_{12}}{2} = \frac{\tilde{C}_{22} - \tilde{C}_{21}}{2}. \quad (3.88)$$

The transformation of the tangential material matrix  $\tilde{\mathbf{C}}$  back to the global coordinate system can be written as

$$C_{ij} = \frac{\partial \sigma_i}{\partial \varepsilon_j} = T_{ki} \tilde{C}_{kl} T_{lj}, \quad (3.89)$$

where  $\mathbf{T}$  is a transformation matrix defined as

$$\mathbf{T} = \begin{bmatrix} n_{1,1}n_{1,1} & n_{1,2}n_{1,2} & n_{1,3}n_{1,3} & n_{1,1}n_{1,2} & n_{1,1}n_{1,3} & n_{1,2}n_{1,3} \\ n_{2,1}n_{2,1} & n_{2,2}n_{2,2} & n_{2,3}n_{2,3} & n_{2,1}n_{2,2} & n_{2,1}n_{2,3} & n_{2,2}n_{2,3} \\ n_{3,1}n_{3,1} & n_{3,2}n_{3,2} & n_{3,3}n_{3,3} & n_{3,1}n_{3,2} & n_{3,1}n_{3,3} & n_{3,2}n_{3,3} \\ 2n_{1,1}n_{2,1} & 2n_{1,2}n_{2,2} & 2n_{1,3}n_{2,3} & n_{1,1}n_{2,2} + n_{1,2}n_{2,1} & n_{1,1}n_{2,3} + n_{1,3}n_{2,1} & n_{1,2}n_{2,3} + n_{1,3}n_{2,2} \\ 2n_{1,1}n_{3,1} & 2n_{1,2}n_{3,2} & 2n_{1,3}n_{3,3} & n_{1,1}n_{3,2} + n_{1,2}n_{3,1} & n_{1,1}n_{3,3} + n_{1,3}n_{3,1} & n_{1,2}n_{3,3} + n_{1,3}n_{3,2} \\ 2n_{2,1}n_{3,1} & 2n_{2,2}n_{3,2} & 2n_{2,3}n_{3,3} & n_{2,1}n_{3,2} + n_{2,2}n_{3,1} & n_{2,1}n_{3,3} + n_{2,3}n_{3,1} & n_{2,2}n_{3,3} + n_{2,3}n_{3,2} \end{bmatrix}. \quad (3.90)$$

According to Rots (1988); Jirásek and Zimmermann (1998b), standard smeared crack models such as the rotating crack model presented above, suffer of stress locking, mesh induced directional bias and, in some cases, material instabilities caused by a negative shear stiffness. In the next subsections, several modifications of the standard rotating crack model are introduced to overcome these deficiencies.

### 3.4.2 Transition to Scalar Damage

In numerical simulations using standard rotating crack models, stress locking, which in this context means spurious stress transfer across a widely open crack, can be observed. This phenomena, caused by the poor kinematic representation of the displacement discontinuity by the finite element interpolation, is investigated in detail in Jirásek and Zimmermann (1998a). Jirásek and Zimmermann (1998b) propose as a remedy to combine the smeared crack model with a scalar damage model. In this approach, the standard rotating crack model is used during the initial stage of cracking. If the crack opening exceeds a certain limit the transition to a damage-type formulation is performed and the final stage of cracking is described by the applied damage model. Using a scalar damage model, the corresponding constitutive equation can be written as

$$\sigma_i = (1 - \omega)C_{ij}^s \varepsilon_j, \quad (3.91)$$

where  $\omega$  is a scalar damage parameter, which increases from zero (at transition) to one if damage propagates, and  $\mathbf{C}^s$  is the secant material matrix computed for the rotating crack model at the moment of transition. Due to the development of cracks, this matrix exhibits, in general, anisotropy. Consequently, the proposed combined model represents, at least partially, the anisotropic character of cracking. Since all stress components vanish if the damage parameter becomes unity, stress locking due to spurious stress transfer is not observed for the combined model. The evolution of the damage parameter  $\omega$  is driven by the so-called equivalent strain  $\varepsilon_{eq}$  which is defined as

$$\varepsilon_{eq} = \frac{1}{E} \max_i s_{eff,i}, \quad (3.92)$$

in which  $s_{eff,i}$  is the  $i$ -th eigenvalue of the effective stress tensor, given by

$$\sigma_{eff,ij} = C_{ijkl}^e \varepsilon_{kl} \quad (3.93)$$

where  $\mathbf{C}^e$  is the linear elastic material tensor. The corresponding damage law reads

$$\omega = 1 - \frac{s(\varepsilon_{eq,max} - \varepsilon_0)}{E_0 \varepsilon_{eq,max}}, \quad (3.94)$$

where  $s$  is given by Eq. (3.69),  $\varepsilon_{eq,max}$  is the maximum equivalent strain ever reached in material history, and  $\varepsilon_0 = f_t/E$  is the elastic limit. The equivalent Young's modulus  $E_0$ , which is determined from the set of active cracks at the moment at which the transition



takes place, is defined as

$$E_0 = \min_i \frac{s_i(e_i^c)}{e_i}, \quad (3.95)$$

where  $e_i$  is the  $i$ -th eigenvalue of the total strain tensor. The presented damage law allows for a smooth transition from rotating cracks to scalar damage. Furthermore, the energy dissipated during the failure process is preserved by the combined model.

As already mentioned above, the transition to scalar damage is performed if, at least for one crack, the corresponding crack opening exceeds a certain limit. Assuming an active crack, this condition can be expressed in terms of the stress  $s_i$  transferred across crack  $i$ , given by Eq. (3.69), and the tensile strength  $f_t$

$$s_i(e_i^c) < \alpha_s f_t, \quad (3.96)$$

where  $e_i^c$  is the corresponding crack strain, and  $\alpha_s$  is a dimensionless parameter ranging from zero to unity. By setting this parameter to unity, the model is switched to scalar damage immediately after a crack initiates. A value of  $\alpha_s = 0$  would avoid the transition to scalar damage. In general,  $\alpha_s$  is chosen as small as possible. It is to be noted that the condition is evaluated during the update of the state variables. Consequently, the transition to scalar damage is not performed until equilibrium is restored for the current load increment.

In numerical simulations with rotating crack models, the shear stiffness values, given by Eq. (3.86), may become negative even if the material unloads, see Jirásek and Zimmermann (1998b). Consequently, the secant material matrix loses positive definiteness which is, under the assumption that the material is not completely damaged, physically inadmissible. This results in material instabilities and, as a consequence, the numerical solution may diverge during the equilibrium iteration. Using a scalar damage model, the secant material matrix is defined as the scalar multiple of the initial “undamaged” material matrix. As a result the secant material matrix remains positive definite, if the initial matrix is positive definite and the damage parameter is not unity. This motivates a second criterion for the transition to scalar damage

$$\tilde{C}_{s,ii} < \alpha_G G^e, \quad (3.97)$$

where the matrix  $\tilde{C}_s$  is given by Eq. (3.86),  $G^e$  is the linear elastic shear modulus, and  $\alpha_G$  is a dimensionless parameter between 0 and 1. Consequently, the rotating crack model is switched to scalar damage if one of the diagonal shear stiffness components becomes smaller than a predefined fraction of the linear elastic shear modulus. Since Eq. (3.97) is also satisfied for a negative shear modulus, the determination of  $\alpha_G$  is more difficult compared to  $\alpha_s$ . Consequently,  $\alpha_G$  has to be chosen in such a way that in the simulation the shear moduli remain positive.

### 3.4.3 Nonlocal Formulation

Mesh induced directional bias of the simulated fracture process zone can be alleviated by introducing the nonlocal concept into the rotating crack model, see Bažant and Lin (1988); Jirásek and Zimmermann (1998b). As shown in Sect. 3.2, the nonlocal concept not only reduces the dependency of the numerical results on the element shape and orientation, but also acts as an efficient localization limiter. According to Jirásek and Zimmermann (1998b), a nonlocal formulation of the rotating crack model can be obtained if the constitutive equations of the local rotating crack model, given in Eq. (3.67), are rewritten as

$$\sigma_i = C_{ij}^s(\bar{\boldsymbol{\varepsilon}})\varepsilon_j, \quad (3.98)$$

where  $\mathbf{C}^s$  is the secant material matrix, and  $\bar{\boldsymbol{\varepsilon}}$  is the vector of nonlocal strains. In the numerical implementation, the computation of the stress vector starts with the determination of the nonlocal strain vector, which is either defined by Eq. (3.4) or given by Eq. (3.18). Then the standard stress-evaluation algorithm of the local model, presented in Sect. 3.4.1, is applied using the nonlocal strain vector as input and by considering that the volume specific fracture energy is defined by Eq. (3.65) with  $\beta = 1.5$ . The corresponding nonlocal secant material matrix is then given by Eq. (3.89). It is to be noted that for the calculation of the secant matrix, the cracking law for unloading, Eq. (3.72), is used to describe the relationship between the stress transferred across the crack and the crack strain. Finally, the stress vector is calculated by multiplying the nonlocal secant matrix with the local strain vector, Eq. (3.98). Depending on the nonlocal formulation – averaging of the local strain field, Sect. 3.2.2, or averaging of the local displacement field, Sect. 3.2.3 – the tangential stiffness matrix of the nonlocal rotating crack model can be obtained using Eq. (3.13) or Eq. (3.37). The corresponding derivatives of the stresses with respect to the components of the nonlocal strain vector can be written as

$$\frac{\partial \sigma_i}{\partial \bar{\varepsilon}_m} = \left( \frac{\partial \bar{T}_{ki}}{\partial \bar{\varepsilon}_m} \bar{C}_{kl}^s \bar{T}_{lj} + \bar{T}_{ki} \frac{\partial \bar{C}_{kl}^s}{\partial \bar{\varepsilon}_m} \bar{T}_{lj} + \bar{T}_{ki} \bar{C}_{kl}^s \frac{\partial \bar{T}_{lj}}{\partial \bar{\varepsilon}_m} \right) \varepsilon_j, \quad (3.99)$$

where  $\bar{\mathbf{C}}^s$  is the secant (unloading) material matrix, Eq. (3.89),  $\mathbf{T}$  is the transformation matrix, Eq. (3.90), and the bar over a quantity indicates that this quantity is calculated using the nonlocal strain vector  $\bar{\boldsymbol{\varepsilon}}$ . In Eq. (3.99), the first derivatives of the principal nonlocal strains and the corresponding eigenvectors with respect to the nonlocal strain components are required for the calculation of the derivatives of the nonlocal secant material matrix  $\bar{\mathbf{C}}^s$  and the derivatives of the transformation matrix  $\mathbf{T}$ . Algorithms for the computation of the derivatives of eigenvalues and eigenvectors can be found in Nelson (1976); Liu et al. (1993); Lee et al. (1996).

In order to avoid spurious stress transfer and material instabilities due to negative shear stiffness values, which are also observed for the nonlocal rotating crack model, a transition to a nonlocal scalar damage model is performed if one of the conditions, given in Eqs. (3.96) and (3.97), is satisfied. The equivalent strain, which controls the evolution of the scalar damage parameter  $\omega$ , is calculated using the nonlocal strain vector.

### 3.5 Microplane Damage Model

Another class of anisotropic damage models is based on the microplane approach, e.g. Bažant and Oh (1983b, 1985); Carol and Bažant (1997); Kuhl and Ramm (1998); Patzák and Jirásek (2004). The microplane concept is motivated by the slip theory of metals, Taylor (1938). In contrast to classical constitutive models, which establish a direct relationship between the stress tensor  $\boldsymbol{\sigma}$  and the strain tensor  $\boldsymbol{\varepsilon}$ , the constitutive law in the microplane approach defines a relationship between the stress vector  $\mathbf{s}$  and the strain vector  $\mathbf{e}$  acting on a plane with arbitrary orientation, the so-called microplane, within the material. The orientation of this plane is characterized by the unit normal vector  $\mathbf{n}$ . Additional constraints are introduced to define the relationship between vector components on each microplane and tensor components on macrolevel. The most natural types of constraints are the static constraint

$$s_i = \sigma_{ij}n_j \quad (3.100)$$

and the kinematic constraint

$$e_i = \varepsilon_{ij}n_j, \quad (3.101)$$

which simply define the microplane stress and strain vectors as projection of the corresponding tensors. Note that it is impossible to use both constraints at the same time and still satisfy a general stress-strain law on every microplane. If the kinematic constraint is used to define the relation between microplane strain vector and macroscopic strain tensor, the microplane stress vector is, in general, not equal to the projection of the macroscopic stress tensor. In Bažant (1984b) it is shown that, by applying the principle of virtual work, the equilibrium between macro- and microlevel can be satisfied in a weak sense. By using this principle, the following condition is obtained

$$\frac{4\pi}{3}\sigma_{ij}\delta\varepsilon_{ij} = 2 \int_{\Omega} s_i\delta e_i \, d\Omega, \quad (3.102)$$

where  $\delta$  denotes the virtual variations. The left-hand side of this equality represents the work of macroscopic stresses on virtual macroscopic strains within a unit sphere and the right-hand side corresponds to the work of microplane stresses on virtual microplane strains integrated over all possible microplane orientations, which can be represented by the surface of the unit hemisphere  $\Omega$ . Assuming that the kinematic constraint is also used for the virtual strain components, Eq. (3.102) can be written as

$$\frac{4\pi}{3}\sigma_{ij}\delta\varepsilon_{ij} = 2 \int_{\Omega} s_i\delta\varepsilon_{ij}n_j \, d\Omega. \quad (3.103)$$

Using the condition that this equality must hold for an arbitrary virtual strain tensor, the components of the macroscopic stress tensor are given by

$$\sigma_{ij} = \frac{3}{2\pi} \int_{\Omega} s_i n_j \, d\Omega. \quad (3.104)$$

Equivalent to this approach, the principle of complementary virtual work

$$\frac{4\pi}{3} \delta\sigma_{ij} \varepsilon_{ij} = 2 \int_{\Omega} \delta s_i e_i \, d\Omega, \quad (3.105)$$

can be used in combination with the static constraint, Eq. (3.100), which is applied to the virtual stress components, to obtain an integral formula for the macroscopic strain tensor

$$\varepsilon_{ij} = \frac{3}{2\pi} \int_{\Omega} e_i n_j \, d\Omega. \quad (3.106)$$

In general, the integrals in Eqs. (3.104) and (3.106) are evaluated numerically. Quadrature rules for the general three-dimensional case can be found in Bažant and Oh (1986). The simplified two-dimensional case is given in appendix A.4.1.

### 3.5.1 Local Formulation

In this work, the microplane-based damage model (MD) developed by Jirásek (1999) is used. This model is based on the concept of effective stresses and effective strains and works with the principle of energy equivalence, Cordebois and Sidoroff (1982), which states that the complementary energy of the damaged material under the nominal stress  $\boldsymbol{\sigma}$  is equal to the complementary energy of the undamaged material under the effective stress  $\tilde{\boldsymbol{\sigma}}$ . Assuming that the effective stresses  $\tilde{\boldsymbol{\sigma}}$  and the effective strains  $\tilde{\boldsymbol{\varepsilon}}$  which represent the conditions in the undamaged material between material defects are linked by the generalized Hooke's law

$$\tilde{\varepsilon}_{ij} = D_{ijkl}^e \tilde{\sigma}_{kl}, \quad (3.107)$$

the principle of energy equivalence can be written as

$$\frac{1}{2} \sigma_{ij} D_{ijkl}^s \sigma_{kl} = \frac{1}{2} \tilde{\sigma}_{ij} D_{ijkl}^e \tilde{\sigma}_{kl} \quad (3.108)$$

where  $\mathbf{D}^e$  is the linear elastic compliance tensor and  $\mathbf{D}^s$  is the secant (unloading) compliance tensor. Furthermore, the evolution of microdefects is taken into account in the relationship between effective stresses and and nominal stresses, which can be written as

$$\tilde{\sigma}_{ij} = M_{ijkl} \sigma_{kl}, \quad (3.109)$$

where  $\mathbf{M}$  is the fourth-order damage effect tensor. By substituting Eq. (3.109) into Eq. (3.108), a direct expression for the damaged (secant) compliance tensor is obtained

$$D_{ijkl}^s = M_{mnij} D_{mnop}^e M_{opkl}, \quad (3.110)$$

and the relationship between nominal stresses and nominal strains can be written as

$$\varepsilon_{ij} = D_{ijkl}^s \sigma_{kl} = M_{mnij} D_{mnop}^e M_{opkl} \sigma_{kl}. \quad (3.111)$$

Further substituting Eqs. (3.109) and (3.107) into Eq. (3.111) yields the relationship between the nominal strain tensor and the effective strain tensor

$$\varepsilon_{ij} = M_{klj} \tilde{\varepsilon}_{kl}. \quad (3.112)$$

Equivalent to the continuum level, presented above, the concept of effective quantities can be applied to the microplane theory. Assuming that the relationship between effective and nominal microplane stresses is given by

$$\tilde{s}_i = \psi s_i, \quad (3.113)$$

where  $\psi$  is a scalar parameter characterizing the relative compliance on the microplane, the principle of energy equivalence leads to the following relationship between nominal and effective microplane strains

$$e_i = \psi \tilde{e}_i. \quad (3.114)$$

Even though  $\psi$  is a scalar parameter, the macroscopic damage effect is anisotropic, since the value of this parameter is, in general, different on each microplane.

In the presented microplane-based damage model, a double constraint is applied to derive the macroscopic damage-effect tensor from the microplane-level. Using the compliance version of this model, the macroscopic nominal stress tensor is related to the nominal microplane stress by the static constraint, Eq. (3.100). On each microplane, the relationship between effective and nominal stress vector is defined by Eq. (3.113). Using Eq. (3.104) and replacing the nominal microplane stress components with the effective ones, the macroscopic effective stress tensor can be obtained. Note that for the derivation of Eq. (3.104) the kinematic constraint is used in the principal of virtual work to relate the effective virtual microplane strains with the components of the virtual effective strain tensor. Substituting Eqs. (3.100) and (3.113) into Eq. (3.104) and considering effective and nominal quantities, the relationship between nominal and effective stress tensor is given by

$$\tilde{\sigma}_{ij} = \frac{3}{2\pi} \int_{\Omega} \tilde{s}_i n_j \, d\Omega = \frac{3}{2\pi} \int_{\Omega} \psi(\mathbf{n}) s_i n_j \, d\Omega \quad (3.115)$$

$$= \frac{3}{2\pi} \int_{\Omega} \psi(\mathbf{n}) \sigma_{il} n_l n_j \, d\Omega = \frac{3}{2\pi} \int_{\Omega} \psi(\mathbf{n}) n_l n_j \delta_{ik} \, d\Omega \sigma_{kl} \quad (3.116)$$

$$= \psi_{lj} \delta_{ik} \sigma_{kl}, \quad (3.117)$$

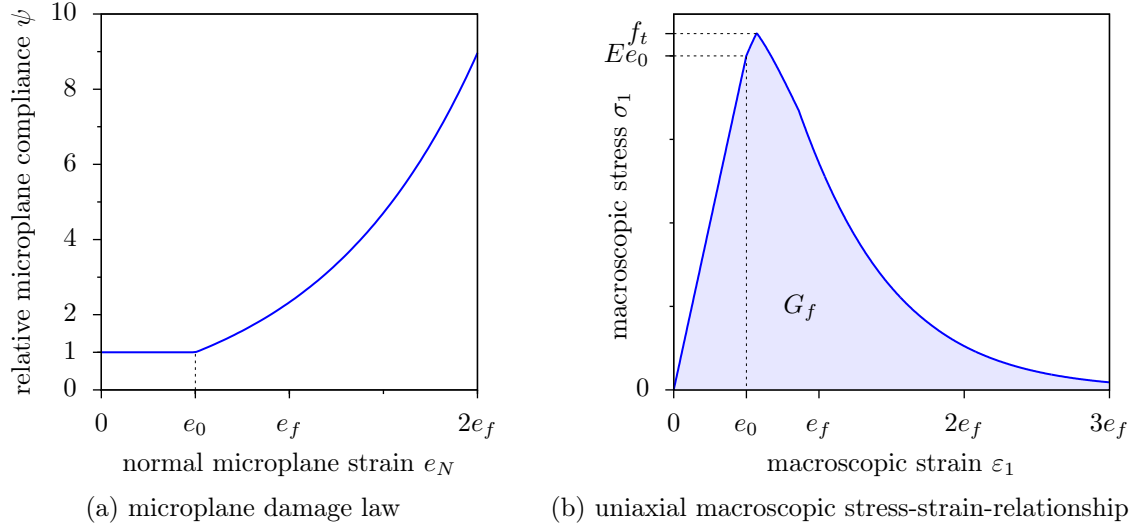


Figure 3.6: Microplane based damage model – microplane damage law and uniaxial macroscopic stress-strain-relationship.

where  $\delta$  is the Kronecker delta, and  $\boldsymbol{\psi}$  is the symmetric second order inverse integrity tensor, whose components are defined as

$$\psi_{ij} = \frac{3}{2\pi} \int_{\Omega} \psi(\mathbf{n}) n_i n_j \, d\Omega. \quad (3.118)$$

Additionally, considering the macroscopic relationship between the nominal stress tensor and the effective stress tensor given by Eq. (3.109), the components of the damage effect tensor  $\mathbf{M}$  can be defined as

$$M_{ijkl} = \psi_{lj} \delta_{ik}. \quad (3.119)$$

Due to the symmetry of the stress tensors, the fourth order damage effect tensor must exhibit minor symmetries  $M_{ijkl} = M_{jikl} = M_{ijlk} = M_{jilk}$  for any  $i, j, k, l$ . Symmetrization of  $\mathbf{M}$  leads to the damage effect tensor

$$M_{ijkl} = \frac{1}{4} (\psi_{lj} \delta_{ik} + \psi_{li} \delta_{jk} + \psi_{kj} \delta_{il} + \psi_{ki} \delta_{il}). \quad (3.120)$$

Due to the symmetry of the inverse integrity tensor this tensor also exhibits major symmetries  $M_{ijkl} = M_{klij}$  for any  $i, j, k, l$ . An alternative derivation of the damage effect tensor, which directly takes into account the symmetry of the stress and strain tensors, is given in appendix A.4.2.

On the microplane with normal vector  $\mathbf{n}$ , the evolution of damage is characterized by the relative compliance  $\psi(\mathbf{n})$ , which is a scalar parameter ranging from  $\psi = 1$  (undamaged material) to  $\psi = \infty$  (fully damaged material). The evolution of this parameter is driven by the equivalent microplane strain  $e_{eq}$ , which is, in the presented implementation of this

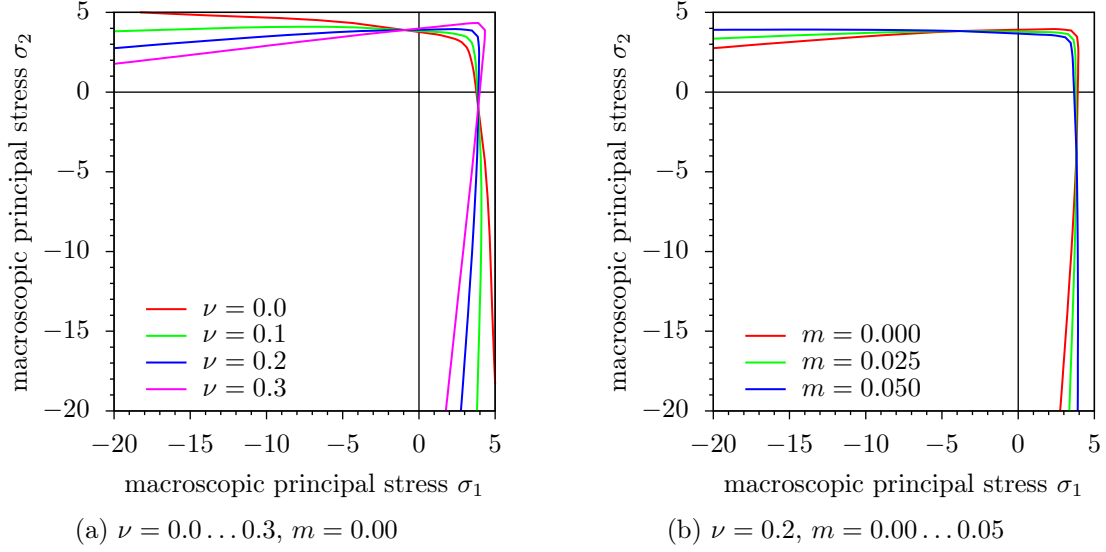


Figure 3.7: Microplane based damage model – influence of Poisson’s ratio  $\nu$  and parameter  $m$  on macroscopic tensile peak stress.

model, equal to the microplane strain component normal to the microplane

$$e_{eq} = e_i n_i = \varepsilon_{ij} n_i n_j. \quad (3.121)$$

A more complex definition of the equivalent microplane strain, which takes into account the normal and tangential microplane strain components, can be found in Jirásek (1999). Using an exponential softening law, the relative compliance can be defined as

$$\psi(\mathbf{n}) = \begin{cases} 1 & \text{if } e_{eq,max} \leq e_0 \\ \sqrt{\frac{e_{eq,max}}{e_0} \exp\left(\frac{e_{eq,max} - e_0}{e_f - e_0}\right)} & \text{if } e_{eq,max} > e_0, \end{cases} \quad (3.122)$$

where  $e_0$  is the elastic limit,  $e_f$  is a parameter controlling the ductility of the material, and  $e_{eq,max}$  is a history variable representing the maximum equivalent microplane strain ever reached in the history of the material. In the diagram in Fig. 3.6(a), this function is illustrated. In the elastic range, the relative compliance remains constant. After reaching the elastic limit, damage occurs and the relative compliance starts growing. Due to the application of an exponential function this parameter might become very large for realistic values of the equivalent microplane strains. In order to avoid numerical problems in the numerical implementation, an upper limit for this parameter is introduced, which represents a fully damaged material. Figure 3.6(b) shows the macroscopic stress-strain diagram for uniaxial tension observed in a single material point. The microplane parameter  $e_0$  indicates the elastic limit, but is not equal to the state corresponding to the macroscopic tensile strength. On the microplane level, softening starts in microplanes almost normal to the loading direction. Since all other microplanes remain linear elastic, this results in a macroscopic hardening behavior of the material. The biaxial macroscopic failure envelope,

which is defined as the tensile peak stress, is shown in the diagram in Fig. 3.7(a). It is clearly visible that this envelope depends on the Poisson's ratio. Furthermore, for typical Poisson's ratios of concrete,  $\nu = 0.15 \dots 0.25$  (cf. Grübl et al. (2001)), the tensile peak stress becomes unrealistically small if moderate compressive stresses appear. In order to prevent this overestimation of damage for compressive loading, Jirásek (1999) proposes the following modified definition of the equivalent microplane strain

$$e_{eq} = \frac{\varepsilon_{ij}n_i n_j}{1 - \frac{m}{Ee_0}\sigma_{kk}}, \quad (3.123)$$

where  $\sigma_{kk}$  is the trace of the stress tensor, and  $m$  is a dimensionless, non-negative parameter that controls the sensitivity to the mean stress. Note that according to Jirásek (1999), the stress tensor of the last converged step is used in Eq. (3.123). The modified failure envelope for a constant Poisson's ratio  $\nu = 0.2$  and varying parameter  $m$  is plotted in the diagram in Fig. 3.7(b). Using the recommended value of 0.05 for parameter  $m$ , the failure envelope becomes almost independent from compressive stresses.

### 3.5.2 Nonlocal Formulation

In Patzák and Jirásek (2004) a nonlocal formulation of the MD which is based on the averaging of the inverse integrity tensor is proposed. In the presented approach, the nonlocal inverse integrity with components

$$\bar{\psi}_{ij}(\mathbf{x}) = \int_V \alpha(\mathbf{x}, \boldsymbol{\xi}) \psi_{ij}(\boldsymbol{\xi}) \, d\boldsymbol{\xi} \quad (3.124)$$

is used for the evaluation of the damage effect tensor

$$M_{ijkl} = \frac{1}{4} (\bar{\psi}_{lj}\delta_{ik} + \bar{\psi}_{li}\delta_{jk} + \bar{\psi}_{kj}\delta_{il} + \bar{\psi}_{ki}\delta_{jl}). \quad (3.125)$$

A detailed description of the applied averaging concept can be found in Sect. 3.2.2.

In this thesis, the nonlocal MD is used for two-dimensional simulations assuming plane stress. The corresponding secant compliance matrix and the derivation of the tangent material matrix is given in appendix A.4.3.

### 3.5.3 Parameter Identification

A general problem of microplane-based material formulations is the determination of the microplane material parameters. In Patzák and Jirásek (2004), the microplane material parameters of the MD are expressed as functions of measurable macroscopic material properties. Since numerical simulations have shown that the proposed functions cannot be applied to the numerical implementation of the MD used in this thesis, the relationship between the microplane parameters  $e_0$  and  $e_f$  and macroscopic material properties



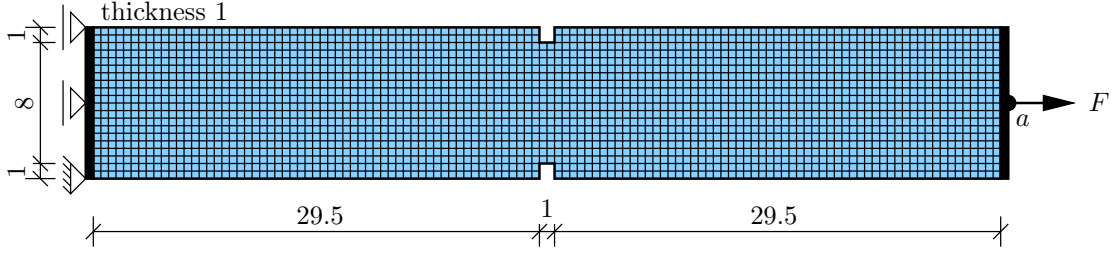


Figure 3.8: Microplane based damage model – finite element model used for parameter identification (dimensions in  $mm$ ).

of concrete – Young’s modulus  $E$ , tensile strength  $f_t$  and fracture energy  $G_f$  – is investigated in this section. Two-dimensional non-linear finite element simulations of uniaxial tension tests on double notched prisms, shown in Fig. 3.8, with varying material parameters, summarized in Table 3.2, are performed. The nonlocal formulation of the MD with averaging of the inverse integrity tensor is applied. All simulations are performed for a tensile loading covering the complete softening response. In order to capture snap-backs during the simulation, an energy-release control, as proposed in Sect. 2.4.3, is applied. For each simulation, the macroscopic tensile strength  $f_t$  and the volume specific fracture energy  $g_f$  can be calculated from the load-displacement-curve

$$f_t = \frac{\max F}{A} \quad (3.126)$$

$$g_f = \frac{G_f}{\beta R} = \frac{1}{A\beta R} \int_{u_a} F du_a, \quad (3.127)$$

where  $u_a$  is the horizontal displacement of point  $a$  and  $A = 8 \text{ mm}^2$  is the area of the reduced cross-section. Assuming that the parameter  $\beta$ , which represents the final distribution of the inelastic energy density, is constant in all simulations, it is more convenient to introduce a modified volume specific fracture energy  $\tilde{g}_f$

$$\tilde{g}_f = \frac{G_f}{R} = \frac{1}{AR} \int_{u_a} F du_a. \quad (3.128)$$

The integral in Eq. (3.128) is evaluated numerically using the trapezoidal rule. In Fig. 3.9, the obtained material properties are plotted for varying microplane parameters  $e_0$  and  $e_n$  and assuming a constant Young’s modulus  $E = 20\,000 \text{ N/mm}^2$ . Note that a bilinear inter-

Table 3.2: Microplane based damage model – material parameters.

Young’s modulus	$E$	$[N/mm^2]$	15 000 ... 30 000	4 sample points
Poisson’s ratio	$\nu$	$[-]$	0.2	
elastic limit	$e_0$	$[10^{-4}]$	0.5 ... 1.5	20 sample points
ductility parameter	$e_f$	$[10^{-4}]$	20 ... 200	20 sample points
nonlocal radius	$R$	$[mm]$	1.0	
scalar parameter	$m$	$[-]$	0.05	

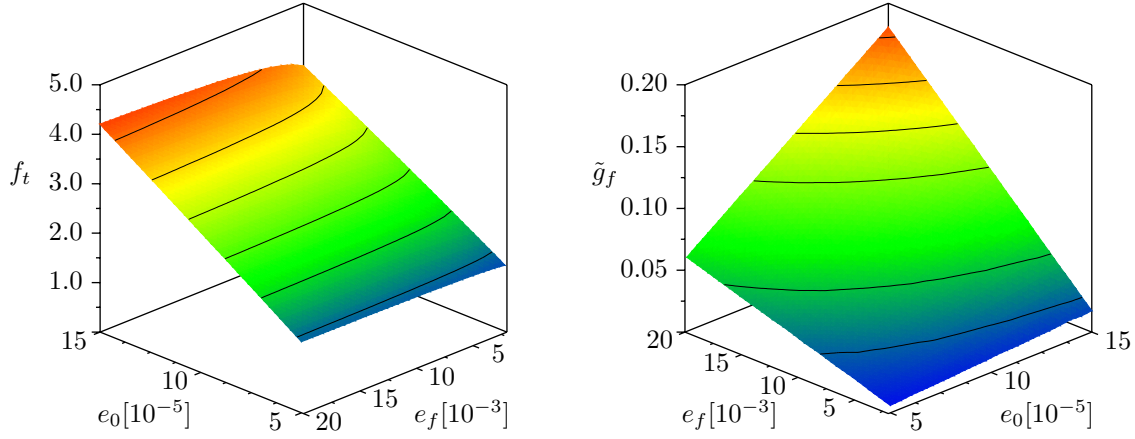


Figure 3.9: Microplane based damage model – macroscopic material properties  $f_t$  and  $\tilde{g}_f$  as function of microplane material parameters  $e_0$  and  $e_f$  ( $E = 20\,000\text{N/mm}^2$ ).

polation is used for values between sample points. Both properties can be approximated with sufficient accuracy by bilinear functions

$$f(e_0, e_f) = c_1 e_0 + c_2 e_f + c_3 e_0 e_f + c_4, \quad (3.129)$$

where  $c_1 \dots c_4$  are free coefficients, which are obtained by fitting this curve to the sample points. In order to incorporate the additional dependency of the macroscopic parameters on the Young's modulus, the coefficients are calculated for different Young's moduli. The final approximation functions are given by

$$f_t(E, e_0, e_f) = E(1.2851e_0 - 8.7923 \cdot 10^{-5}e_f + 4.8581e_0e_f + 4.6375 \cdot 10^{-6}) \quad (3.130)$$

$$\tilde{g}_f(E, e_0, e_f) = -22.425e_0 - \frac{2441.9}{E}e_f + 3.0708Ee_0e_f + \frac{39.053}{E}. \quad (3.131)$$

Assuming that the macroscopic material properties  $E, f_t, G_f, R$  are given and considering  $e_0 > 0$  and  $e_f > e_0$ , this system of equations can be solved for the microplane material parameters. The diagrams in Fig. 3.10 show the inverse relationships – the microplane material parameters as functions of the calculated macroscopic properties assuming a constant Young's modulus  $E = 20\,000\text{N/mm}^2$ .

## 3.6 Interface Material Model

In this thesis, the nonlinear behavior of material interfaces is described by a cohesive zone model, presented by Unger and Könke (2006). This model is based on Tvergaard (2003). In these models, the constitutive equations, representing the relationship between the normal and tangential tractions  $T_n$  and  $T_{t,i}$  and the corresponding displacement differences across the interface  $\Delta u_n$  and  $\Delta u_{t,i}$ , are expressed by a nonlinear traction-separation law. An

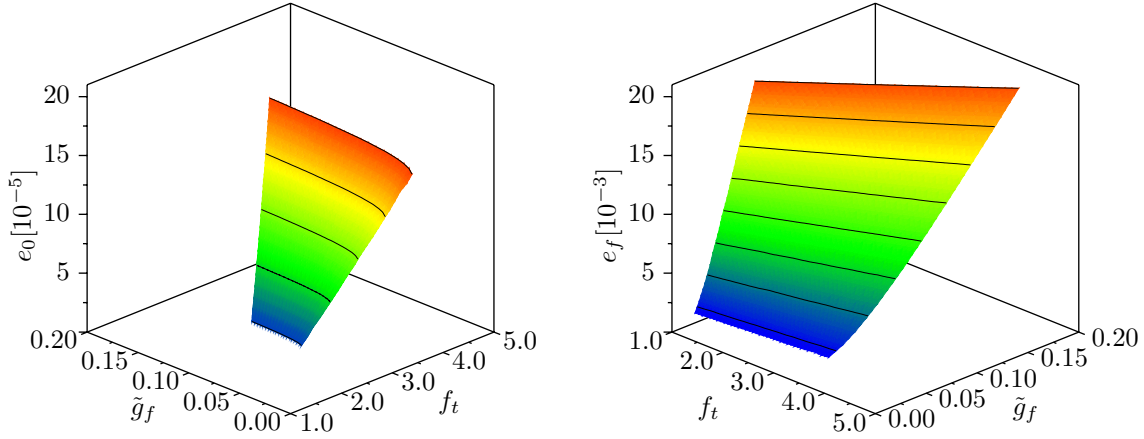


Figure 3.10: Microplane based damage model – microplane material parameters  $e_0$  and  $e_f$  as function of macroscopic material properties  $f_t$  and  $\tilde{g}_f$  ( $E = 20\,000\text{N/mm}^2$ ).

equivalent interface opening  $\lambda$  is defined as

$$\lambda = \sqrt{\langle \Delta u_n \rangle^2 + \sum_{i=1}^{n_t} (\alpha^2 \Delta u_{t,i}^2)}, \quad (3.132)$$

where the brackets  $\langle \dots \rangle$  indicate that only a positive interface opening is taken into account, and  $n_t$  is the number of tangential components, which is  $n_t = 1$  for two-dimensional models and  $n_t = 2$  in the three-dimensional case. The dimensionless parameter  $\alpha$  controls the weighting between the normal and tangential interface opening. Figure 3.11(a) shows the influence of this parameter on the failure surface which is defined by  $\lambda = \lambda_0$ . Furthermore, a nonlinear traction-separation law, describing the relationship between the

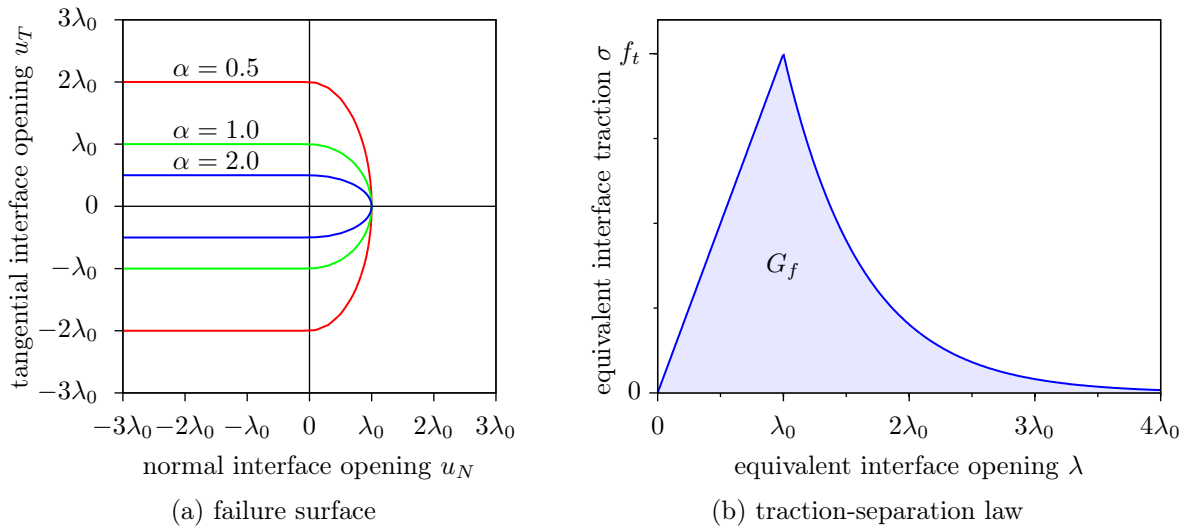


Figure 3.11: Cohesive zone model – failure surface (two-dimensional case) and equivalent traction separation law.

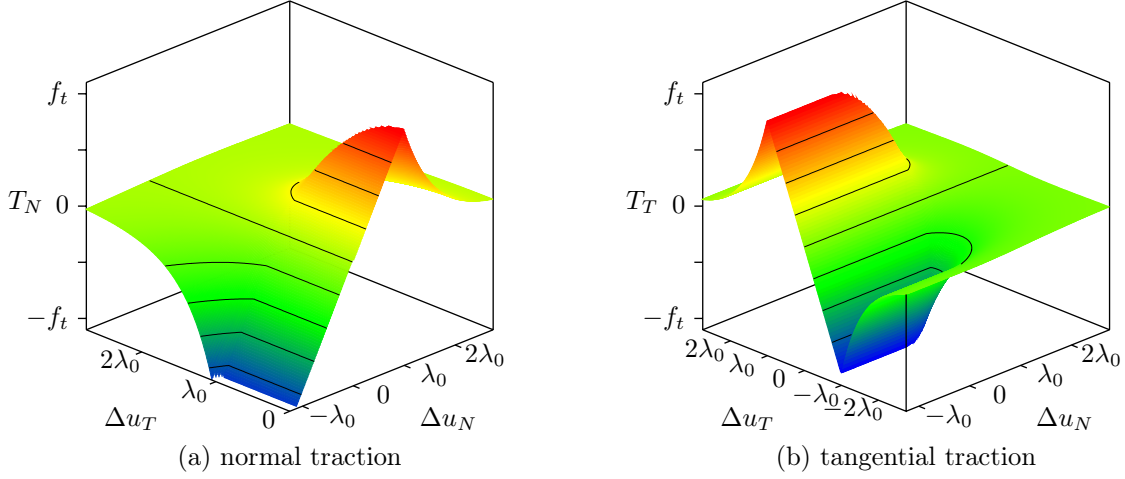


Figure 3.12: Cohesive zone model – traction separation law.

equivalent interface opening and the equivalent traction  $\sigma$ , is introduced

$$\sigma(\lambda) = \begin{cases} K_p \lambda & \lambda < \lambda_0 \\ f_t \exp \frac{-f_t(\lambda - \lambda_0)}{G_f} & \text{otherwise} \end{cases}, \quad (3.133)$$

where  $\lambda_0 = f_t/K_p$  defines the elastic limit,  $K_p$  is the penalty stiffness,  $f_t$  is the tensile strength, and  $G_f$  is the fracture energy. The relationship between the equivalent quantities is plotted in the diagram in Fig. 3.11(b). Assuming that there exists a potential  $\Phi$

$$\Phi = \int_0^\lambda \sigma(\lambda') d\lambda', \quad (3.134)$$

the normal and tangential interface tractions can be defined as the derivatives of that potential with respect to the corresponding interface opening

$$T_n = \frac{\partial \Phi}{\partial \Delta u_n} = \sigma(\lambda) \frac{\Delta u_n}{\lambda} \quad (3.135)$$

$$T_{t,i} = \frac{\partial \Phi}{\partial \Delta u_{t,i}} = \sigma(\lambda) \frac{\alpha^2 \Delta u_{t,i}}{\lambda}. \quad (3.136)$$

It is to be noted that Eq. (3.135) applies if the interface is in tension, which is represented by a positive interface opening in normal direction. If the interface is in compression, the normal interface traction is approximated by the penalty stiffness

$$T_n = K_p \Delta u_n. \quad (3.137)$$

The value of the penalty stiffness, which controls the penetration of the two interface sides under compression, has to be chosen carefully, because large values of the penalty stiffness lead to an ill-conditioned stiffness matrix. The relationship between interface tractions

and relative interface displacements is shown in the diagrams in Fig. 3.12. The nonlinear traction separation law, Equation (3.133), applies for an increasing  $\lambda$  and  $\lambda = \lambda_{max}$ , where  $\lambda_{max}$  is a history variable describing the maximum equivalent interface opening ever reached during the loading process. If  $\lambda$  decreases an elastic unloading to the origin is assumed. The corresponding interface tractions are given by

$$T_n = \sigma(\lambda_{max}) \frac{\Delta u_n}{\lambda_{max}} \quad (3.138)$$

$$T_{t,i} = \sigma(\lambda_{max}) \frac{\alpha^2 \Delta u_{t,i}}{\lambda_{max}}. \quad (3.139)$$

It is to be noted that regularization techniques, as presented in Sect. 3.2, are not required for cohesive zone models. In these models the physical description of the fracture process is objective because the crack opening is explicitly modeled by a displacement discontinuity. Consequently, the numerical results do not exhibit pathological mesh sensitivity.

Using the potential formulation, given by Eq. (3.134), the tangential material matrix is defined as the second derivative of the potential with respect to the interface openings

$$\mathbf{C} = \frac{\partial \mathbf{T}}{\partial \Delta \mathbf{u}} = \begin{bmatrix} \frac{\partial^2 \Phi}{\partial \Delta u_N^2} & \frac{\partial^2 \Phi}{\partial \Delta u_N \partial \Delta u_{T,1}} & \frac{\partial^2 \Phi}{\partial \Delta u_N \partial \Delta u_{T,2}} \\ \frac{\partial \Delta u_{T,1} \partial \Delta u_N}{\partial^2 \Phi} & \frac{\partial \Delta u_{T,1}^2}{\partial^2 \Phi} & \frac{\partial \Delta u_{T,1} \partial \Delta u_{T,2}}{\partial^2 \Phi} \\ \frac{\partial \Delta u_{T,2} \partial \Delta u_N}{\partial^2 \Phi} & \frac{\partial \Delta u_{T,2} \partial \Delta u_{T,1}}{\partial^2 \Phi} & \frac{\partial \Delta u_{T,2}^2}{\partial^2 \Phi} \end{bmatrix}. \quad (3.140)$$

Since  $\partial^2 \Phi / (\partial \Delta u_N \partial \Delta u_{T,i}) = \partial^2 \Phi / (\partial \Delta u_{T,i} \partial \Delta u_N)$  the tangent material matrix is always symmetric, independently from the chosen softening function. A detailed derivation of the corresponding components of this matrix is given in appendix A.5.

# 4 Mesoscale Modeling of Concrete

## 4.1 Introduction

Concrete is a composite material consisting of inhomogeneities, e.g. aggregates embedded in the mortar matrix, and structural defects, such as cracks, voids and pores, with varying sizes. The level of detail with which the numerical model must describe the heterogeneous material structure of concrete depends on the physical phenomena which should be considered in the numerical simulation. Zaitsev and Wittmann (1981) propose a hierarchic system of four different characteristic levels on which the internal structure of concrete can be observed. On the macrolevel, which is related to the structural length scale, concrete is treated as a homogeneous continuum. The heterogeneity of the material structure is taken into account on the mesolevel, at which concrete is, in general, described as a three phase composite consisting of aggregates, mortar-matrix and the interfacial transition zone (ITZ) in between. On this level, the typical edge length of a representative volume element is of order of magnitude of  $10^2$  mm. The main constituent on the microlevel, with a characteristic length of order of magnitude of  $10^{-1}$  mm, is the hardened cement paste, which is composed of cement gel and capillary pores, Cusatis et al. (2006). Finally, the nanolevel describes the hardened cement gel containing nanopores. On this level, the typical dimension of a representative volume element is of order of magnitude of  $10^{-4}$  mm. It is to be noted that models on a given level of observation are based on the results of the next smaller length scale, Schlangen (1993).

In this thesis, quasi-brittle failure of concrete structures is investigated using numerical simulations with mesoscale models. Figure 4.1 shows a load-displacement curve which is typically observed in uniaxial tensile test of normal strength concrete specimens if the load is applied under deformation control. The measured macroscopic nonlinear response can be attributed to the initiation, propagation and coalescence of microcracks within the heterogeneous internal material structure on the mesolevel, see for instance Sluys (1992). For small displacements, the response is practically linear. At about 60% of the maximum load, interface cracks between aggregates and mortar matrix initiate. Consequently, the slope of the load-displacement curve decreases. If the load is further increased, the interface cracks propagate into the mortar matrix and additional microcracks initiate within the mortar matrix. When the maximum load is reached the microcracks at the interface and within the mortar matrix start to interact. After the peak point, the load starts to decrease at increasing deformation. The post-peak softening behavior is characterized by a localization of the deformations in small fracture zones and the formation of a macroscopic crack. In macroscale simulations, the evolution of microcracks can only be represented

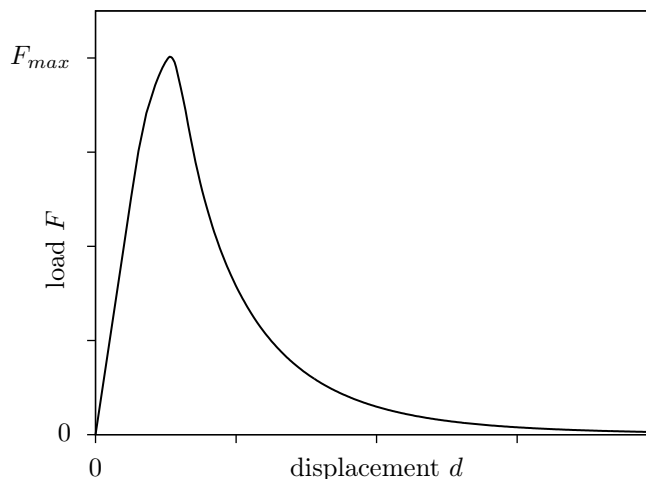


Figure 4.1: Characteristic load-displacement curve of concrete in tension.

in a phenomenological way. Mesoscale models allow for an explicit consideration of the individual physical phenomena in numerical simulations.

## 4.2 Generation of the Internal Material Structure on the Mesoscale

A crucial point in mesoscale simulations is an appropriate description of the internal material structure by the numerical model. On the mesoscale, the material structure of concrete is characterized by the spatial distribution and the size distribution of the aggregates. In the literature, two different concepts can be found for obtaining the concrete mesostructure for numerical simulations. In the first approach, experiments, e.g. X-ray tomography, Garboczi (2002), or digital images of concrete cross sections, Nagai et al. (2000), are used to determine the actual mesoscopic structure of an existing concrete specimen. In the second approach, which is also followed in this thesis, numerical simulations are used to artificially generate possible realizations of the mesostructure for virtual specimens. In these models, the aggregates are, in general, idealized by simple geometrical shapes such as circles, Schlangen and van Mier (1992), spheres, Wriggers and Moftah (2006), ellipsoids, Leite et al. (2004) or polygons, Wang et al. (1999). Consequently, the surface texture of the aggregates is neglected in these models. Häfner et al. (2006) combine a modified ellipsoid with a sine function to take into account the roundness, the sphericity and the surface roughness of the aggregates. A popular method for the simulation of the aggregates in concrete is the so-called take-and-place method. During the take-process, the aggregates are created, taking into account the aggregate shape and the aggregate size distribution, and fitting a prescribed volume fraction. The grading of the aggregates is either approximated by Fuller's curve, Walraven (1980); Wriggers and Moftah (2006), or explicitly given by a grading curve, Wang et al. (1999); Leite et al. (2004); Häfner et al. (2006). The final mesoscopic material structure is generated during the place-process. The aggregate particles are randomly placed one by one into the specimen in such a way that there are no

overlapping regions with already placed particles. This procedure starts with the largest particle and is successively repeated for smaller ones until all particles are placed into the specimen.

### 4.2.1 Simulation of the Aggregate Size Distribution (Take-Process)

In the presented approach, the aggregates are idealized as ellipsoids. Consequently, the aggregate surface is approximated by

$$\left(\frac{x}{r_1}\right)^2 + \left(\frac{y}{r_2}\right)^2 + \left(\frac{z}{r_3}\right)^2 = 1, \quad (4.1)$$

where  $r_1$ ,  $r_2$  and  $r_3$  are the three radii of the ellipsoid, with  $r_1 \geq r_2 \geq r_3$ . Furthermore, it is assumed that the radii  $r_1$  and  $r_3$  can be expressed as a function of the second largest radius  $r_2$

$$r_1 = \left(1 + X_2 \frac{\eta_{13} - 1}{\eta_{13} + 1}\right) r_2 \quad (4.2)$$

$$r_3 = \left(1 - X_3 \frac{\eta_{13} - 1}{\eta_{13} + 1}\right) r_2, \quad (4.3)$$

where  $X_2$  and  $X_3$  are uniformly distributed random numbers between 0 and 1. The parameter  $\eta_{13}$ , which is defined as the maximum ratio between the radii  $r_1$  and  $r_3$ , controls the shape of the aggregates. Using a ratio of 1 the aggregates are idealized as spheres, whereas higher values result in ellipsoidal particles. As a result, the expected value  $E(V)$  of the volume of an aggregate particle can be expressed as a function of  $r_2$

$$E(V) = \frac{4}{3}\pi r_2^3 \left(1 - \frac{1}{2} \frac{\eta_{13} - 1}{\eta_{13} + 1}\right) \left(1 + \frac{1}{2} \frac{\eta_{13} - 1}{\eta_{13} + 1}\right). \quad (4.4)$$

The radius  $r_2$  is determined in such a way that the aggregates fit a given aggregate size distribution. In concrete, the aggregate size distribution is, in general, described by grading curves, see for instance Neville (1996), which are obtained from sieve analysis. As a result, the aggregates are divided into several mineral-size-classes, which are bounded by the sieve aperture diameters  $d_{min}$  and  $d_{max}$ . From a mathematical point of view, the grading curve can be interpreted as a cumulative distribution function of the aggregates mass. In the presented approach, the passing of a particle through a sieve is defined by an equivalent particle diameter  $d_{eqv} = 2r_2$ . Furthermore, the grading curve is approximated by multi-linear functions on a logarithmic scale for the equivalent diameter. As a result, the aggregate size distribution within one mineral-size-class is defined as

$$\Phi_m(d_{eqv}) = \frac{1}{\ln d_{max} - \ln d_{min}} \ln d_{eqv} - \frac{\ln d_{min}}{\ln d_{max} - \ln d_{min}}. \quad (4.5)$$



The value of  $\Phi_m$  at a given diameter  $d$  represents the mass fraction of aggregates with an equivalent diameter smaller than  $d$  related to the total mass of the aggregates. By differentiating  $\Phi_m(d_{eqv})$  with respect to the equivalent diameter  $d_{eqv}$ , the associated density function  $\varphi_m$  is obtained

$$\varphi_m(d_{eqv}) = \frac{d\Phi_m}{dd_{eqv}} = \frac{1}{\ln d_{max} - \ln d_{min}} \frac{1}{d_{eqv}}. \quad (4.6)$$

Assuming a constant mass density for all aggregates in one mineral-size-class, the probability of finding an aggregate with equivalent diameter  $d_{eqv}$  can be defined as

$$\varphi_d(d_{eqv}) = \frac{1}{\int_{d=d_{min}}^{d_{max}} \frac{\varphi_m(d)}{E(V(d))} dd} \frac{\varphi_m(d_{eqv})}{E(V(d_{eqv}))}, \quad (4.7)$$

where  $E(V)$  is the expected value of the volume of a single particle, given by Eq. (4.4). Substituting Eqs. (4.6) and (4.4) into Eq. (4.7) results in the final probability density function of the equivalent aggregate diameter

$$\varphi_d(d_{eqv}) = \frac{1}{\int_{d=d_{min}}^{d_{max}} \frac{1}{d^4} dd} \frac{1}{d_{eqv}^4} = \frac{3d_{min}^3 d_{max}^3}{d_{max}^3 - d_{min}^3} \frac{1}{d_{eqv}^4}. \quad (4.8)$$

By integrating the probability density function, the associated cumulative distribution function is obtained

$$\Phi_d(d_{eqv}) = \int_{d=d_{min}}^{d_{eqv}} \varphi_d(d) dd = \frac{d_{min}^3 d_{max}^3}{d_{max}^3 - d_{min}^3} \left( \frac{1}{d_{min}^3} - \frac{1}{d_{eqv}^3} \right). \quad (4.9)$$

The inversion method, e.g. Devroye (1986), is applied to generate diameters according to this distribution function from uniformly distributed random numbers  $X$

$$d_{eqv} = 2r_2 = \frac{d_{max} d_{min}}{\sqrt[3]{X d_{min}^3 + (1 - X) d_{max}^3}} \quad (0 \leq X \leq 1). \quad (4.10)$$

The derivation of the equivalent aggregate diameter for Fuller's curve can be found in Häfner et al. (2006).

In addition to the mass fraction of each mineral-size-class, given in the grading curve, the final concrete density  $\rho_c$ , the total mass fraction of aggregates  $\varphi_a$  and the aggregate density  $\rho_a$  are used as input parameters in the simulation. In the first step of the take-process, the aggregate volume for each mineral-size-class is calculated from the final specimen volume and the input parameters. In a second step, starting with the largest aggregates, the particles are successively generated for each mineral-size-class until the desired volume is exceeded. The last generated aggregate particle is removed and the difference between the

simulated and the prescribed volume of the mineral-size-class is added to the next smaller class.

### 4.2.2 Simulation of the Spatial Aggregate Distribution (Place-Process)

The place-process is successively performed for each mineral-size-class starting with the class with the largest aggregates and followed by the next smaller classes. In a first step, all aggregates are sorted according to their volume. Afterwards, the aggregates are randomly placed within the specimen one by one starting with the aggregate with the largest volume. In order to take into account a minimum distance between the aggregates and between the aggregates and the specimen boundary surfaces, the radii of the ellipsoid to be placed are temporarily enlarged by  $\Delta r$ . In the presented approach, the enlargement length is a function of the second largest radius of the ellipsoid  $r_2$

$$\Delta r = \varepsilon_r r_2, \quad (4.11)$$

where  $\varepsilon_r$  is the relative enlargement factor, which is introduced as an additional input parameter. Physically, this minimum distance can be interpreted as a thin mortar film around each aggregate, Wittmann et al. (1985). In numerical simulations in which the mesoscale geometry is discretized using finite elements, the minimum distance is also required to improve the quality of the finite element mesh. As a general rule, the enlargement factor is chosen in such a way that the minimum distance between two ellipsoids is approximately half of the average element size used for the mortar matrix.

The position and orientation of an ellipsoid within the specimen geometry, is defined by the center point coordinates  $c_x, c_y, c_z$  and by the Euler angles  $\theta, \psi, \phi$ . During the place-process, these parameters are computed using uniformly distributed random variables. A valid parameter set is obtained if the ellipsoid is completely inside the specimen and if there are no overlapping regions with already placed ellipsoids. If one of these conditions is not satisfied, a new position and orientation is calculated for this ellipsoid and the testing procedure is repeated. Assuming that the ellipsoids are small compared to the specimen dimensions, the first condition is fulfilled if the center point of the ellipsoid is inside the specimen and there is no intersection between the ellipsoid and the specimen boundary surfaces. The separation of two ellipsoids is, in a first step, tested by the separation of their bounding boxes. If this test fails, an exact separation check, which is based on a very efficient algorithm introduced by Wang et al. (2001), is performed. This algorithm uses a matrix representation of an ellipsoid

$$\mathbf{x}^T \mathbf{E} \mathbf{x} = 0, \quad (4.12)$$

where  $\mathbf{x} = [x, y, z, 1]^T$  are homogeneous coordinates and  $\mathbf{E}$  is a 4x4 matrix, which incorporates the radii of the ellipsoid and its position and orientation in space. Assuming an ellipsoid with its center at the origin and the radii aligned with the coordinate axes, this

matrix is given by

$$\overline{\mathbf{E}} = \begin{bmatrix} 1/r_1^2 & 0 & 0 & 0 \\ 0 & 1/r_2^2 & 0 & 0 \\ 0 & 0 & 1/r_3^2 & 0 \\ 0 & 0 & 0 & -1 \end{bmatrix}. \quad (4.13)$$

By introducing the transformation matrices  $\mathbf{D}_t$  for translations

$$\mathbf{D}_t = \begin{bmatrix} 1 & 0 & 0 & -c_x \\ 0 & 1 & 0 & -c_y \\ 0 & 0 & 1 & -c_z \\ 0 & 0 & 0 & 1 \end{bmatrix}, \quad (4.14)$$

and  $\mathbf{D}_r$  for rotations

$$\mathbf{D}_r = \begin{bmatrix} c_\psi c_\phi - c_\theta s_\psi s_\phi & s_\psi c_\phi + c_\theta c_\psi s_\phi & s_\theta s_\phi & 0 \\ -c_\psi s_\phi - c_\theta s_\psi c_\phi & -s_\psi s_\phi + c_\theta c_\psi c_\phi & s_\theta c_\phi & 0 \\ s_\theta s_\psi & -s_\theta c_\psi & c_\theta & 0 \\ 0 & 0 & 0 & 1 \end{bmatrix}, \quad (4.15)$$

with

$$\begin{aligned} s_\theta &= \sin \theta & s_\psi &= \sin \psi & s_\phi &= \sin \phi \\ c_\theta &= \cos \theta & c_\psi &= \cos \psi & c_\phi &= \cos \phi, \end{aligned}$$

the final matrix  $\mathbf{E}$  for an ellipsoid with arbitrary position and orientation can be obtained

$$\mathbf{E} = \mathbf{D}_t^T \mathbf{D}_r^T \overline{\mathbf{E}} \mathbf{D}_r \mathbf{D}_t. \quad (4.16)$$

The separation of two ellipsoids, given by  $\mathbf{x}^T \mathbf{E}_1 \mathbf{x} = 0$  and  $\mathbf{x}^T \mathbf{E}_2 \mathbf{x} = 0$ , is determined by evaluating the characteristic polynomial, which is defined as

$$f(\lambda) = \det(\lambda \mathbf{E}_1 + \mathbf{E}_2). \quad (4.17)$$

In Wang et al. (2001) it is shown that two ellipsoids are separated by a plane if and only if their characteristic equation  $f(\lambda) = 0$  has two distinct positive roots. An advantage of this method is that the characteristic equation must not be solved for the exact roots. Sturm sequences, cf. Barbeau (2003), are used to determine the number of real roots in the interval  $(0, +\infty]$ .

A drawback of the presented place-process is that each ellipsoid must be tested with all previously inserted ellipsoids to accept its position and orientation. Since the number of placed ellipsoids successively increases, the numerical effort for placing one ellipsoid increases significantly during the simulation, even though the bounding box check is already sufficient in most cases. In the presented new approach, the specimen is subdivided into regular cuboids, which are aligned with the coordinate axes. During the simulation, the number of cuboids is successively increased with decreasing mineral-size-class. The corre-

sponding number of subdivisions  $N_{div,i}$  in each direction  $i$  is defined as a function of the total number of ellipsoids  $N_{el}$  of the already inserted mineral-size-classes and the current mineral-size-class

$$N_{div,i} = \sqrt[3]{\frac{N_{el}}{l_x l_y l_z}} l_i \quad i = x, y, z, \quad (4.18)$$

where  $l_x, l_y, l_z$  are the dimensions of the specimen bounding box. It is to be noted that  $N_{div,i}$  is rounded to an integer value. After having placed an ellipsoid within the specimen, this ellipsoid is assigned to all cuboids which are within or cut by an enlarged bounding box of this ellipsoid. The standard ellipsoid bounding box is enlarged in each direction by

$$\Delta l = \left[ 1 + \frac{\eta_{13} - 1}{\eta_{13} + 1} + \varepsilon \right] \frac{d_{max,k}}{2}, \quad (4.19)$$

where  $d_{max,k}$  is the upper sieve aperture diameter of the current mineral-size-class  $k$ . As a result, the separation checks can be reduced to all ellipsoids which are assigned to the same cuboid. Due to the regular subdivision, the cuboid  $C$  which is associated to the ellipsoid to be placed can be calculated from the center point coordinates of that ellipsoid

$$C = \left\lfloor \frac{c_x - min_x}{l_x} \right\rfloor N_{div,x} + \left\lfloor \frac{c_y - min_y}{l_y} \right\rfloor N_{div,y} N_{div,x} + \left\lfloor \frac{c_z - min_z}{l_z} \right\rfloor N_{div,z} N_{div,y} N_{div,x}, \quad (4.20)$$

where  $min_i$  are the minimum coordinates of the specimen bounding box, and the brackets  $\lfloor \dots \rfloor$  indicate the floor function. Consequently, the several summands are rounded to the next smallest integer. With this modification of the place-process, the number of separation tests for one parameter set is significantly reduced. Due to the successive adaptation of the cuboid size, the number of separation checks becomes almost independent of the total number of already inserted ellipsoids.

The result of the presented algorithm is one sample of a three-dimensional mesoscopic material structure of concrete. An intersection between the three-dimensional structure and a plane, as proposed in Leite et al. (2004), is used for two-dimensional simulations of the material response, leading to aggregates, which are represented by ellipses.

### 4.2.3 Example

As an example, the generation of the mesoscale geometry within a concrete cube with edge length of 100 mm is presented to show the performance of this algorithm. The prescribed grading curve is given in Fig. 4.2(a) and the following input parameters are used: mass density of aggregates  $\rho_a = 2.67 t/m^3$ , mass density of macroscopic concrete  $\rho_c = 2.30 t/m^3$ , mass fraction of aggregates  $\varphi_a = 80 \%$ , and the maximum ratio between the ellipsoid radii  $\eta_{13} = 3$ . In order to investigate the influence of the relative enlargement factor  $\varepsilon_r$

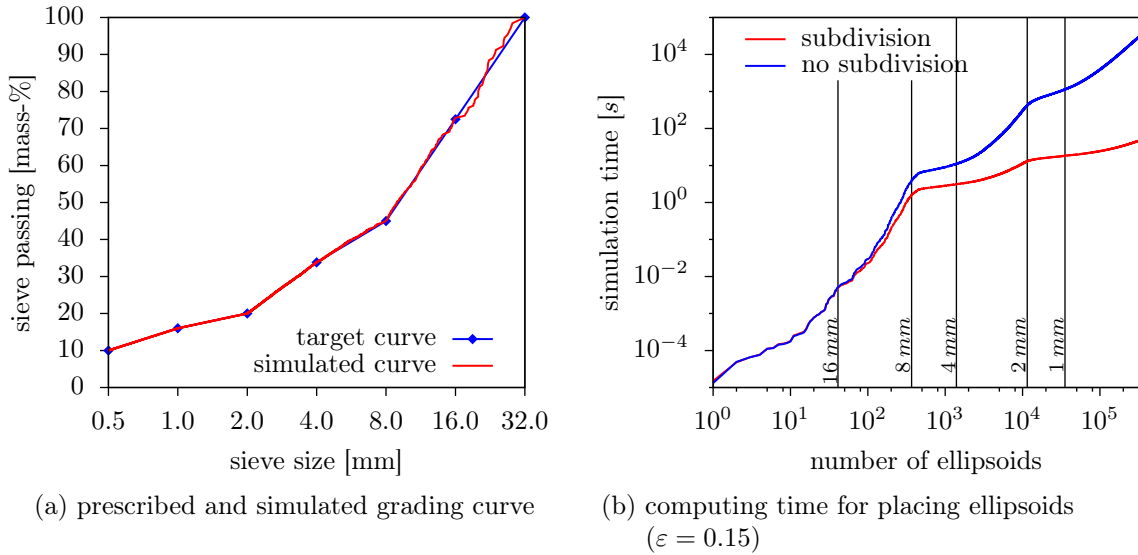


Figure 4.2: Simulation of the mesoscale geometry of concrete.

on the simulation time, this parameter is varied from 0.00 to 0.15. In all simulations, a constant seed is used for the generation of the random numbers. As a result, the aggregate size distribution and the aggregate shapes are constant in all simulations. Due to the variation of the enlargement factor, the simulations result in different spatial distributions of the aggregates. Approximately 320 000 aggregates with diameters between 0.5 mm and 32.0 mm are generated within a cube with an edge length of 100 mm. The volume fraction of the aggregates is 62 %, which is equivalent to the prescribed mass fraction. The diagram in Fig. 4.2(a) illustrates that the aggregate size distribution obtained in the simulation statistically fits the given size distribution for a sufficiently large number of ellipsoids. Figure 4.3(a) shows the three-dimensional aggregate arrangement of the mineral-size-classes 8/16 (321 ellipsoids, light-gray) and 16/32 (40 ellipsoids, dark-gray).

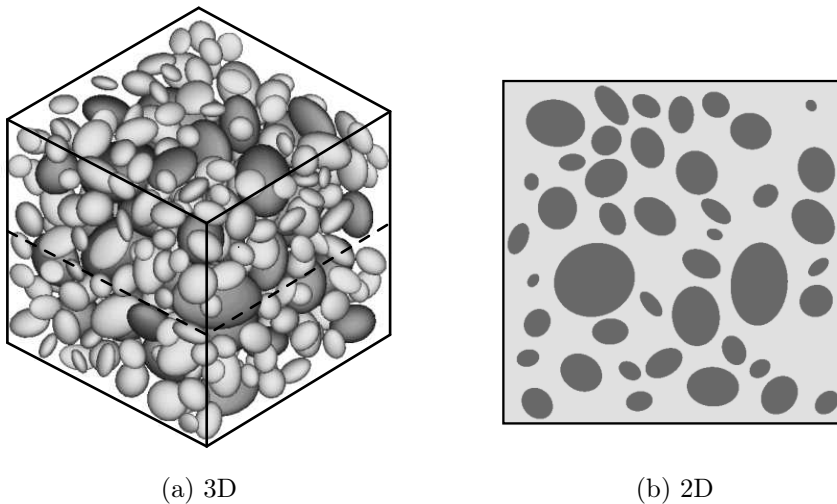


Figure 4.3: Artificially generated aggregate distribution.

Table 4.1: Average time for the simulation of the three-dimensional aggregate distribution.

relative enlargement factor $\varepsilon$	with subdivision	without subdivision
0.00	23 s	18 652 s (5.18 h)
0.05	27 s	23 108 s (6.42 h)
0.10	35 s	24 965 s (6.93 h)
0.15	48 s	29 379 s (8.16 h)

The result of an intersection between the cube and a plane parallel to the base of the cube is plotted in Fig. 4.3(b). Only aggregates with diameters larger than 8 mm are shown in this plot. The area fraction of these aggregates in this cross-section is 35 %. In Table 4.1, the simulation times on a standard PC (Pentium4, 3.40 GHz) running 64-Bit Linux are summarized. The numerical effort for generating the mesoscale structure increases with increasing minimum distance between the aggregates, since it becomes more difficult to place the temporarily enlarged ellipsoid. Using an enlargement factor larger than 15 % not all ellipsoids can be placed into the specimen and the mesoscale geometry is not build with the given parameter set. Figure 4.2(b) shows the computing time for placing the ellipsoids as a function of the number of ellipsoids. The vertical lines in the diagram indicate the boundaries of the mineral-size-classes. If the number of ellipsoids is small, the performance gain by using the subdivision algorithm is negligible. With increasing number of ellipsoids the time for placing an ellipsoid is significantly reduced compared to a simulation without the subdivision algorithm, e.g. factor 638 for the simulation of all ellipsoids.

### 4.3 Numerical Model

Compared to macroscale simulations, a considerably finer resolution of the numerical model, e.g. a very fine finite element discretization, is required in mesoscale simulations to represent the mesoscale geometry of concrete with sufficient accuracy. Since in mesoscale simulations the numerical model explicitly considers the several physical phenomena leading to macroscopic failure, such as the propagation of microcracks within the mortar matrix or debonding effects at the interface between aggregates and matrix, rather simple material models can be used for each constituent to describe the complex macroscopic material behavior of concrete.

Various different approaches for mesoscale models of concrete can be found in literature. Several models, e.g. Schlangen (1993); Vervuurt (1997); Leite et al. (2004), are based on beam or truss lattices. In order to incorporate the heterogeneity of the material, the lattice is projected onto the grain structure and every single beam is assigned to one constituent of the mesoscale geometry (aggregate, mortar matrix or interfacial transition zone). The properties of the beams are determined in such a way that simulations with the lattice model matches macroscopic parameters obtained in experiments, e.g. Young's modulus or Poisson's ratio. The failure of a beam is modeled either by tension cut-off, Schlangen (1993); Vervuurt (1997), where the beam is deleted after reaching the tensile strength, or by damage models, Leite et al. (2004); Grassl et al. (2006), which take into account

material softening. An essential problem of the lattice models is the determination of the material parameters, since a relationship between the homogenized macroscopic properties and the beam parameters must be obtained. Furthermore, the obtained crack pattern is strongly influenced by the structure of the lattice.

Another group of models are particle models (discrete element method), which idealize the mesoscale structure by a finite number of particles, which interact through contact conditions with each other. In order to simulate cohesive materials such as concrete with particle models, beam or interface elements are inserted between neighboring particles. In Bažant et al. (1990), the particles explicitly represent the aggregates. Another approach is shown in D'Addetta (2004). In this model, the particles are significantly smaller than the aggregates. As a result, aggregates and mortar matrix consist of a high number of small particles. In order to model the mesostructure of concrete, different material parameters are assigned to the cohesive components. As for the lattice models, the determination of the material parameters for the cohesive components is difficult and a mesh-induced directional bias of the crack pattern is observed, Jirásek and Bažant (1995).

Besides the above-mentioned discontinuous models, the continuum approach is also applied to mesoscale simulations of concrete. Aligned discretizations, Fig. 4.4(b), where the finite element mesh explicitly represents the aggregate boundary surfaces, are e.g. used in Wittmann et al. (1985); Carol et al. (2001); Wriggers and Moftah (2006). In these models various approaches for the simulation of damage are used. In Wang et al. (1992), microcracks are modeled in a discrete way, that is the cracks are explicitly represented by the finite element mesh. Consequently, remeshing is required if a crack propagates. Initial cracks are introduced in the interfacial zone between aggregates and matrix and the propagation of these cracks is based on linear elastic fracture mechanics. In Carol et al. (2001), zero-thickness interface elements, representing cohesive cracks, are applied between all finite elements. The nonlinear behavior of the structure is only considered by the material model of the interface elements. Since the crack paths are predefined by the element edges, the results depend on the finite element discretization. A smeared crack concept is used in Roelfstra (1989) for the simulation of microcracks within the mortar matrix. In this model, a framework of nonlinear springs, softening elements and friction elements represent the interfacial zone. A problem of these smeared crack models is the mesh-induced directional bias of the crack pattern, Rots (1988). Nonlocal material formulations can circumvent this major drawback. In Wriggers and Moftah (2006), a nonlocal isotropic damage model is applied to the mortar matrix. In this model, rigid bond between aggregates and matrix is assumed and interface cracks are represented by damaged zones within the mortar matrix close to the aggregates. As a result, the strength of the interfacial zone is overestimated. Using aligned discretizations, the numerical effort for mesh generation increases significantly with the complexity and the size of the mesoscale structure. An alternative approach, that uses orthogonal (grid-type) meshes, Fig. 4.4(c), is presented in Zohdi and Wriggers (2001); Häfner et al. (2006); Häfner (2007). In these models, the mesostructure is taken into account by multiphase finite elements, which allow for different material properties for each integration point of the finite element. As a result, a smeared representation of the interfacial zone is obtained. In Unger and Könke (2006), the extended finite element method is used for an explicit representation of the aggregate boundaries independent from the finite element discretization, Fig. 4.4(d). The major ad-

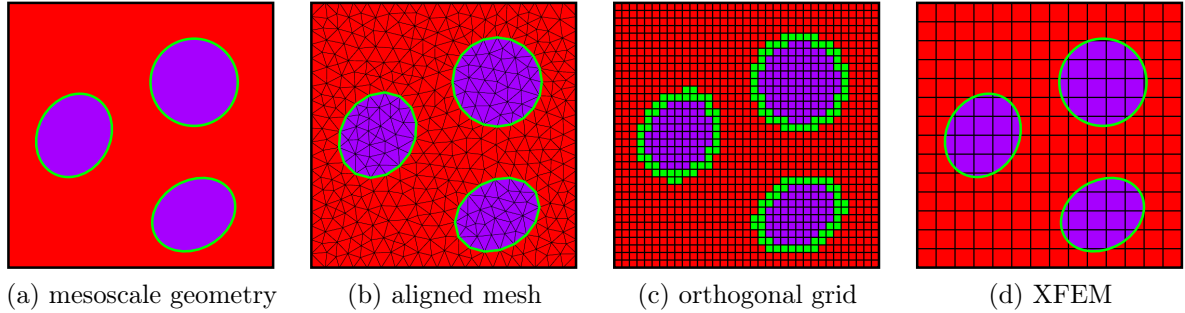


Figure 4.4: Finite element discretizations of the mesoscale geometry.

vantage of orthogonal, grid-type meshes is that the numerical effort for mesh generation is negligible small compared to models with aligned meshes.

In the presented approach, an aligned finite element discretization, as shown in Fig. 4.4(b), of the mesoscale geometry is used and zero-thickness interface elements are introduced between aggregates and matrix to model the interfacial transition zone. This implies that the actual width of the interfacial transition zone is neglected in the numerical simulations. The initial finite element mesh, without interface elements, is generated with Gmsh, Geuzaine and Remacle (2009). Triangular finite elements with quadratic interpolation functions are used in two-dimensional simulations. Furthermore, plane stress conditions are assumed. In three-dimensional simulations, the mesoscale geometry is discretized with tetrahedrons. Due to the complexity of the mesoscale geometry, the numerical effort for mesh generation is very high and it increases with the number of aggregates embedded in the mortar matrix. The quality of the finite element mesh is mainly controlled by the minimum distance between the aggregates, which is introduced during the geometry generation process. If the minimum distance is chosen too small compared to the average finite element size, very small or highly distorted finite elements are created. Especially for three-dimensional models, a small minimum distance might lead to a situation where the meshing becomes impossible. After the initial mesh has been created, interface elements are introduced between elements with different material properties.

In the presented mesoscale simulations, debonding of the ITZ and tensile failure within the mortar matrix, which corresponds to the initiation, propagation and coalescence of microcracks, are considered to describe the macroscopic nonlinear material behavior of concrete. This implies the assumption that compressive failure on the macroscale can be reduced to tensile failure perpendicular to the direction of compressive stresses on the mesoscale. For normal-strength concrete, the nonlinear material behavior of the aggregates can be neglected. Consequently, the material behavior of the aggregates is described by a linear elastic, isotropic material model. The opening of the material interfaces between aggregates and matrix is considered by a nonlinear cohesive zone model, presented in Sect. 3.6. Nonlocal continuum damage models, as introduced in Sects. 3.3 to 3.5, are used to describe the evolution of microcracks within the mortar matrix.



## 4.4 Examples

In this section, three examples taken from literature are presented to illustrate the main features of the proposed mesoscale approach. Several numerical simulations with varying model and material parameters are performed to investigate the influence of the interfacial transition zone, the influence of the spatial aggregate distribution and the influence of the continuum damage model used for the mortar matrix on the macroscopic response, such as the global load-displacement curve, the ultimate load or the macroscopic fracture energy. The numerical results obtained in these simulations are compared to experimental results documented in literature.

In general, it is difficult to determine the material parameters of the mesoscale models, even if the material models are characterized by parameters with a clear physical meaning, such as Young's modulus, tensile strength or fracture energy. Theoretically, these material properties can be obtained from experiments. Due to the size of the constituents of the mesoscale model, for instance as shown in Hashin and Monteiro (2002), the interfacial transition zone has a typical width of  $15 - 40 \mu m$ , the experiments are rather difficult. Alternatively, a parameter fitting for a reference experiment can be performed to determine the mesoscale material parameters. This parameter set can be used in simulations of structures with the same material. In this thesis, the Young's modulus of the mortar matrix is calculated from the macroscopic Young's modulus of concrete using the Reuss bound, Reuss (1929),

$$\frac{1}{E_c} = \frac{\varphi_a}{E_a} + \frac{\varphi_m}{E_m}, \quad (4.21)$$

where  $\varphi$  is the volume fraction and the subscripts stands for concrete (macroscale):  $c$ , aggregates:  $a$ , and mortar matrix:  $m$ . The Young's modulus of the aggregates is either given in the literature or a fixed ratio between the Young's moduli of aggregates and mortar matrix is assumed. In all simulations, the macroscopic Poisson's ratio of concrete is also used for the aggregates and the mortar matrix. The fracture energy and the tensile strength are iteratively identified such that the numerical simulations almost coincide with the macroscopic load-displacement curve obtained in the experiments. As discussed in Sect. 3.2.2 the nonlocal radius is interpreted as numerical parameter which is chosen with respect to the average element size used for the mortar matrix.

All simulations were run on an Opteron workstation ( $2 \times 2 \times 2.4 GHz$ ,  $16 GB$  RAM). The calculation of the element stiffness matrices, the element internal force vectors and the assembling of the global stiffness matrix was performed on 4 parallel processors. In order to avoid that two or more processes concurrently try to update the same entry of the stiffness matrix, the elements are divided into maximal independent sets, see Unterkircher and Reissner (2005), and the parallel assembling of the stiffness matrix is only performed for all elements in one set. The MUltifrontal Massively Parallel Solver (MUMPS) package, Amestoy et al. (2000, 2002, 2006), is used to directly solve the global system of equations which arises in each iteration step of the simulation, cf. Sect. 2.4.

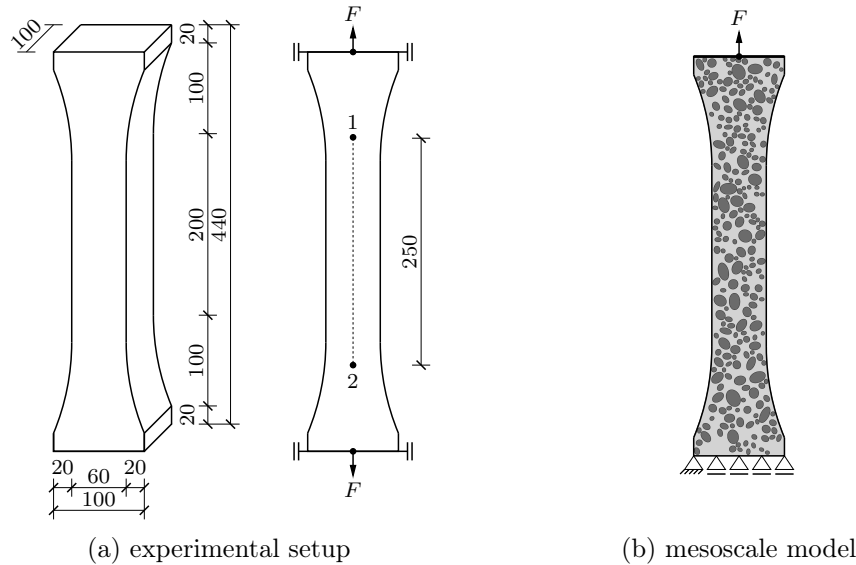


Figure 4.5: Uniaxial tension test – specimen dimensions of the concrete prism, test setup and mesoscale model (all dimensions in  $mm$ ).

#### 4.4.1 Uniaxial Tension Test

In the first example, several aspects of mesoscale simulations are investigated using a uniaxial tension test of an unnotched concrete prism with a tapered cross-section. The advantage of such a specimen is that in a uniaxial tension test the localization of damage is only triggered by the heterogeneous internal material structure and not by the specimen shape. Furthermore, due to the increasing cross-section at the specimen supports the influence of the boundary conditions on the failure mechanism is negligible. The specimen was designed and experimentally tested by Kessler-Kramer (2002) at the University of Karlsruhe. Figure 4.5(a) shows the macroscopic specimen dimensions, the position of the monitoring points and the applied boundary and loading conditions. It is to be noted that due to the fixation of the specimen in the testing machine the mutual rotation of the specimen ends is prevented. In order to investigate the post-peak behavior of the specimen, a combination of load and displacement control was applied. During the experiment the load is adjusted such that a prescribed relative displacement value is observed between the monitoring points. Table 4.2 summarizes the mixture parameters used for the preparation of the normal strength concrete specimens.

The numerical simulations are performed with two-dimensional mesoscale models. Consequently, the aggregates are simplified as cylinders with ellipsoidal cross-section. Figure 4.5(b) shows one realization of the mesoscale geometry. As shown in Sect. 4.2, the internal material structure of concrete is obtained by numerical simulations, using the mixture properties given in Table 4.2 and assuming an enlargement factor  $\varepsilon = 0.25$ . In the numerical model, only aggregates with diameters larger than  $4\text{ mm}$  are considered. The geometry is discretized by triangular finite elements with quadratic shape functions. Using an average element size of  $0.5\text{ mm}$ , the finite element mesh approximately consists of 270 000 elements, 550 000 nodes and 1 100 000 degrees of freedom, respectively. Additional

Table 4.2: Uniaxial tension test – concrete mixture parameters.

	mass [ $kg/m^3$ ]	density [ $kg/m^3$ ]	volume [ $m^3$ ]
cement	318	3 100	0.103
water	175	1 000	0.175
air voids (estimated)			0.020
aggregates 0/2	555	2 635	0.211
aggregates 2/8	703	2 635	0.267
aggregates 8/16	592	2 635	0.224
concrete	2 343	2 343	1.000

simulations, considering only aggregates with a minimum diameter of  $8\text{ mm}$ , are performed to investigate the influence of the mesh size. In order to investigate the post-peak response of the specimen, as in the experiments an indirect displacement control, cf. Sect. 2.4.3, is applied.

### Influence of the Mesh Size

In a first simulation, the sensitivity of the numerical results, such as the macroscopic load-displacement curve or the mesoscopic damage distribution, with respect to mesh refinement is investigated. In order to reduce the numerical effort in these simulations, only ellipses with a minimum diameter of  $8\text{ mm}$  are considered. This allows for varying the average mesh size  $l_e$  between  $0.5\text{ mm}$  and  $2.0\text{ mm}$ . In all simulations, linear elastic behavior is assumed for the aggregates. The nonlinear behavior of the mortar matrix is described by the isotropic damage model given in Sect. 3.3, assuming  $\alpha = 0.01$  for the Rankine criterion. A nonlocal averaging of the displacement field, Sect. 3.2.3, is applied to regularize this damage model. It is to be noted that in all simulations a constant nonlocal radius  $R = 2.0\text{ mm}$  is used. The nonlinear behavior of the interface is represented by the cohesive zone model, introduced in Sect. 3.6. Table 4.3 summarizes all material parameters used in the simulations.

Table 4.3: Uniaxial tension test – material parameters for simulations with varying mesh sizes.

mortar matrix	Young's modulus	$E_m$	[ $N/mm^2$ ]	35 338
	Poisson's ratio	$\nu_m$	[-]	0.18
	tensile strength	$f_{t,m}$	[ $N/mm^2$ ]	4.50
	fracture energy	$G_{f,m}$	[ $Nmm/mm^2$ ]	0.300
	nonlocal radius	$R$	[ $mm$ ]	2.0
aggregates	Young's modulus	$E_a$	[ $N/mm^2$ ]	70 677
	Poisson's ratio	$\nu_a$	[-]	0.18
ITZ	penalty stiffness	$K_p$	[ $N/mm^3$ ]	500 000
	tensile strength	$f_{t,i}$	[ $N/mm^2$ ]	3.40
	fracture energy	$G_{f,i}$	[ $Nmm/mm^2$ ]	0.100
	weight factor	$\alpha$	[-]	1.0

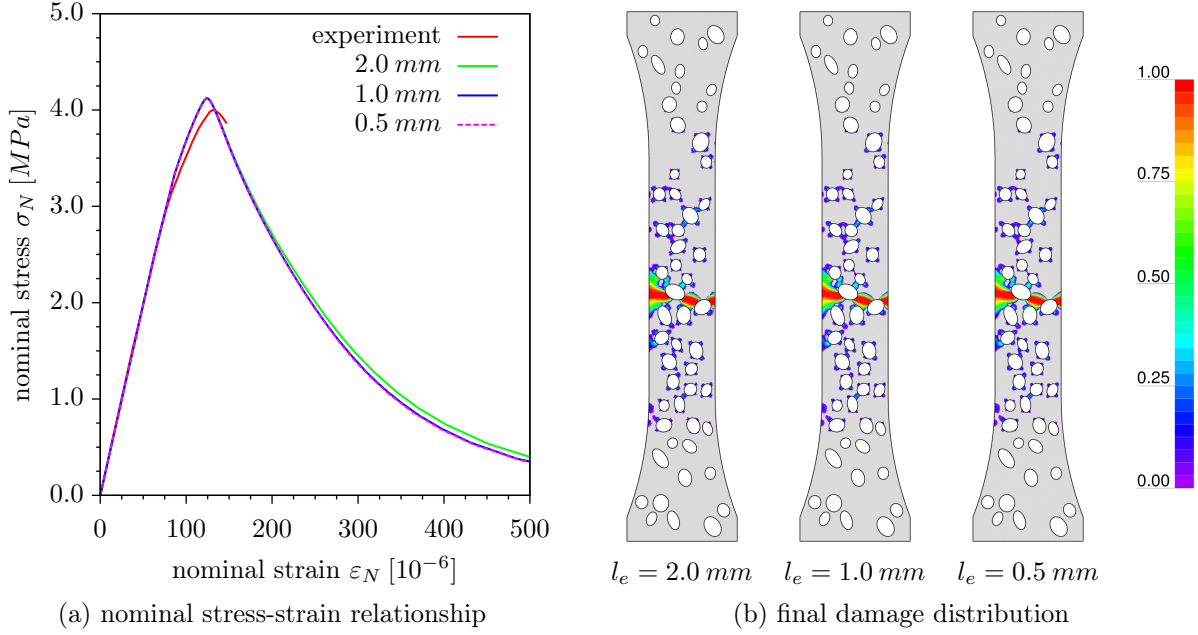


Figure 4.6: Uniaxial tension test – nominal stress-strain relationship and final damage distribution for varying mesh sizes.

Figure 4.6(b) shows the macroscopic response of the specimen in terms of nominal stress and nominal strain, which are defined as

$$\sigma_N = \frac{F_y [N]}{6000 \text{ mm}^2} \quad \varepsilon_N = \frac{\Delta u_y [mm]}{250 \text{ mm}}, \quad (4.22)$$

where  $F_y$  is the resulting vertical force observed at the top of the specimen and  $\Delta u_y$  is the vertical relative displacement between the monitoring points. A difference between the simulations is only distinguishable in the post-peak branch of the curve. Consequently, a good approximation is already obtained for the coarse mesh, where a ratio of 1 between nonlocal radius and average element size is used. Compared to simulations with smaller elements, a slightly larger amount of inelastic energy is dissipated in this simulation, leading to a small deviation in the post-peak branch of the nominal stress-strain curve. Due to the coarse discretization, compared to the nonlocal radius, the area of the damaged region is marginally increased and, as a consequence, the damage profile becomes slightly different. However, in the plots of the final damage distribution, which are shown in Fig. 4.6(b), these differences are not distinguishable. In simulations with finite elements with an average size of  $1.0 \text{ mm}$  or smaller, the deviation in the post-peak branch of the nominal stress-strain curve becomes negligible. Consequently, a ratio of 2 between nonlocal radius and average element size is sufficiently large to represent the damage profile in an appropriate way.

Table 4.4 illustrates the numerical effort for simulations with varying mesh size. The number of unknown degrees of freedom increases approximately by a factor of four when the average element size is halved. Furthermore, the computing time increases significantly. On the one hand, this is the result of the increasing number of degrees of freedom. On the other hand, for each material point the number of elements inside the nonlocal radius

Table 4.4: Uniaxial tension test – number of active degrees of freedom and computing time for varying mesh sizes.

average element size $l_e$	degrees of freedom	computing time
2.0 mm	62 595	9 min
1.0 mm	266 944	4 h 22 min
0.5 mm	1 101 248	77 h 30 min

increases. Consequently, the number of material points which are considered in the nonlocal averaging procedure increases as well. As a result, the computation of the stresses and of the stiffness matrix becomes more time-consuming and the bandwidth of the stiffness matrix increases for elements, in which damage develops.

### Rigid Bond vs. Cohesive Interface

In order to investigate the influence of the interfacial transition zone, simulations with two different mesoscale models are performed. In the first model, concrete is considered as a two phase material consisting of aggregates and mortar matrix. This implies the assumption of rigid bond between aggregates and matrix. In the second model, the interfacial transition zone is explicitly considered as an additional phase using zero thickness interface elements, Sect. 2.2.1. The nonlinear behavior of this phase is described by the cohesive zone model, Sect. 3.6. In both simulations, the nonlocal isotropic damage model, Sect. 3.3 with displacement averaging, Sect. 3.2.3, is applied to the mortar matrix and linear elastic behavior of the aggregates is assumed. The corresponding material parameters are summarized in Table 4.5. It is to be noted that the material parameters, which are obtained by fitting the macroscopic response of the numerical models to the experimental results, are determined separately for each model.

The diagram in Fig. 4.7(a) shows the macroscopic nominal stress-strain relationship. It is to be noted that in both simulations a nonlinear pre-peak behavior is observed, even though

Table 4.5: Uniaxial tension test – material parameters (rigid bond vs. cohesive interface).

				rigid bond	cohesive ITZ
mortar matrix	Young's modulus	$E_m$	$[N/mm^2]$	31 908	31 908
	Poisson's ratio	$\nu_m$	[-]	0.18	0.18
	tensile strength	$f_{t,m}$	$[N/mm^2]$	4.00	4.50
	fracture energy	$G_{f,m}$	$[Nmm/mm^2]$	0.150/0.151	0.300
	nonlocal radius	$R$	$[mm]$	1.0	1.0
aggregates	Young's modulus	$E_a$	$[N/mm^2]$	63 818	63 818
	Poisson's ratio	$\nu_a$	[-]	0.18	0.18
ITZ	penalty stiffness	$K_p$	$[N/mm^3]$		500 000
	tensile strength	$f_{t,i}$	$[N/mm^2]$		3.40
	fracture energy	$G_{f,i}$	$[Nmm/mm^2]$		0.10
	weight factor	$\alpha$	[-]		1.0

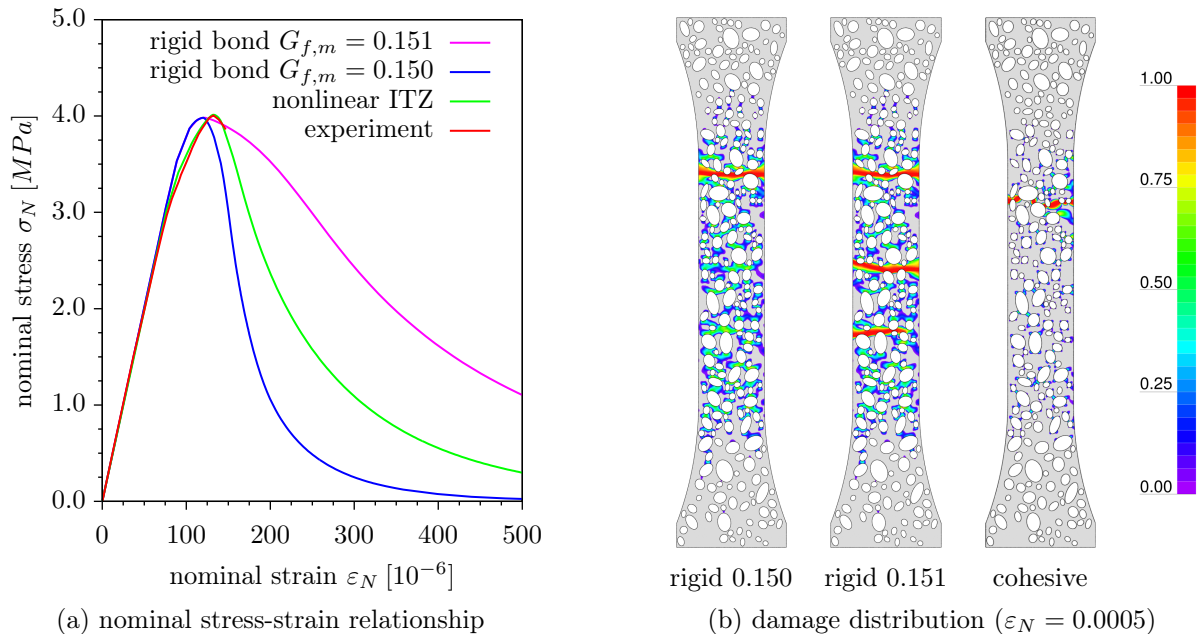


Figure 4.7: Uniaxial tension test – nominal stress strain relationship and final damage distribution (rigid bond vs. cohesive interface).

no hardening is considered in the material formulations. As illustrated in Fig. 4.7(b), which shows the final damage distribution, this phenomenon is the result of the explicit representation of the heterogeneous internal material structure on the mesoscale, leading to a successive initiation and propagation of microcracks. Consequently, both models are capable of representing the evolution of microcracks and the formation of macroscopic cracks. Since the material parameters are determined in such a way that the numerical simulation accurately approximates the experimental curve, both simulations can represent the peak load. But the simulation with cohesive interface elements shows a better approximation of the entire curve. Assuming rigid bond, the pre-peak behavior of the material is overestimated and the nominal strain at the peak-point is too small. A better approximation of the post-peak behavior is not possible for this model. As shown in Fig. 4.7(b), a small variation of the fracture energy results, in the simulations with rigid bond, in a completely different damage distribution. Using a fracture energy of  $0.150 \text{ Nmm/mm}^2$  for the mortar matrix a single macroscopic crack is observed. A slight increase of the fracture energy leads to three competing macroscopic cracks. As a result, the area of the damaged regions and the inelastic energy dissipated during the simulation significantly increases compared to the simulation with  $G_{f,m} = 0.150 \text{ Nmm/mm}^2$ . This leads to significant deviations in the nominal stress-strain curve. Consequently, the post-peak behavior is either underestimated for  $G_{f,m} = 0.150 \text{ Nmm/mm}^2$  or overestimated for  $G_{f,m} = 0.151 \text{ Nmm/mm}^2$ . It is to be noted that the formation of multiple competing macroscopic damage zones is not restricted to mesoscale models in which rigid bond is assumed between aggregates and matrix. As shown in Unger (2009), this phenomenon is also observed for mesoscale models which explicitly consider the ITZ as an additional phase. Figure 4.8 shows a detailed plot of the damage distribution in the vicinity of the final macroscopic crack. Assuming rigid bond, Fig. 4.8(a), failure of the interface between aggregates and matrix is represented

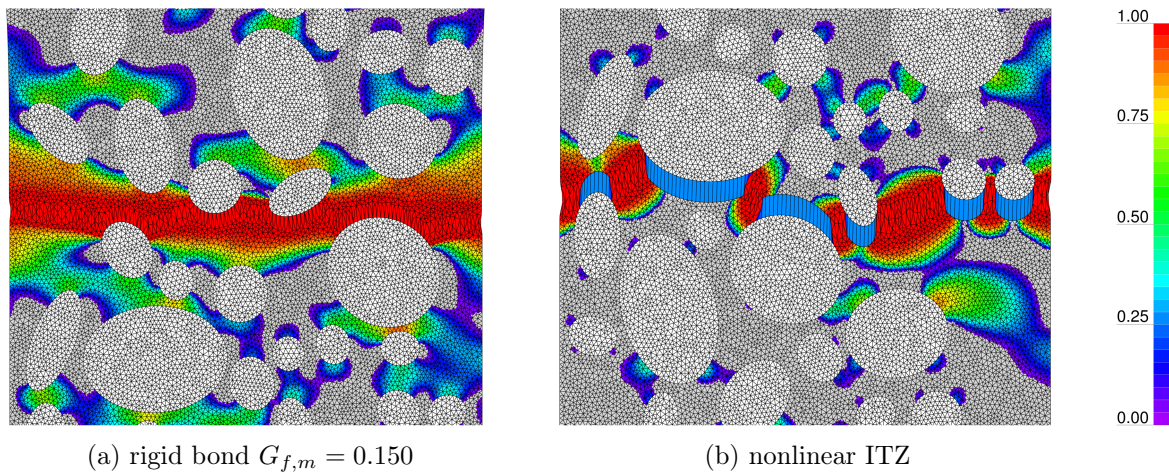


Figure 4.8: Uniaxial tension test – damage distribution in the vicinity of the final macroscopic crack (displacements 10-times magnified).

by the isotropic damage model, leading to damage zones within the mortar matrix. This results in an artificial enlargement of damage zones in the vicinity of aggregates. As a further result, the strength of the ITZ is, in general, overestimated. In the simulation with cohesive interface elements, the ITZ is considered as the weakest link in the mesoscale model. Consequently, a lower tensile strength and a lower fracture energy compared to the mortar matrix is assumed for the ITZ. As a result, the formation of a macroscopic crack is not only influenced by the spatial aggregate distribution itself, as in the simulations with rigid bond, but also by the material properties of the ITZ. Figure 4.7(b) illustrates that due to the explicit consideration of the ITZ, damage within the mortar matrix is significantly reduced. As shown in detail in Fig. 4.8(b), the failure of the ITZ is represented as discrete crack by the cohesive interface formulation. As a result, only microcracks inside the mortar matrix and interface cracks which start to develop into the mortar matrix are described by the nonlocal isotropic damage model. As a further result, the numerical effort is, compared to simulations with rigid bond, reduced due to the lower number of elements in which nonlocal damage develops. Furthermore, the iterative solution procedure shows a better convergence behavior for the model with cohesive interfaces.

In summary, the application of cohesive interface elements allows for an explicit consideration of the specific material characteristic of the ITZ which is different from the mortar matrix, Liao et al. (2004). As a result, initial microcracks start to develop inside the ITZ which corresponds, for normal-strength concrete, to experimental observations, van Vliet and van Mier (1995). This leads, in the numerical simulation of a uniaxial tension test, to a more precise approximation of the pre-peak behavior of concrete. Furthermore, the numerical simulations illustrate the essential influence of the ITZ on the macroscopic behavior of concrete.

Table 4.6: Uniaxial tension test – material parameters (varying continuum damage models).

mortar matrix	Young's modulus	$E_m$	$[N/mm^2]$	31 525
	Poisson's ratio	$\nu_m$	$[-]$	0.18
	tensile strength	$f_{t,m}$	$[N/mm^2]$	4.90
	fracture energy	$G_{f,m}$	$[Nmm/mm^2]$	0.350
	nonlocal radius	$R$	$[mm]$	0.5
aggregates	Young's modulus	$E_a$	$[N/mm^2]$	63 050
	Poisson's ratio	$\nu_a$	$[-]$	0.18
ITZ	Penalty stiffness	$K_p$	$[N/mm^3]$	500 000
	tensile strength	$f_{t,i}$	$[N/mm^2]$	3.30
	fracture energy	$G_{f,i}$	$[Nmm/mm^2]$	0.170
	weight factor	$\alpha$	$[-]$	1.0

### Comparison of Damage Models

In this paragraph, different continuum damage models, such as the scalar damage model (SD), Sect. 3.3, the rotating crack model with transition to scalar damage (RCSD), Sect. 3.4, and the microplane based damage model (MD), Sect. 3.5, are analyzed with respect to their ability to describe the evolution of microcracks in the mortar matrix. In order to avoid a spurious mesh sensitivity of the numerical results, the corresponding nonlocal material formulations are applied. A nonlocal averaging of the displacement field, Sect. 3.2.3, is used for the scalar damage model and for the rotating crack model. The nonlocal formulation of the microplane damage model is based on the averaging of the inverse integrity tensor. Furthermore, linear elastic behavior of the aggregates is assumed and the cohesive zone model, Sect. 3.6, is used to describe the nonlinear behavior of the ITZ. The corresponding material parameters, which are determined in such a way that the numerical results obtained with the scalar damage model fit the experimental results, are summarized in Table 4.6. It is to be noted that for the rotating crack model a transition to scalar damage is performed if the shear modulus in the secant material matrix becomes smaller than 10 % of the initial elastic shear modulus corresponding to  $\alpha_G = 0.1$  in Eq. (3.97). The material parameters of the microplane damage model,  $e_0 = 9.36132 \cdot 10^{-5}$  and  $e_f = 0.076828$ , are derived from the material parameters given in Table 4.6 using Eqs. (3.130) and (3.131) and assuming  $m = 0.05$ . It is to be noted that the relationship between microplane parameters and macroscopic material properties, given in Eqs. (3.130) and (3.131), was obtained from macroscale simulations.

As illustrated in Figure 4.9(a), which shows the macroscopic nominal stress-strain curves, a good approximation of the experimental results is obtained in the simulations with the scalar damage model and with the rotating crack model. Differences between both simulations can be identified in the post-peak branch of the curve, which can be attributed to the different scaling of the fracture energy in both material formulations ( $\beta = 1, 7$  in the scalar damage model and  $\beta = 1.5$  in the rotating crack model). A deviation from the experimental curve, especially in the vicinity of the peak-point, is observed for the simulation with the microplane based damage model. With this model, the peak-load is underestimated which is probably due to the parameter set. Obviously, Eqs. (3.130) and



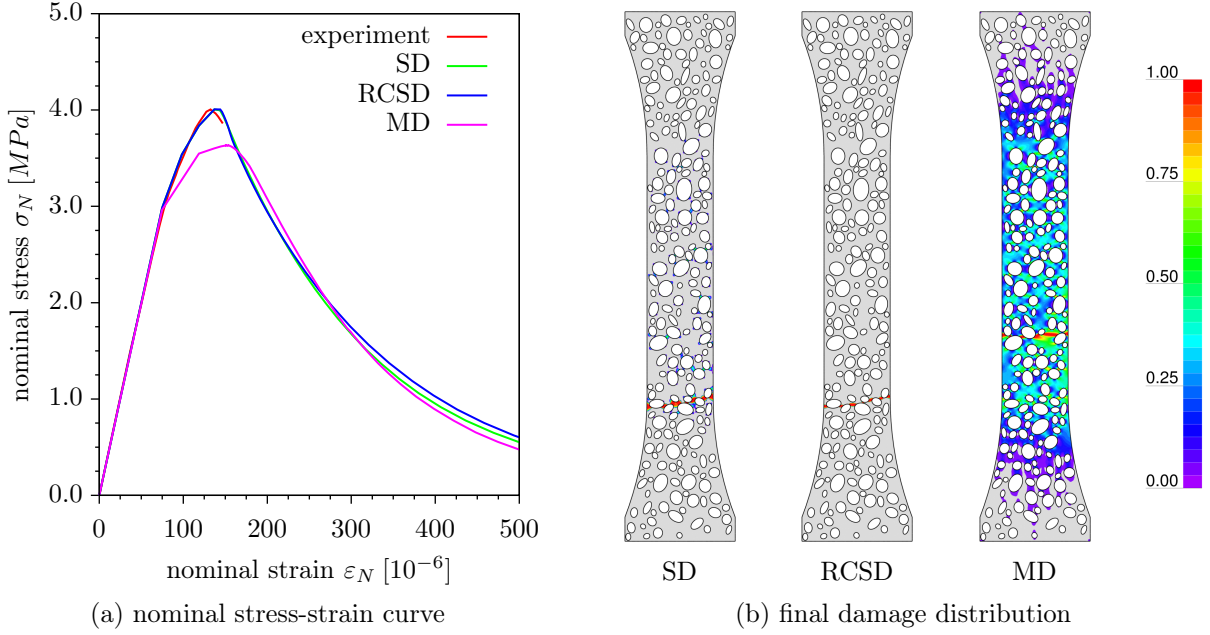


Figure 4.9: Uniaxial tension test – nominal stress-strain curve and final damage model obtained in simulations with the isotropic damage model (SD), the rotating crack model with transition to scalar damage (RCSD) and the microplane based damage model (MD).

(3.131) give only an estimation of the microplane material parameters. Furthermore, a larger nominal strain at the peak-point is observed, which is the result of the microplane approach. On the microplane level, damage starts to develop on microplanes almost normal to the loading direction. Since all other microplanes remain linear elastic, a nonlinear pre-peak behavior is observed on the macroscale. The macroscopic peak-stress is reached, if the damage expands to a sufficiently large number of microplanes. Due to this nonlinear pre-peak behavior, the pre-peak branch of the nominal stress-strain curve becomes more pronounced as in the experiments and in the simulations with the scalar damage model and the rotating crack model.

In Fig. 4.9(b), the final damage distribution is shown. It is to be noted that for the rotating crack model damage is only plotted for elements for which the transition to scalar damage is performed. Consequently, the actual final crack pattern is slightly larger. For the microplane damage model, an equivalent damage value is defined as

$$\omega_{MD} = 1 - \frac{1}{\left(\max_{I=1,2} \bar{\psi}_I\right)^2}, \quad (4.23)$$

where  $\bar{\psi}_I$  is the  $I$ -th eigenvalue of the nonlocal inverse integrity tensor  $\bar{\psi}$ . An almost identical crack pattern is obtained for the scalar damage model and the rotating crack model. Furthermore, the shape and the position of the final macroscopic crack is identical for both models. Consequently, the improved representation of the microcracks due to the anisotropic formulation of the rotating crack model does not, at least for this example,

result in a significant different structural response. From the numerical point of view, the scalar damage model is less complex and, as a consequence, more robust as the rotating crack model. A completely different damage distribution is observed for the simulation with the microplane based damage model. Damage initiates in almost all elements associated to that part of the specimen with the reduced cross-section, which is due to the nonlinear pre-peak behavior explicitly considered in this model. As a consequence, the numerical effort increases significantly compared to the other simulations. Due to the non-local formulation of the material model, the bandwidth of the stiffness matrix increases for elements in which damage develops. Furthermore, due to the high number of damaged elements, the localization of damage in the vicinity of the peak-point becomes more difficult. However, the formation of a macroscopic crack is also observed in the simulation with the microplane model. Compared to the other simulations, a different shape and position of the macroscopic crack is obtained.

In summary, assuming macroscopic tensile failure, a realistic crack pattern is already obtained for the scalar damage model. Consequently, the assumption of isotropic damage is sufficient to represent the anisotropic propagation of microcracks in the mortar matrix. Compared to the simulations with the other two material formulations, the simulation with the scalar damage model is, from a computational point of view, less time-consuming and shows the most robust convergence behavior during the iterative solution procedure.

### Influence of the Spatial Aggregate Distribution

In this thesis, the internal material structure of concrete is artificially generated using numerical simulations. As illustrated in Sect. 4.2, the shape, the position and the orientation of an aggregate are expressed as functions of uniformly distributed random numbers. As a result, a different aggregate distribution is obtained in each simulation, assuming that the seed of the random-number generator is not constant. This corresponds to reality, where two specimen prepared in a similar way differ in their aggregate configuration. In this paragraph, the sensitivity of the macroscopic response to the spatial aggregate distribution is investigated. Ten simulations with varying aggregate distributions are performed and the macroscopic fracture energy  $G_f$  and the macroscopic tensile strength  $f_t$  are determined. It is to be noted that both parameters can be evaluated from the global load-displacement curve

$$G_f = \frac{\int_{u_y=0}^{0.25} F_y(u_y) \, du_y}{6000 \, \text{mm}^2} \quad [N, \text{mm}] \quad (4.24)$$

$$f_t = \frac{\max F_y}{6000 \, \text{mm}^2}, \quad (4.25)$$

where  $F_y$  is the resulting vertical force and  $u_y$  the corresponding vertical displacement observed at the top of the specimen. In all simulations, linear elastic behavior of the aggregates is assumed. Furthermore, the cohesive interface model, Sect. 3.6, is applied to represent the material behavior of the ITZ, and the evolution of microcracks in the mortar

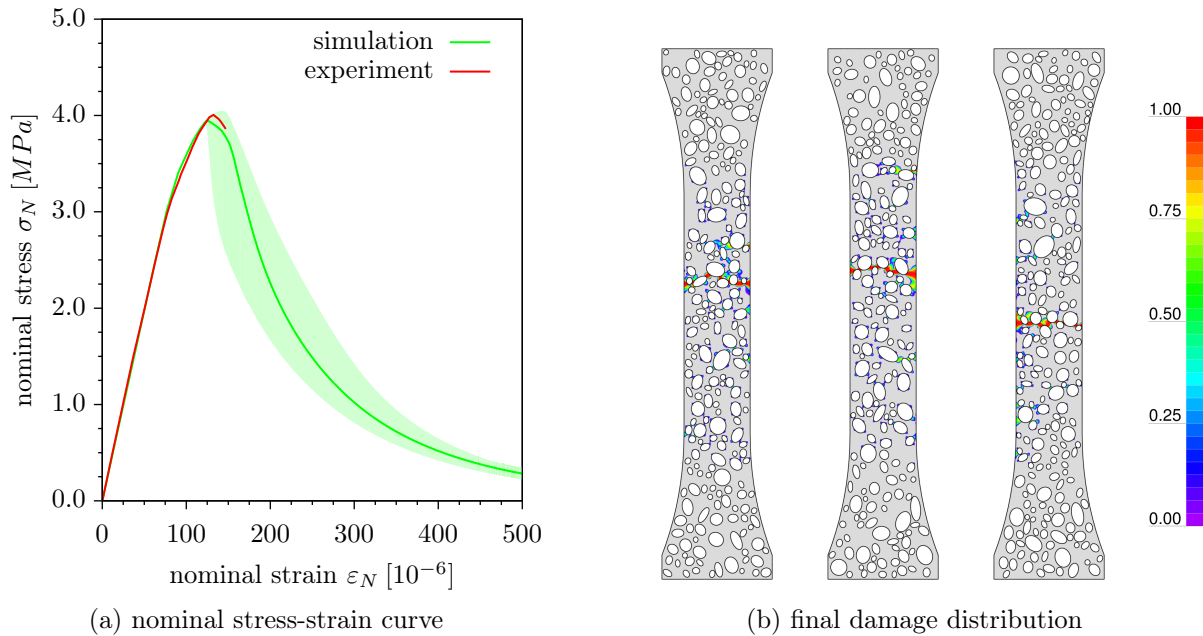


Figure 4.10: Uniaxial tension test – nominal stress-strain curve and final damage distribution for varying aggregate configurations.

matrix is described by the isotropic damage model, Sect. 3.3, with nonlocal averaging of the displacement field, Sect. 3.2.3. The corresponding material parameters, which are determined for the aggregate distribution shown in Fig. 4.5, are summarized in Table 4.5 on page 87. It is to be noted that in each simulation the Young's moduli of the aggregates and the mortar matrix are adapted to the actual area fraction of the aggregates, using Eq. (4.21). The generation of the aggregates is performed in 3D assuming a constant volume fraction for the aggregates. Afterwards, the two-dimensional model is obtained by calculating the intersection of the three-dimensional aggregate distribution and a plane. As a result, a slightly different area fraction of the aggregates is obtained in each simulation. In the simulations, the Young's modulus of the mortar matrix ranges from  $31\,618\text{ N/mm}^2$  to  $32\,177\text{ N/mm}^2$ .

The diagram in Fig. 4.10(a) shows the mean values of the stress-strain curves and the corresponding envelope. The influence of the spatial aggregate distribution is negligible for the pre-peak behavior of concrete, since this state is characterized by the initiation of microcracks uniformly distributed over the entire specimen. Reaching the ultimate load, a localization of damage occurs and a macroscopic crack is formed. As illustrated in Fig. 4.10(b), which shows the final damage distribution for the first three samples, a different shape and position of the macroscopic crack is obtained in each simulation. Consequently, the macroscopic crack path and, related to this, the macroscopic post-peak behavior strongly depends on the internal material structure. It is to be noted that the influence of the aggregate configuration is amplified in this tension test, since the localization of damage is only triggered by the heterogeneous material structure and not by the loading conditions or the macroscopic specimen geometry. In Table 4.7, the mean value and the standard deviation of the macroscopic fracture energy and the macroscopic tensile strength are summarized. It is to be noted that the standard deviation of the

Table 4.7: Uniaxial tension test – macroscopic material parameters.

material parameter		simulation		experiments	
		mean	std. dev.	mean	std. dev.
$f_t$	$[N/mm^2]$	3.98	0.04	4.01	0.28
$G_f$	$[Nmm/mm^2]$	0.21	0.02	0.23	–

fracture energy was not calculated for the experiments, since in most cases the experiments became unstable after having reached the peak load, cf. Kessler-Kramer (2002). Since the material parameters of the numerical simulations are explicitly determined in such a way that the nominal stress-strain curve fits the experimental curve, the mean values of the macroscopic fracture energy and of the macroscopic tensile strength obtained for the numerical simulations almost coincide with the experimental values. Compared to the experiments, the standard deviation of the tensile strength is significantly smaller, which is due to the assumption that all material parameters in the numerical simulation are deterministic values. In order to consider these additional stochastic effects, the mesoscopic material parameters can be modeled as random variables or random fields, cf. Unger (2009).

#### 4.4.2 Size Effect

In the second example, the ability of mesoscale models to represent the size effect is investigated. The numerical simulations are based on the experiments by van Vliet and van Mier (2000). Figure 4.11 shows the specimen dimensions and the range of specimen sizes which were investigated in the experiments. The corresponding concrete mixture parameters used for the preparation of the specimens are given in Table 4.8. Based on these parameters and assuming an enlargement factor  $\varepsilon = 0.25$ , the mesoscale geometry of the numerical model is artificially generated. The numerical simulations are performed with two-dimensional finite element models assuming an average element size of  $0.75\text{ mm}$ . In these models, only aggregates with diameters larger than  $2\text{ mm}$  are considered. A full mesoscale model, as

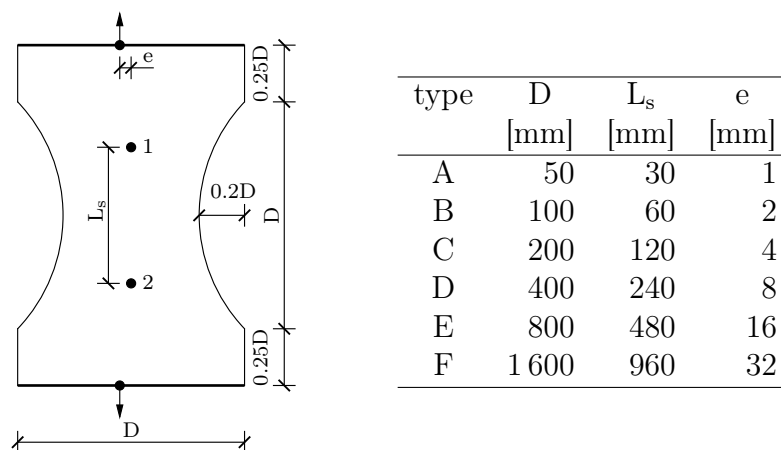


Figure 4.11: Size effect – specimen properties and test setup (specimen thickness: 100 mm).

Table 4.8: Size effect – concrete mixture parameters.

	mass [ $kg/1 m^3$ ]	density [ $kg/m^3$ ]	volume [ $m^3$ ]
cement	375	3 100	0.121
water	187	1 000	0.187
air voids (estimated)			0.020
aggregates 0.125/0.250	127	2 690	0.047
aggregates 0.250/0.500	234	2 690	0.087
aggregates 0.500/2.000	544	2 690	0.202
aggregates 2.000/4.000	363	2 690	0.135
aggregates 4.000/8.000	540	2 690	0.201
concrete	2 370	2 370	1.000

shown in Fig. 4.12(a), is used for the numerical simulation of specimen types A, B and C. The diagram in Figure 4.12(c) shows in a log-log plot the corresponding mean value of the total number of degrees of freedom in the numerical model. The number of degrees of freedom increases approximately by a factor of four if the specimen size is doubled. As a consequence, the nonlinear analysis using a full mesoscale model becomes, from the numerical point of view, already for specimen type D (approximately 2 819 000 dofs) extremely time-consuming. Furthermore, a nonlinear full mesoscale simulation of specimen types E (approximately 11 253 000 dofs) and F (approximately 44 911 000 dofs) is not possible with the available computational power, which allows two-dimensional simulations with up to 3 500 000 degrees of freedom. It is to be noted that, due to the limited amount of memory available, the mesh generation for specimen type F failed and that the number of degrees of freedom is extrapolated. In order to decrease the numerical effort, the simulation of specimen type D is performed with a reduced mesoscale model. As shown in Fig. 4.12(b), only that part of the specimen between the monitoring points is simulated on the mesoscale. In the remaining parts the mesh is coarsened and a homogeneous macroscale model with

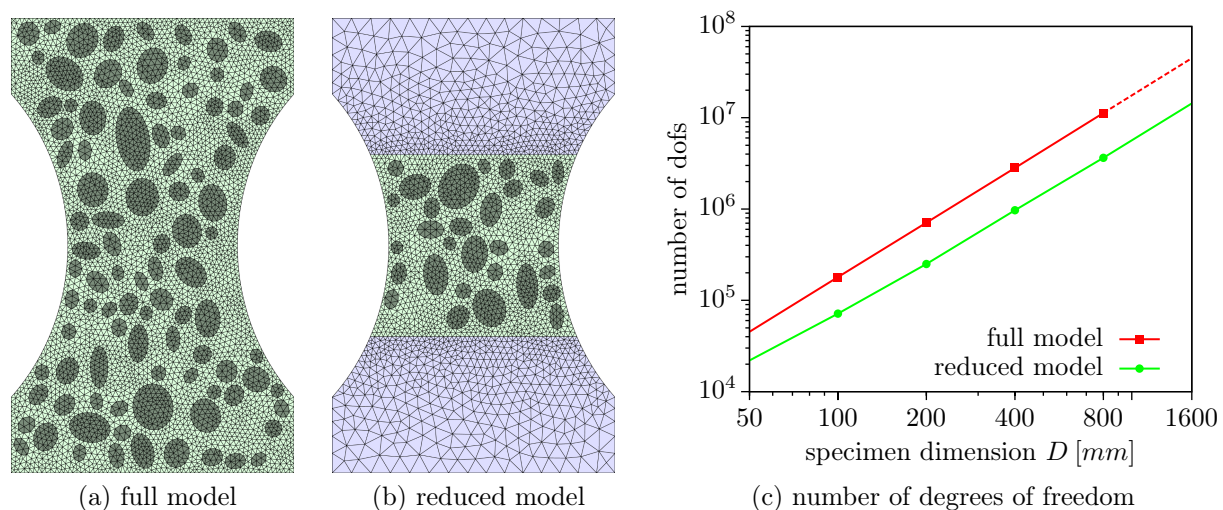


Figure 4.12: Size effect – full and reduced mesoscale models exemplarily shown for specimen type A and corresponding number of elements as functions of the specimen size.

Table 4.9: Size effect – material parameters.

concrete	Young's modulus	$E_c$	$[N/mm^2]$	31 000
	Poisson's ratio	$\nu_c$	$[-]$	0.18
mortar matrix	Young's modulus	$E_m$	$[N/mm^2]$	Eq. (4.21)
	Poisson's ratio	$\nu_m$	$[-]$	0.18
	tensile strength	$f_{t,m}$	$[N/mm^2]$	3.60
	fracture energy	$G_{f,m}$	$[Nmm/mm^2]$	0.250
	nonlocal radius	$R$	$[mm]$	1.0
aggregates	Young's modulus	$E_a$	$[N/mm^2]$	$2E_m$
	Poisson's ratio	$\nu_a$	$[-]$	0.18
ITZ	penalty stiffness	$K_p$	$[N/mm^3]$	500 000
	tensile strength	$f_{t,i}$	$[N/mm^2]$	2.70
	fracture energy	$G_{f,i}$	$[Nmm/mm^2]$	0.028
	weight factor	$\alpha$	$[-]$	1.0

linear elastic material properties of concrete is assumed. For the specimen types E and F, the reduced model consists of approximately 3 643 000 and 14 339 000 degrees of freedom. Consequently, the nonlinear analysis of these specimen types is due to the limited computational power available also not possible with the reduced model. However, the numerical results presented in this section for the specimen types E and F are obtained by using the adaptive heterogeneous multiscale approach which is introduced in Chapter 5. A detailed description of these simulations and a comparison to mesoscale simulations is given in Sect. 5.6.2.

As in the experiments, rotating boundary conditions, cf. van Vliet and van Mier (1998), are imposed in the numerical simulations. Furthermore, the load is applied with a small eccentricity  $e$ . In order to capture snap-back phenomena during the iterative solution procedure, which are also observed in the experiments of the large specimens, the numerical simulations are performed using a load-displacement-constraint method with a constraint based on the dissipated inelastic energy. As shown in Sect. 2.4.3, the external load-vector is parametrized and the unknown load factor is determined in such a way that a prescribed amount of inelastic energy is dissipated in each load step.

In the numerical simulations, the development of microcracks within the mortar matrix is described by the isotropic damage model, Sect. 3.3, with nonlocal averaging of the displacement field, Sect. 3.2.3. Furthermore, the nonlinear behavior of the ITZ is represented by the cohesive interface material model, Sect. 3.6, and a linear elastic material behavior is assumed for the aggregates. The corresponding material parameters are summarized in Table 4.9. It is to be noted that the parameter fitting is performed for one single aggregate configuration for a specimen of type B considering the ultimate load and the shape of the corresponding experimental load-displacement curve.

In order to take into account the stochastic character of the aggregate distribution, ten simulations with varying particle distributions are performed for each specimen type. In each simulation, the macroscopic nominal strength  $\sigma_N$  and the macroscopic fracture energy

Table 4.10: Size effect – mean values and standard deviation of the nominal strength and the fracture energy.

type	nominal strength $\sigma_N$ [ $N/mm^2$ ]				fracture energy $G_f$ [ $Nmm/mm^2$ ]			
	experiment		simulation		experiment		simulation	
	mean	std. dev.	mean	std. dev.	mean	std. dev.	mean	std. dev.
A	2.54	0.41	2.98	0.06	0.097	0.012	0.113	0.013
B	2.97	0.19	2.90	0.07	0.126	0.018	0.127	0.016
C	2.75	0.21	2.78	0.07	0.124	0.014	0.116	0.007
D	2.30	0.09	2.66	0.05	0.125	0.014	0.120	0.007
E	2.07	0.12	2.62	0.04	0.142	0.010	–	–
F	1.86	0.16	2.53	0.02	0.141	0.010	–	–

$G_f$  are determined

$$\sigma_N = \frac{\max F_y}{0.6D} \quad (4.26)$$

$$G_f = \frac{1}{0.6D} \int_{u_y=0}^{u_y, end} F_y(u_y) du_y, \quad (4.27)$$

where  $F_y$  is the vertical load measured at the top of the specimen,  $u_y$  is the corresponding vertical displacement value, and  $u_{y,end}$  is the vertical displacement value for which, in the post-peak branch, the vertical load becomes equal to 3% of the ultimate load  $\max F_y$ . The mean value and the standard deviation of the nominal strength and the fracture energy are summarized in Table 4.10. The influence of the specimen size on these parameters is illustrated in the diagrams in Fig. 4.13. The diagram in Fig. 4.13(a) shows the

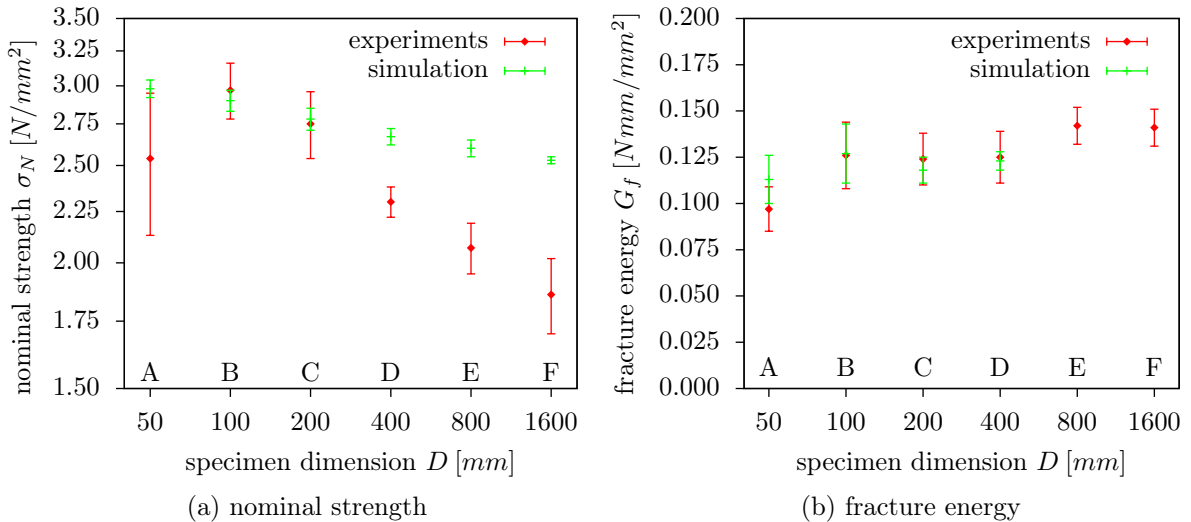


Figure 4.13: Size effect – mean values and standard deviation of the nominal macroscopic strength and the macroscopic fracture energy as a function of the specimen dimension.

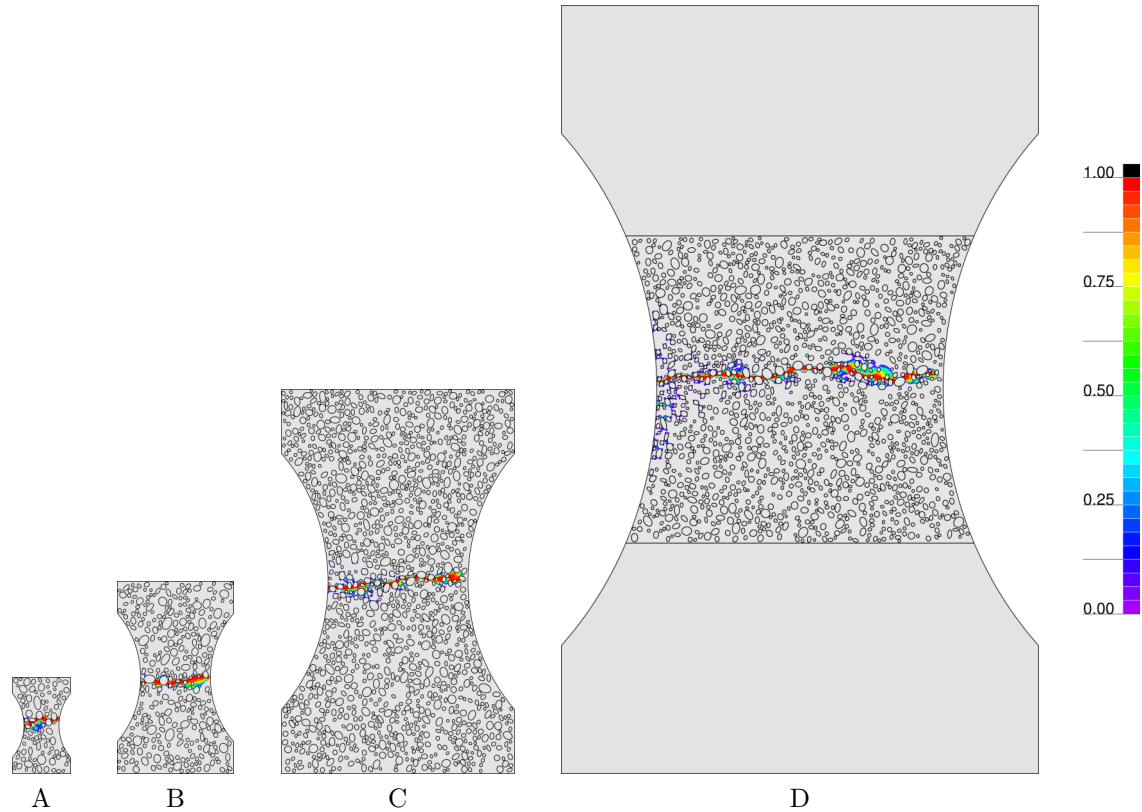


Figure 4.14: Size effect – final damage distribution for varying specimen types.

mean values of the nominal strength  $\sigma_N$  as a function of the specimen dimension  $D$  in a bi-logarithmic plot. A clear size effect on the nominal strength is recognizable. As in the experiments, the nominal strength decreases with increasing specimen dimension. As shown in Fig. 4.13(a), the difference in the nominal strength between specimen types B and F is, in the numerical simulations, about 13% which is considerably smaller compared to the experiments for which a difference of about 37% is observed. Size effects are not only caused by the spatial aggregate distribution, but also by the stochastic character of the material parameters. Since in the presented simulations deterministic material parameters are used on the mesoscale, the influence of the specimen size on the nominal strength is not as strong as in the experiments. Furthermore, the standard deviation of the nominal strength is smaller compared to the experimental results. As already mentioned in the first example, cf. Sect. 4.4.1, these additional stochastic effects can be considered in the numerical model using random variables or random fields for the mesoscale material parameters. In Fig. 4.13(b), the fracture energy is plotted as a function of the specimen size. As already observed in the experiments of specimen types B, C and D, the macroscopic fracture energy is almost independent of the specimen size. Figure 4.14 shows, for one aggregate configuration, the final damage distribution observed in the numerical simulations of specimen types A, B, C and D. In all simulations, damage localizes close to the center of the specimen, which is due to the shape of the specimen. Consequently, the influence of the heterogeneous material structure on the final position of the macroscopic crack is not as pronounced as in the first example, cf. Sect. 4.4.1. However, the shape of the macro-



scopic crack still strongly depends on the actual aggregate distribution. Furthermore, an almost identical width of the zone of localized damage is observed in all simulations. Consequently, the width of this zone is not strongly correlated with the specimen size. It is to be noted that, especially for the larger specimens, additional zones of localized damage, which are considerably smaller than the final zone, are observed close to the boundary of the specimen. Due to the small eccentricity of the applied load these minor cracks are restricted to the left side of the specimen.

### 4.4.3 Compression Test

The last example shows the simulation of compression tests for normal-strength concrete cubes. At first, a two-dimensional simulation is performed for a cube with edge length of  $100\text{ mm}$ , which coincides with the experiments by van Vliet and van Mier (1995). In a second simulation, a three-dimensional model is used. A three-dimensional analysis with the same resolution of the mesoscale material structure as in the two-dimensional model is not possible with the available computational power. Consequently, the three-dimensional simulations are performed with a coarser model. The specimen size is reduced to a cube with edge length of  $25\text{ mm}$ . In order to compare the numerical results to the experiments, which were performed for a  $100\text{ mm}$  specimen, the experimental results are scaled accordingly. It is to be noted that the influence of the specimen size on the numerical results (size-effect) is neglected in the comparison. In all simulations, high friction boundary conditions are imposed. Consequently, the displacements at top and bottom surfaces are restrained in vertical as well as in horizontal direction. In order to capture snap-back phenomena, which are especially observed in the two-dimensional analysis, the numerical simulations are performed with the energy release control presented in Sect. 2.4.3. On the mesoscale, a three-phase model consisting of aggregates, mortar matrix and interfacial transition zone is used. The nonlinear behavior of the mortar matrix is described by the nonlocal isotropic damage model, Sect. 3.3. In contrast to the previous examples, Sect. 4.4.1 and 4.4.2, where the nonlocal formulation is based on the nonlocal displacement field, the nonlocal averaging is, in this example, performed for the equivalent strain, Sect. 3.2.2. Furthermore, the failure surface is described by the rounded Rankine criterion with parameter  $\alpha = 1$ . The nonlinear behavior of the ITZ, which is, in the numerical model, represented by zero thickness interface elements, is described by the cohesive zone model, Sect. 3.6. Furthermore linear elastic material behavior is assumed for the aggregates. It is to be noted that in all material formulations failure due to compressive stresses is not explicitly considered. This implies the assumption that due to the heterogeneous material structure, which is explicitly represented in mesoscale models, compressive failure can be described by the development of microcracks which initiate due to tensile stresses perpendicular to the principal compressive stresses. In the experiments, the same concrete mixture was used as in the size effect experiments. As a consequence, no additional parameter fitting is performed for the compression test and the material parameters as given in Table 4.9 are used in the simulations.

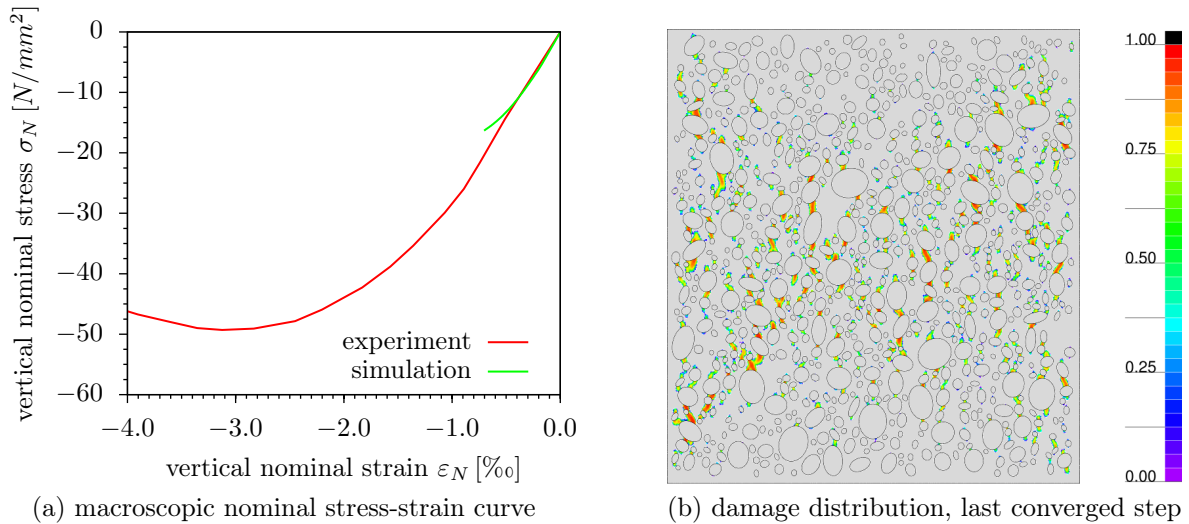


Figure 4.15: Compression test – macroscopic nominal stress-strain curve and damage distribution (100 mm specimen).

## Two-Dimensional Simulation

In the two-dimensional simulation, the mesoscale model consists of aggregates with a mean diameter between 1 mm and 8 mm. The mesoscale material structure is discretized using 6-node triangular elements with quadratic interpolation functions. Additionally, zero-thickness interface elements are introduced at the boundary between aggregates and mortar matrix. Assuming an average element size of 0.5 mm, the numerical model consists approximately of 92 000 elements, 185 000 nodes and 370 000 degrees of freedom, respectively. Figure 4.15(a) shows the macroscopic vertical nominal stress-strain curve. It is to be noted that for the numerical simulation very small snap-backs, not noticeable in the plot, are observed in this curve. Due to divergence of the iterative solution procedure, the simulation stops at a vertical top displacement of approximately  $-0.07\text{ mm}$  ( $\varepsilon_N = -0.7\%$ ). Up to this point, a nonlinear pre-peak behavior is already observed. Compared to the experiments, a more pronounced degradation of the macroscopic specimen stiffness is obtained with the numerical simulation. The nonlinear pre-peak branch of this curve is closely related to the damage distribution on the mesoscale, which is shown in Fig. 4.15(b) for the last converged load-step. First of all, interface elements start to open in horizontal direction and damage initiates above and below the aggregates and develops into the mortar matrix. With increasing load, these damage zones coalesce and a macroscopic damage zone is built. The small snap-backs in the macroscopic load displacement curve are in general caused by the coalescence of two smaller damage zones. A further localization of damage, which would result in a macroscopic softening behavior, is not observed until the simulation is stopped. Obviously, the complex failure mechanism of concrete in compression is only insufficiently represented by the two-dimensional model. Especially the simplifying assumption of a constant aggregate and damage distribution over the specimen thickness (in two-dimensional models the aggregates are considered as elliptic cylinders) results, in combination with the isotropic damage model, in numerical instabilities during the iterative solution procedure and leads to the small snap-backs in

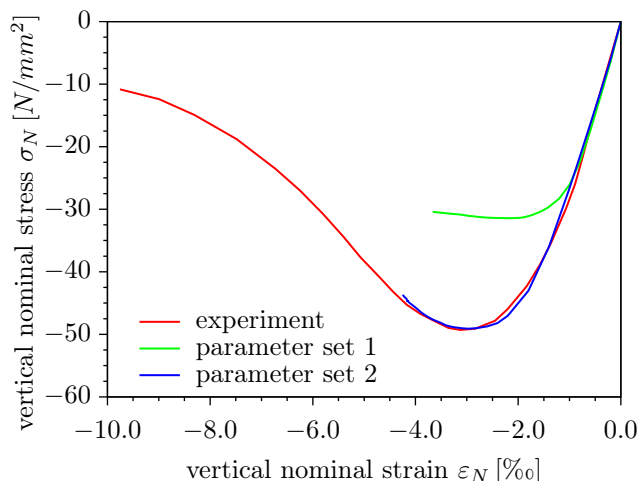


Figure 4.16: Compression test – nominal stress-strain curve observed in three-dimensional simulations.

the nominal stress-strain curve. Furthermore, the assumption that the evolution of microcracks on the mesoscale is the same in each cross-section over the specimen thickness does not coincide with experimental observations. Since the nonlinear pre-peak behavior of concrete is in compression considerably more pronounced as in tension, this assumption is highly questionable for the simulation of compression tests.

### Three-Dimensional Simulation

A three-dimensional model with a similar resolution of the mesoscale material structure and a comparable finite element discretization as in the two dimensional model presented before would result in a finite element model with approximately  $300 \cdot 10^6$  degrees of freedom. The nonlinear analysis of such a model is not possible with the available computational power. As a consequence, the specimen dimensions are, in the three-dimensional simulation, reduced to  $25 \text{ mm}$ . Furthermore, only aggregates with a nominal diameter larger than  $2 \text{ mm}$  are considered in the numerical model. The aggregates and the mortar matrix are discretized with 4-node tetrahedral elements with linear interpolation functions and the ITZ is modeled by zero-thickness interface elements. Assuming an average element size of  $1 \text{ mm}$ , the finite element model approximately consists of 285 000 elements, 87 500 nodes, and 175 000 dofs respectively. It is to be noted that a comparable two-dimensional model would consist of 1 300 triangles. Consequently, the three-dimensional simulation is performed with a very coarse mesoscale model. In a first simulation (set 1), the material parameters determined for the size effect simulations are used. As illustrated in Fig. 4.16, which shows the nominal stress-strain curve, the pre-peak behavior of the material and the ultimate load is considerably underestimated in the numerical simulation, which corresponds to the results obtained with the two-dimensional model. It is to be noted that in contrast to the two-dimensional simulations no spurious snap-backs are observed in the nominal stress-strain curve of the three-dimensional model. As a result, a better convergence behavior of the iterative solution procedure is observed for the three-dimensional simulations. In a second simulation (set 2), the material parameters are modified such

Table 4.11: Compression test – material parameters (three-dimensional model).

				set 1	set 2
concrete	Young's modulus	$E_c$	$[N/mm^2]$	31 000	29 000
	Poisson's ratio	$\nu_c$	$[-]$	0.18	0.18
mortar matrix	Young's modulus	$E_m$	$[N/mm^2]$	26 738	25 013
	Poisson's ratio	$\nu_m$	$[-]$	0.18	0.18
	tensile strength	$f_{t,m}$	$[N/mm^2]$	3.60	8.40
	fracture energy	$G_{f,m}$	$[Nmm/mm^2]$	0.250	0.090
	nonlocal radius	$R$	$[mm]$	1.0	1.0
aggregates	Young's modulus	$E_a$	$[N/mm^2]$	53 476	50 026
	Poisson's ratio	$\nu_a$	$[-]$	0.18	0.18
ITZ	penalty stiffness	$K_p$	$[N/mm^3]$	500 000	500 000
	tensile strength	$f_{t,i}$	$[N/mm^2]$	2.70	2.50
	fracture energy	$G_{f,i}$	$[Nmm/mm^2]$	0.028	0.020
	weight factor	$\alpha$	$[-]$	1.0	1.0

that the nominal stress-strain curve, observed in the simulation, almost coincides with the experimental results. The corresponding material parameters for both simulations are summarized in Table 4.11. Compared to the first parameter set, in particular the fracture energy and the tensile strength of the mortar matrix are altered. Especially the tensile strength is increased to an unrealistic value. As illustrated in Fig. 4.16, the numerical simulation allows for a good approximation of the pre-peak branch and the first part of the post-peak branch of the nominal stress-strain curve. It is to be noted that for both models, the simulation is stopped due to divergence of the iterative solution procedure. In contrast to the nominal stress-strain curve, the final damage distribution, which is plotted in Fig. 4.17 for the last converged load-increment, does not, for both parameter sets, coincide with the experimental results. As shown in van Mier (1986), in the experiments primary cracks (the cracks with the greatest widths) are situated close to the free specimen edges, leading to a splitting of the outer concrete layers. Furthermore, the formation of

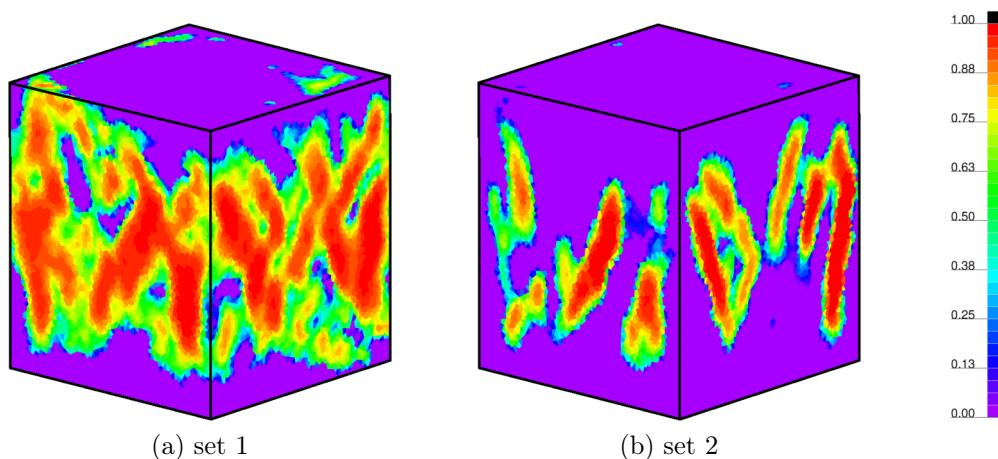


Figure 4.17: Compression test – damage distribution (last converged step).

localized shear-zones is observed in compression tests. Both phenomena are not recognized in the numerical simulations, in which highly irregular crack patterns are obtained.

The main problem of the proposed mesoscale model is, at least for compressive failure, the assumption of isotropic damage for the mortar matrix. Assuming a vertical compressive loading, initial microcracks within the mortar matrix develop almost parallel to the loading direction. In reality, a crack leads to a reduction of the initial material stiffness perpendicular to the crack surface. Consequently, the material stiffness in vertical direction is almost not affected by these initial vertical cracks. Assuming isotropic damage, the anisotropic character of the cracks is neglected and the material stiffness is reduced simultaneously in all directions. As a result, the load-bearing capacity of the material decreases considerably. This phenomenon is amplified by the nonlocal material formulation, in which the damage is distributed over several elements. As illustrated in Fig. 4.17, relatively large damage zones compared to the specimen dimensions are observed in the numerical simulations. The size of the damage zone can be reduced by decreasing the nonlocal radius, which requires the refinement of the finite element mesh. In order to represent the anisotropic character of the microcracks in mesoscale models by an isotropic damage model, the width of the damage zones has to be significantly smaller than the aggregates. Consequently, the total size of damaged zones perpendicular to the loading direction has to become small compared to the specimen dimensions. An alternative approach is to use anisotropic material formulations. In Unger (2009), a combined damage plasticity model, in which the anisotropic degradation of the material is considered by the plasticity part of the model, is applied to describe in a mesoscale model the development of microcracks within the mortar matrix. It is furthermore shown that compressive failure of concrete can not be properly represented only by tensile failure on the mesoscale. As a consequence, the combination of a Rankine criterion in tension and the Drucker-Prager criterion in compression is proposed in Unger (2009) to describe the failure of the mortar matrix.

# 5 Multiscale Modeling of Concrete

## 5.1 Introduction

As illustrated in the previous chapter, the macroscopic behavior of concrete structures (coarse scale) strongly depends on the heterogeneous internal material structure on the mesoscale (fine scale). It is to be noted that such a multiscale character of the structural behavior is observed not merely for concrete, but for materials with microheterogeneities in general. In fine scale simulations, as presented in Chapter 4, the numerical model explicitly resolves the individual components of the internal material structure. If the finite element method is applied to fine scale simulations, the internal material structure is discretized by finite elements with an average element length considerably smaller than the size of the inhomogeneities considered in the model. As a result, already for small structures such as specimens usually used in experiments, the numerical model consists of a large number of elements, nodes and active degrees of freedom. Since the average element size is defined by the size of the individual material components, the numerical effort and the memory demand of fine scale simulations increases significantly if the macroscopic dimensions of the structure are enlarged. As illustrated in Sect. 4.4.2, the number of active degrees of freedom increases in two-dimensional simulations approximately by a factor of four if the structure is scaled by a factor of two. In three-dimensional simulations, this effect is more pronounced since the number of unknowns increases approximately by a factor of eight if the size of the structure is doubled. As a consequence, fine scale simulations are only suited for virtual experiments with small specimens. Fine scale simulations of full large-scale engineering structures are, due to the numerical effort and the memory demand of such simulations, impossible to solve with the computational power available nowadays.

In multiscale approaches, the numerical efficiency of coarse scale models is combined with the accuracy of the material description on the fine scale. Consequently, the influence of the material heterogeneity on the structural response can be, at least partially, considered in multiscale simulations while the numerical effort and the memory demand can, in general, be significantly reduced compared to fine scale simulations. According to Hund (2007), multiscale approaches can be divided into two different classes. In the first class of multiscale approaches, the constitutive behavior of an infinitesimal material point on the coarse scale is described by the homogenized response of a representative sample of the heterogeneous material structure on the fine scale. Such an approach implies the assumption of separation of scales. According to Nemat-Nasser and Hori (1999), separation of scales is obtained if the structural dimensions are significantly larger than the dimensions of material inhomogeneities. As a result, a representative volume element (RVE) can be defined and the averaging can be performed for the RVE. According to Hill (1963), an

RVE is “a sample that (a) is structurally entirely typical of the whole composite on average, and (b) contains a sufficient number of inclusions for the apparent overall moduli to be effectively independent of the surface values of traction and displacement, so long as these values are ‘macroscopically uniform’”. Consequently, the RVE should be large compared to the characteristic dimensions of the microstructure, e.g. particle diameters, but is still small compared to the entire body. In Hashin (1983), the definition of the RVE size is expressed by the MMM-principle

$$l_{micro} \ll l_{mini} \ll l_{macro}, \quad (5.1)$$

in which  $l_{micro}$  corresponds to the typical dimensions of the individual components on the fine scale,  $l_{mini}$  is the dimension of the RVE, and  $l_{macro}$  is the dimension of the structure on the coarse scale. A comprehensive overview on different definitions of an RVE and a detailed investigation on the existence and on the size of an RVE can be found in Gitman (2006); Gitman et al. (2007). It is to be noted that due to the initiation and accumulation of microdefects, such as microcracks or microvoids, the assumption of scale separation may become invalid during the simulation. Gitman (2006) has shown that, in case of softening, which leads to a localization of microdefects and the formation of macroscopic damage zones, an RVE cannot be found or that the RVE would be equivalent to the complete macro-structure, which is of little practical use in computational mechanics. The second class of multiscale approaches does not require the assumption of scale separation. In contrast to the first class of multiscale approaches, in which a representative volume of the fine scale model is associated to an infinitesimal small coarse scale material point, coarse scale sub-domains are directly linked to fine scale sub-domains of equal size. Consequently, coarse scale sub-domains are hierarchically refined such that the heterogeneous material structure observed on the fine scale can be explicitly resolved in these sub-domains. In general, the refinement is performed locally only for those parts of the model in which, for example due to the propagation of microdamage, the explicit representation of the heterogeneous material structure is necessary.

### 5.1.1 Multiscale Approaches Based on Homogenization

In simulations in which the assumption of scale separation is satisfied, homogenization techniques can be applied to consider the influence of material inhomogeneities on the structural response. Using an uncoupled homogenization approach, the behavior of the heterogeneous material structure on the fine scale is, on the coarse scale, described by a homogeneous effective material formulation. The corresponding effective material parameters are obtained by averaging of the structural response of the heterogeneous material on the fine scale over an RVE. This implies the additional assumption of statistical homogeneity. According to Hashin (1983), a material with microheterogeneity is statistically homogeneous if “all global geometrical characteristics such as volume fractions [...] are the same in any RVE, irrespective of its position”. As a consequence, the body averages and the averages over the RVE are identical. In the concept of effective properties, introduced by Kröner (1958); Hill (1963), the effective stiffness tensor  $\mathbf{C}^{eff}$  describes the relationship between effective stresses and effective strains, and the effective compliance tensor  $\mathbf{D}^{eff}$

defines the inverse relationship

$$\langle \sigma \rangle_{ij} = C_{ijkl}^{eff} \langle \varepsilon \rangle_{kl} \quad \mathbf{C}^{eff} = (\mathbf{D}^{eff})^{-1} \quad \langle \varepsilon \rangle_{ij} = D_{ijkl}^{eff} \langle \sigma \rangle_{kl}, \quad (5.2)$$

in which the effective (coarse scale) stresses  $\langle \sigma \rangle_{ij}$  and strains  $\langle \varepsilon \rangle_{ij}$  are the volume averages of the corresponding microscopic quantities within a volume  $V$  of the RVE

$$\langle \sigma \rangle_{ij} = \frac{1}{V} \int_V \sigma_{ij} dV \quad \langle \varepsilon \rangle_{ij} = \frac{1}{V} \int_V \varepsilon_{ij} dV. \quad (5.3)$$

In the general anisotropic case, the constitutive relationship on the coarse scale is defined by 21 effective parameters. Assuming linear elastic behavior for all material components and statistical isotropy of the heterogeneous material structure, the number of effective parameters can be reduced to two, the bulk and the shear moduli  $\kappa$  and  $\mu$ . In Voigt (1889), it is assumed that the strain is uniform throughout the heterogeneous material structure. As a result, the effective parameters can be obtained by a volume weighting of the corresponding phase stiffnesses

$$\kappa_V = \sum_{i=1}^n \varphi_i \kappa_i \quad \mu_V = \sum_{i=1}^n \varphi_i \mu_i \quad \sum_{i=1}^n \varphi_i = 1, \quad (5.4)$$

where  $n$  is the number of phases,  $\kappa_i$  and  $\mu_i$  are the individual bulk and shear moduli of phase  $i$ , and  $\varphi_i$  the corresponding volume fraction. The dual assumption of uniform stress, introduced by Reuss (1929), leads to a volume averaging of the compliances

$$\frac{1}{\kappa_R} = \sum_{i=1}^n \frac{\varphi_i}{\kappa_i} \quad \frac{1}{\mu_R} = \sum_{i=1}^n \frac{\varphi_i}{\mu_i}. \quad (5.5)$$

In Hill (1952, 1963), it is shown that neither assumption is correct for a statistically isotropic material. Assuming a uniform strain, the tractions at the phase boundaries would not be in equilibrium. If uniform stresses are assumed, the inclusions and the matrix could not remain bonded. Furthermore, it is shown that the Voigt values always exceed the Reuss ones and that both values bound the actual elastic moduli

$$\kappa \geq \kappa_R \quad \kappa \leq \kappa_V \quad \mu \geq \mu_R \quad \mu \leq \mu_V. \quad (5.6)$$

Hashin and Shtrikman (1963) propose improved bounds on the effective moduli, which can be obtained using a variational approach. Assuming a two-phase material ( $\kappa_1 < \kappa_2$  and  $\mu_1 < \mu_2$ ), the corresponding bounds are given by

$$\kappa_{HS}^L = \kappa_1 + \frac{\varphi_2}{\frac{1}{\kappa_2 - \kappa_1} + \frac{3\varphi_1}{3\kappa_1 + 4\mu_1}} \quad \mu_{HS}^L = \mu_1 + \frac{\varphi_2}{\frac{1}{\mu_2 - \mu_1} + \frac{6(\kappa_1 + 2\mu_1)\varphi_1}{5\mu_1(3\kappa_1 + 4\mu_1)}} \quad (5.7)$$

$$\kappa_{HS}^U = \kappa_2 + \frac{\varphi_1}{\frac{1}{\kappa_1 - \kappa_2} + \frac{3\varphi_2}{3\kappa_2 + 4\mu_2}} \quad \mu_{HS}^U = \mu_2 + \frac{\varphi_1}{\frac{1}{\mu_1 - \mu_2} + \frac{6(\kappa_2 + 2\mu_2)\varphi_2}{5\mu_2(3\kappa_2 + 4\mu_2)}}, \quad (5.8)$$



where the superscripts  $L$  and  $U$  indicate the lower and the upper bound. It is to be noted that neither for the Voigt and the Reuss bounds nor for the Hashin-Shtrikman bounds, an assumption about the phase geometry and about the spatial distribution of the phases has been made. Hashin and Shtrikman (1963) show that for this general case the Hashin-Shtrikman bounds are the most restrictive ones. A comprehensive overview of more advanced analytical methods for the determination of the effective moduli, taking into account the shape of the particles and their spatial distribution, can be found in the classical textbooks of micromechanics, e.g. Mura (1982); Aboudi (1991); Nemat-Nasser and Hori (1999).

Analytical homogenization methods are, in general, restricted to simple particle geometries such as spheres. For more complex internal material structures, numerical homogenization techniques are required to determine the components of the effective stiffness and compliance tensors. As shown in Zohdi et al. (1998), a set of six linearly independent loading regimes, leading on the coarse scale either to a uniform stress or a uniform strain, are required to determine the 21 independent parameters of the general three-dimensional anisotropic case. Each loading is imposed in terms of homogeneous boundary conditions, cf. Aboudi (1991), on the boundary of the RVE and the corresponding fine scale boundary value problem is solved. In a second step, the average stresses and strains are calculated using Eqs. (5.3). As a result, a set of 36 equations, describing the relationship between effective stresses and effective strains, is obtained, which can be solved for the unknown effective parameters. Due to the symmetry of the effective stiffness and of the effective compliance tensor, the number of independent effective parameters reduces to 21.

Uncoupled homogenization techniques can be also applied to nonlinear material behavior. Suquet (1987) develops a homogenized plasticity model to describe the nonlinear behavior of flat aluminum specimens with small perforations on the coarse scale. In this model, the yield surface and the plastic strains are, at least in an approximate manner, defined on the fine scale. Zohdi et al. (1998) describe the progressive damaged response of an aluminum-boron composite on the coarse scale as a series of effective linear elastic secant material tensors which are directly determined from nonlinear fine scale simulations of representative material samples. As illustrated in Eqs. (5.2), the effective macroscopic linear elasticity tensor can be derived from the volume averages of the fine scale stresses and strains over the RVE. Döbert (2001) uses an anisotropic continuum damage material model to describe the macroscopic nonlinear behavior of fiber-reinforced composites. The material model is based on the local analysis of the damage evolution in a representative volume element. In particular, the macroscopic damage functions which describe the evolution of the individual damage parameters are derived from the effective stress-strain relationship observed in nonlinear fine scale simulations. In Reese (2003), the nonlinear behavior of fiber-reinforced rubber-like composites is described by a phenomenological material formulation on the macroscale. Mesoscale simulations are used to understand the characteristic deformation behavior of the composite material and to derive a physically reasonable continuum mechanical model of finite anisotropic elastoplasticity. Furthermore, these computer experiments are used to identify the parameters of the macroscopic material model. In Unger and Könke (2008), the constitutive relationship of concrete on the macroscale is approximated by neural networks. The homogenized results of numerical simulations on the mesoscale are used as training data for the approximation of the

material response.

The advantage of uncoupled homogenization techniques is the numerical efficiency. Time-consuming fine scale simulations explicitly resolving the heterogeneous internal material structure are, in general, only used to design the macroscopic material model and to determine the corresponding effective material parameters. The simulation of macroscopic structures is completely performed on the coarse scale using the effective material formulation. On the other hand, the behavior of individual material components on the fine scale are only considered in an approximate manner. Consequently, the actual damage state within the internal heterogeneous material structure on the fine scale is only described in a homogenized way.

In coupled homogenization techniques, the stress-strain relationship at a material (integration) point of the coarse scale model is not defined by effective constitutive equations, but is solely described by the constitutive behavior of a representative sample of the microstructure associated to that point. Consequently, no assumptions on the macroscopic constitutive behavior are required. As a result, coupled homogenization techniques are more flexible than uncoupled methods. They allow, for example, the incorporation of geometrical nonlinearity, Smit (1998); Smit et al. (1998), or the consideration of time dependent material behavior, Kouznetsova et al. (2001). Smit et al. (1998) propose a strain-driven coupled homogenization procedure which is based on multilevel finite element modeling. In this approach, an RVE resolving the heterogeneous fine scale material structure is assigned to each integration point of the coarse scale finite element discretization. As a first step, the boundary value problem is solved for the coarse scale model. Secondly, based on the resulting macroscopic deformation field, appropriate boundary conditions are imposed on the RVE in such a way that the volume average of the fine scale strain field coincides with the macroscopic strain tensor. In general, three different types of boundary conditions can be distinguished: linear displacements, constant tractions and a combination of periodic deformation and antiperiodic tractions. The boundary conditions are either directly imposed on the RVE, Smit et al. (1998); Kouznetsova et al. (2001), considered as additional constraints using Lagrange multipliers, Miehe and Koch (2002), or applied via a penalty approach, Bayreuther (2004). Using finite element simulations, the corresponding boundary value problem is solved separately for each RVE. Finally, the macroscopic stress tensor is obtained by averaging the resulting fine scale stress field over the volume of the RVE. Furthermore, the consistent tangential material matrix at a material point of the coarse scale model can be derived through static condensation, Wilson (1974), from the total tangential stiffness matrix of the RVE. Since the determination of the macroscopic stresses and the macroscopic stiffness matrix requires separate finite element simulations for each integration point, fully coupled homogenization techniques are computationally expensive. Feyel and Chaboche (2000) propose parallel computation techniques to reduce the simulation time in multilevel finite element approaches. Alternatively, Ghosh et al. (2001) use an adaptive multilevel approach, in which coupled homogenization methods are only applied in critical regions of the structure, to reduce the numerical effort.

Classical (first order) homogenization techniques, as presented above, cannot be used if the assumption of scale separation is not satisfied, e.g. materials with softening behavior. Kouznetsova (2002); Gitman (2006) have shown that, in the case of softening, the

results of classical coupled homogenization techniques depend on the size of the coarse scale finite element discretization and the size of the RVE. In order to overcome the mesh dependency, Kouznetsova (2002); Kouznetsova et al. (2002, 2004) propose a gradient enhanced (second order) computational homogenization scheme, which is an extension of the classical homogenization techniques. In this approach, the macroscopic deformation gradient and the gradient of the macroscopic deformation gradient are imposed in terms of generalized periodic boundary conditions on the microstructural RVE. The fine scale components considered in the RVE are modeled with a classical continuum formulation. A full second gradient continuum formulation is required on the coarse scale. The constitutive response of the second gradient macro-continuum is, in terms of the macroscopic stress tensor, the macroscopic higher-order stress tensor and the corresponding tangents, directly derived from the solution of the fine scale (RVE) boundary value problem. As shown in Kouznetsova (2002), the second-order homogenization scheme allows for the analysis of softening and localization phenomena without spurious dependency of the results on the macroscopic mesh size. Gitman (2006) demonstrates that, in a second-order homogenization procedure, the macroscopic length-scale is proportional to the RVE size. Consequently, the results strongly depend on the size of the RVE.

In Gitman (2006); Gitman et al. (2008), the coupled volume approach which is based on classical first order computational homogenization techniques is used for the simulation of the nonlinear behavior of quasi-brittle materials. In order to avoid – in the case of softening – a spurious dependency of the results on the macroscopic mesh size and on the RVE size the assumption of scale separation is abandoned. The homogenized stress-strain relationship of a material point on the coarse scale is not described by the fine scale response of an RVE but by the fine scale behavior of a material sample whose size coincides with the domain associated to the corresponding coarse scale material point. Consequently, the size and the shape of the fine scale sub-model is directly linked to the coarse scale mesh. In the coupled volume approach, the macroscopic stress tensor is determined from a fine scale sub-model using a computational homogenization technique. Based on the macroscopic strain tensor, displacement boundary conditions are imposed on the fine scale sub-model and the corresponding fine scale boundary value problem is solved. It is to be noted that the fine scale problem can be solved for each coarse scale material point separately. The macroscopic stress tensor is obtained as volume average of the resultant fine scale stress field. Using the concept of static condensation, the corresponding tangent material matrix can be determined from the tangential stiffness matrix of the fine scale model. Since the fine scale model describes the material behavior of a coarse scale sub-domain with identical size, the coupled volume approach is capable to objectively represent softening phenomena.

### 5.1.2 Hierarchical Multiscale Approaches

Hierarchical multiscale approaches can be used if the assumption of scale separation is not satisfied since the fine scale response is not described by the behavior of a representative volume element. In hierarchical multiscale models, the structure is, at least in sub-domains, directly resolved on the fine scale. Consequently, the size of the fine scale model is identical

to the size of the associated coarse scale sub-domain. In this class of multiscale models, the solution obtained with the coarse model is improved by a hierarchical refinement of the model.

In sub-structuring methods, as, e.g., presented in Noor et al. (1978), the number of unknowns of the initial problem is reduced by the introduction of super-elements. In this method, each super-element represents a patch of finite elements of the initial fine mesh. The corresponding nodes are divided into internal nodes inside the super-element and interface nodes on the boundary of that super-element. Using static condensation, Wilson (1974), which is performed for each super-element independently, the internal nodal degrees of freedom are expressed in terms of interface nodal degrees of freedom. As a result, the global system of equations is reduced to the interface degrees of freedom. As a post-processing step the internal degrees of freedom are determined from the interface degrees of freedom. From a multiscale point of view, the static condensation can be interpreted as the solution of a fine scale problem, whereas the reduced global system of equations involving only the interface degrees of freedom represents the coarse scale problem.

In the exact zooming method, proposed by Hirai et al. (1984), the finite element model is locally refined in a successive manner. In a first step, the unknown displacement values are determined for a coarse mesh. Secondly, a refined sub-model is created based on the finite element discretization of the coarse model. Consequently, all nodes of the coarse mesh in the refined region are also part of the refined discretization. Using static condensation and structural reanalysis methods, the displacements of the refined sub-model and the improved displacements of the coarse model can be derived from the initial displacement field. In contrast to sub-structuring methods, a hierarchical improvement of the initial coarse scale solution is obtained with each level of zooming.

Another approach to improve the efficiency of finite element analysis is the refined global-local method proposed by Mao and Sun (1991) and the iterative global-local method introduced by Whitcomb (1991). In a first step, the entire structure is analyzed using a relatively coarse finite element mesh. The displacement field obtained with the coarse mesh is, in a second step, used to derive boundary conditions for local regions of interest which are analyzed separately with refined finite element discretizations. In a third step, based on the stress distribution obtained in the refined regions, improved internal forces are determined on the coarse mesh. In general, the improved internal forces are not in equilibrium with the external forces. Mao and Sun (1991) and Whitcomb (1991) propose an iterative procedure to reduce the residual between the results of the coarse model and of the refined sub-models.

Numerous multiscale methods are based on a hierarchical decomposition of the solution into global (coarse scale) and local (fine scale) effects. In general, the local effects are only resolved in critical regions of the structure. In order to enforce compatibility of the solution, homogeneous boundary conditions on the local effects are imposed at the interface between the global models and the locally refined models. Consequently, it is assumed that the local effects vanish outside the critical region. Since the global solution is locally enriched by the fine scale solution, this class of methods is also referred to as superposition based multiscale methods. The various methods mainly differ in the approximations of the global and the local fields and in the selection of the global local interface. In the global-local

finite element methods, proposed by Mote (1971); Noor and Peters (1980), finite element approximations are combined with classical Ritz approximations. Belytschko et al. (1990) use a spectral approximation for the fine scale and the finite element method for the coarse scale. In the variational multiscale method, presented by Hughes (1995); Hughes et al. (1998), the coarse scale field is solved numerically using finite elements, whereas the fine scale solution is determined analytically. It is furthermore assumed that the fine scale field vanishes at the element boundaries. A superposition of finite element meshes with arbitrary element size and polynomial order is used in the s-version of the finite element method developed by Fish (1992). Since, in this method, the boundary of the refined mesh does not necessarily coincide with the edges of the underlying coarse mesh, the exact integration of the system matrices may become rather complex. In Fish (1992), an approximate numerical integration scheme is employed to avoid this complexity. A hierarchical multiscale method similar to the s-version of the finite element method is proposed by Rank and Krause (1997); Krause and Rank (2003). The so-called hp-d method combines a p-version finite element approximation on the coarse scale with an h-version finite element mesh on the fine scale. Furthermore, it is assumed that elements of the fine mesh do not overlap with element edges of the coarse mesh. As a result, standard numerical integration schemes can be applied in this method for the exact integration of the system matrices. Hund (2007); Hund and Ramm (2007); Hettich et al. (2008) demonstrate the application of superposition based multiscale methods to simulations of the nonlinear behavior, including softening and localization phenomena, of materials with a heterogeneous microstructure. The finite element method is employed on both scales. In contrast to the s-version of the finite element method and the hp-d method, each fine scale sub-domain exactly coincides with one element of the coarse scale mesh. As a consequence, additional boundary or coupling conditions on the fine scale field are required for adjacent fine scale sub-domains, Hund and Ramm (2007). In Hettich et al. (2008), the nonlinear material behavior is represented by a discrete crack approach using the extended finite element method on the fine scale. Hund and Ramm (2007) use a gradient enhanced isotropic continuum damage formulation to describe the damage evolution on the fine scale.

## 5.2 Heterogeneous Multiscale Approach

Figure 5.1(a) shows the final damage distribution in a three-point bending beam obtained by a nonlinear finite element simulation on the macroscale using the nonlocal isotropic damage model presented in Sect. 3.3. This example illustrates that damage in concrete structures is in general a local phenomenon. The size of the fracture process zone, in which damage develops, is small compared to the macroscopic specimen dimensions. This phenomenon allows for the usage of the heterogeneous multiscale approach in a nonlinear simulation of these structures.

Such a heterogeneous multiscale model which consists of several sub-domains describing the material on different length scales is shown in Fig. 5.1(b) for the three-point bending beam. Mesoscale models are only used in those parts of the structure in which damage develops.

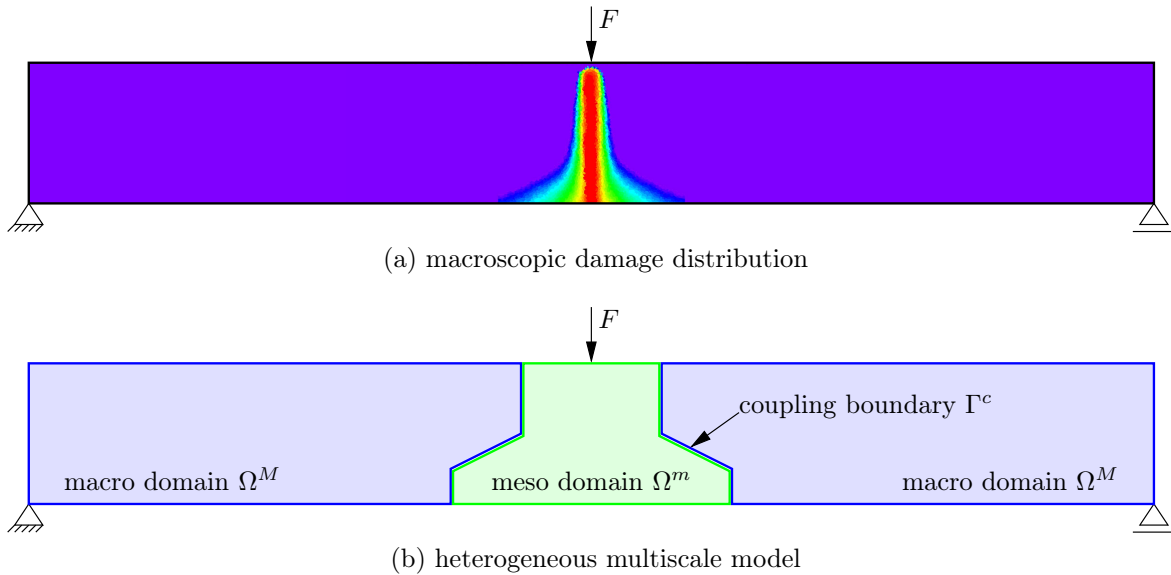


Figure 5.1: Macroscopic damage distribution and corresponding heterogeneous multiscale model of a three-point bending beam.

The nonlinear material behavior is considered only in mesoscale sub-domains. Undamaged or sparsely damaged regions of the structure are simulated on the macroscale assuming a linear elastic material behavior which can be characterized by effective material parameters. The several sub-models with different scales of resolution are combined into one numerical model, the so-called heterogeneous multiscale model. Consequently, such an approach combines the advantages of both scales, the numerical efficiency of macroscale models and the detailed representation of the failure mechanism in mesoscale models. Compared to simulations using full mesoscale models, the numerical effort can be, in general, significantly reduced by heterogeneous multiscale models without losing accuracy.

Two major problems arise in simulations with heterogeneous multiscale models. The first one is the coupling between sub-domains which describe the material on different length scales. The second one is the determination of the size and the position of the mesoscale sub-domains. Both problems will be addressed in the next sections.

## 5.3 Coupling Conditions

One crucial point in heterogeneous multiscale models is the coupling between macro- and mesoscale sub-domains. Figure 5.2 shows for a heterogeneous multiscale model the finite element discretization in the vicinity of a coupling boundary  $\Gamma^c$  between a macroscale sub-domain  $\Omega^M$  and a mesoscale sub-domain  $\Omega^m$ . It is illustrated that the sub-domains vary not only in the size of the finite elements but also in the resolution of the material structure. A homogeneous material is assumed for the macroscale part of the model. In the mesoscale sub-domain, the finite element mesh explicitly represents the heterogeneity of the material structure.

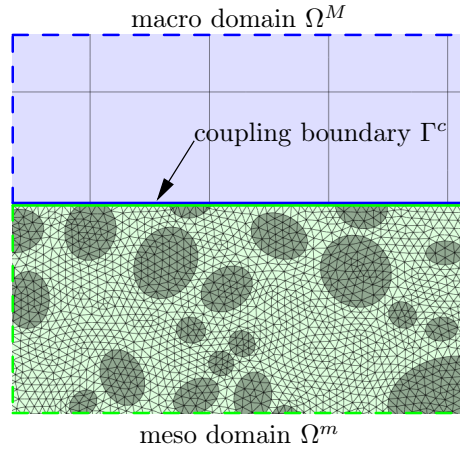


Figure 5.2: Heterogeneous multiscale model in the vicinity of a coupling domain.

In Fig. 5.3, three different methods for the coupling of sub-domains with non-matching finite element discretizations are shown. Using a strong coupling approach, such as constraint equations, displacement compatibility of the sub-domains is enforced. Consequently, the relative displacements between two adjacent sub-domains have to vanish in all points  $\mathbf{x}$  of the coupling boundary  $\Gamma^c$

$$\mathbf{u}^M(\mathbf{x}) - \mathbf{u}^m(\mathbf{x}) = \mathbf{0} \quad \forall \mathbf{x} \in \Gamma^c = \Omega^M \cap \Omega^m, \quad (5.9)$$

where  $\mathbf{u}^M$  and  $\mathbf{u}^m$  are the displacements of the sub-domains  $\Omega^M$  and  $\Omega^m$ . In a weak coupling approach, which can be realized by the mortar method or the arlequin method, the coupling condition Eq. (5.9) is only satisfied in an average sense. The integral of the relative sub-domain displacements over the coupling boundary  $\Gamma^c$  of non-overlapping

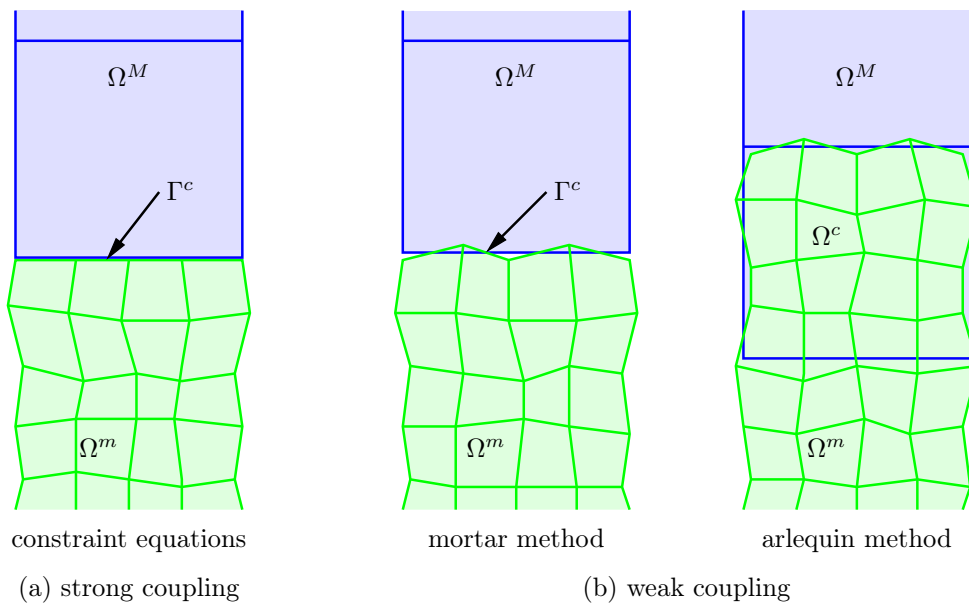


Figure 5.3: Coupling methods for non-matching finite element meshes.

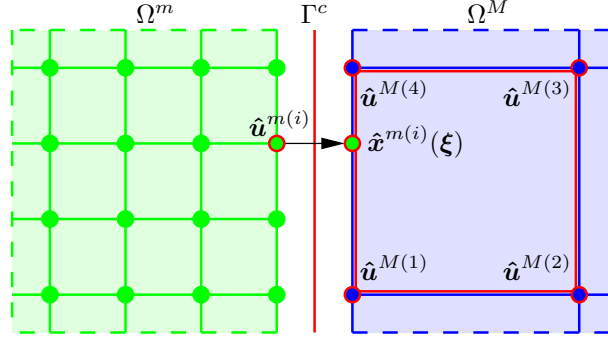


Figure 5.4: Strong displacement coupling with constraint equations.

sub-domains

$$\int_{\Gamma^c} \mathbf{u}^M(\mathbf{x}) - \mathbf{u}^m(\mathbf{x}) \, d\mathbf{x} = \mathbf{0} \quad \Gamma^c = \Omega^M \cap \Omega^m, \quad (5.10)$$

or the coupling domain  $\Omega^c$  of overlapping sub-domains

$$\int_{\Omega^c} \mathbf{u}^M(\mathbf{x}) - \mathbf{u}^m(\mathbf{x}) \, d\mathbf{x} = \mathbf{0} \quad \Omega^c = \Omega^M \cap \Omega^m, \quad (5.11)$$

has to vanish. Consequently, displacement compatibility between the sub-domains may not be satisfied, which may result in small gaps or overlaps. In the following sections, the three coupling methods illustrated in Fig. 5.3 are presented for the two-dimensional case. However, the extension to the three-dimensional case is straightforward.

### 5.3.1 Constraint Equations

A strong coupling between sub-domains with non-matching finite element discretizations can be realized using constraint equations. Assuming that in both sub-domains finite elements with the same interpolation order are used, displacement compatibility between the sub-domains is enforced. As shown in Fig. 5.4, the nodal degrees of freedom on the coupling boundary of the mesoscale sub-domain are expressed by the displacement interpolation of the adjacent finite element in the macroscale sub-domain. Consequently, the corresponding constraint equation can be written as

$$\hat{\mathbf{u}}^{m(i)} = \sum_{j=1}^{n_N^M} N^{M(j)}(\boldsymbol{\xi}^M(\hat{\mathbf{x}}^{m(i)})) \hat{\mathbf{u}}^{M(j)}, \quad (5.12)$$

where  $\hat{\mathbf{u}}^{m(i)}$  is the vector of nodal degrees of freedom of the mesoscale node  $i$ ,  $\hat{\mathbf{x}}^{m(i)}$  are the corresponding node coordinates,  $n_N^M$  is the number of nodes of the adjacent macroscale element,  $\hat{\mathbf{u}}^{M(j)}$  is the vector of degrees of freedom of the  $j$ -th macroscale element node, and  $N^{M(j)}$  is the corresponding element shape function. In general, the element shape



functions are defined in the local natural element coordinate system. Consequently, a transformation of the global node coordinates  $\hat{\mathbf{x}}$  to local natural element coordinates  $\boldsymbol{\xi}$  is required. Due to the direct coupling between a certain set of degrees of freedom, the size of the global system of equations is reduced by the number of constraint equations.

### Numerical Implementation

For the sake of simplicity, geometrical and physical linearity is assumed. Consequently, the equilibrium problem can be solved in one step. In general, constraint equations can be written as

$$\mathbf{A}\mathbf{d} = \hat{\mathbf{d}}, \quad (5.13)$$

where  $\mathbf{d}$  is the global vector of nodal degrees of freedom,  $\mathbf{A}$  is the corresponding coefficient matrix, and  $\hat{\mathbf{d}}$  is the vector of prescribed displacement values. It is to be noted that the number of rows of matrix  $\mathbf{A}$  is equal to the number of constraint equations, and the number of columns correspond to the total number of degrees of freedom. By applying Gauss elimination, the set of nodal displacement values  $\mathbf{d}$  can be subdivided into a set of free displacement values  $\mathbf{d}_f$ , which are actually unknown, and a set of depending displacement values  $\mathbf{d}_d$ , which can be calculated using the constraint equations if the vector  $\mathbf{d}_f$  is known. As a result, the constraint equations can be rewritten as

$$\mathbf{d}_d = \bar{\mathbf{d}} - \bar{\mathbf{A}}\mathbf{d}_f, \quad (5.14)$$

where  $\bar{\mathbf{A}}$  is the modified coefficient matrix, and  $\bar{\mathbf{d}}$  is the modified right hand side of the constraint equations. By reordering the global degrees of freedoms, the corresponding partitioned global system of equations can be obtained

$$\begin{bmatrix} \mathbf{K}_{ff} & \mathbf{K}_{fd} \\ \mathbf{K}_{df} & \mathbf{K}_{dd} \end{bmatrix} \begin{bmatrix} \mathbf{d}_f \\ \mathbf{d}_d \end{bmatrix} = \begin{bmatrix} \mathbf{f}_{ext,f} \\ \mathbf{f}_{ext,d} \end{bmatrix}. \quad (5.15)$$

By substituting Eq. (5.14) into Eq. (5.15), the global system of equations reads

$$\begin{bmatrix} \mathbf{K}_{ff} & \mathbf{K}_{fd} \\ \mathbf{K}_{df} & \mathbf{K}_{dd} \end{bmatrix} \left( \begin{bmatrix} \mathbf{I} \\ -\bar{\mathbf{A}} \end{bmatrix} [\mathbf{d}_f] + \begin{bmatrix} \mathbf{0} \\ \bar{\mathbf{d}} \end{bmatrix} \right) = \begin{bmatrix} \mathbf{f}_{ext,f} \\ \mathbf{f}_{ext,d} \end{bmatrix}, \quad (5.16)$$

where  $\mathbf{I}$  is the identity matrix. In order to preserve the symmetric shape of the stiffness matrix, the system of equations is multiplied from the left-hand side by the matrix  $\begin{bmatrix} \mathbf{I} & -\bar{\mathbf{A}}^T \end{bmatrix}$

$$\begin{bmatrix} \mathbf{I} & -\bar{\mathbf{A}}^T \end{bmatrix} \begin{bmatrix} \mathbf{K}_{ff} & \mathbf{K}_{fd} \\ \mathbf{K}_{df} & \mathbf{K}_{dd} \end{bmatrix} \left( \begin{bmatrix} \mathbf{I} \\ -\bar{\mathbf{A}} \end{bmatrix} [\mathbf{d}_f] + \begin{bmatrix} \mathbf{0} \\ \bar{\mathbf{d}} \end{bmatrix} \right) = \begin{bmatrix} \mathbf{I} & -\bar{\mathbf{A}}^T \end{bmatrix} \begin{bmatrix} \mathbf{f}_{ext,f} \\ \mathbf{f}_{ext,d} \end{bmatrix}. \quad (5.17)$$

The final system of equations for the unknown nodal displacement values is given by

$$\begin{aligned} \left( \mathbf{K}_{ff} - \bar{\mathbf{A}}^T \mathbf{K}_{df} - \mathbf{K}_{fd} \bar{\mathbf{A}} + \bar{\mathbf{A}}^T \mathbf{K}_{dd} \bar{\mathbf{A}} \right) \mathbf{d}_f &= \mathbf{f}_{ext,f} - \bar{\mathbf{A}}^T \mathbf{f}_{ext,d} \\ &- \left( \mathbf{K}_{fd} - \bar{\mathbf{A}}^T \mathbf{K}_{dd} \right) \bar{\mathbf{d}}. \end{aligned} \quad (5.18)$$

After having solved Eq. (5.18) for the unknown degrees of freedom  $\mathbf{d}_f$ , the remaining dependent degrees of freedom  $\mathbf{d}_d$  can be determined using Eq. (5.14).

In nonlinear simulations, the equilibrium state of a structure is obtained by applying an iterative solution procedure, cf. Sects. 2.3 and 2.4. Using direct load control or direct displacement control, the global system of equations solved in the  $i$ -th iteration of the  $n$ -th load step can be written as

$$\left. \begin{aligned} \mathbf{f}_{int}^{(n,i)} + \frac{\partial \mathbf{f}_{int}^{(n,i)}}{\partial \mathbf{d}} \Delta \mathbf{d}^{(n,i+1)} &= \mathbf{f}_{ext}^{(n)} \\ \mathbf{d}^{(n,i+1)} &= \mathbf{d}^{(n,i)} + \Delta \mathbf{d}^{(n,i+1)} \end{aligned} \right\} \quad i = 0, 1, 2, \dots \quad (5.19)$$

It is to be noted that the displacements of the last equilibrium state are used as start values for the Newton-Raphson iteration ( $\mathbf{d}^{(n,0)} = \mathbf{d}^{(n-1)}$ ). In each iteration step the constraint equations, given by

$$\underbrace{\mathbf{d}_d^{(n,i)} + \Delta \mathbf{d}_d^{(n,i+1)}}_{\mathbf{d}_d^{(n,i+1)}} = \bar{\mathbf{d}}^{(n)} - \bar{\mathbf{A}} \underbrace{\left( \mathbf{d}_f^{(n,i)} + \Delta \mathbf{d}_f^{(n,i+1)} \right)}_{\mathbf{d}_f^{(n,i+1)}} \quad (5.20)$$

have to be satisfied. By considering that

$$\mathbf{d}_d^{(n,i)} + \bar{\mathbf{A}} \mathbf{d}_f^{(n,i)} = \begin{cases} \bar{\mathbf{d}}^{(n-1)} & i = 0 \\ \bar{\mathbf{d}}^{(n)} & i > 0 \end{cases} \quad (5.21)$$

the constraint equations can be rewritten as

$$\Delta \mathbf{d}_d^{(n,i+1)} = -\bar{\mathbf{A}} \Delta \mathbf{d}_f^{(n,i+1)} + \begin{cases} \bar{\mathbf{d}}^{(n)} - \bar{\mathbf{d}}^{(n-1)} & i = 0 \\ 0 & i > 0 \end{cases}. \quad (5.22)$$

By substituting Eq. (5.22) into the partitioned global system of equations, which is given by

$$\begin{bmatrix} \frac{\partial \mathbf{f}_{int,f}^{(n,i)}}{\partial \mathbf{d}_f} & \frac{\partial \mathbf{f}_{int,f}^{(n,i)}}{\partial \mathbf{d}_d} \\ \frac{\partial \mathbf{f}_{int,d}^{(n,i)}}{\partial \mathbf{d}_f} & \frac{\partial \mathbf{f}_{int,d}^{(n,i)}}{\partial \mathbf{d}_d} \end{bmatrix} \begin{bmatrix} \Delta \mathbf{d}_f^{(n,i+1)} \\ \Delta \mathbf{d}_d^{(n,i+1)} \end{bmatrix} = \begin{bmatrix} \mathbf{f}_{ext,f}^{(n)} \\ \mathbf{f}_{ext,d}^{(n)} \end{bmatrix} - \begin{bmatrix} \mathbf{f}_{int,f}^{(n,i)} \\ \mathbf{f}_{int,d}^{(n,i)} \end{bmatrix}, \quad (5.23)$$

and by multiplying from the left-hand side with matrix  $\begin{bmatrix} \mathbf{I} & -\bar{\mathbf{A}}^T \end{bmatrix}$  the final system of

equations for the unknown (free) nodal degrees of freedom is obtained

$$\begin{aligned} & \left( \frac{\partial \mathbf{f}_{int,f}^{(n,i)}}{\partial \mathbf{d}_f} - \bar{\mathbf{A}}^T \frac{\partial \mathbf{f}_{int,d}^{(n,i)}}{\partial \mathbf{d}_f} - \frac{\partial \mathbf{f}_{int,f}^{(n,i)}}{\partial \mathbf{d}_d} \bar{\mathbf{A}} + \bar{\mathbf{A}}^T \frac{\partial \mathbf{f}_{int,d}^{(n,i)}}{\partial \mathbf{d}_d} \bar{\mathbf{A}} \right) \Delta \mathbf{d}_f^{(n,i+1)} = \mathbf{f}_{ext,f}^{(n)} - \mathbf{f}_{int,f}^{(n,i)} \\ & - \bar{\mathbf{A}}^T \left( \mathbf{f}_{ext,d}^{(n)} - \mathbf{f}_{int,d}^{(n,i)} \right) - \begin{cases} \left( \frac{\partial \mathbf{f}_{int,f}^{(n,i)}}{\partial \mathbf{d}_d} - \bar{\mathbf{A}}^T \frac{\partial \mathbf{f}_{int,d}^{(n,i)}}{\partial \mathbf{d}_d} \right) \left( \bar{\mathbf{d}}^{(n)} - \bar{\mathbf{d}}^{(n-1)} \right) & i = 0 \\ 0 & i > 0 \end{cases}. \end{aligned} \quad (5.24)$$

### 5.3.2 Mortar Method

The mortar method, originally introduced by Bernardi et al. (1994) for the coupling of spectral elements, is a domain decomposition technique, which can be used for the coupling of different physical models, different discretization schemes or non-matching triangulations, Wohlmuth (2001); Lamichhane and Wohlmuth (2004). The general idea of the mortar method is to replace the strong point-wise displacement continuity, Eq. (5.9), at the interface between two adjacent sub-domains by a weak integral condition, Eqs. (5.10) or (5.11). According to Wohlmuth (1999), such a weak displacement continuity condition can be either imposed in terms of constraints on the ansatz space of the displacement approximation, Bernardi et al. (1994), which results in a nonconforming positive definite formulation, or in terms of Lagrange multipliers, Belgacem (1999), which yields a saddle point problem.

In this thesis, the mortar method with Lagrange multipliers is used for the coupling of finite elements, because it allows for a straightforward parallelization in the framework of domain decomposition. For the sake of simplicity, it is assumed that the total domain  $\Omega$  is decomposed into two non-overlapping polygonal sub-domains  $\Omega^M$  and  $\Omega^m$  such that

$$\Omega = \Omega^M \cup \Omega^m. \quad (5.25)$$

Furthermore, both sub-domains share a common edge  $\Gamma^c$  defining the mortar element

$$\Gamma^c = \Omega^M \cap \Omega^m. \quad (5.26)$$

Lagrange multipliers, which are considered as an additional unknown field in the global equilibrium problem, are used on that interface to join the sub-domains. The Lagrange multipliers  $\boldsymbol{\lambda}$  can be interpreted as interface tractions  $\mathbf{t}^M$  and  $\mathbf{t}^m$  acting on the sub-domain boundaries

$$\boldsymbol{\lambda} = -\mathbf{t}^M = \mathbf{t}^m. \quad (5.27)$$

Consequently, the equilibrium state of the problem can be expressed using the principal

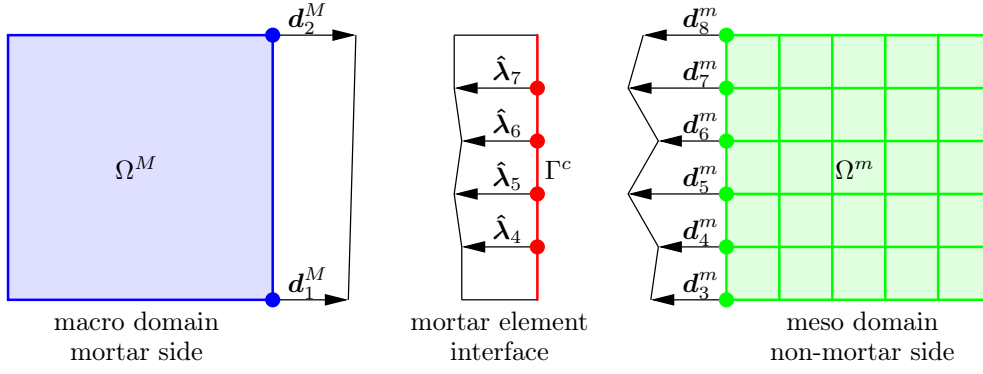


Figure 5.5: Mortar method – finite element discretization and interpolation.

of virtual work, which reads in vector notation

$$\int_{\Omega^M} \sigma_i^M \delta \varepsilon_i^M d\Omega^M + \int_{\Gamma^c} \lambda_i \delta u_i^M d\Gamma^c = \int_{\Omega^M} \bar{b}_i \delta u_i^M d\Omega^M + \int_{\Gamma_t^M} \bar{t}_i \delta u_i^M d\Gamma_t^M \quad (5.28)$$

with  $u_i^M = \bar{u}_i^M$  and  $\delta u_i^M = 0 \quad \forall \mathbf{x} \in \Gamma_u^M$ ,

$$\int_{\Omega^m} \sigma_i^m \delta \varepsilon_i^m d\Omega^m - \int_{\Gamma^c} \lambda_i \delta u_i^m d\Gamma^c = \int_{\Omega^m} \bar{b}_i \delta u_i^m d\Omega^m + \int_{\Gamma_t^m} \bar{t}_i \delta u_i^m d\Gamma_t^m \quad (5.29)$$

with  $u_i^m = \bar{u}_i^m$  and  $\delta u_i^m = 0 \quad \forall \mathbf{x} \in \Gamma_u^m$ ,

$$\int_{\Gamma^c} \delta \lambda_i (u_i^M - u_i^m) d\Gamma^c = 0. \quad (5.30)$$

It is assumed that in Eqs. (5.28) to (5.30) no boundary conditions,  $\bar{\mathbf{t}}$  and  $\bar{\mathbf{u}}$ , are imposed on the common edge

$$\Gamma^c \cap \Gamma_t = \emptyset \quad \Gamma^c \cap \Gamma_u = \emptyset. \quad (5.31)$$

Equations (5.28) and (5.29) must be satisfied for an arbitrary, but kinematically compatible, virtual displacement state  $\delta \mathbf{u}^M, \delta \boldsymbol{\varepsilon}^M$  and  $\delta \mathbf{u}^m, \delta \boldsymbol{\varepsilon}^m$ . The coupling condition, Eq. (5.30), has to be fulfilled for any arbitrary virtual traction state  $\delta \boldsymbol{\lambda}$ .

The equilibrium problem given in Eqs. (5.28) to (5.30) is solved using the finite element method. Figure 5.5 shows the corresponding finite element discretization. In the mortar method, the one-dimensional discretization of the interface is inherited from the finite element mesh of one of the two sub-domains  $\Omega^M$  or  $\Omega^m$ . Assuming that the discretization of  $\Gamma^c$  is derived from  $\Omega^m$ , the side of  $\Gamma^c$  which is associated with  $\Omega^m$  is labeled non-mortar or slave side and the other one is labeled mortar or master side. The displacements in each sub-domain and the Lagrange multipliers on the interface are approximated using standard finite element shape functions  $\mathbf{N}$

$$\mathbf{u}^M = \mathbf{N}^M \mathbf{d}^M \quad \mathbf{u}^m = \mathbf{N}^m \mathbf{d}^m \quad \boldsymbol{\lambda} = \mathbf{N}^\lambda \hat{\boldsymbol{\lambda}}, \quad (5.32)$$

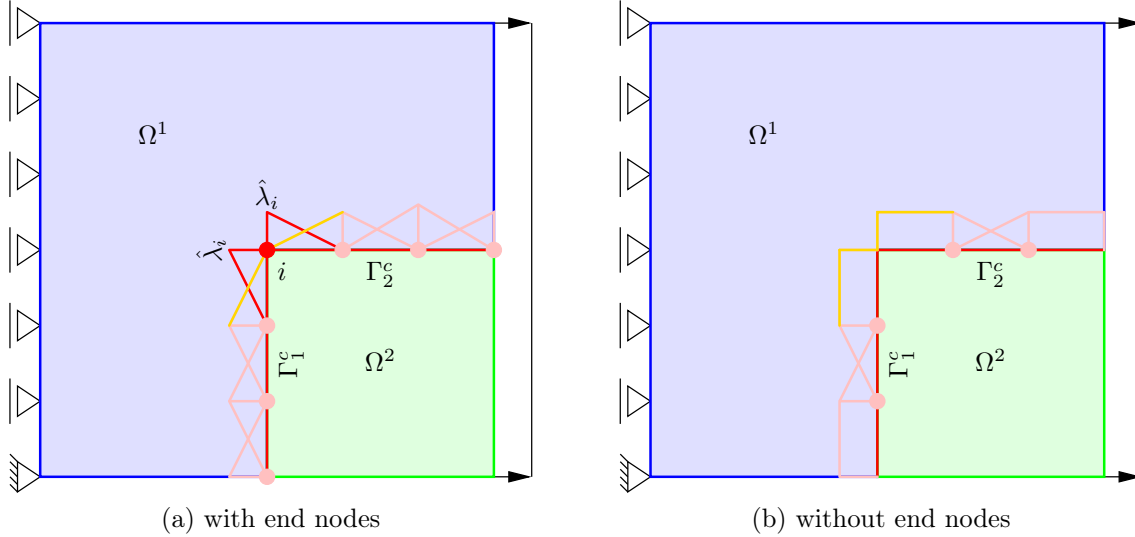


Figure 5.6: Mortar method – discretization of the Lagrange multipliers at the corner between two coupling interfaces.

where  $\mathbf{d}^M$  and  $\mathbf{d}^m$  are nodal displacement values, and  $\hat{\lambda}$  are discrete Lagrange multipliers introduced at the interior nodes of the mortar element, Fig. 5.5. In the presented mortar formulation, the shape functions  $N^\lambda$  in the interior of the mortar element coincide with the shape functions  $N^m$  used for the displacement interpolation on the non-mortar side. Since no support points are located at the ends of the interface, the polynomial order of the approximation of the Lagrange multipliers is reduced by one in the end segments of the mortar element. An overview of mortar methods using alternative approximations for the Lagrange multipliers can be found in Wohlmuth (2001).

As illustrated in Fig. 5.5, no support points for the Lagrange multipliers are located at the ends of the interface. This is due to the fact that the Lagrange multipliers can be interpreted as coupling tractions. At the corner between two interfaces the direction of the tractions might change. If a support point is located at the corner, the tractions cannot be properly represented in both interfaces. This is illustrated in Fig. 5.6 for a specimen which is loaded in such a way that a uniform stress distribution is obtained. The specimen is subdivided into two non-overlapping sub-domains  $\Omega^1$  and  $\Omega^2$ . Matching finite element discretizations are used in both sub-domains. Furthermore, identical material behavior is assumed. In order to couple both sub-domains, Lagrange multipliers are introduced at the interfaces  $\Gamma_1^c$  and  $\Gamma_2^c$ . For the applied loading, the normal tractions should be constant and nonzero in  $\Gamma_1^c$  and the tangential traction should vanish in  $\Gamma_2^c$ . If a support point  $i$  is introduced at the corner between both interfaces, as in Fig. 5.6(a), the horizontal component of the corresponding Lagrange multiplier  $\hat{\lambda}_i$  is used for the approximation of the normal tractions in  $\Gamma_1^c$  and the tangential tractions in  $\Gamma_2^c$ . Consequently, if the normal tractions are nonzero in  $\Gamma_1^c$ , the tangential tractions in  $\Gamma_2^c$  automatically become nonzero. As a result, such a model cannot represent the uniform stress distribution. If no support points are introduced at the ends of both mortar elements, as in Fig. 5.6(b), the correct distribution of the coupling tractions can be obtained and the stress distribution becomes

uniform.

The same approximations as for the displacements and the Lagrange multipliers are used for the virtual displacement fields and the virtual field of Lagrange multipliers

$$\delta \mathbf{u}^M = \mathbf{N}^M \delta \mathbf{d}^M \quad \delta \mathbf{u}^m = \mathbf{N}^m \delta \mathbf{d}^m \quad \delta \boldsymbol{\lambda} = \delta \mathbf{N}^\lambda \delta \hat{\boldsymbol{\lambda}}. \quad (5.33)$$

By substituting the constitutive equations, Eq. (2.13), the kinematic equations, Eq. (2.21), and the approximation of the displacements and the Lagrange multiplier field, Eqs. (5.32) and (5.33), into the principle of virtual work, Eqs. (5.28) to (5.30), and by considering that the principle of virtual work must hold for arbitrary virtual nodal displacement values  $\delta \mathbf{d}^M$ ,  $\delta \mathbf{d}^m$  and arbitrary virtual Lagrange multipliers  $\delta \hat{\boldsymbol{\lambda}}$ , the final system of equations is obtained

$$\begin{bmatrix} \mathbf{K}^M & \mathbf{0} & (\mathbf{m}^M)^T \\ \mathbf{0} & \mathbf{K}^m & (\mathbf{m}^m)^T \\ \mathbf{m}^M & \mathbf{m}^m & \mathbf{0} \end{bmatrix} \begin{bmatrix} \mathbf{d}^M \\ \mathbf{d}^m \\ \hat{\boldsymbol{\lambda}} \end{bmatrix} = \begin{bmatrix} \mathbf{f}_{ext}^M \\ \mathbf{f}_{ext}^m \\ \mathbf{0} \end{bmatrix}, \quad (5.34)$$

where the sub-matrices  $\mathbf{K}^M$  and  $\mathbf{K}^m$  are the standard finite element stiffness matrices of the two sub-domains

$$K_{ij}^M = \int_{\Omega^M} B_{ki}^M C_{kl}^{e,M} B_{lj}^M d\Omega^M, \quad (5.35)$$

$$K_{ij}^m = \int_{\Omega^m} B_{ki}^m C_{kl}^{e,m} B_{lj}^m d\Omega^m, \quad (5.36)$$

the sub-vectors  $\mathbf{f}_{ext}^M$  and  $\mathbf{f}_{ext}^m$  are the corresponding equivalent external force vectors

$$f_{ext,i}^M = \int_{\Omega^M} N_{ki}^M \bar{b}_k d\Omega^M + \int_{\Gamma_t^M} N_{ki}^M \bar{t}_k d\Gamma_t^M, \quad (5.37)$$

$$f_{ext,i}^m = \int_{\Omega^m} N_{ki}^m \bar{b}_k d\Omega^m + \int_{\Gamma_t^m} N_{ki}^m \bar{t}_k d\Gamma_t^m, \quad (5.38)$$

and the sub-matrices  $\mathbf{m}^M$  and  $\mathbf{m}^m$  are the mortar mass matrices

$$m_{ij}^M = + \int_{\Gamma^c} N_{ki}^\lambda N_{kj}^M d\Gamma^c, \quad (5.39)$$

$$m_{ij}^m = - \int_{\Gamma^c} N_{ki}^\lambda N_{kj}^m d\Gamma^c. \quad (5.40)$$

It is to be noted that linear elastic material behavior and small displacements are assumed in the derivation of the global system of equation presented above. However, an extension to nonlinear material formulations based on the assumptions presented in Sect. 2.3 is

straightforward.

The integrals in the computation of the mortar mass matrices, Eqs. (5.39) and (5.40), are evaluated numerically using a Gauss quadrature. For an exact integration, the mortar element is divided into integration cells. The integration cells are defined in such a way that each node associated to one of the three discretizations at the mortar element is an end-point of an integration cell and no nodes are inside an integration cell. Under the assumption of polynomial interpolation functions for the displacements and the Lagrange multipliers, the product of the corresponding shape functions is also a polynomial which can be integrated exactly, if a Gauss quadrature rule with an appropriate number of integration points is applied.

First simulations with the mortar finite element method have shown that the global system of equations, Eq. (5.34), may become ill-conditioned. This is caused by the different physical units of the unknowns. In order to avoid numerical problems during the solution of the global system of equations the conditioning of the corresponding coefficient matrix is improved by a constant scaling of the mortar mass matrices. The preconditioned system of equations is given by

$$\begin{bmatrix} \mathbf{I}_{n^M} & \mathbf{0} & \mathbf{0} \\ \mathbf{0} & \mathbf{I}_{n^m} & \mathbf{0} \\ \mathbf{0} & \mathbf{0} & \mathbf{P}_{n^\lambda} \end{bmatrix} \begin{bmatrix} \mathbf{K}^M & \mathbf{0} & (\mathbf{m}^M)^T \\ \mathbf{0} & \mathbf{K}^m & (\mathbf{m}^m)^T \\ \mathbf{m}^M & \mathbf{m}^m & \mathbf{0} \end{bmatrix} \begin{bmatrix} \mathbf{I}_{n^M} & \mathbf{0} & \mathbf{0} \\ \mathbf{0} & \mathbf{I}_{n^m} & \mathbf{0} \\ \mathbf{0} & \mathbf{0} & \mathbf{P}_{n^\lambda} \end{bmatrix} \begin{bmatrix} \mathbf{d}^M \\ \mathbf{d}^m \\ \bar{\boldsymbol{\lambda}} \end{bmatrix} = \begin{bmatrix} \mathbf{f}_{ext}^M \\ \mathbf{f}_{ext}^m \\ \mathbf{0} \end{bmatrix}, \quad (5.41)$$

where  $\mathbf{I}$  is the identity matrix,  $n^M$ ,  $n^m$  are the dimensions of the sub-matrices  $\mathbf{K}^M$  and  $\mathbf{K}^m$ ,  $n^\lambda$  is the number of unknown Lagrange multipliers,  $\bar{\boldsymbol{\lambda}}$  are the scaled Lagrange multipliers

$$\bar{\boldsymbol{\lambda}} = \mathbf{P}^{-1} \boldsymbol{\lambda}, \quad (5.42)$$

and  $\mathbf{P}$  is a diagonal matrix defined as

$$P_{ii} = \max(|K_{jj}^M|; |K_{kk}^m|) \quad i = 1 \dots n^\lambda, j = 1 \dots n^M, k = 1 \dots n^m. \quad (5.43)$$

In Eq. (5.41), a left and right preconditioning is applied in order to preserve the symmetry properties of the initial system given in Eq. (5.34).

Using the mortar finite element method with Lagrange multipliers, the global system of equations is augmented by additional unknowns. In an alternative mortar approach, proposed by Bernardi et al. (1994), the weak continuity condition, Eq. (5.10), is considered in a similar way as the essential boundary conditions. Consequently, the displacement approximation must satisfy not only the essential boundary conditions but also the weak coupling condition. Using the method of weighted residuals, the corresponding constraint

equations can be written as

$$\int_{\Gamma_c} w_i(\mathbf{x}) (\mathbf{u}^M(\mathbf{x}) - \mathbf{u}^m(\mathbf{x})) \, d\mathbf{x} = \mathbf{0} \quad i = 1 \dots n^w, \quad (5.44)$$

where  $\mathbf{w}$  are arbitrary weight functions, and  $n^w$  is the number of weight functions. In general, the functions  $\mathbf{N}^\lambda$ , which in the first approach are used for the approximation of the Lagrange multipliers, are chosen as weight functions. Substituting the displacement approximation, Eq. (5.32), into Eq. (5.44), the continuity condition can be written in terms of the unknown nodal displacement values  $\mathbf{d}^M$  and  $\mathbf{d}^m$

$$m_{ij}^M d_j^M + m_{ik}^m d_k^m = 0 \quad i = 1 \dots n^w, j = 1 \dots n^M, k = 1 \dots n^m, \quad (5.45)$$

where the coefficient matrices  $\mathbf{m}^M$  and  $\mathbf{m}^m$  are the standard mortar mass matrices given by Eqs. (5.39) and (5.40). The imposition of such constraint equations, which results in a reduction of the global system of equations by the number of constraints, is already discussed in Sect. 5.3.1.

In this thesis, the mortar finite element method is used for the coupling of sub-domains which resolve the material on different length-scales. Consequently, the average mesh size in one sub-domain is significantly smaller than the other one. As a result, the coupling converges either to a displacement compatibility, if the discretization of the Lagrange multipliers is obtained from the mesoscale sub-domain with a fine mesh, or a compatibility of tractions, if the discretization of the Lagrange multipliers is inherited from the macroscale sub-domain with a coarse mesh. In general, the mortar finite element method is used to ensure continuity of tractions, since displacement continuity can directly be realized using constraint equations, which are presented in Sect. 5.3.1.

### 5.3.3 Arlequin Method

In the previous sections, coupling methods for non-overlapping sub-domains are introduced. In contrast to these methods, the Arlequin approach, proposed by Ben Dhia (1998, 1999); Rateau (2003); Ben Dhia and Rateau (2004a,b); Ben Dhia (2005), allows for a superposition of different mechanical and numerical models. As shown in Fig. 5.7(b), the total domain  $\Omega$  is partitioned into two overlapping sub-domains  $\Omega^M$  and  $\Omega^m$ . The gluing zone  $\Omega^c$  is defined as the intersection between both sub-domains. According to Ben Dhia (1999), the general idea of the Arlequin method is to double in  $\Omega^c$  the number of mechanical states and to distribute the energies between the two states. In general, Lagrange multipliers, which can be interpreted as gluing tractions, are introduced to realize a weak and compatible gluing of both states in  $\Omega^c$ . As an alternative, the penalty approach can be used to couple both states, cf. Ben Dhia (1999) and Ben Dhia (2005). Using the principle of virtual work and assuming that the coupling constraint is given by Eq. (5.11) the



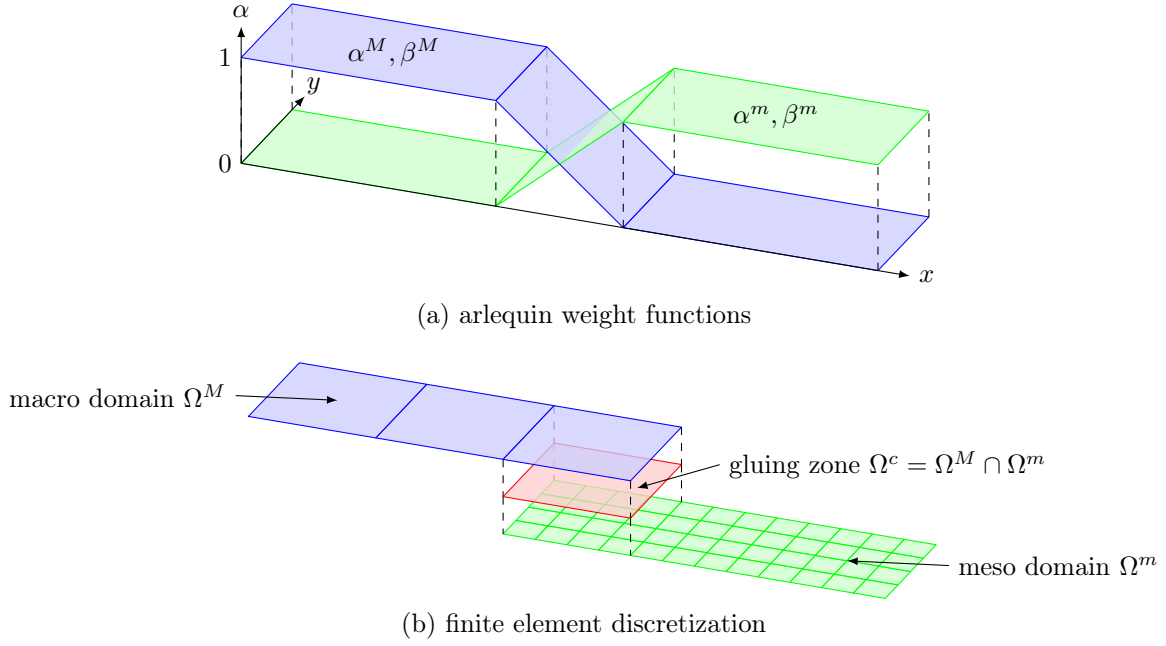


Figure 5.7: General idea of the arlequin method.

equilibrium state of the Arlequin problem with Lagrange multipliers can be expressed as

$$\int_{\Omega^M} \alpha^M \sigma_i^M \delta \varepsilon_i^M d\Omega^M + \int_{\Omega^c} \lambda_i \delta u_i^M d\Omega^c = \int_{\Omega^M} \beta^M \bar{b}_i \delta u_i^M d\Omega^M + \int_{\Gamma_t^M} \beta^M \bar{t}_i \delta u_i^M d\Gamma_t^M \quad (5.46)$$

with  $u_i^M = \bar{u}_i^M$  and  $\delta u_i^M = 0 \quad \forall \mathbf{x} \in \Gamma_u^M,$

$$\int_{\Omega^m} \alpha^m \sigma_i^m \delta \varepsilon_i^m d\Omega^m - \int_{\Omega^c} \lambda_i \delta u_i^m d\Omega^c = \int_{\Omega^m} \beta^m \bar{b}_i \delta u_i^m d\Omega^m + \int_{\Gamma_t^m} \beta^m \bar{t}_i \delta u_i^m d\Gamma_t^m \quad (5.47)$$

with  $u_i^m = \bar{u}_i^m$  and  $\delta u_i^m = 0 \quad \forall \mathbf{x} \in \Gamma_u^m,$

$$\int_{\Omega^c} \delta \lambda_i (u_i^M - u_i^m) d\Omega^c = 0, \quad (5.48)$$

where  $\delta \mathbf{u}^M, \delta \boldsymbol{\varepsilon}^M$  and  $\delta \mathbf{u}^m, \delta \boldsymbol{\varepsilon}^m$  denote any arbitrary but kinematically compatible virtual displacement state, and  $\delta \boldsymbol{\lambda}$  is an arbitrary virtual traction state. In order to prevent that the energy of the total domain is considered twice in the gluing zone, special Arlequin weight functions  $\alpha^m, \alpha^M$  and  $\beta^m, \beta^M$  are introduced to balance the internal and external virtual works associated to each sub-domain. As shown in Fig. 5.7(a), each pair of weight functions form a partition of unity on the total domain

$$\alpha^M(\mathbf{x}) = \beta^M(\mathbf{x}) = 1 \quad \alpha^m(\mathbf{x}) = \beta^m(\mathbf{x}) = 0 \quad \forall \mathbf{x} \in \Omega^M \setminus \Omega^c \quad (5.49)$$

$$\alpha^M(\mathbf{x}) = \beta^M(\mathbf{x}) = 0 \quad \alpha^m(\mathbf{x}) = \beta^m(\mathbf{x}) = 1 \quad \forall \mathbf{x} \in \Omega^m \setminus \Omega^c \quad (5.50)$$

$$\alpha^M(\mathbf{x}) + \alpha^m(\mathbf{x}) = 1 \quad \beta^M(\mathbf{x}) + \beta^m(\mathbf{x}) = 1 \quad \forall \mathbf{x} \in \Omega^c = \Omega^M \cap \Omega^m. \quad (5.51)$$

In general, positive piecewise continuous functions are used as Arlequin weight functions. A comparison of different weight functions is presented in the next paragraph for a one-dimensional example.

The finite element method is used to solve the equilibrium problem given in Eqs. (5.46) to (5.48). Thus, the unknown displacements  $\mathbf{u}^M$ ,  $\mathbf{u}^m$  and Lagrange multipliers  $\boldsymbol{\lambda}$  are discretized and the interpolation of these fields and the corresponding virtual fields are given by Eqs. (5.32) and (5.33). It is to be noted that in contrast to the mortar method also the boundary nodes of the gluing zone are used as support points for the interpolation of the Lagrange multipliers. Assuming linear elastic material behavior and small strains the discretized constitutive and kinematic equations are given by Eqs. (2.13) and (2.21). By substituting Eqs. (2.13), (2.21), (5.32) and (5.33) into Eqs. (5.46) to (5.48) and by considering that the principle of virtual work must hold for arbitrary nodal displacement values  $\delta \mathbf{d}^M$ ,  $\delta \mathbf{d}^m$  and arbitrary virtual Lagrange multipliers  $\delta \boldsymbol{\lambda}$ , the discrete formulation of the Arlequin problem can be obtained

$$\begin{bmatrix} \mathbf{K}^M & \mathbf{0} & (\mathbf{c}^M)^T \\ \mathbf{0} & \mathbf{K}^m & (\mathbf{c}^m)^T \\ \mathbf{c}^M & \mathbf{c}^m & \mathbf{0} \end{bmatrix} \begin{bmatrix} \mathbf{d}^M \\ \mathbf{d}^m \\ \hat{\boldsymbol{\lambda}} \end{bmatrix} = \begin{bmatrix} \mathbf{f}_{ext}^M \\ \mathbf{f}_{ext}^m \\ \mathbf{0} \end{bmatrix}, \quad (5.52)$$

where the sub-matrices  $\mathbf{K}^M$  and  $\mathbf{K}^m$  are the standard finite element stiffness matrices scaled by the Arlequin weight functions  $\alpha^M$ ,  $\alpha^m$  of the two sub-domains

$$K_{ij}^M = \int_{\Omega^M} \alpha^M B_{ki}^M C_{kl}^{e,M} B_{lj}^M d\Omega^M, \quad (5.53)$$

$$K_{ij}^m = \int_{\Omega^m} \alpha^m B_{ki}^m C_{kl}^{e,m} B_{lj}^m d\Omega^m, \quad (5.54)$$

the sub-vectors  $\mathbf{f}_{ext}^M$  and  $\mathbf{f}_{ext}^m$  are the corresponding equivalent external force vectors which are weighted by the functions  $\beta^M$  and  $\beta^m$ , respectively

$$f_{ext,i}^M = \int_{\Omega^M} \beta^M N_{ki}^M \bar{b}_k d\Omega^M + \int_{\Gamma_t^M} \beta^M N_{ki}^M \bar{t}_k d\Gamma_t^M, \quad (5.55)$$

$$f_{ext,i}^m = \int_{\Omega^m} \beta^m N_{ki}^m \bar{b}_k d\Omega^m + \int_{\Gamma_t^m} \beta^m N_{ki}^m \bar{t}_k d\Gamma_t^m, \quad (5.56)$$

and the sub-matrices  $\mathbf{c}^M$  and  $\mathbf{c}^m$  are the coupling matrices

$$c_{ij}^M = + \int_{\Omega^c} N_{ki}^\lambda N_{kj}^M d\Omega^c, \quad (5.57)$$

$$c_{ij}^m = - \int_{\Omega^c} N_{ki}^\lambda N_{kj}^m d\Omega^c. \quad (5.58)$$

In order to improve the conditioning of the global system of equations a scaling of the coupling matrices and the Lagrange multipliers is performed as proposed for the mortar method in Eqs. (5.41) to (5.43).

In the literature, Ben Dhia and Rateau (2004a); Hu et al. (2008), the coupling presented in Eq. (5.48) is labeled  $L^2$ -norm or  $L^2$ -coupling, respectively. In general, an alternative coupling strategy based on the  $H^1$ -norm is used in the Arlequin method, cf. Ben Dhia and Rateau (2004a). The corresponding weak form of that coupling constraint is given by

$$\int_{\Omega^c} \delta \lambda_i (u_i^M - u_i^m) + \ell^2 \varepsilon_{kl}(\boldsymbol{\delta \lambda}) \varepsilon_{kl}(\mathbf{u}^M - \mathbf{u}^m) d\Omega^c = 0, \quad (5.59)$$

where  $\boldsymbol{\varepsilon}$  is given by the kinematic equation, Eq. (2.2), and  $\ell$  is a strictly positive parameter homogeneous to a length. By substituting Eqs. (5.32) and (5.33) into Eq. (5.59) the coupling matrices  $\mathbf{c}^M$  and  $\mathbf{c}^m$  of the discrete form are obtained

$$c_{ij}^M = + \int_{\Omega^c} N_{ki}^\lambda N_{kj}^M + \ell^2 P_l B_{li}^\lambda B_{lj}^M d\Omega^c, \quad (5.60)$$

$$c_{ij}^m = - \int_{\Omega^c} N_{ki}^\lambda N_{kj}^m + \ell^2 P_l B_{li}^\lambda B_{lj}^m d\Omega^c, \quad (5.61)$$

where  $\mathbf{B}$  is the well known strain-displacement matrix defined by Eq. (2.22). The vector

$$P^T = \begin{bmatrix} 1 & 1 & 1 & \frac{1}{2} & \frac{1}{2} & \frac{1}{2} \end{bmatrix} \quad (5.62)$$

is introduced due to the vector notation of the strain-like quantities in Eqs. (5.60) and (5.61). Both coupling strategies,  $H^1$ -coupling and  $L^2$ -coupling, are investigated in the following paragraph.

In general, the Arlequin method allows for the coupling of sub-models with different spatial dimensions, Hu et al. (2008), or the intermixing of different mechanical models as for example particle models and continuum models, Bauman et al. (2008). In this thesis, the Arlequin method is used for the coupling of sub-domains with the same spatial dimension but different resolution of the internal material structure. Furthermore, it is assumed that all sub-domains are discretized by finite elements and that the Lagrange multipliers are established on the macroscale sub-domains. Consequently, the finite element mesh of the gluing zone is inherited from the coarse mesh of the macroscale sub-domain and the same finite element interpolation is used in this region for the Lagrange multipliers and the macroscale displacements.

### One-dimensional Example

In this paragraph, the Arlequin method is applied to a one-dimensional mechanical problem. In this example, the influence of the coupling strategy –  $L^2$ -coupling or  $H^1$ -coupling

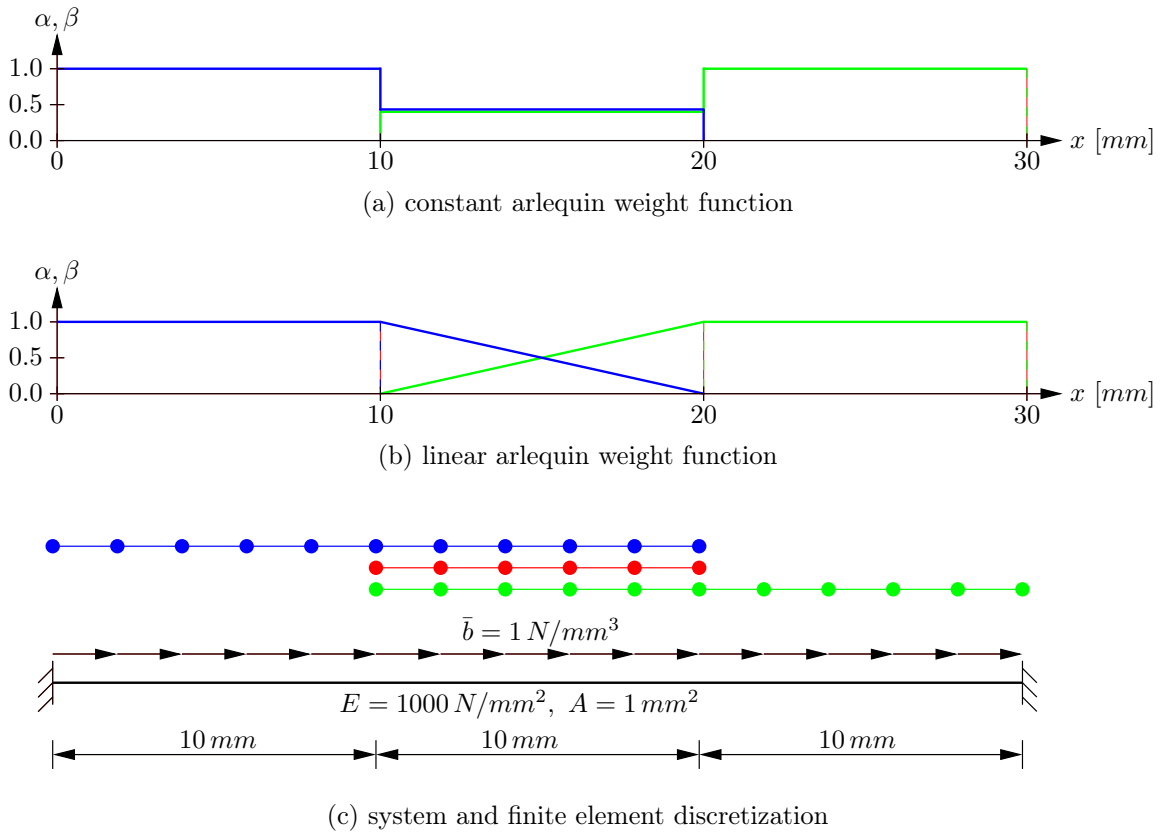


Figure 5.8: One-dimensional bar with different Arlequin weight functions.

– and the Arlequin weight functions is investigated. As shown in Fig. 5.8(c), a bar of constant cross-section is fixed at both ends and a constant body force is imposed. The corresponding Arlequin model consists of two overlapping sub-domains with equally fine finite element meshes with element size  $h_e$ . Furthermore, the gluing zone coincides with the overlap of both sub-domains. Inside this gluing zone, either constant, Fig. 5.8(a), or linear, Fig. 5.8(b), weight functions  $\alpha$  and  $\beta$  are applied. As shown in the diagrams in Fig. 5.9, neither the coupling strategy nor the Arlequin weight function have an influence on the horizontal displacements. In all simulations the same nodal displacement values are obtained. In contrast to the displacements, the Lagrange multipliers plotted in the diagrams in Fig. 5.10 depend on the coupling method and the Arlequin weight function. As already shown in Ben Dhia and Rateau (2004a) for a similar example, numerical singularities which vary with the element size can be observed at both ends of the gluing zone if  $L^2$ -coupling and constant weight functions are applied. These singularities are caused by the sudden change of the sub-domain stiffness inside the gluing zone. The application of an  $H^1$ -coupling with  $\ell = 1 \text{ mm}$  leads, for a constant weight function, to a smooth field of Lagrange multipliers. As for the  $L^2$ -coupling, the Lagrange multipliers deviate from the exact solution at both ends of the gluing zone. Assuming a sufficiently fine finite element discretization, these deviations do not depend on the finite element size. The application of linear weight functions result in a continuous blending from one sub-domain to the other. This leads for both coupling strategies to a linear distribution of the Lagrange multipliers which almost coincides with the exact solution. It is to be noted that the influence of

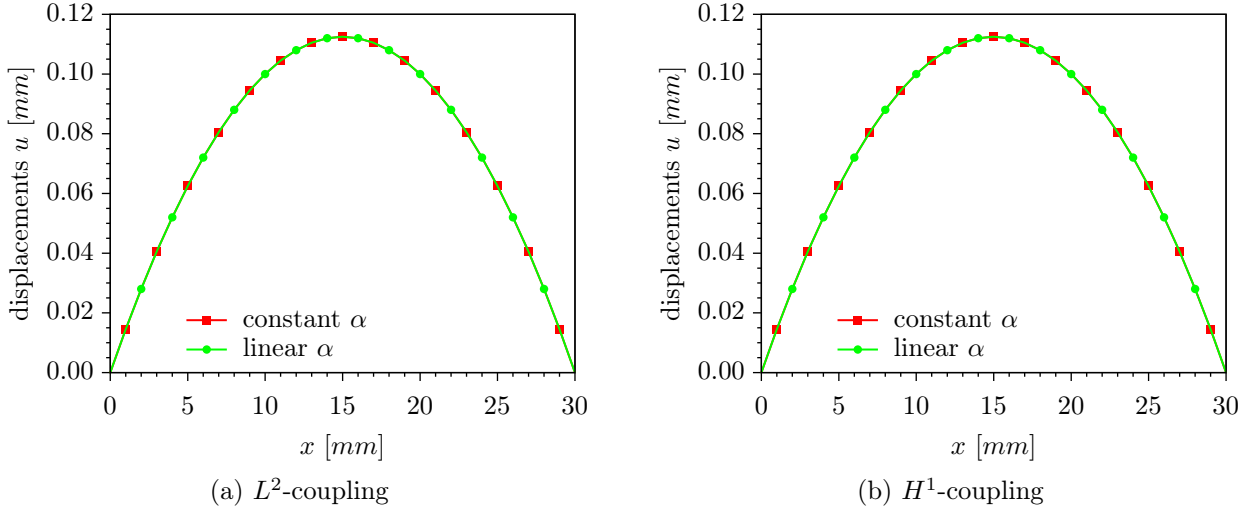


Figure 5.9: Horizontal displacements in the one-dimensional bar with element size  $h_e = 1 \text{ mm}$ .

the parameter  $\ell$  in the  $H^1$  coupling is not further investigated in this work. However, the definition of the  $H^1$ -coupling, Eq. (5.59), implies that by setting the parameter  $\ell$  smaller than one the  $H^1$ -coupling converges to a  $L^2$ -coupling. For values larger than one, the clear physical meaning of the Lagrange multipliers as coupling tractions is lost, since the first term of Eq. (5.59) becomes negligible if  $\ell \gg 1 \text{ mm}$  and the Lagrange multipliers are not constant.

In addition to the numerical singularities observed for an  $L^2$ -coupling with constant weight functions, Ben Dhia and Rateau (2004a) criticize that for an  $L^2$ -coupling the conditioning of the global system of equations, Eq. (5.52), increases for a decreasing element size by  $1/h_e^4$ , whereas for an  $H^1$ -coupling the condition number is increasing by  $1/h_e^2$ , which is

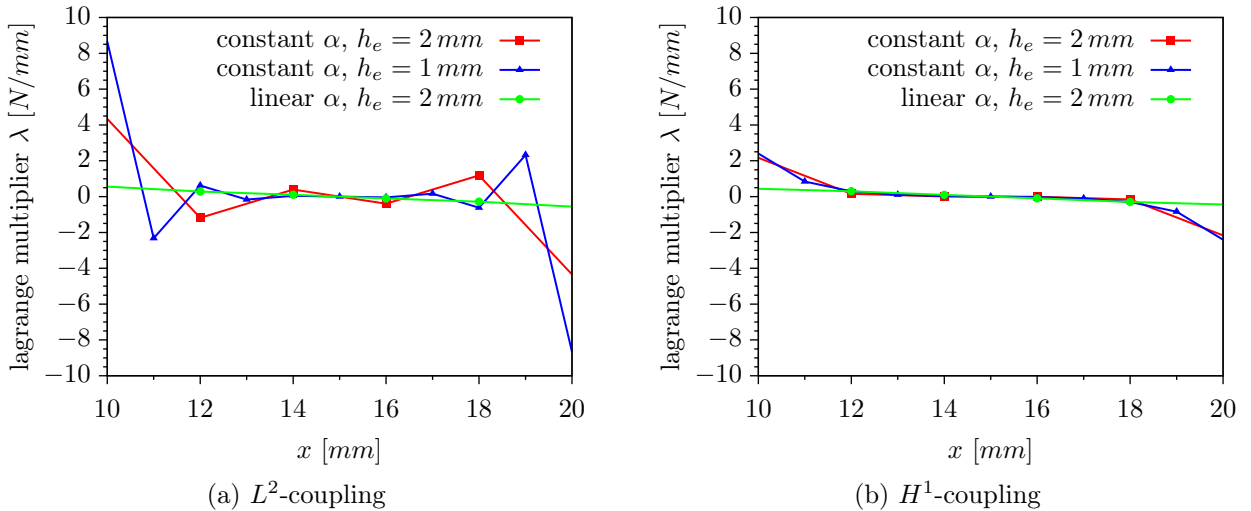


Figure 5.10: Lagrange multipliers inside the gluing zone of the one-dimensional bar.

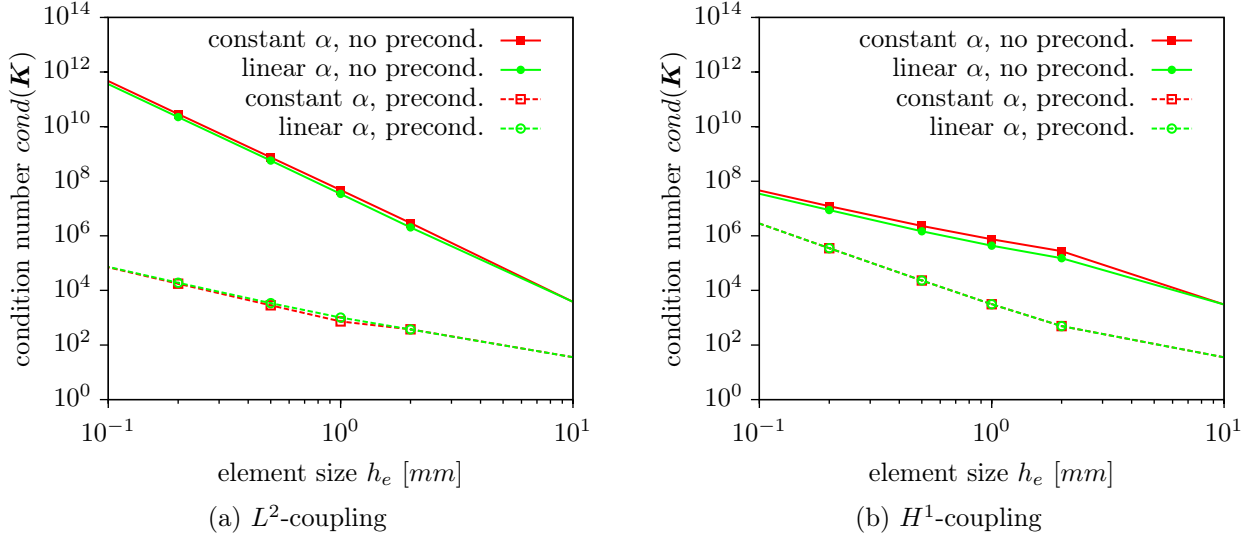


Figure 5.11: Conditioning of the global stiffness matrix for the one-dimensional bar.

usual for finite element matrices. The condition number of a matrix is defined as

$$\text{cond}(\mathbf{K}) = \|\mathbf{K}\|_{\infty} \|\mathbf{K}^{-1}\|_{\infty} \quad (5.63)$$

where  $\|\dots\|_{\infty}$  denotes the infinity norm of a matrix

$$\|\mathbf{A}\|_{\infty} = \max_{i=1,\dots,r} \sum_{j=1}^c |A_{ij}|, \quad (5.64)$$

where  $r$  is the number of rows and  $c$  the number of columns of the matrix. As shown in the diagrams in Fig. 5.11, the same correlation between condition number and element size is observed for this example. Furthermore, the plots illustrate that for both coupling strategies the condition number is almost independent from the Arlequin weight functions. The scaling of the coupling matrices and the Lagrange multipliers, proposed in this thesis for preconditioning of the global system of equations, leads for an  $L^2$ -coupling to a significant improvement of the conditioning. As a result, the condition number increases for a decreasing element size by  $1/h_e^{1.6}$ . If the  $H^1$ -coupling is applied, the improvement of the conditioning due to the proposed preconditioning is not as pronounced as for the  $L^2$ -coupling.

## Numerical Integration

In the numerical implementation of the Arlequin method, the integrals in Eqs. (5.53) to (5.58) are evaluated numerically using Gauss quadrature. As shown in Fig. 5.12, the gluing zone is partitioned into triangular integration cells. In a first step, the geometric intersection of the finite element meshes of both sub-domains is determined, Fig. 5.12(a). In a second step, the result of this intersection is triangulated Fig. 5.12(b). The integration is performed over these triangular integration cells. Assuming that the displacements and

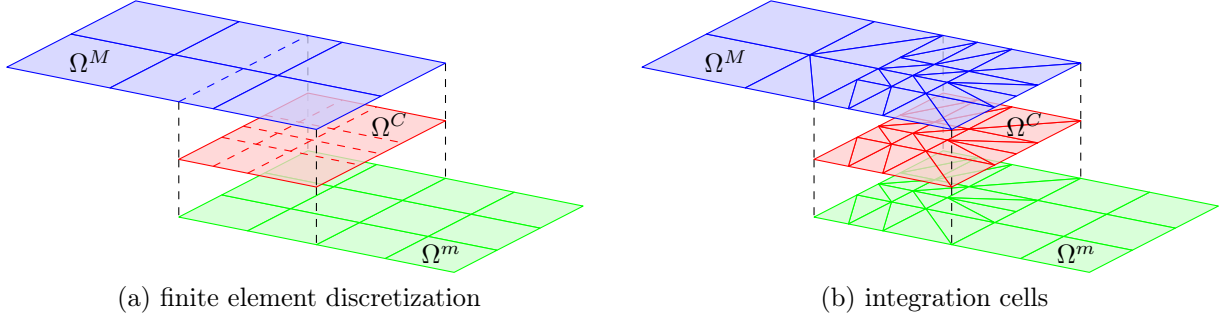


Figure 5.12: Arlequin method – numerical integration.

Lagrange multipliers are approximated by polynomials, the proposed integration procedure allows for an exact integration of the coupling matrices, given in Eqs. (5.57) and (5.58) or Eqs. (5.60) and (5.61), if Gauss quadrature rules with an appropriate number of integration points are applied. The integration cells are also used in finite elements which are associated to the gluing zone for the computation of the stiffness matrices and the equivalent external force vectors. It is to be noted that for non-constant Arlequin weight functions higher order integration rules are required for finite elements inside the gluing zone.

### Weight Function

The one-dimensional example presented above has illustrated that linear Arlequin weight functions allow for a continuous blending between the sub-domains. As a result, numerical singularities, which are observed at the end of the gluing zone for an  $L^2$ -coupling with constant weight functions, can be avoided. In general, the definition of such continuous weight functions in two- or three-dimensional models is not straightforward. In this thesis, the Arlequin weight function inside the gluing zone is represented as level set function describing the normalized shortest distance of point  $P$  to the sub-domain boundaries, Fig. 5.13. As a result, the Arlequin weight functions of the mesoscale sub-domain can be written as

$$\alpha^m(\mathbf{x}_P) = \frac{\Delta x_P^m}{\Delta x_P^M + \Delta x_P^m} \quad \forall \mathbf{x}_P \in \Omega^c, \quad (5.65)$$

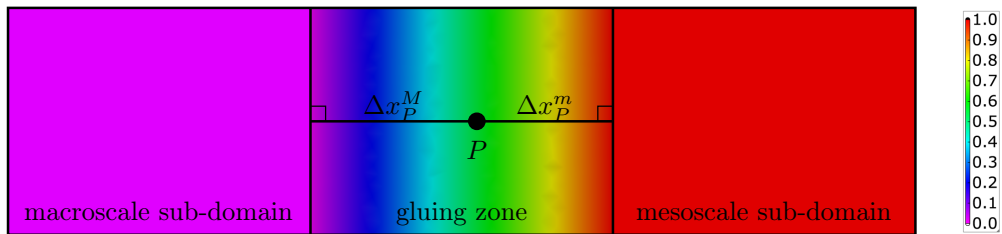


Figure 5.13: Arlequin weight function of the slave side as level set function.

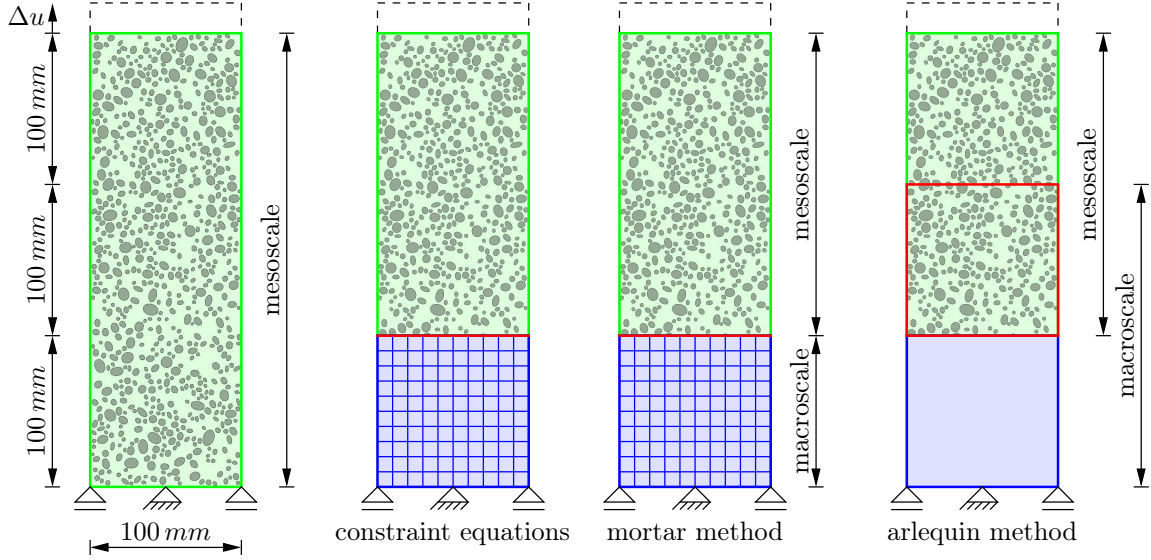


Figure 5.14: Coupling example – uniaxial tension test using mesoscale and heterogeneous multiscale models with different coupling methods (geometry, material structure and boundary conditions).

where  $\mathbf{x}_P$  is the coordinate of point  $P$ , and  $\Delta x_P^M$  and  $\Delta x_P^m$  are the shortest distances of the point to the corresponding sub-domain boundaries. It is to be noted that only those boundaries are considered for the calculation of the level set value which are not boundaries of the total domain. For numerical efficiency, Eq. (5.65) is only evaluated at the corner vertices of the triangular integration cells. Inside the integration cell, the interpolation of the level set function is given by

$$\alpha^m(\mathbf{x}) = \sum_{i=1}^3 N^{(i)}(\mathbf{x}) \hat{\alpha}^{m(i)} \quad \forall \mathbf{x} \in \Omega_c, \quad (5.66)$$

where  $\hat{\alpha}$  are the level set values evaluated at the integration cell vertices, and  $N$  are the corresponding standard linear finite element shape functions. As a result, the Arlequin weight functions in each integration cell are linear. This approach allows for an exact integration of the element contributions, such as the element stiffness matrices, inside the gluing zone if an appropriate numerical integration scheme such as a Gauss-quadrature rule is applied. Another advantage of this approach is that by using the same integration cells on both sides of the gluing zone, the Arlequin weight functions automatically satisfy the partition of unity.

### 5.3.4 Example

In this section, the application of the coupling strategies, presented in Sects. 5.3.1 to 5.3.3, to heterogeneous multiscale models of concrete is investigated. Linear elastic simulations of a concrete specimen under uniaxial tension are performed using heterogeneous multiscale models and, for comparison, a full mesoscale model. The different models with their



Table 5.1: Coupling example – material parameters of the concrete specimen.

constituent	material parameter			
concrete	Young's modulus	$E_c$	$[N/mm^2]$	22 000
	Poisson's ratio	$\nu_c$	[-]	0.20
mortar matrix	Young's modulus	$E_m$	$[N/mm^2]$	20 000
	Poisson's ratio	$\nu_m$	[-]	0.18
aggregates	Young's modulus	$E_a$	$[N/mm^2]$	30 000
	Poisson's ratio	$\nu_a$	[-]	0.20

geometrical dimensions are summarized in Fig. 5.14. The specimen is fixed at the bottom and a uniform vertical displacement  $\Delta u = 0.1 \text{ mm}$  is applied at the top. In the macroscale sub-domain, concrete is considered as a homogeneous isotropic material. A two phase model consisting of aggregates and mortar matrix is applied in the mesoscale sub-domain. All material parameters are summarized in Table 5.1. The concrete mixture parameters are given in Table 4.8. In the two-dimensional models only aggregates with diameter greater than  $2 \text{ mm}$  are considered. As a result, the area fraction of the aggregates is 28%. It is to be noted that the aggregate distribution is identical in all simulations. The mesoscale part of the models is always discretized with triangular finite elements with an average size of  $0.75 \text{ mm}$ . In multiscale models with non-overlapping sub-domains, the mesh size on the macroscale is  $10 \text{ mm}$ . Elements with an edge length of  $100 \text{ mm}$  are used for the macroscale sub-domain in the Arlequin method. Consequently, in all simulations the average element size in the mesoscale sub-domain is significantly smaller than in the macroscale sub-domain. In simulations with the mortar method or the Arlequin method, the coupling condition is realized by Lagrange multipliers which are established on the coarse mesh of the macroscale sub-domain. The coupling in the Arlequin model is realized by the standard  $L^2$ -norm. Inside the gluing zone, the sub-domains are scaled by linear Arlequin weight functions.

Figure 5.15 shows the vertical stress distribution observed for the different models. The plots illustrate that with all models a similar structural response is obtained. In the multiscale models the stress on the macroscale sub-domain corresponds in an average way to the mesoscale stress. Differences in the stress distributions of the four models, especially in the mesoscale sub-domains, are recognizable in the vicinity of the coupling. The mesoscale stresses in this region are shown in detail in Fig. 5.16. In these plots, the red line indicates the coupling boundary. In the multiscale model with constraint equations, a direct displacement coupling between both sub-domains is realized. Consequently, the boundary displacements of the sub-domains are mainly defined by the coarse displacement approximation of the sub-domain on the macroscale. This leads in the mesoscale sub-domain to small stress concentrations at the coupling boundary if aggregates are located in the direct vicinity of that boundary or if aggregates are crossed by that boundary. In non-linear simulations, these stress concentrations might result in an artificial initiation of damage or to a spurious localization of damage at the boundary. Compared to the mesoscale simulation, higher stress values are, in general, observed in finite elements in the direct vicinity of the boundary. The influence of the strong coupling condition becomes negligible in finite elements with a distance of about twice the maximum aggregate diameter from the

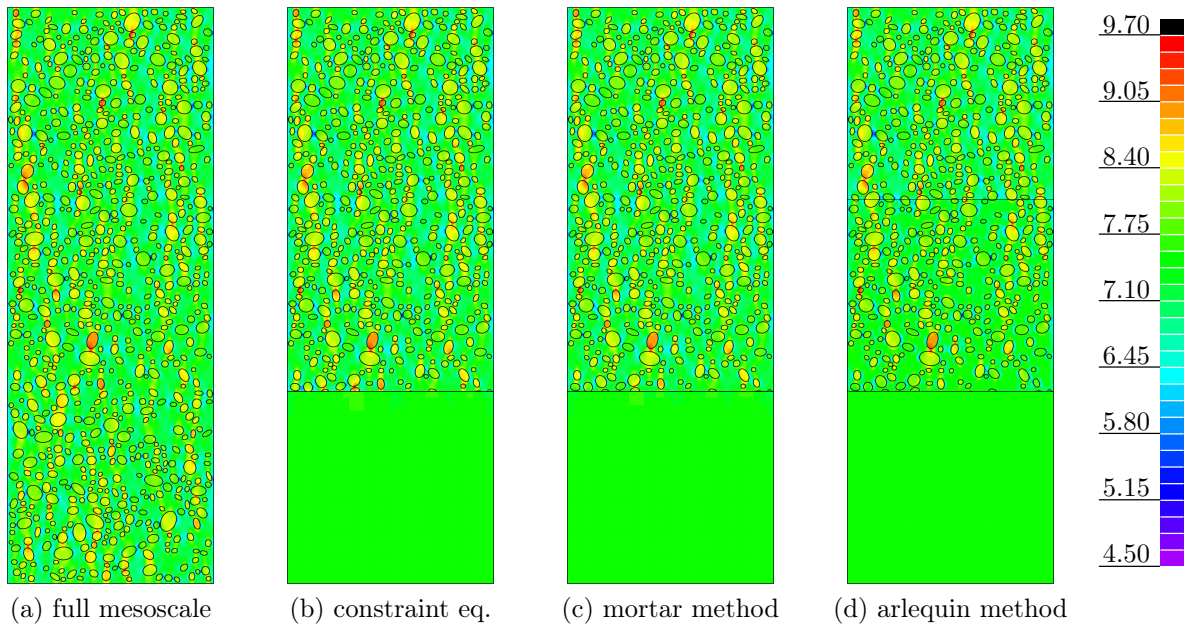


Figure 5.15: Coupling example – vertical stress.

coupling boundary. In multiscale simulations with the mortar method and the Arlequin method, a weak coupling is realized. Since the Lagrange multipliers are introduced on the coarse mesh, the coupling converges to traction continuity. As a result, lower stress values are observed near the coupling boundary compared to the mesoscale model. In the

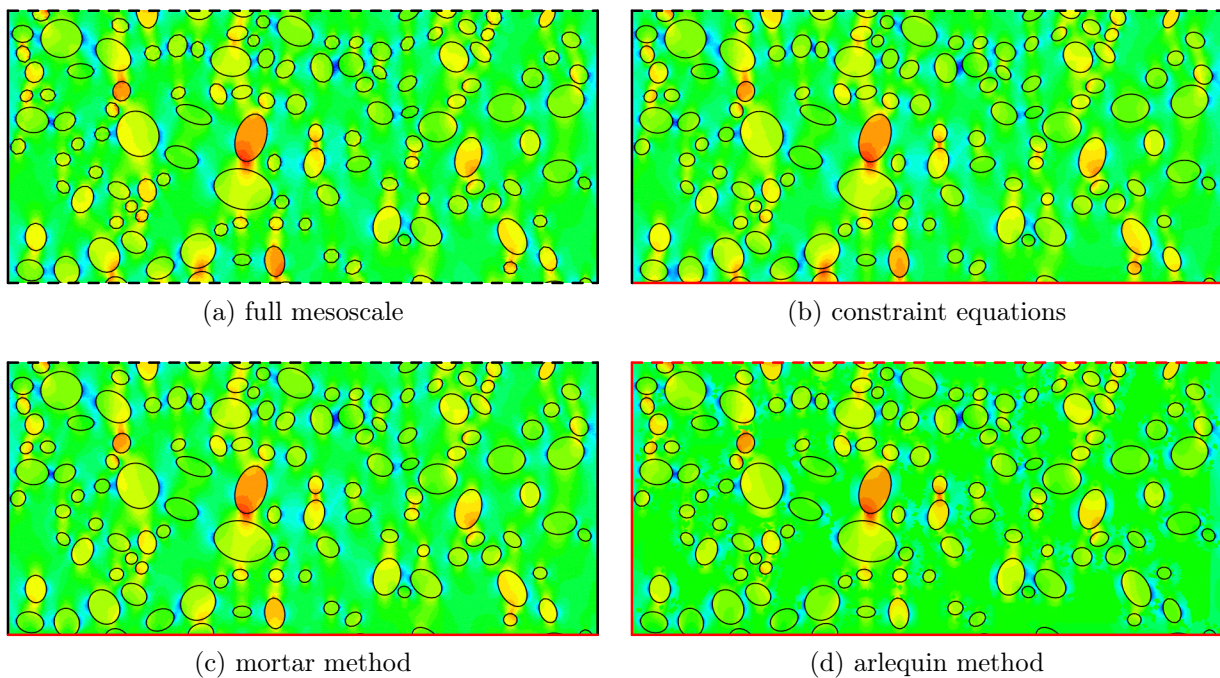


Figure 5.16: Coupling example – vertical stress, detail coupling zone.

Table 5.2: Coupling example – computing times.

	constraint equations	mortar method	Arlequin method
number of unknowns	364 325	364 619	363 765
coupling	0.002 s	0.057 s	1272.662 s
stiffness matrix	2.351 s	2.363 s	2641.723 s
solving	7.677 s	7.727 s	10.607 s

simulation with the mortar method, the width of the region which is influenced by the coupling is approximately twice the maximum aggregate diameter, which is similar to the value observed for the coupling with constraint equations. Using the Arlequin method, the specimen is partitioned into overlapping sub-domains. Consequently, the domain which is influenced by the coupling is considerably larger than by multiscale models with non-overlapping sub-domains. Furthermore, it is observed that outside the gluing zone the differences compared to the mesoscale simulation are negligible.

The numerical effort for the different coupling methods is illustrated in Table 5.2, which shows the computing time for the application of the coupling (the time required for the determination of the coefficients of the constraint equations, or the time required for the generation of the integration cells in the mortar method and the arlequin method), for the building of the global stiffness matrix and for solving the global system of equations. The simulation with constraint equations is marginally faster than the simulation with the mortar method. In the Arlequin model, already the application of the coupling takes significantly longer as for the multiscale models with non-overlapping sub-domains. This is due to the generation of the triangular integration cells in the gluing zone which involves the expensive computation of the intersection of each mesoscale element with the macroscale elements. Since in all three finite element discretizations which are associated to the gluing zone the numerical integration is performed over the triangular integration cells and due to the evaluation of the Arlequin weight function for each integration point, the numerical effort for building the global stiffness matrix also increases significantly. In all simulations, the number of unknowns is roughly the same. Compared to the mortar method, the computational time for solving the global system of equations increases for the Arlequin method due to the large bandwidth of the coupling sub-matrices.

The same example is used to investigate the influence of the finite element discretization of the macroscale sub-domain in multiscale models with the Arlequin method. It is to be noted that inside the gluing zone the finite element mesh of the macroscale sub-domain coincides with the discretization of the Lagrange multipliers. In the first simulation, already presented above, the element size is  $100\text{ mm}$  which is approximately  $12 d_{max}$ , where  $d_{max}$  is the diameter of the largest aggregate. Thus, the gluing zone is discretized with only one element. In the second simulation, the number of macroscale elements inside the gluing zone is increased to 16, leading to elements with  $25\text{ mm}$  edge length. As a result, the ratio between element edge length and maximum aggregate diameter is reduced to approximately 3.

The results of both simulations are summarized in Fig. 5.17. In these plots, the vertical Lagrange multiplier and the vertical stress are shown for elements associated to the gluing

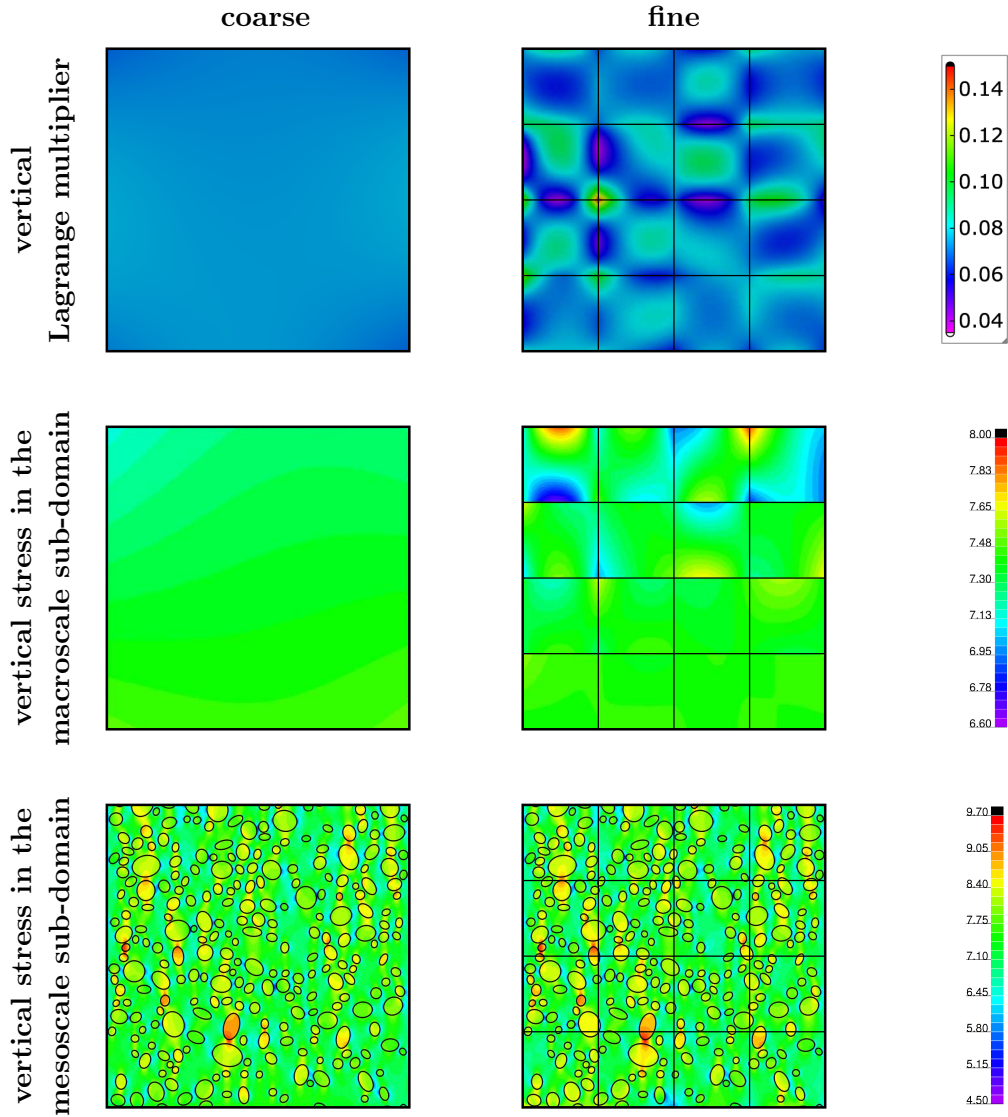


Figure 5.17: Coupling example – influence of macro domain discretization in the arlequin method.

zone. Using only one element, an almost constant distribution of the vertical Lagrange multiplier and the vertical macroscale stress is obtained, which corresponds to the applied boundary conditions. In the simulation with the refined macroscale mesh, spurious oscillations in the vertical Lagrange multiplier can be observed. Furthermore, the vertical stress in the macroscale sub-domain becomes discontinuous. Differences in the stress distributions of both simulations are particularly prominent in regions in which the corresponding Arlequin weight function becomes small.

In the Arlequin method, the coupling leads to a homogenization of the mesoscale stresses in the gluing zone. Since the discretization of the Lagrange multipliers is inherited from the macroscale sub-domain, the homogenization is constraint by the polynomial order of the Lagrange multiplier interpolation. The averaging is performed over all mesoscale elements associated to one macroscale element. As a consequence, a minimum macroscale

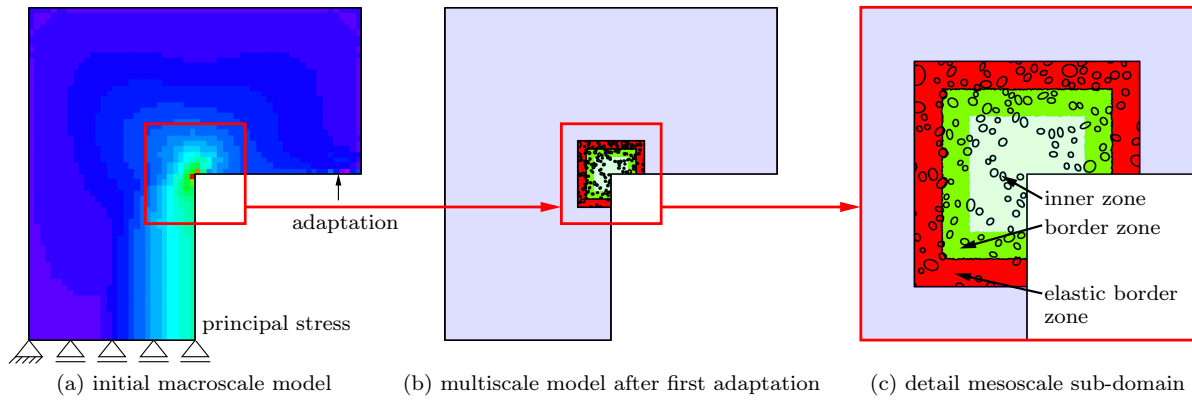


Figure 5.18: Heterogeneous multiscale model – generation of the initial mesoscale sub-domain.

element size, which depends on the maximum aggregate diameter, is required to represent the entire mesoscale material structure. In the first simulation, the macroscale element is large enough so that the associated mesoscale sub-domain is representative. As a result, the homogenized stress is not influenced by the actual spatial aggregate distribution. In accordance with the boundary conditions, an almost constant distribution of the Lagrange multiplier and the macroscale stress is obtained. In the second simulation, the averaging domain becomes too small. As a result, the homogenized stress depends on the position of individual aggregates. This leads to the oscillations in the Lagrange multiplier and a discontinuous macroscopic stress field.

Due to the high numerical effort and the dependency of the macroscale element size on the maximum aggregate diameter, the Arlequin method is not further investigated in this thesis. In the following sections, it is assumed that the total domain is partitioned into non-overlapping sub-domains. The coupling is either realized with constraint equations or with the mortar method.

## 5.4 Model Adaptation from Macro- to Mesoscale

In the heterogeneous multiscale approach, nonlinear material behavior is only considered on the mesoscale. Since, in general, the final damage distribution is not known in advance, an adaptation of the multiscale model becomes necessary during the simulation. In this section, indicators are introduced which trigger the conversion of sub-domains from the macro- to the mesoscale. Consequently, the adaptation results either in the creation of a new mesoscale sub-domain, as shown in Fig. 5.18 or in an enlargement of an existing mesoscale sub-domain, as illustrated in Fig. 5.19.

The first step of a simulation with a heterogeneous multiscale model is the generation of the internal material structure, as for example the size distribution and the spatial distribution of the aggregates. The simulation starts with a macroscale model of the entire structure. As in standard nonlinear simulations an incremental solution strategy as proposed in Sect. 2.4 is applied. In general, an update of the history variables is performed after the solution has converged. A slightly modified update procedure is required in simulations with the

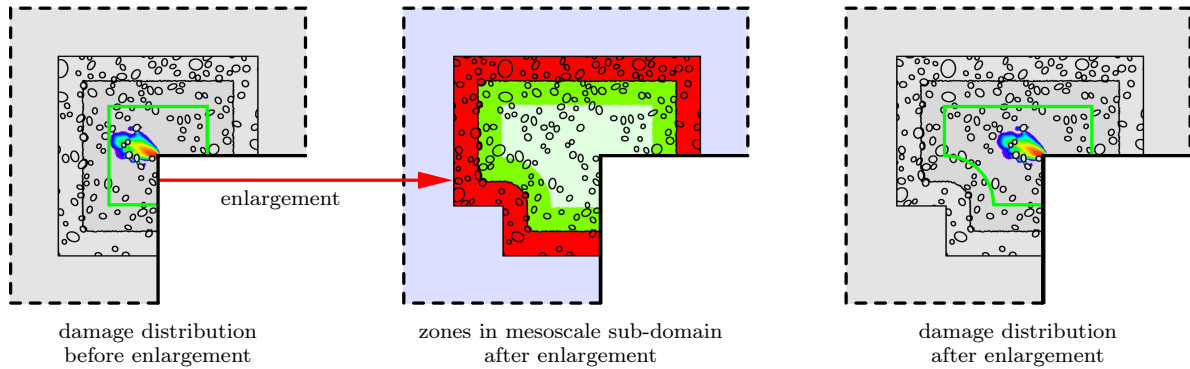


Figure 5.19: Heterogeneous multiscale model – enlargement of the mesoscale sub-domain.

adaptive heterogeneous multiscale model. In a first step of the update procedure, the criteria for model adaptation are tested. If no adaptation is required, the history variables are updated and the iterative solution procedure is continued with the next load increment. In the case of model adaptation, either new mesoscale sub-domains are created or existing mesoscale sub-domains are enlarged and the equilibrium state is again determined for the last converged load step. Consequently, multiple equilibrium states, each associated to one numerical model, may exist for one load-increment.

In the presented approach, linear elastic material behavior is assumed for sub-domains on the macroscale. On this scale the stress distribution is used as an indicator for a model adaptation. If in at least one integration point the principal stress exceeds a certain limit, the numerical model is adapted. As illustrated in Fig. 5.18, the integration point with the largest principal stress value is selected and macroscale elements in the vicinity of that point are replaced by a mesoscale sub-domain. On the mesoscale, the initiation of damage near a coupling boundary indicates a model adaptation. As shown in Fig. 5.18(c), the mesoscale sub-domain is subdivided into three zones. Non-linear material behavior is only considered in the inner and the border zone, whereas linear elastic material behavior is assumed in elements associated to the elastic border zone. In order to avoid that the damage distribution in the inner zone is artificially influenced by boundary effects, the total width of both zones is at least  $5 d_{max}$ , where  $d_{max}$  is the maximum diameter of the aggregates considered in the numerical model. If damage initiates in the border zone or if damage develops into this zone the corresponding mesoscale sub-domain is adapted. As illustrated in Fig. 5.19, the sub-domain is enlarged into the direction of damage evolution. It is to be noted that in the damage plots of Fig. 5.19 the green line indicates the boundary of the inner zone. Assuming that the nonlinear behavior is described by the isotropic damage model, presented in Sect. 3.3, the evolution of the scalar damage parameter  $\omega$  can be used as indicator for model adaptation. If in at least one integration point of elements associated to the border zone the damage parameter becomes nonzero, a model adaptation is performed. A more general indicator is based on the inelastic energy density  $u_{inel}$ , which can be defined by Eq. (A.18) independently from the material formulation. Consequently, the model is adapted if inelastic energy is dissipated in the border zone of a mesoscale sub-domain.

Depending on the coupling between adjacent sub-domains, a third zone, in Fig. 5.18(c)

indicated by the red color, is considered in mesoscale sub-domains. If a weak coupling is realized with the mortar method, this zone is not required. The linear border zone is only introduced if a strong displacement coupling between the sub-domains is applied. As shown in Sect. 5.3.4, the application of constraint equations may result in small stress concentrations in the direct vicinity of the coupling boundary. In order to prevent spurious damage initiation due to these stress concentrations, which would lead to a further enlargement of the mesoscale sub-domain, linear elastic material behavior is assumed for finite elements within a distance of twice the maximum aggregate diameter. These elements build the elastic border zone. As a consequence of this approach, the stresses in the elastic border zone may exceed the material strength. Due to the small size of this domain, the influence of this overestimation of the material strength on the nonlinear structural response of the entire specimen can be neglected. An advantage of the presented approach is that the mesoscale model is not artificially modified near coupling boundaries. As shown in Fig. 5.19, such an approach allows for aggregates which are cut by the coupling boundary. An alternative approach to avoid the initiation of spurious damage due to the coupling with constraint equations is presented in Eckardt and Könke (2008). A minimum distance between coupling boundary and aggregates is introduced, leading to a layer of mortar matrix elements at the boundary. If the width of this element layer is large enough, spurious stress concentrations near the boundary can be avoided. As a consequence, nonlinear material models can also be used in the direct vicinity of a coupling boundary. A drawback of this approach is that due to the omission of certain aggregates, an artificial wall effect is introduced into the mesoscale model at coupling boundaries, leading to a modified structural response in this region.

The adaptation process starts if, after convergence of the iterative solution procedure, a certain criterion in an integration point is satisfied. In order to obtain a representative sample of the internal material structure, the region to be refined on the mesoscale is defined by a rectangle with a minimum edge length of  $15 d_{max}$ . The center point of this rectangle is the integration point under consideration. In a first step, all macroscale elements in the vicinity of this point are determined. A macroscale element is selected for adaptation, if at least one element node is inside that rectangle. In the next step, the outer boundary of the element patch, which is the result of this selection procedure, is calculated and the intersection between this boundary and the boundaries of existing mesoscale sub-domains is determined. If no common boundary segments are found, a new mesoscale sub-domain is generated. Otherwise, the corresponding existing mesoscale sub-domains are enlarged. This may also lead to a unification of mesoscale sub-domains. In order to improve the mesh quality in sub-domains which are enlarged, all mesoscale elements within a distance of  $2 d_{max}$  from common boundary segments are additionally selected for adaptation. Consequently, the outer boundary of the new element patch, which includes now macroscale and mesoscale elements, is determined. This boundary describes the macroscopic geometry of the domain of adaptation. In a next step, the corresponding internal material structure is determined. After that, the geometry is discretized by finite elements using the finite element mesh generator Gmsh, Geuzaine and Remacle (2009). All elements which are previously selected for adaptation are replaced by the new finite element mesh. In order to obtain a first prediction for the displacement field in the adapted domain, a linear elastic analysis is performed for the new finite element mesh. Therefore,

the displacements calculated for the last converged load increment are imposed on the boundary of this element patch. In the presented approach, it is assumed that before an adaptation is performed, the material in the corresponding domain is still in the elastic range. As a result, no further transfer of history variables between both element meshes is required. As a last step of the adaptation process, the coupling between the sub-domains is established and the new equilibrium state of the modified numerical model is calculated for the last converged load increment. If the iterative solution procedure diverges, the model is unloaded and the equilibrium state is determined for a reduced load level. It is to be noted that the adaptation procedure is always performed for only one integration point. In general, the integration point with the largest principal stress value on the macroscale or with the highest inelastic energy density on the mesoscale is chosen. Afterwards, the new equilibrium state is computed and the adaptation criteria are tested again.

In the presented approach, the stress distribution on the macroscale and the damage evolution in mesoscale sub-domains are applied as indicators for model adaptation. Consequently, local stress concentrations on the macroscale and a localization of damage on the mesoscale are required for an effective application of the proposed adaptive heterogeneous multiscale approach. Assuming a constant stress field on the macroscale, which is, for example, observed in macroscale simulations of uniaxial tension tests, the adaptation procedure would result in a mesoscale model of the entire structure. In such a case, localization of damage is only triggered by the internal material structure on the mesoscale. In order to capture this phenomenon, the simulation has to start on the mesoscale.

## 5.5 Model Adaptation from Meso- to Macroscale

In this section, several ideas for a further improvement of the adaptation procedure are outlined. It is to be noted that the algorithms proposed in this section are neither implemented nor tested for their application to heterogeneous multiscale models.

The post-peak behavior of concrete is characterized by the coalescence of microcracks, leading to the formation of macroscopic large cracks and to a spatial localization of damage. Simultaneously, an elastic unloading is observed in regions adjacent to these cracks. As shown in Sect. 4.4.1, these phenomena can be represented with mesoscale models. The main advantage of mesoscale models is that the numerical model is capable to describe changes in the internal material structure, such as the evolution of microcracks. Due to the, in general, high numerical effort of mesoscale simulations, such an approach is only reasonable if microstructural changes actually occur. In concrete, the final opening of a (stress-free) crack or the elastic unloading of a certain region is, in general, not accompanied by a further evolution of microcracks in that region. Consequently, both phenomena can be described with sufficient accuracy by macroscale models. This allows for a further reduction of the numerical effort in simulations with heterogeneous multiscale models.

In an additional adaptation procedure, mesoscale sub-domains in which the evolution of microcracks has stopped can be transferred back to the macroscale. The inelastic energy



dissipation on the mesoscale can be applied as indicator for model adaptation. If no inelastic energy is dissipated in a certain region, the model adaptation from meso- to macroscale is performed for this region. In order to account for the microcracks on the mesoscale, a numerical homogenization procedure, as proposed by Hashin (1983), can be applied to calculate the effective linear elastic material matrix on the macroscale. Depending on the spatial distribution of the microcracks, the macroscopic material behavior may become anisotropic. The major problem of such an approach is to determine the size of the region over which the averaging is performed. On the macroscale, the region of localized damage can be considered by a discrete crack approach. Consequently, the crack is represented either as additional geometrical boundary of the macroscale finite element mesh, or by an extended finite element approach, Belytschko and Black (1999); Moës et al. (1999), which allows to describe the crack independently from the underlying finite element mesh. It is to be noted that the definition of the macroscopic crack path based on the damage distribution on the mesoscale may become difficult.

As an alternative approach, sub-structuring techniques, Noor et al. (1978), can be used to reduce the number of degrees of freedom in mesoscale sub-domains. Elements in which the evolution of microcracks has stopped are merged together to a super-element. Using static condensation, Wilson (1974), the nodal degrees of freedom inside a super-element are expressed in terms of the nodal degrees of freedom on the boundary of that super-element. Consequently, the behavior of the elements inside the super-element are represented by the condensed stiffness matrix. Based on the displacement state for which the static condensation has been performed a linear elastic behavior is assumed for the super-element. This implies the assumption that the elements inside the super-element are either in the elastic regime or in a linear unloading/reloading situation. The advantage of such a procedure is that no modification of the corresponding mesoscale sub-domain, such as remeshing, is required and that no homogenization procedure has to be performed. Furthermore, the mesoscale solution inside a super-element can be computed in a straightforward way if the boundary displacements are known. This allows to verify if the assumption of linear material behavior inside the super-element is still satisfied.

A model adaptation in a heterogeneous multiscale approach from mesoscale sub-domains back to the macroscale has the potential to significantly reduce the numerical effort in such simulations. As a result, only those parts of the model with evolving micro-cracks would be resolved on the mesoscale.

## 5.6 Examples

### 5.6.1 L-shaped Panel

The first example illustrates the application of the adaptive heterogeneous multiscale approach to the nonlinear analysis of an L-shaped panel. The specimen was designed and experimentally tested by Winkler (2001) at the University of Innsbruck. Figure 5.20(a) shows the specimen geometry and the test setup. Furthermore, the experimental scatter

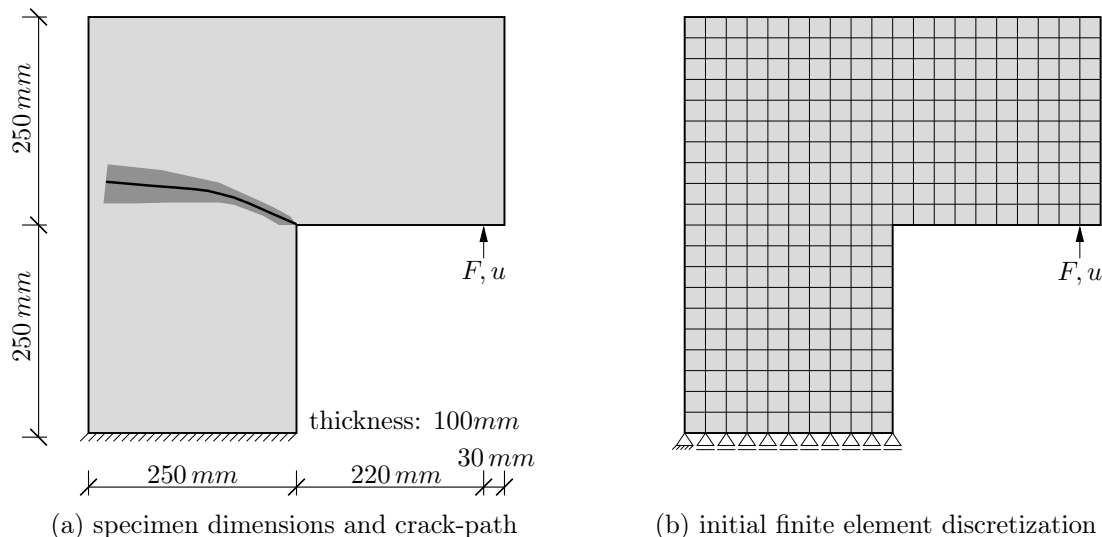


Figure 5.20: L-shaped panel.

of the crack paths which were observed in the experiments of three identical specimens is plotted.

Figure 5.20(b) shows the initial macroscale finite element model and the applied boundary conditions. The specimen is regularly discretized with 9-node quadrilateral elements assuming an average element size of approximately  $25\text{ mm}$ . As a result, the initial finite element model consists of 300 elements, 1 200 nodes and 2 540 active degrees of freedom, respectively. On the macroscale, linear elastic material behavior is assumed.

Nonlinear material behavior is considered in mesoscale sub-domains, which are successively generated and adapted during the simulation. On the mesoscale, a three-phase model consisting of aggregates, mortar matrix and interfacial transition zone (ITZ) is considered. Based on the mixture parameters, given in Table 5.3, aggregates with a nominal diameter between  $2\text{ mm}$  and  $8\text{ mm}$  are generated in the entire specimen. In mesoscale sub-domains, the aggregates and the mortar matrix are discretized by 6-node triangular elements, assuming an average element size of  $0.5\text{ mm}$ . Furthermore, the ITZ is represented by zero-thickness interface elements which are introduced between aggregates and

Table 5.3: L-shaped panel – concrete mixture parameters.

	mass [ $kg/1\text{ m}^3$ ]	density [ $kg/m^3$ ]	volume [ $m^3$ ]
cement	340	3100	0.110
water	180	1000	0.180
air voids (estimated)			0.020
aggregates 0/2	1316	2720	0.483
aggregates 2/4	470	2720	0.172
aggregates 4/8	94	2720	0.035
concrete	2400	2400	1.000

Table 5.4: L-shaped panel – material parameters.

concrete	Young's modulus	$E_c$	$[N/mm^2]$	20 000
	Poisson's ratio	$\nu_c$	$[-]$	0.18
mortar matrix	Young's modulus	$E_m$	$[N/mm^2]$	18 500
	Poisson's ratio	$\nu_m$	$[-]$	0.18
	tensile strength	$f_{t,m}$	$[N/mm^2]$	2.60
	fracture energy	$G_{f,m}$	$[Nmm/mm^2]$	0.14
	nonlocal radius	$R$	$[mm]$	0.75
aggregates	Young's modulus	$E_a$	$[N/mm^2]$	37 000
	Poisson's ratio	$\nu_a$	$[-]$	0.18
ITZ	penalty stiffness	$K_p$	$[N/mm^3]$	500 000
	tensile strength	$f_{t,i}$	$[N/mm^2]$	1.30
	fracture energy	$G_{f,i}$	$[Nmm/mm^2]$	0.07
	weight factor	$\alpha$	$[-]$	1.00

mortar matrix. The nonlinear behavior of the mortar matrix is described by the isotropic damage model, Sect. 3.3, with nonlocal averaging of the total strains, Sect. 3.2.2. Furthermore, linear elastic behavior is assumed for the aggregates. The specific behavior of the ITZ is represented by the cohesive zone model presented in Sect. 3.6. In Table 5.4 the corresponding material parameters are summarized. These parameters are determined in an iterative procedure, such that the numerical simulation gives a good approximation of the experimental load-displacement curve, shown in Fig. 5.21(a). It is to be noted that the Young's moduli of aggregates and mortar matrix are determined from the macroscopic Young's modulus of concrete, using the Reuss bound, given by Eq. (4.21), and taking into account the actual area fraction of the aggregates in the total specimen.

In the presented numerical simulations, a mesoscale sub-domain is created if in at least one point of the macroscale sub-domain the maximum principal stress exceeds the tensile strength of the mortar matrix. The size of the domain, which is transferred to the mesoscale, is defined by a square with an edge length of  $23d_{max} = 184\text{ mm}$ . An edge length larger than the minimum value ( $15d_{max}$ ) has been chosen in order to avoid a frequent adaptation of the model. An existing mesoscale sub-domain is enlarged, if in the boundary part of this sub-domain the damage parameter of the isotropic damage model becomes in at least one point nonzero. The border part of a mesoscale sub-domain comprises all elements with a distance smaller than  $6d_{max} = 48\text{ mm}$  from a coupling boundary. It is to be noted that, in order to reduce the numerical effort, in the presented simulations the opening of the interface elements, describing the failure of the ITZ, is not considered as adaptation criterion. Consequently, it is assumed that the initial opening of the interface cracks does not significantly influence the response of the specimen. The reduction of the stress limit on the macroscale sub-domain to the tensile strength of the ITZ and the application of an additional criterion based on the equivalent interface opening and its corresponding elastic limit to the border part of the mesoscale sub-domain is straightforward, but the size of the mesoscale sub-domains and, as a consequence, the numerical effort would considerably be increased.

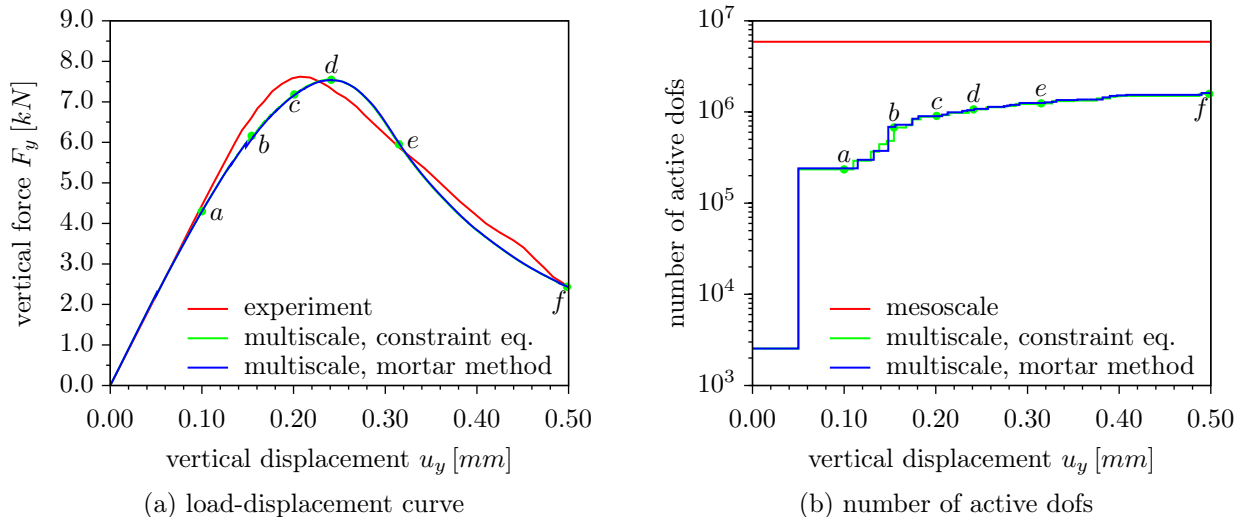


Figure 5.21: L-shaped panel – load-displacement curve and number of active dofs as function the applied displacement.

In a first simulation, the coupling between the sub-domains is realized with constraint equations. In order to avoid spurious damage initiation on the mesoscale due the strong coupling condition, linear elastic material behavior is assumed for all elements within a distance of  $3d_{max} = 24 \text{ mm}$  from the coupling boundary. In a second simulation, the mortar method is applied. Since the Lagrange multipliers are established on the coarse mesh of the macroscale sub-domain, a weak coupling, enforcing continuity of tractions, between adjacent sub-domains is obtained. As a consequence, nonlinear material formulations can be used in all elements of the mesoscale sub-domains. It is to be noted that in both simulations the same aggregate configuration is considered. In order to capture the global softening behavior of the specimen, direct displacement control is applied.

Figure 5.21(a) shows the relationship between the load and the vertical displacement at the point of load application. In both simulations, an almost identical load-displacement curve is obtained. Compared to the experimental curve, a more pronounced pre-peak branch is observed. As a consequence, the displacements corresponding to the peak load is about 7% larger than in the experiments. The differences between numerical solution and experimental results can probably be ascribed to the simplified boundary and loading conditions assumed in the numerical simulations. Furthermore, small jumps can be noticed in the load-displacement curves observed in the numerical simulations. These jumps can be attributed to the adaptation criteria. On the macroscale, a new mesoscale model is created if the maximum principal stress exceeds the tensile strength of the mortar matrix. Afterwards, the new equilibrium state is determined for the last converged load level. Due to the heterogeneous material structure of concrete, stress concentrations with higher stress values as on the macroscale are observed in the mortar matrix of the mesoscale sub-domain. Furthermore, the tensile strength of the ITZ is considerably smaller than the tensile strength of the mortar matrix. As a result, damage is, in general, already developing in the newly created mesoscale sub-domain. Immediately before the adaptation is performed, the stiffness of the specimen is, in general, slightly overestimated. Using

direct displacement control, the load decreases for a constant displacement value at the point of load application. Furthermore, the amount of inelastic energy dissipated during the simulation is slightly increased. The same holds for the enlargement of an existing mesoscale sub-domain. Since, the adaptation procedure is triggered by the initiation of damage in the mortar matrix, interface cracks might already develop in those parts of the model which are currently transferred to the mesoscale. As a result, the global stiffness of the specimen slightly decreases after model adaptation. It is to be noted that this effect is observed for both coupling methods.

Figure 5.21(b) shows the number of active degrees of freedoms as a function of the applied vertical displacement. Note that a logarithmic scaling is used for the active dofs. In both simulations, the curves are almost identical. Small differences between the models can be attributed to varying step lengths in the iterative solution procedure which are the result of the automatic step size adaptation. The staircase characteristic of the curve is a result of the applied adaptation procedure. For a given load-level different numerical models exist and, as a consequence, different equilibrium states exist. Furthermore, the plot shows the increasing numerical effort due to the successive enlargement of mesoscale sub-domains during the simulation. Compared to a full mesoscale model, the number of unknowns is significantly reduced by the adaptive heterogeneous multiscale approach. In the multiscale model, the area of the sub-domains which are simulated on the mesoscale is about 18 % of the total specimen area at the peak point and approximately 27 % at the final stage.

The successive adaptation of the model during the simulation is illustrated in Fig. 5.22, which shows the damage distribution at selected load levels for the model with constraint equations. The individual load levels are also indicated in the load-displacement curve, Fig. 5.21(a), by the labels *a* to *f*. As shown in Fig. 5.22(a), the initial mesoscale sub-domain is created at the corner of the specimen at about 57 % of the ultimate load. Furthermore, an initial damage zone is observed at this corner. Until the ultimate load is reached, the mesoscale sub-domain is successively enlarged towards the lower specimen boundary, Figs. 5.22(b) to 5.22(d). The initial damage zone propagates into the specimen and minor damage zones initiate in the lower part of the specimen. After having reached the ultimate load, the development of these minor damage zones stops. Only the initial damage zone further develops and a macroscopic crack is formed. As a consequence, the upper part of the mesoscale sub-domain is enlarged towards the left specimen boundary, Figs. 5.22(d) to 5.22(f). The damage plots illustrate that, with the criteria proposed in this thesis, the model adaptation is only performed in those parts of the specimen in which damage actually develops.

Figure 5.23 shows for both multiscale models the final damage distribution. As in the experiments, a curved macroscopic crack is observed in the simulations. The influence of the internal material structure on the final crack pattern is clearly visible. Adjacent to the macroscopic crack, several smaller cracks can be distinguished. Furthermore, a branching of the macroscopic crack is observed. It is to be noted that the width of the fracture process zone is, due to the influence of the material heterogeneity, considerably larger than the nonlocal radius assumed for the mortar matrix, which is in contrast to a nonlinear analysis on the macroscale. In both simulations, an identical damage distribution is obtained. Consequently, the damage distribution is not artificially influenced by the different coupling

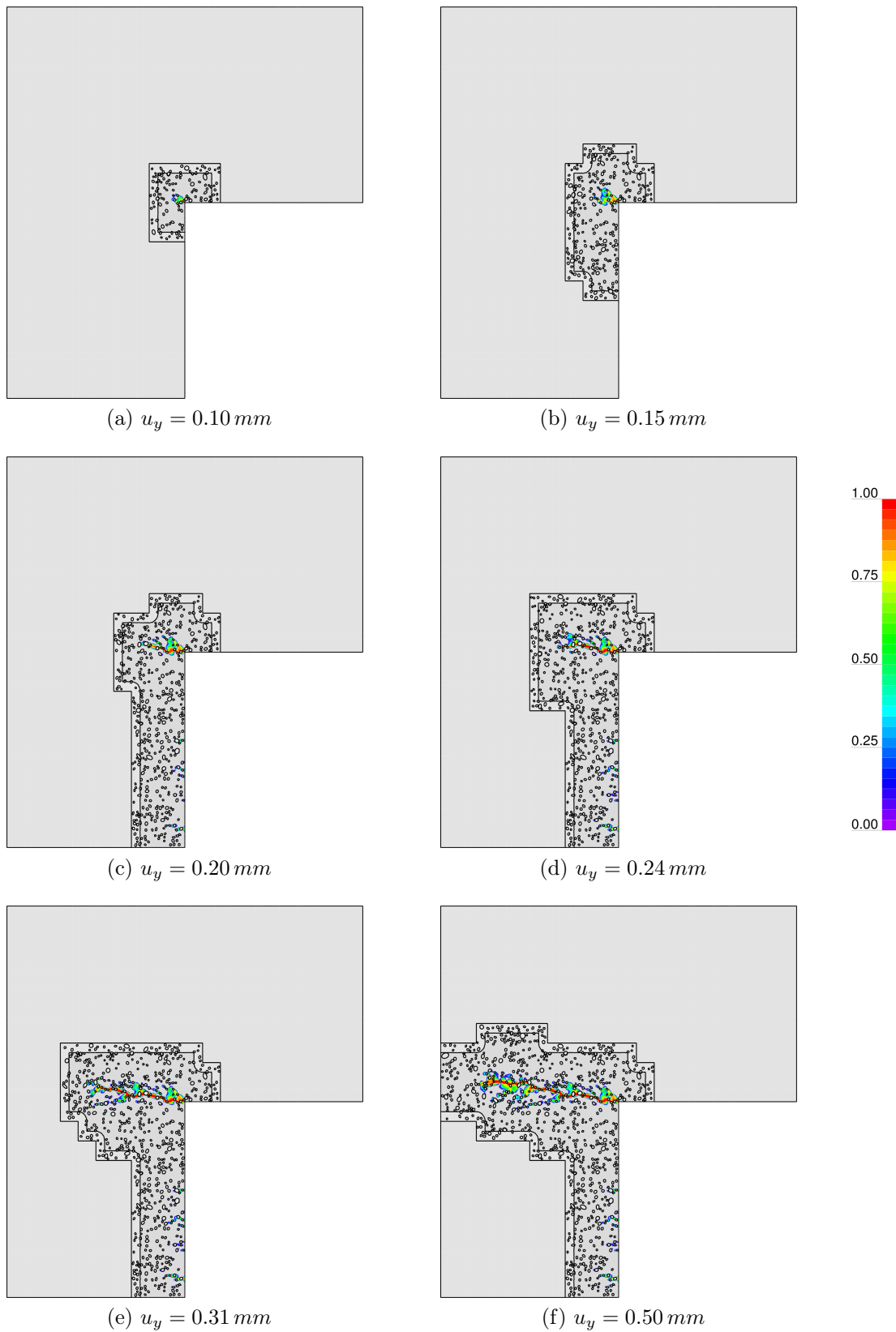


Figure 5.22: L-shaped panel – damage distribution obtained with the multiscale model with constraint equations for different load levels.

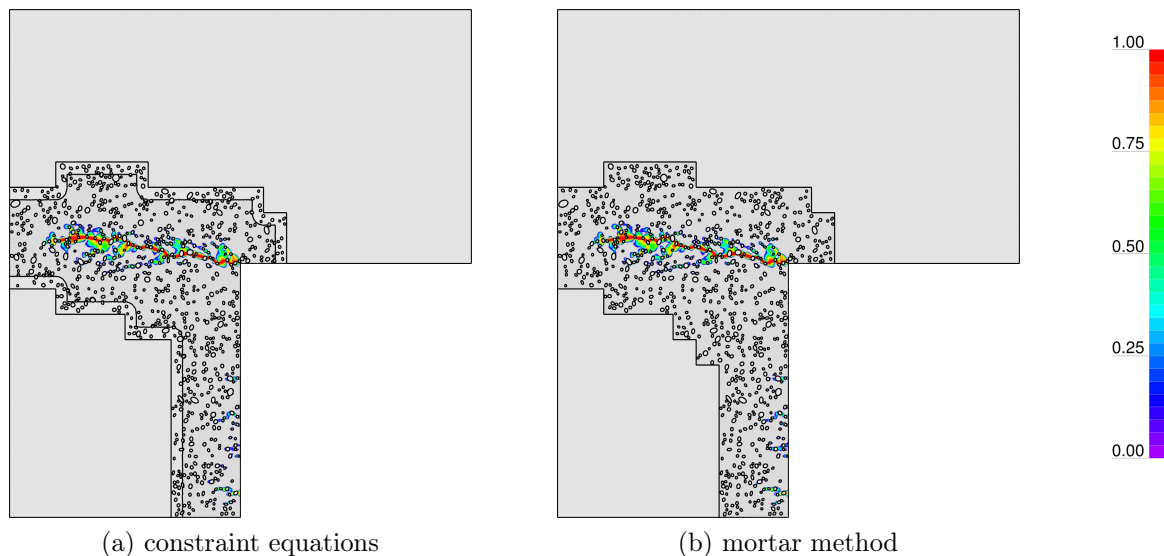


Figure 5.23: L-shaped panel – comparison of the final damage distribution ( $u_y = 0.57 \text{ mm}$ ) observed for multiscale models with different coupling conditions.

conditions. Furthermore, the shape and the position of the final mesoscale sub-domain is almost the same. Accordingly, it is verified that an elastic border domain is not required if a weak coupling is realized using the mortar method. The artificial initiation of damage due to the influence of the coupling constraint in the direct vicinity of common sub-domain boundaries, leading to an additional enlargement of the mesoscale sub-domain, is not observed for this model. Furthermore, the numerical simulations with constraint equations have shown that the influence of high local stress values within the elastic border domain, which are the result of the direct coupling between adjacent sub-domains, is negligible.

For both simulations, Table 5.5 summarizes the total computing time and the total number of load-increments. As proposed in Sect. 2.4.5, the step size is automatically adapted for each load increment. The adaptation is based on the number of iteration steps required to solve the nonlinear equilibrium problem for the previous load increment. Both simulations start with the same step length. Compared to the simulation with constraint equations, a larger number of iteration steps is, in general, required in the simulation with the mortar method to solve the nonlinear equilibrium problem for a single load increment. As a consequence, the step size is reduced in the next load increment. Altogether, the number of load increments required to reach the final displacement state increases. As a result, the total number of iteration steps performed during the nonlinear analysis is in the simulation with the mortar method considerably larger than in the simulation with

Table 5.5: L-shaped panel – total computing times for multiscale simulations.

	computing time	number of load increments
constraint equations	45 416 s (12 h 37 min)	117
mortar method	63 916 s (17 h 45 min)	136

constraint equations. Since in each iteration step a linear system of equations is solved and the corresponding residual is calculated, the numerical simulation with the mortar method becomes significantly more time-consuming.

### 5.6.2 Size Effect

In the second example, the adaptive heterogeneous multiscale approach is applied to the nonlinear analysis of the large specimens (type E and F) of the size effect experiments by van Vliet and van Mier (2000). Furthermore, it is shown for specimens of type D that with the adaptive heterogeneous multiscale approach almost identical results as with a mesoscale model can be obtained. As illustrated in Sect. 4.4.2, the smaller specimens are numerically analyzed using full mesoscale models for type A, B and C and reduced mesoscale models for type D. In the heterogeneous multiscale model, the same mesoscale model as in the mesoscale simulations is considered for mesoscale sub-domains. The corresponding material parameters, which are determined for a full mesoscale model of a specimen of type B, are summarized in Table 4.9 on page 96. In the multiscale simulations, the initial macroscale model is discretized by triangular 6-node elements leading to an irregular finite element mesh. The average element size assumed for the initial macroscale model depends on the specimen type ( $16\text{ mm}$ ,  $32\text{ mm}$  and  $64\text{ mm}$  for the specimen types D, E and F). A constant average element size of  $0.75\text{ mm}$  is assumed in all simulations for mesoscale sub-domains. As in the previous example, the criteria for model adaptation are defined in terms of the tensile strength of the mortar matrix on the macroscale and of the damage distribution within the mortar matrix on the mesoscale. The macroscale element patch for which the adaptation is performed is defined by a square of size  $30d_{max} = 120\text{ mm}$ . It is to be noted that an edge length larger than the minimum value ( $15d_{max}$ ) has been chosen in order to avoid a frequent adaptation of the model. Furthermore, the border part in mesoscale sub-domains comprises all elements within a distance of  $6d_{max} = 24\text{ mm}$  from common sub-domain boundaries. A direct displacement coupling realized using constraint equations is applied between adjacent sub-domains. In order to avoid spurious damage initiation due to the strong coupling, linear elastic material behavior is assumed in all elements within a distance of  $3d_{max} = 12\text{ mm}$  from a coupling boundary. As in the mesoscale simulations, a load-displacement-constraint solution procedure, in which the additional constraint is defined by the amount of dissipated inelastic energy, is applied in order to investigate the global softening behavior and in order to capture snap-back phenomena in the global response.

In a first test, the simulations with the adaptive heterogeneous multiscale approach are compared to mesoscale simulations. Due to the strong influence of the internal material structure on the macroscopic crack path and, as a consequence, on the macroscopic nominal strength and the macroscopic fracture energy, the comparison is performed for the mean value and the standard deviation of these parameters determined from ten simulations with varying aggregate configurations. Figure 5.24 shows the individual values, the mean value and the standard deviation of the macroscopic nominal strength  $\sigma_N$  and the macroscopic fracture energy  $G_f$  for specimen type D. It is to be noted that both parameters can be determined from the global load-displacement curve using Eqs. (4.26) and (4.27). The



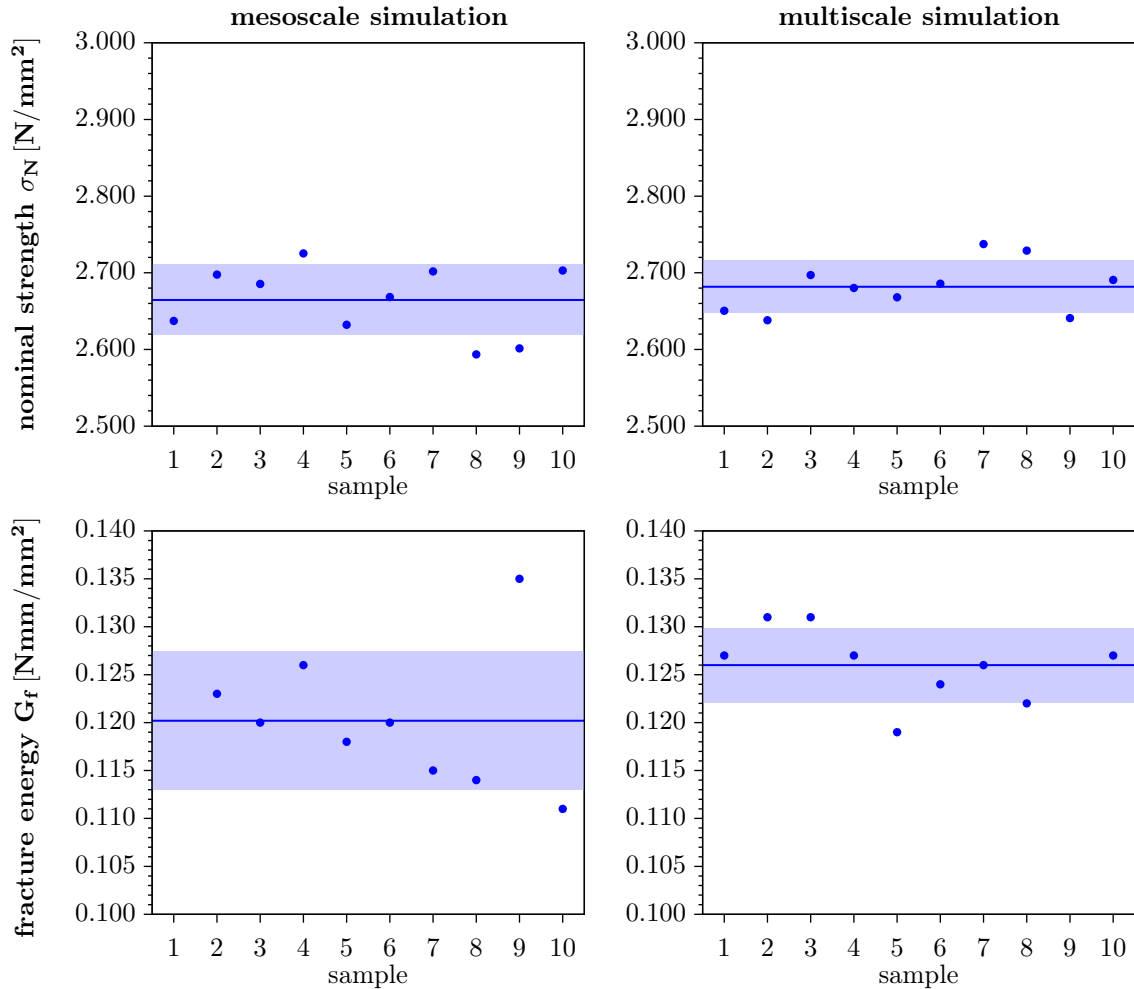


Figure 5.24: Size effect – individual values, mean value and standard deviation of the macroscopic nominal strength and of the macroscopic fracture energy of specimen type D.

mean value and the standard deviation of the nominal strength is almost identical for both approaches. The slight deviations between both approaches can be attributed to the small number of samples considered. Due to the adaptation criteria applied in the adaptive heterogeneous multiscale approach, the mean value of the fracture energy is for the multiscale simulations slightly larger (about 5%) as for the mesoscale simulations. In order to reduce the numerical effort for the multiscale simulations, an adaptation of the numerical model is performed either if in macroscale sub-domains the maximum principal stress exceeds the tensile strength of the mortar matrix or if in mesoscale sub-domains damage initiates within the mortar matrix near common sub-domain boundaries. Both criteria neglect the influence of interface cracks which, in general, initiate within the ITZ before damage starts to develop within the mortar matrix. As a consequence, the specimen stiffness is overestimated before the model is adapted. Furthermore, the macroscopic fracture energy slightly increases in multiscale simulations. The standard deviation of the fracture energy is considerably smaller in the multiscale simulations as in the mesoscale simulations. As illustrated in the plot of the fracture energy for the mesoscale simulation

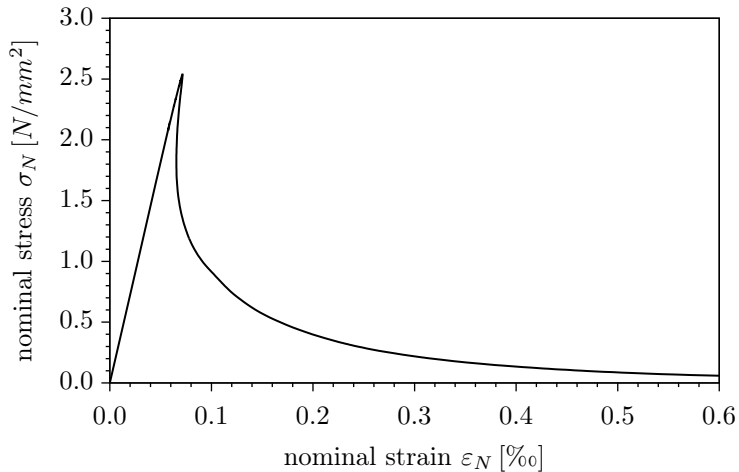


Figure 5.25: Size effect – nominal stress-strain curve obtained for specimens of type E.

in Fig. 5.24, a considerably higher fracture energy is obtained for the ninth sample. If this sample is not considered in the stochastic evaluation of the fracture energy, the standard deviation decreases significantly and an almost identical standard deviation is obtained for both approaches. This indicates that either the ninth sample in the mesoscale simulations is an outlier or that too few samples are used in both simulations.

In a second test, the specimen types E and F are investigated using the adaptive heterogeneous multiscale approach. Ten simulations with varying aggregate configuration are performed for each specimen type. Figure 5.25 shows the nominal stress-strain curve for the first sample of specimen type E. The nominal stress and the nominal strain are defined as

$$\sigma_N = \frac{F_y}{0.6D} \quad \varepsilon_N = \frac{\Delta u_y}{L_s}, \quad (5.67)$$

where  $F_y$  is the vertical resulting force observed at the top of the specimen, and  $\Delta u_y$  is the vertical relative displacement between the two monitoring points. Figure 5.26 shows the corresponding final damage distribution. Due to the large size of the specimen compared to the final damage zone, a snap back is observed in the nominal stress-strain curve. Furthermore, it is illustrated that the failure mechanism observed in the mesoscale simulations can also be represented by the adaptive heterogeneous multiscale model. The pre-peak behavior of the specimen is characterized by the initiation and propagation of small damage zones (microcracks) near the left specimen boundary. When the peak-load is reached, a macroscopic damage zone is formed close to the center of the specimen. The post-peak behavior is accompanied by a further development of the macroscopic damage zone and by the initiation of microcracks in the fracture process zone in front of the macroscopic damage zone. Consequently, a relatively large width of the mesoscale sub-domain perpendicular to the final crack surface is obtained at the beginning of the simulation. After reaching the peak-load the width of the mesoscale sub-domain decreases due to the localization of damage. At the end of the simulation, approximately 13 % of the specimen is represented on the mesoscale. The corresponding numerical model consists of approximately 1 422 000 active degrees of freedom which is about 39 % of the number of unknowns in the reduced

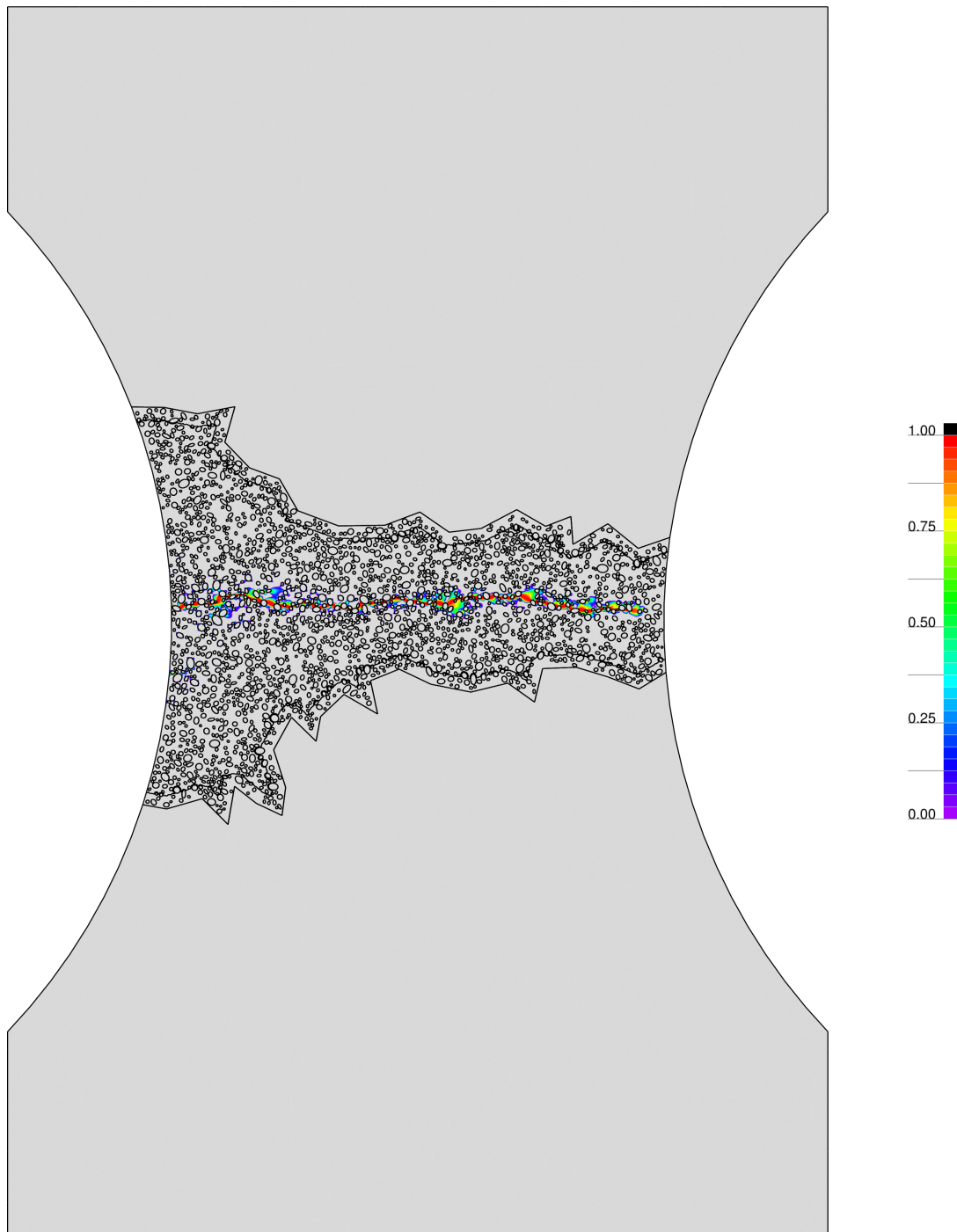


Figure 5.26: Size effect – final damage distribution for a specimen of type E.

mesoscale model. However, the simulation is still extremely time-consuming. Altogether, the simulation of the full loading regime requires a computing time of  $67 h$ . In order to reduce the computing time, all the other simulations of the specimen types E and F are stopped immediately after reaching the peak-load. As a consequence, the average computing time for specimen type E can be reduced to  $6 h$  ( $24 h$  for specimen type F). At the peak-load the average size of the mesoscale sub-domains is approximately 7% (5%)

of the total specimen area which corresponds to a numerical model with approximately 750 000 (2 125 000) active degrees of freedom. As a further consequence, the influence of the specimen size on the macroscopic fracture energy can not be investigated for specimen types E and F. The mean value and the standard deviation of the nominal strength are summarized in Table 4.10 on page 97. Figure 4.13(a) illustrates the influence of the specimen size on this parameter. As in the mesoscale simulations, a clear size effect on the nominal strength is noticeable for the specimen types E and F. Thus, the nominal strength decreases with increasing specimen dimension. Due to the assumption of deterministic material parameters, the size effect in the numerical simulations is less pronounced as in the experiments. As a further consequence, a considerably smaller standard deviation of the nominal strength is observed in the numerical simulations. It is to be noted that, as in the mesoscale simulations, these additional stochastic effects can be explicitly considered in the heterogeneous multiscale model using random variables or random fields for the material parameters.

## 6 Conclusions

The overall goal of this thesis was to improve the description of the material behavior in nonlinear simulations of concrete structures. For this purpose, the material was, at least in critical regions, not idealized as a homogeneous material, but the heterogeneous internal material structure of concrete, mainly characterized by aggregates and mortar matrix, was explicitly resolved in the numerical model. In this context, several aspects had to be considered.

As a first step, a mesoscale model for concrete was developed which is capable of describing the propagation of microcracks inside the heterogeneous internal material structure. In this model, the coarse aggregates, the mortar matrix and the interfacial transition zone (ITZ) between aggregates and matrix are explicitly considered as separate components. One important point within the generation of the mesoscale model is an appropriate description of the size distribution and the spatial distribution of the aggregates. Based on the take-and-place method, an efficient algorithm for the numerical simulation of three-dimensional mesoscale geometries with a large number of aggregates was introduced. The aggregates are approximated by ellipsoids which allows for a variable shape of the particles. Starting from the mathematical representation of grading curves, which characterize the aggregate size distribution in concrete, an algorithm for the generation of the ellipsoids was derived. It was shown that the size distribution of the ellipsoids simulated with the proposed algorithm almost coincides with the prescribed grading-curve. The final spatial distribution of the aggregates was obtained by randomly placing the ellipsoids one by one into the specimen. In order to prevent overlapping of particles, separation checks were performed. In this thesis, a combination of an inexact separation check using bounding boxes and a very efficient exact separation check for ellipsoids was applied. The speed of the algorithm was further increased by subdividing the specimen into regular cuboids, which allows for a significant reduction of the number of separation checks. Using this new subdivision approach, a substantial improvement in the performance of the particle placement procedure was obtained. The performance gain was illustrated using a three-dimensional example with approximately 300 000 ellipsoids. Two-dimensional aggregate distributions were simulated by cutting a slice out of the three-dimensional model.

For numerical simulations, an aligned finite element discretization was applied allowing to represent the ITZ by zero-thickness interface elements. It was observed that an appropriate description of the specific material behavior of the ITZ using a cohesive zone approach is important for a realistic simulation. Otherwise, the failure of the ITZ is modeled inside the mortar matrix leading to an overestimation of the ITZ's strength and to artificial damage zones around the aggregates. Different material formulations based on the continuum damage approach or on the smeared crack concept were investigated for their ability to

represent tensile failure of the mortar matrix which is accompanied by a softening behavior. By applying nonlocal material formulations, spurious mesh sensitivity, which is induced by the representation of the material as strain-softening continuum, was significantly reduced. The convergence of the iterative solution of the generally nonlinear global system of equations was considerably improved by calculating the tangential material matrix for the nonlocal material models. For tensile failure, a good agreement with experimental results was already obtained in two-dimensional simulations with the isotropic damage model and the rotating crack model. Using the microplane based damage model, the pre-peak behavior is characterized by an almost homogeneous damage distribution within the mortar matrix. As a result, the numerical effort increases significantly compared to the simulations with the isotropic damage model or the rotating crack model. Furthermore, it was realized that the identification of the material parameters of the microplane based damage model was rather complex, because these parameters cannot be related in a straightforward way to material properties measurable on the macroscale. Comparing the different constitutive models, it was observed that the nonlocal isotropic damage model is the most robust material formulation with respect to convergence speed and stability.

In simulations of uniaxial tension tests, it was demonstrated that a localization of damage automatically occurs on the mesoscale without introducing any artificial local defects, which is an important advantage of mesoscale models. Due to the random generation of the aggregates, a stochastic scatter of the results is naturally included in the model. Furthermore, the ability of mesoscale models to represent size effects on the macroscopic nominal strength was illustrated. For the large specimens of the size effect experiments, the load-displacement curves exhibit snap backs. By applying a path-following algorithm based on the load-displacement-constraint method within the iterative solution procedure, the simulation was able to capture these snap-backs. In this thesis, a new path-following constraint which is based on the dissipation of the inelastic energy was proposed allowing for an efficient simulation of snap-back phenomena. By defining the constraint in terms of the internal energy, the proposed path-following algorithm is not restricted to continuum damage models, but can be applied to any material formulation for which the inelastic energy can be defined. It was shown that this constraint is especially advantageous in nonlinear mesoscale simulations of concrete, which are characterized by the propagation of multiple cracks, since no a priori knowledge about the final failure zone is required.

In this thesis, it was assumed that, due to the mutual interaction between the individual components within the heterogeneous internal material structure, compressive failure on the macroscale can be reduced to tensile failure perpendicular to the direction of compressive stresses on the mesoscale. The presented results of a compression test which was simulated on the mesoscale, could not confirm this assumption. It was shown that, in contrast to tensile failure, the two-dimensional mesoscale model is not able to represent the complex failure mechanism of concrete in compression. Using a three-dimensional model, significantly better results were obtained, but the deviations from the experimental results are still unacceptably large. The main problem was the numerical complexity, i.e. the computing time and the memory demand, of three-dimensional mesoscale simulations. As a consequence, the simulation of the compression test was performed for a small specimen using a relatively coarse finite element discretization, allowing to consider only a small number of large aggregates. In order to obtain meaningful results, the spa-

tial resolution of the mesoscale model has to be increased in the future. Especially the influence of the fine aggregates has to be further investigated. In this context, additional research is required regarding the application of advanced parallelization techniques in three-dimensional mesoscale simulations which allow for computations using distributed systems.

In a second step, the adaptive heterogeneous multiscale approach was introduced, in which only critical parts of the structure, e.g. in which damage develops, are resolved on the mesoscale. It was demonstrated that such an approach allows to incorporate mesoscale models in simulations of large structures. Consequently, the advantages of mesoscale models and macroscale simulations are combined. On the one hand, the complex nonlinear behavior of concrete is precisely described in critical parts of the structure using mesoscale models. On the other hand, the computational effort is significantly reduced compared to full scale mesoscale simulations by using macroscale models in those parts of the structure which are still in the elastic domain.

A crucial point in the heterogeneous multiscale approach is the coupling between sub-domains which are represented on different length-scales. In this thesis, three different approaches for the coupling of non-matching finite element discretizations were presented. In the first approach, constraint equations were used to enforce displacement compatibility between the sub-domains. As a result, artificial stress concentrations in the vicinity of coupling boundaries were observed in mesoscale sub-domains. In order to avoid spurious damage initiation due to these stress concentrations, linear elastic material models were applied in elements in the direct vicinity of the coupling boundary. In the second approach, the mortar method with Lagrange multipliers was applied in which the coupling condition is only satisfied in an integral sense. By establishing the Lagrange multipliers at the boundary nodes of the macroscale sub-domains, slightly lower stress values were observed near the coupling boundary compared to a full mesoscale simulation. Consequently, the coupling does not result in any spurious initiation of damage, which allows for the usage of nonlinear material formulations in elements in the direct vicinity of a coupling boundary. As demonstrated in the example of an L-shaped panel, both coupling methods – constraint equations and the mortar method – are well suited for the coupling between mesoscale sub-domains and macroscale sub-domains in heterogeneous multiscale models. In contrast to the first two approaches which assume that the sub-domains do not overlap, the third coupling approach – the arlequin method – requires overlapping sub-domains. As in the mortar method a weak coupling, in which the coupling condition is only satisfied in an integral sense, is realized using Lagrange multipliers which were introduced on the coarse mesh. Different arlequin weight functions were investigated using a one-dimensional linear-elastic example. Applying constant weight functions, singularities in the field of Lagrange multipliers, which represent the coupling tractions, were observed at the boundary of the coupling domain. It was demonstrated that these singularities can be avoided by using linear arlequin weight functions. Furthermore, it was illustrated that the conditioning of the global system of equations is significantly improved compared to simulations with constant weight functions. One problem in the implementation of the arlequin method was the integration of the stiffness and the coupling matrices in elements inside the coupling domain. In this thesis, an integration procedure was proposed which is based on a subdivision of the coupling domain into triangular integration cells. On the one hand, this

approach allows for an almost exact integration of the matrices. On the other hand, as shown in the two-dimensional linear elastic example, the generation of the integration cells, which requires the calculation of the intersection between the finite element discretizations of both sides, is very time-consuming. Furthermore, it was illustrated that, due to the evaluation of the arlequin weight function in each integration point, the computing time for the calculation of the element stiffness matrices increases dramatically compared to non-overlapping methods. Another problem was that in the coupling domain the material is described by two different models – homogeneous in the macroscale sub-domain and heterogeneous in the mesoscale sub-domain. It was shown that each macroscopic element has to be representative for the associated set of mesoscale elements. As a consequence, a minimal size of the macroscopic element, which is related to the nominal size of the material inhomogeneities considered on the mesoscale, is required.

Another crucial point in simulations using adaptive heterogeneous multiscale models was the detection of critical regions. In this thesis, an adaptive solution procedure allowing for the transfer of macroscale sub-domains to the mesoscale was presented. On the macroscale, a criterion based on the maximum principal stress was proposed as indicator for the model adaptation. A second criterion which is based on the spatial distribution of damage was introduced in mesoscale sub-domains. As illustrated in the nonlinear simulations of the L-shaped panel and the large specimens of the size effect experiments, the combination of both criteria allow for an efficient adaptation of the heterogeneous multiscale model only in those parts of the structure in which damage develops. Furthermore, it was illustrated that the usage of heterogeneous multiscale models results in a similar damage distribution compared to full mesoscale models while significantly reducing the numerical effort.

In summary, it can be concluded that the explicit representation of the heterogeneous internal material structure in mesoscale models allows for a precise simulation of the complex nonlinear behavior of concrete. Using the proposed adaptive heterogeneous multiscale approach the numerical effort can be significantly reduced compared to full mesoscale simulations. As a result, mesoscale models can be incorporated in nonlinear simulations of large structures.



# Bibliography

- Aboudi, J. (1991). Mechanics of composite materials: a unified micromechanical approach. In *Studies in applied mechanics 29*. Elsevier.
- Amestoy, P. R., Duff, I. S., and L'Excellent, J.-Y. (2000). Multifrontal parallel distributed symmetric and unsymmetric solvers. *Computer Methods in Applied Mechanics and Engineering*, 184(2-4):501–520.
- Amestoy, P. R., Duff, I. S., L'Excellent, J.-Y., and Koster, J. (2002). A fully asynchronous multifrontal solver using distributed dynamic scheduling. *SIAM Journal on Matrix Analysis and Applications*, 23(1):15–41.
- Amestoy, P. R., Guermouche, A., L'Excellent, J.-Y., and Pralet, S. (2006). Hybrid scheduling for the parallel solution of linear systems. *Parallel Computing*, 32(2):136–156.
- Askes, H. and Sluys, L. J. (2000). Remeshing strategies for adaptive ALE analysis of strain localization. *European Journal of Mechanics, A/Solids*, 19(3):447–467.
- Badel, P.-B. and Leblond, J.-B. (2004). A note on integration schemes for the microplane model of the mechanical behaviour of concrete. *Communications in Numerical Methods in Engineering*, 20(1):75–81.
- Barbeau, E. J. (2003). *Polynomials*. Springer.
- Bathe, K. J. (1995). *Finite Element Procedures*. Prentice Hall.
- Bauman, P. T., Dhia, H. B., Elkhodja, N., Oden, J. T., and Prudhomme, S. (2008). On the application of the arlequin method to the coupling of particle and continuum models. *Computational Mechanics*, 42(4):511–530.
- Bažant, Z. P. (1976). Instability, ductility, and size effect in strain-softening concrete. *Journal of the engineering mechanics division, ASCE*, 102(2):331–344.
- Bažant, Z. P. (1983). Comment on orthotropic models for concrete and geomaterials. *Journal of Engineering Mechanics*, 109(3):849–865.
- Bažant, Z. P. (1984a). Imbricate continuum and its variational derivation. *Journal of Engineering Mechanics*, 110(12):1693–1712.
- Bažant, Z. P. (1984b). Microplane model for strain-controlled inelastic behaviour. In Desai, C. S. and Gallagher, R. H., editors, *Mechanics of engineering materials*, pages 45–59. Wiley.
- Bažant, Z. P. (1991). Why continuum damage is nonlocal: micromechanics arguments. *Journal of Engineering Mechanics*, 117(5):1070–1087.

- Bažant, Z. P. (1994). Nonlocal damage theory based on micromechanics of crack interactions. *Journal of Engineering Mechanics*, 120(3):593–617.
- Bažant, Z. P. and Gambarova, P. (1980). Rough cracks in reinforced concrete. *Journal of the Structural Division, ASCE*, 106(4):819–842.
- Bažant, Z. P. and Jirásek, M. (2002). Nonlocal integral formulations of plasticity and damage: Survey of progress. *Journal of Structural Engineering ASCE*, 128(11):1119–1149.
- Bažant, Z. P. and Lin, F.-B. (1988). Nonlocal smeared cracking model for concrete fracture. *Journal of Structural Engineering*, 114(11):2493–2510.
- Bažant, Z. P. and Oh, B. H. (1983a). Crack band theory for fracture of concrete. *Materiaux et constructions*, 16(93):155–177.
- Bažant, Z. P. and Oh, B. H. (1983b). Microplane model for fracture analysis of concrete structures. In *Proceedings of the symposium on the interaction of non-nuclear munitions with structure*, pages 49–55. U.S. Air Force Academy.
- Bažant, Z. P. and Oh, B. H. (1985). Microplane model for progressive fracture of concrete and rock. *Journal of Engineering Mechanics*, 111(4):559–582.
- Bažant, Z. P. and Oh, B. H. (1986). Efficient numerical integration on the surface of a sphere. *Zeitschrift für angewandte Mathematik und Mechanik*, 66(1):37–49.
- Bažant, Z. P. and Ožbolt, J. (1990). Nonlocal microplane model for fracture, damage, and size effect in structures. *Journal of Engineering Mechanics*, 116(11):2485–2505.
- Bažant, Z. P. and Pijaudier-Cabot, G. (1988). Nonlocal continuum damage, localization instability and convergence. *Journal of Applied Mechanics*, 55(2):287–293.
- Bažant, Z. P. and Pijaudier-Cabot, G. (1989). Measurement of characteristic length of nonlocal continuum. *Journal of Engineering Mechanics*, 115(4):755–767.
- Bažant, Z. P., Tabbara, M. R., Kazemi, M. T., and Pijaudier-Cabot, G. (1990). Random particle model for fracture. *Journal of Engineering Mechanics, ASCE*, 116(8):1686–1705.
- Bayreuther, C. (2004). *Mehrskalennmodelle in der Festkörpermechanik und Kopplung von Mehrgittermethoden mit Homogenisierungsverfahren*. Dissertation, Universität Stuttgart.
- Belgacem, F. B. (1999). The mortar finite element method with lagrange multipliers. *Numerische Mathematik*, 84(2):173–197.
- Belytschko, T. and Black, T. (1999). Elastic crack growth in finite elements with minimal remeshing. *International Journal for Numerical Methods in Engineering*, 45(5):601–620.
- Belytschko, T., Fish, J., and Bayliss, A. (1990). The spectral overlay on finite elements for problems with high gradients. *Computer Methods in Applied Mechanics and Engineering*, 81(1):71–89.

- 
- Ben Dhia, H. (1998). Problèmes mécaniques multi-échelles: la méthode arlequin (multiscale mechanical problems: the arlequin method). *Comptes Rendus de l'Académie des Sciences - Series IIB - Mechanics-Physics-Astronomy*, 326(12):899–904.
- Ben Dhia, H. (1999). Numerical modelling of multiscale mechanical problems: the arlequin method. In *Proceedings of ECCM '99*, München.
- Ben Dhia, H. (2005). Approches locales-globales méthode arlequin. In *7ème Colloque national en calcul des structures*, Giens.
- Ben Dhia, H. and Rateau, G. (2004a). The arlequin method as a flexible engineering design tool. *International Journal for Numerical Methods in Engineering*, 62(11):1442–1462.
- Ben Dhia, H. and Rateau, G. (2004b). The arlequin method as a multiscale numerical tool. In *Proceedings of WCCM VI*, Beijing.
- Bernardi, C., Maday, Y., and Patera, A. T. (1994). A new nonconforming approach to domain decomposition: the mortar element method. In Brezis, H. and Lions, J. L., editors, *Nonlinear partial differential equations and their applications. Collège de France Seminar, Vol. XI (Paris, 1989–1991)*, volume 299 of *Pitman research notes in mathematics series*, pages 13–51. Harlow: Longman Scientific & Technical.
- Borino, G., Failla, B., and Parrinello, F. (2003). A symmetric nonlocal damage theory. *International Journal of Solids and Structures*, 40(13-14):3621–3645.
- Bronstein, I. N., Semendjajew, K. A. and Musiol, G., and Mühlig, H. (1997). *Taschenbuch der Mathematik*. Verlag Harri Deutsch, 3<sup>rd</sup> edition.
- Carol, I. and Bažant, Z. P. (1997). Damage and plasticity in microplane theory. *International Journal of Solids and Structures*, 34(29):3807–3835.
- Carol, I., López, C. M., and Roa, O. (2001). Micromechanical analysis of quasi-brittle materials using fracture-based interface elements. *International Journal for Numerical Methods in Engineering*, 52(1-2):193 – 215.
- Cope, R. J., Rao, P. V., Clark, L. A., and Norris, P. (1980). Modelling of reinforced concrete behaviour for finite element analysis of bridge slabs. In Taylor, C., Hinton, E., and Owen, D. R. J., editors, *Numerical Methods for Nonlinear Problems 1*, page 457–470, Swansea. Pineridge Press.
- Cordebois, J. P. and Sidoroff, F. (1982). Damage induced elastic anisotropy. In *Mechanical behavior of anisotropic solids: Proceedings of the Euromech Colloquium 295*, Colloques internationaux du Centre National de la Recherche Scientifique. Nijhoff.
- Crisfield, M. A. (1982). Accelerated solution techniques and concrete cracking. *Computer methods in applied mechanics and engineering*, 33(1-3):585–607.
- Crisfield, M. A. (1983). An arc-length method including line searches and accelerations. *International Journal for Numerical Methods in Engineering*, 19:1269–1289.
- Crisfield, M. A. (1991). *Non-linear finite element analysis of solid and structures*, volume 1. John Wiley and Sons.

- 
- Cusatis, G., Bažant, Z. P., and Cedolin, L. (2006). Confinement-shear lattice CSL model for fracture propagation in concrete. *Computer Methods in Applied Mechanics and Engineering*, 195(52):7154–7171.
- D’Addetta, G. A. (2004). *Discrete models for cohesive frictional materials*. PhD thesis, University of Stuttgart.
- Döbert, C. (2001). *Meso- Makromechanische Modellierung von Faserverbundwerkstoffen mit Schädigung*. Dissertation, Universität Hannover.
- de Borst, R. and Nauta, P. (1985). Non-orthogonal cracks in a smeared finite element model. *Engineering computations*, 2(1):35–46.
- de Vree, J. H. P., Brekelmans, W. A. M., and van Gils, M. A. J. (1995). Comparison of nonlocal approaches in continuum damage mechanics. *Computers and Structures*, 55(4):581–588.
- Devroye, L. (1986). *Non-Uniform Random Variate Generation*. Springer.
- Eckardt, S., Häfner, S., and Könke, C. (2004). Simulation of the fracture behaviour of concrete using continuum damage models at the mesoscale. In Neittaanmäki, P., Rossi, T., Majavs, K., and Pironeau, O., editors, *Proceedings of the 4<sup>th</sup> European Congress on Computational Methods in Applied Sciences and Engineering - ECCOMAS 2004*, Jyväskylä, Finland.
- Eckardt, S. and Könke, C. (2008). Adaptive damage simulation of concrete using heterogeneous multiscale models. *Journal of Algorithms & Computational Technology*, 2(2):275–297.
- Eringen, A. C. (1966). A unified theory of thermomechanical materials. *International Journal of Engineering Science*, 4(2):179–202.
- Feyel, F. and Chaboche, J.-L. (2000). FE<sup>2</sup> multiscale approach for modelling the elasto-viscoplastic behaviour of long fibre SiC/Ti composite materials. *Computer Methods in Applied Mechanics and Engineering*, 183(3-4):309–330.
- Fish, J. (1992). The s-version of the finite element method. *Computers and Structures*, 43(3):539–547.
- Garboczi, E. J. (2002). Three-dimensional mathematical analysis of particle shape using X-ray tomography and spherical harmonics: application to aggregates used in concrete. *Cement and Concrete Research*, 32(10):1621–1638.
- Gens, A., Carol, I., and Alonso, E. E. (1989). An interface element formulation for the analysis of soil- reinforcement interaction. *Computers & Geotechnics*, 7(1-2):133–151.
- Geuzaine, C. and Remacle, J.-F. (2009). Gmsh: a three-dimensional finite element mesh generator with built-in pre- and post-processing facilities. *International Journal for Numerical Methods in Engineering*, Accepted for publication, 2009.
- Ghosh, S., Lee, K., and Raghavan, P. (2001). A multi-level computational model for multi-scale damage analysis in composite and porous materials. *International Journal of Solids and Structures*, 38(14):2335–2385.

- 
- Gitman, I. M. (2006). *Representative volumes and multi-scale modelling of quasi-brittle materials*. PhD thesis, Delft University of Technology.
- Gitman, I. M., Askes, H., and Sluys, L. J. (2007). Representative volume: Existence and size determination. *Engineering Fracture Mechanics*, 74(16):2518–2534.
- Gitman, I. M., Askes, H., and Sluys, L. J. (2008). Coupled-volume multi-scale modelling of quasi-brittle material. *European Journal of Mechanics, A/Solids*, 27(3):302–327.
- Grassl, P., Bažant, Z. P., and Cusatis, G. (2006). Lattice-cell approach to quasibrittle fracture modeling. In Meschke, G., de Borst, R., Mang, H., and Bićanić, N., editors, *Computational Modelling of Concrete Structures, EURO-C*.
- Grübl, P., Weigler, H., and Karl, S. (2001). *Beton: Arten, Herstellung und Eigenschaften*. Ernst & Sohn.
- Gupta, A. K. and Akbar, H. (1984). Cracking in reinforced concrete analysis. *Journal of Structural Engineering*, 110(8):1735–1746.
- Gutiérrez, M. A. (2004). Energy release control for numerical simulations of failure in quasi-brittle solids. *Communications in Numerical Methods in Engineering*, 20(1):19–29.
- Hashin, Z. (1983). Analysis of composite materials - a survey. *Journal of Applied Mechanics, Transactions ASME*, 50(3):481–505.
- Hashin, Z. and Monteiro, P. J. M. (2002). An inverse method to determine the elastic properties of the interphase between the aggregate and the cement paste. *Cement and Concrete Research*, 32(8):1291–1300.
- Hashin, Z. and Shtrikman, S. (1963). A variational approach to the theory of the elastic behavior of multiphase materials. *Journal of the mechanics and physics of solids*, 11(2):127–140.
- Hellweg, H.-B. and Crisfield, M. A. (1998). A new arc-length method for handling sharp snap-backs. *Computers and Structures*, 66(5):705–709.
- Hettich, T., Hund, A., and Ramm, E. (2008). Modeling of failure in composites by x-fem and level sets within a multiscale framework. *Computer Methods in Applied Mechanics and Engineering*, 197(5):414–424.
- Häfner, S. (2007). *Grid-based procedures for the mechanical analysis of heterogeneous solids*. PhD thesis, Bauhaus-University Weimar.
- Häfner, S., Eckardt, S., Luther, T., and Könke, C. (2006). Mesoscale modeling of concrete: Geometry and numerics. *Computers & Structures*, 84(7):450–461.
- Hill, R. (1952). The elastic behaviour of a crystalline aggregate. *Proceedings of the Physical Society. Section A*, 65(5):349–354.
- Hill, R. (1963). Elastic properties of reinforced solids: some theoretical principles. *Journal of the mechanics and physics of solids*, 11(5):357–372.

- 
- Hirai, I., Wang, B. P., and Pilkey, W. D. (1984). Efficient zooming method for finite element analysis. *International Journal for Numerical Methods in Engineering*, 20(9):1671–1683.
- Hofstetter, G. and Mang, H. A. (1995). *Computational mechanics of reinforced concrete structures*. Vieweg.
- Hu, H., Belouettar, S., Potier-Ferry, M., and Daya, E. M. (2008). Multi-scale modelling of sandwich structures using the Arlequin method Part I: Linear modelling. *Finite Elements in Analysis and Design*, 45(1):37–51.
- Hughes, T. J. R. (1995). Multiscale phenomena: Green’s functions, the dirichlet-to-neumann formulation, subgrid scale models, bubbles and the origins of stabilized methods. *Computer Methods in Applied Mechanics and Engineering*, 127(1-4):387–401.
- Hughes, T. J. R., Feijóo, G. R., Mazzei, L., and Quincy, J.-B. (1998). The variational multiscale method - a paradigm for computational mechanics. *Computer Methods in Applied Mechanics and Engineering*, 166(1-2):3–24.
- Hund, A. and Ramm, E. (2007). Locality constraints within multiscale model for non-linear material behaviour. *International Journal for Numerical Methods in Engineering*, 70(13):1613–1632.
- Hund, A. S. (2007). *Hierarchische Mehrskalenmodellierung des Versagens von Werkstoffen mit Mikrostruktur*. Dissertation, Universität Stuttgart.
- Jirásek, M. (1998a). Comparison of nonlocal models for damage and fracture. LSC Internal Report 98/02, Swiss Federal Institute of Technology (EPFL), Laboratory of Structural and Continuum Mechanics.
- Jirásek, M. (1998b). Nonlocal models for damage and fracture: Comparison of approaches. *International Journal of Solids and Structures*, 35(31-32):4133–4145.
- Jirásek, M. (1999). Comments on microplane theory. In Pijaudier-Cabot, G., Bittnar, Z., and Gérard, B., editors, *Mechanics of quasi-brittle materials and structures*. Hermès Science Publications, Paris.
- Jirásek, M. and Bažant, Z. P. (1994). Localization analysis of nonlocal model based on crack interactions. *Journal of Structural Engineering ASCE*, 120(7):1521–1542.
- Jirásek, M. and Bažant, Z. P. (1995). Particle model for quasibrittle fracture and application to sea ice. *Journal of Engineering Mechanics, ASCE*, 121(9):1016–1025.
- Jirásek, M. and Bažant, Z. P. (2001). *Inelastic Analysis of Structures*. John Wiley and Sons.
- Jirásek, M. and Grassl, P. (2008). Evaluation of directional mesh bias in concrete fracture simulations using continuum damage models. *Engineering Fracture Mechanics*, 75(8):1921–1943.
- Jirásek, M. and Marfia, S. (2005). Non-local damage model based on displacement averaging. *International Journal for Numerical Methods in Engineering*, 63(1):77–102.

- 
- Jirásek, M. and Patzák, B. (2002). Consistent tangent stiffness for nonlocal damage models. *Computers & Structures*, 80(14-15):1279–1293.
- Jirásek, M. and Zimmermann, T. (1998a). Analysis of rotating crack model. *Journal of Engineering Mechanics ASCE*, 124:842–851.
- Jirásek, M. and Zimmermann, T. (1998b). Rotating crack model with transition to scalar damage. *Journal of Engineering Mechanics ASCE*, 124:277–284.
- Kachanov, L. (1986). *Introduction to continuum damage mechanics*. Nijhoff.
- Kessler-Kramer, C. (2002). *Zugtragverhalten von Beton unter Ermüdungsbeanspruchung*. Dissertation, Universität Karlsruhe (TH).
- Kouznetsova, V. G. (2002). *Computational homogenization for the multi-scale analysis of multi-phase materials*. PhD thesis, Eindhoven University of Technology.
- Kouznetsova, V. G., Brekelmans, W. A. M., and Baaijens, F. P. T. (2001). Approach to micro-macro modeling of heterogeneous materials. *Computational Mechanics*, 27(1):37–48.
- Kouznetsova, V. G., Geers, M. G. D., and Brekelmans, W. A. M. (2002). Multi-scale constitutive modelling of heterogeneous materials with a gradient-enhanced computational homogenization scheme. *International Journal for Numerical Methods in Engineering*, 54(8):1235–1260.
- Kouznetsova, V. G., Geers, M. G. D., and Brekelmans, W. A. M. (2004). Multi-scale second-order computational homogenization of multi-phase materials: A nested finite element solution strategy. *Computer Methods in Applied Mechanics and Engineering*, 193(48-51):5525–5550.
- Krajcinovic, D. (1996). *Damage mechanics*. Elsevier.
- Krause, R. and Rank, E. (2003). Multiscale computations with a combination of the h- and p-versions of the finite-element method. *Computer Methods in Applied Mechanics and Engineering*, 192(35-36):3959–3983.
- Kröner, E. (1958). Berechnung der elastischen Konstanten des Vielkristalls aus den Konstanten des Einkristalls. *Zeitschrift für Physik*, 151:504–518.
- Kröner, E. (1967). Elasticity theory of materials with long range cohesive forces. *International Journal of Solids and Structures*, 3(5):731–742.
- Kuhl, E. and Ramm, E. (1998). On the linearization of the microplane model. *Mechanics of Cohesive-Frictional Materials*, 3:343–364.
- Lamichhane, B. P. and Wohlmuth, B. I. (2004). Mortar finite elements for interface problems. *Computing*, 72:333–348.
- Lasry, D. and Belytschko, T. (1988). Localization limiters in transient problems. *International Journal of Solids and Structures*, 24(6):581–597.

- 
- Lee, I.-W., Jung, G.-H., and Lee, J.-W. (1996). Numerical method for sensitivity analysis of eigensystems with non-repeated and repeated eigenvalues. *Journal of Sound and Vibration*, 195(1):17–32.
- Leite, J. P. B., Slowik, V., and Mihashi, H. (2004). Computer simulation of fracture processes of concrete using mesolevel models of lattice structures. *Cement and Concrete Research*, 34:1025–1033.
- Lemaitre, J. (1984). How to use damage mechanics. *Nuclear Engineering and Design*, 80(2):233–245.
- Lemaitre, J. and Chaboche, J.-L. (1990). *Mechanics of solid materials*. Cambridge University Press.
- Liao, K.-Y., Chang, P.-K., Peng, Y.-N., and Yang, C.-C. (2004). A study on characteristics of interfacial transition zone in concrete. *Cement and Concrete Research*, 34(6):977–989.
- Liu, Z.-S., Chen, S.-H., Zhao, Y.-Q., and Shao, C.-S. (1993). Computing eigenvector derivatives in structural dynamics. *Acta Mechanica Solida Sinica*, 6(3):291–299.
- Mančevski, D. (1998). *Nonlinear analysis of reinforced concrete structures by consistent simulation algorithms*. PhD thesis, Ruhr University Bochum.
- Mao, K. M. and Sun, C. T. (1991). Refined global-local finite element analysis method. *International Journal for Numerical Methods in Engineering*, 32(1):29–43.
- MATLAB PDE Toolbox (2008). *MATLAB: Partial Differential Equation Toolbox, User's Guide, Release 2008a*. The MathWorks, Inc.
- Matthies, H. and Strang, G. (1979). Solution of nonlinear finite element equations. *International Journal for Numerical Methods in Engineering*, 14(11):1613–1626.
- Mehlhorn, G. and Kolleger, J. (1995). *Der Ingenieurbau*, chapter Grundwissen Band 6: Rechnerorientierte Baumechanik, pages 293–425. Ernst & Sohn.
- Miehe, C. and Koch, A. (2002). Computational micro-to-macro transitions of discretized microstructures undergoing small strains. *Archive of Applied Mechanics*, 72(4-5):300–317.
- Moës, N., Dolbow, J., and Belytschko, T. (1999). A finite element method for crack growth without remeshing. *International Journal for Numerical Methods in Engineering*, 46(1):131–150.
- Mote, C. D. (1971). Global-local finite element. *International Journal for Numerical Methods in Engineering*, 3(4):565–574.
- Mura, T. (1982). *Micromechanics of defects in solids*. Nijhoff.
- Nagai, G., Yamada, T., and Wada, A. (2000). Three-dimensional nonlinear finite element analysis of the macroscopic compressive failure of concrete materials based on real digital image. In *Proceedings of the 8th ICCCB*, pages 449–456, Stanford University, California, USA.



- 
- Nelson, R. B. (1976). Simplified calculation of eigenvector derivatives. *AIAA Journal*, 14(9):1201–1205.
- Nemat-Nasser, S. and Hori, M. (1999). *Micromechanics: overall properties of heterogeneous materials*. Elsevier, 2nd edition.
- Neville, A. M. (1996). *Properties of Concrete*. Longman.
- Nocedal, J. and Wright, S. J. (2006). Numerical optimization. In Mikosch, T. V., Resnick, S. I., and Robinson, S. M., editors, *Springer series in operations research and financial engineering*. Springer, 2<sup>nd</sup> edition.
- Noor, A. K., Kamel, H. A., and Fulton, R. E. (1978). Substructuring techniques-status and projections. *Computers and Structures*, 8(5):621–632.
- Noor, A. K. and Peters, J. M. (1980). Nonlinear analysis via global-local mixed finite element approach. *International Journal for Numerical Methods in Engineering*, 15(9):1363–1380.
- Oliver, J. (1989). Consistent characteristic length for smeared cracking models. *International Journal for Numerical Methods in Engineering*, 28(2):461–474.
- Patzák, B. and Jirásek, M. (2004). Adaptive resolution of localized damage in quasibrittle materials. *Journal of Engineering Mechanics ASCE*, 130:720–732.
- Peerlings, R. H. J. (1999). *Enhanced damage modelling for fracture and fatigue*. PhD thesis, Technische Universiteit Eindhoven.
- Peerlings, R. H. J., de Borst, R., Brekelmans, W. A. M., and de Vree, J. H. P. (1996). Gradient enhanced damage for quasi-brittle materials. *International Journal for Numerical Methods in Engineering*, 39:3391–3403.
- Pietruszczak, S. and Mróz, Z. (1981). Finite element analysis of deformation of strain-softening materials. *International Journal for Numerical Methods in Engineering*, 17(3):327–334.
- Pijaudier-Cabot, G. and Bažant, Z. P. (1987). Nonlocal damage theory. *Journal of Engineering Mechanics*, 113(10):1512–1533.
- Ramm, E. (1980). Strategies for tracing the nonlinear response near limit points. In Wunderlich, W., Stein, E., and Bathe, K.-J., editors, *Nonlinear Finite Element Analysis in Structural Mechanics – Proceedings of the Europe-U.S. Workshop*.
- Rank, E. and Krause, R. (1997). A multiscale finite-element method. *Computers and Structures*, 64(1-4):139–144.
- Rashid, Y. R. (1968). Ultimate strength analysis of prestressed concrete pressure vessels. *Nuclear Engineering and Design*, 7(4):334–344.
- Rateau, G. (2003). *Méthode Arlequin pour les problèmes mécaniques multi-échelles. Applications à des problèmes de jonction et de fissuration de structures élancées*. PhD thesis, École Centrale Paris.

- Reese, S. (2003). Meso-macro modelling of fibre-reinforced rubber-like composites exhibiting large elastoplastic deformation. *International Journal of Solids and Structures*, 40(4):951–980.
- Reuss, A. (1929). Berechnung der Fließgrenze von Mischkristallen auf Grund der Plastizitätsbedingung für Einkristalle. *Zeitschrift für angewandte Mathematik und Mechanik*, 9:49–58.
- Riks, E. (1972). Application of newton’s method to the problem of elastic stability. *Journal of Applied Mechanics, Transactions ASME*, 39 Ser E(4):1060–1065.
- Roelfstra, P. E. (1989). Simulation of failure in computer generated structures. In Mihashi, H., editor, *Fracture Toughness and Fracture Energy: Test Methods for Concrete and Rock: Proceedings of the International Workshop*, pages 313–324.
- Rots, J. G. (1988). *Computational modeling of concrete failure*. PhD thesis, Delft University of Technology.
- Schellekens, J. C. J. and de Borst, R. (1993). On the numerical integrations of interface elements. *International Journal for Numerical Methods in Engineering*, 36(1):43–66.
- Schlangen, E. (1993). *Experimental and Numerical Analysis of Fracture Processes in Concrete*. PhD thesis, Delft University of Technology.
- Schlangen, E. and van Mier, J. G. M. (1992). Simple lattice model for numerical simulation of fracture of concrete materials and structures. *Materials and Structures*, 25(9):534–542.
- Schweizerhof, K. (1993). Consistent concept for line search algorithms in combination with arc-length constraints. *Communications in Numerical Methods in Engineering*, 9(9):773–784.
- Sluys, L. J. (1992). *Wave propagation, localisation and dispersion in softening solids*. PhD thesis, Delft University of Technology.
- Smit, R. J. M. (1998). *Toughness of heterogeneous polymeric systems: a modeling approach*. PhD thesis, Eindhoven University of Technology.
- Smit, R. J. M., Brekelmans, W. A. M., and Meijer, H. E. H. (1998). Prediction of the mechanical behavior of nonlinear heterogeneous systems by multi-level finite element modeling. *Computer Methods in Applied Mechanics and Engineering*, 155(1-2):181–192.
- Suquet, R. M. (1987). Elements of homogenization for inelastic solid mechanics. In Sanchez-Palencia, E. and Zaoui, A., editors, *Homogenization Techniques for Composite Media: Lectures Delivered at the CISM International Center for Mechanical Sciences Udine, Italy, July 1–5, 1985*, volume 272 of *Lecture Notes in Physics*, pages 193–278. Springer.
- Taylor, G. I. (1938). Plastic strains in metals. *Journal of the Institute of Metals*, 62:307–324.
- Tvergaard, V. (2003). Cohesive zone representations of failure between elastic or rigid solids and ductile solids. *Engineering Fracture Mechanics*, 70(14):1859–1868.

- Unger, J. F. (2009). *Neural networks in a multiscale approach for concrete*. PhD thesis, Bauhaus-University Weimar.
- Unger, J. F. and Könke, C. (2006). Simulation of concrete using the extended finite element method. In Meschke, G., de Borst, R., Mang, H., and Bićanić, N., editors, *Computational Modelling of Concrete Structures, EURO-C*.
- Unger, J. F. and Könke, C. (2008). Coupling of scales in a multiscale simulation using neural networks. *Computers & Structures*, 86(21-22):1994–2003.
- Unterkircher, A. and Reissner, J. (2005). Parallel assembling and equation solving via graph algorithms with an application to the FE simulation of metal extrusion processes. *Computers & Structures*, 83(8-9):627–638.
- van Mier, J. G. M. (1986). Fracture of concrete under complex stress. *Heron*, 31(3).
- van Vliet, M. R. A. and van Mier, J. G. M. (1995). Softening behaviour of concrete under uniaxial compression. In Wittmann, F., editor, *Fracture Mechanics of Concrete Structures*, volume 1, pages 383–396.
- van Vliet, M. R. A. and van Mier, J. G. M. (1998). Experimental and numerical investigation of size scale effects in concrete fracture. In de Borst, R. and van der Giessen, E., editors, *Material Instabilities in Solids*. Wiley.
- van Vliet, M. R. A. and van Mier, J. G. M. (2000). Experimental investigation of size effect in concrete and sandstone under uniaxial tension. *Engineering Fracture Mechanics*, 65(2-3):165–188.
- Červenka, V. and Pukl, R. (1994). SBETA analysis of size effect in concrete structures. In Mihashi, H., Okamura, H., and Bažant, Z. P., editors, *Size effect in concrete structures*.
- Vervuurt, A. (1997). *Interface Fracture in Concrete*. PhD thesis, Delft University of Technology.
- Voigt, W. (1889). Über die Beziehung zwischen den beiden Elastizitätskonstanten isotroper Körper. *Annalen der Physik*, 274(12):573 – 587.
- Walraven, J. C. (1980). *Aggregate Interlock: a Theoretical and Experimental Analysis*. PhD thesis, Delft University of Technology.
- Wang, J., Navi, P., and Huet, C. (1992). Numerical study of granule influences on the crack propagation in concrete. In Bažant, Z. P., editor, *Fracture Mechanics of concrete structures, FraMCoS1*.
- Wang, W., Wang, J., and Kim, M.-S. (2001). An algebraic condition for the separation of two ellipsoids. *Computer Aided Geometric Design*, 18(6):531–539.
- Wang, Z. M., Kwan, A. K. H., and Chan, H. C. (1999). Mesoscopic study of concrete I: generation of random aggregate structure and finite element mesh. *Computers & Structures*, 70(5):533–544.
- Wempner, G. A. (1971). Discrete approximations related to nonlinear theories of solids. *International Journal of Solids and Structures*, 7(11):1581–1599.

- Whitcomb, J. D. (1991). Iterative global/local finite element analysis. *Computers and Structures*, 40(4):1027–1031.
- Willam, K., Pramono, E., and Sture, S. (1987). Fundamental issues of smeared crack models. In Shah, S. P. and Swartz, S. E., editors, *Fracture of concrete and Rock: SEM-RILEM international conference*, Houston, Texas, USA. Springer.
- Wilson, E. L. (1974). The static condensation algorithm. *International Journal for Numerical Methods in Engineering*, 8(1):198–203.
- Winkler, B. (2001). *Traglastuntersuchungen von unbewehrten und bewehrten Betonstrukturen auf der Grundlage eines objektiven Werkstoffgesetzes für Beton*. Dissertation, Universität Innsbruck.
- Wittmann, F. H., Roelfstra, P. E., and Sadouki, H. (1985). Simulation and analysis of composite structures. *Materials Science and Engineering*, 68(2):239–248.
- Wohlmuth, B. I. (1999). Hierarchical a posteriori error estimators for mortar finite element methods with lagrange multipliers. *SIAM Journal on Numerical Analysis*, 36(5):1636–1658.
- Wohlmuth, B. I. (2001). Discretization methods and iterative solvers based on domain decompositions. *Lectures Notes in Computational Science and Engineering*, 17.
- Wriggers, P. and Moftah, S. O. (2006). Mesoscale models for concrete: Homogenisation and damage behaviour. *Finite Elements in Analysis and Design*, 42:623–636.
- Zaitsev, Y. B. and Wittmann, F. H. (1981). Simulation of crack propagation and failure of concrete. *Materials and Structures*, 14(5):357–365.
- Zienkiewicz, O. C., Taylor, R. L., and Zhu, J. Z. (2005). *The Finite Element Method*. Elsevier Butterworth-Heinemann, 6<sup>th</sup> edition.
- Zohdi, T., Feucht, M., Gross, D., and Wriggers, P. (1998). A description of macroscopic damage through microstructural relaxation. *International Journal for Numerical Methods in Engineering*, 43(3):493–506.
- Zohdi, T. I. and Wriggers, P. (2001). Computational micro-macro material testing. *Archives of Computational Methods in Engineering*, 8(2):131–228.

# A Appendix

## A.1 Transformation and Projection of Stresses and Strains

### A.1.1 Orthogonal Transformation

The orthogonal transformation, e.g. rotation, of the stress and strain tensor between two cartesian coordinate systems defined by their basis vectors  $\{\mathbf{e}_1, \mathbf{e}_2, \mathbf{e}_3\}$  and  $\{\mathbf{e}'_1, \mathbf{e}'_2, \mathbf{e}'_3\}$  can be written as

$$\sigma'_{ij} = T_{ki}\sigma_{kl}T_{lj} \qquad \sigma_{ij} = T_{ik}\sigma'_{kl}T_{jl} \qquad (\text{A.1})$$

$$\varepsilon'_{ij} = T_{ki}\varepsilon_{kl}T_{lj} \qquad \varepsilon_{ij} = T_{ik}\varepsilon'_{kl}T_{jl}, \qquad (\text{A.2})$$

where  $\mathbf{T}$  is a second order tensor which describes the transformation of vector  $\mathbf{v}$

$$v'_i = T_{ji}v_j = \frac{\partial e_j}{\partial e'_i}v_j. \qquad (\text{A.3})$$

Using vector notation, the transformation of stresses and strains reads

$$\sigma'_i = T_{ij}^\sigma \sigma_j \qquad \sigma_i = T_{ij}^{\sigma'} \sigma'_j \qquad (\text{A.4})$$

$$\varepsilon'_i = T_{ij}^\varepsilon \varepsilon_j \qquad \varepsilon_i = T_{ij}^{\varepsilon'} \varepsilon'_j \qquad (\text{A.5})$$

with

$$T^\sigma = \begin{bmatrix} T_{11}T_{11} & T_{21}T_{21} & T_{31}T_{31} & 2T_{11}T_{21} & 2T_{11}T_{31} & 2T_{21}T_{31} \\ T_{12}T_{12} & T_{22}T_{22} & T_{32}T_{32} & 2T_{12}T_{22} & 2T_{12}T_{32} & 2T_{22}T_{32} \\ T_{13}T_{13} & T_{23}T_{23} & T_{33}T_{33} & 2T_{13}T_{23} & 2T_{13}T_{33} & 2T_{23}T_{33} \\ T_{11}T_{12} & T_{21}T_{22} & T_{31}T_{32} & T_{11}T_{22} + T_{12}T_{21} & T_{11}T_{32} + T_{12}T_{31} & T_{31}T_{22} + T_{21}T_{32} \\ T_{11}T_{13} & T_{21}T_{23} & T_{33}T_{31} & T_{11}T_{23} + T_{13}T_{21} & T_{11}T_{33} + T_{13}T_{31} & T_{33}T_{21} + T_{23}T_{31} \\ T_{12}T_{13} & T_{22}T_{23} & T_{33}T_{32} & T_{12}T_{23} + T_{13}T_{22} & T_{12}T_{33} + T_{13}T_{32} & T_{33}T_{22} + T_{23}T_{32} \end{bmatrix} \qquad (\text{A.6})$$

$$T^{\sigma'} = \begin{bmatrix} T_{11}T_{11} & T_{12}T_{12} & T_{13}T_{13} & 2T_{11}T_{12} & 2T_{11}T_{13} & 2T_{12}T_{13} \\ T_{21}T_{21} & T_{22}T_{22} & T_{23}T_{23} & 2T_{21}T_{22} & 2T_{21}T_{23} & 2T_{22}T_{23} \\ T_{31}T_{31} & T_{32}T_{32} & T_{33}T_{33} & 2T_{31}T_{32} & 2T_{31}T_{33} & 2T_{32}T_{33} \\ T_{11}T_{21} & T_{12}T_{22} & T_{13}T_{23} & T_{11}T_{22} + T_{12}T_{21} & T_{11}T_{23} + T_{21}T_{13} & T_{13}T_{22} + T_{12}T_{23} \\ T_{11}T_{31} & T_{12}T_{32} & T_{33}T_{13} & T_{11}T_{32} + T_{31}T_{12} & T_{11}T_{33} + T_{13}T_{31} & T_{33}T_{12} + T_{32}T_{13} \\ T_{21}T_{31} & T_{22}T_{32} & T_{33}T_{23} & T_{21}T_{32} + T_{31}T_{22} & T_{21}T_{33} + T_{31}T_{23} & T_{33}T_{22} + T_{23}T_{32} \end{bmatrix} \quad (\text{A.7})$$

$$T^{\varepsilon} = \begin{bmatrix} T_{11}T_{11} & T_{21}T_{21} & T_{31}T_{31} & T_{11}T_{21} & T_{11}T_{31} & T_{21}T_{31} \\ T_{12}T_{12} & T_{22}T_{22} & T_{32}T_{32} & T_{12}T_{22} & T_{12}T_{32} & T_{22}T_{32} \\ T_{13}T_{13} & T_{23}T_{23} & T_{33}T_{33} & T_{13}T_{23} & T_{13}T_{33} & T_{23}T_{33} \\ 2T_{11}T_{12} & 2T_{21}T_{22} & 2T_{31}T_{32} & T_{11}T_{22} + T_{12}T_{21} & T_{11}T_{32} + T_{12}T_{31} & T_{31}T_{22} + T_{21}T_{32} \\ 2T_{11}T_{13} & 2T_{21}T_{23} & 2T_{33}T_{31} & T_{11}T_{23} + T_{13}T_{21} & T_{11}T_{33} + T_{13}T_{31} & T_{33}T_{21} + T_{23}T_{31} \\ 2T_{12}T_{13} & 2T_{22}T_{23} & 2T_{33}T_{32} & T_{12}T_{23} + T_{13}T_{22} & T_{12}T_{33} + T_{13}T_{32} & T_{33}T_{22} + T_{23}T_{32} \end{bmatrix} \quad (\text{A.8})$$

$$T^{\varepsilon'} = \begin{bmatrix} T_{11}T_{11} & T_{12}T_{12} & T_{13}T_{13} & T_{11}T_{12} & T_{11}T_{13} & T_{12}T_{13} \\ T_{21}T_{21} & T_{22}T_{22} & T_{23}T_{23} & T_{21}T_{22} & T_{21}T_{23} & T_{22}T_{23} \\ T_{31}T_{31} & T_{32}T_{32} & T_{33}T_{33} & T_{31}T_{32} & T_{31}T_{33} & T_{32}T_{33} \\ 2T_{11}T_{21} & 2T_{12}T_{22} & 2T_{13}T_{23} & T_{11}T_{22} + T_{12}T_{21} & T_{11}T_{23} + T_{21}T_{13} & T_{13}T_{22} + T_{12}T_{23} \\ 2T_{11}T_{31} & 2T_{12}T_{32} & 2T_{33}T_{13} & T_{11}T_{32} + T_{31}T_{12} & T_{11}T_{33} + T_{13}T_{31} & T_{33}T_{12} + T_{32}T_{13} \\ 2T_{21}T_{31} & 2T_{22}T_{32} & 2T_{33}T_{23} & T_{21}T_{32} + T_{31}T_{22} & T_{21}T_{33} + T_{31}T_{23} & T_{33}T_{22} + T_{23}T_{32} \end{bmatrix}. \quad (\text{A.9})$$

### A.1.2 Projection

The projection of the stress tensor onto a surface with normal vector  $\mathbf{n}$  is given by

$$t_i = \sigma_{ij}n_j, \quad (\text{A.10})$$

where  $\mathbf{t}$  is the vector of tractions. In vectorial notation this equation reads

$$t_i = P_{ij}\sigma_j, \quad (\text{A.11})$$

where  $\mathbf{P}$  is a special projection matrix

$$\mathbf{P} = \begin{bmatrix} n_1 & 0 & 0 & n_2 & n_3 & 0 \\ 0 & n_2 & 0 & n_1 & 0 & n_3 \\ 0 & 0 & n_3 & 0 & n_1 & n_2 \end{bmatrix}. \quad (\text{A.12})$$

## A.2 Energies and Energy Derivatives

The total energy stored in an element with volume  $V$  can be written as a function of the total energy density  $u_{tot}$

$$U_{tot} = \int_V u_{tot} dV. \quad (\text{A.13})$$

In this thesis, the density of the total energy is approximated by the trapezoidal rule

$$u_{tot} = \tilde{u}_{tot} + \frac{1}{2} (\tilde{\sigma}_i + \sigma_i) (\varepsilon_i - \tilde{\varepsilon}_i), \quad (\text{A.14})$$

where  $\boldsymbol{\sigma}$  is the stress vector,  $\boldsymbol{\varepsilon}$  is the strain vector, and the tilde symbol indicates that the quantity is calculated at the last converged equilibrium state. In material formulations based on plasticity and/or damage the total energy density, and the total energy respectively, can be split into an elastic and an inelastic part

$$u_{tot} = u_{el} + u_{inel} \quad (\text{A.15})$$

$$U_{tot} = U_{el} + U_{inel} = \int_V u_{el} dV + \int_V u_{inel} dV. \quad (\text{A.16})$$

In general, the elastic part can be defined as

$$u_{el} = \frac{1}{2} \sigma_i (\varepsilon_i - \varepsilon_{pl,i}), \quad (\text{A.17})$$

where  $\boldsymbol{\varepsilon}_{pl}$  denotes the vector of plastic strains. It is to be noted that if a damage material model is used, the plastic strains vanish. By substituting Eqs. (A.14) and (A.17) into Eq. (A.15), the inelastic part can be written as

$$u_{inel} = u_{tot} - u_{el} = \tilde{u}_{tot} + \frac{1}{2} (\tilde{\sigma}_i (\varepsilon_i - \tilde{\varepsilon}_i) + \sigma_i (\varepsilon_{pl,i} - \tilde{\varepsilon}_i)). \quad (\text{A.18})$$

Assuming a local material formulation the energy densities at a given point depend only on the stresses and the strains at that point. The corresponding derivatives of the energy densities with respect to the strains can be written as

– total energy density

$$\frac{\partial u_{tot}}{\partial \varepsilon_j} = \frac{1}{2} \left( \tilde{\sigma}_j + \sigma_j + \frac{\partial \sigma_i}{\partial \varepsilon_j} (\varepsilon_i - \tilde{\varepsilon}_i) \right) \quad (\text{A.19})$$

– elastic energy density

$$\frac{\partial u_{el}}{\partial \varepsilon_j} = \frac{1}{2} \left( \sigma_j + \frac{\partial \sigma_i}{\partial \varepsilon_j} (\varepsilon_i - \varepsilon_{pl,i}) - \sigma_i \frac{\partial \varepsilon_{pl,i}}{\partial \varepsilon_j} \right) \quad (\text{A.20})$$

– inelastic energy density

$$\frac{\partial u_{inel}}{\partial \varepsilon_j} = \frac{\partial u_{tot}}{\partial \varepsilon_j} - \frac{\partial u_{el}}{\partial \varepsilon_j} = \frac{1}{2} \left( \tilde{\sigma}_j + \frac{\partial \sigma_i}{\partial \varepsilon_j} (\varepsilon_{pl,i} - \tilde{\varepsilon}_i) + \sigma_i \frac{\partial \varepsilon_{pl,i}}{\partial \varepsilon_j} \right). \quad (\text{A.21})$$

By considering the strain-displacement-relationship, given in Eq. (2.21), and by applying the chain rule the derivative of the energy with respect to the displacements reads

$$\frac{\partial U_{...}}{\partial d_j} = \int_V B_{ij} \frac{\partial u_{...}}{\partial \varepsilon_i} dV. \quad (\text{A.22})$$

In the numerical implementation the integrals in Equations (A.13), (A.16) and (A.22) are evaluated numerically. As a result, the integrals are replaced by sums. After calculating the energy derivatives of each element, the global vector of the energy derivatives respect to the nodal displacements is obtained by assembling the corresponding element contributions.

## A.3 Line Search for Load-Displacement-Constraint Methods

If a line-search is applied in simulations using load-displacement-constraint methods, cf. Sect. 2.4.4, the correction of the load factor can be rewritten as

– arc-length method

$$\delta \mu^{(n,i)}(\eta) = \frac{-a_2 \pm \sqrt{a_2^2 - a_1 a_3}}{a_1} \quad (\text{A.23})$$

with

$$a_1 = \delta \mathbf{d}_f^{(n,i)T} \delta \mathbf{d}_f^{(n,i)} + b \hat{\mathbf{f}}^T \hat{\mathbf{f}} \quad (\text{A.24})$$

$$a_2 = \delta \mathbf{d}_f^{(n,i)T} \left( \Delta \mathbf{d}^{(n,i-1)} + \eta \delta \mathbf{d}_0^{(n,i)} \right) + b \Delta \mu^{(n,i-1)} \hat{\mathbf{f}}^T \hat{\mathbf{f}} \quad (\text{A.25})$$

$$a_3 = \left( \Delta \mathbf{d}^{(n,i-1)} + \eta \delta \mathbf{d}_0^{(n,i)} \right)^T \left( \Delta \mathbf{d}^{(n,i-1)} + \eta \delta \mathbf{d}_0^{(n,i)} \right) + b \Delta \mu^{(n,i-1)2} \hat{\mathbf{f}}^T \hat{\mathbf{f}} - \Delta l^2; \quad (\text{A.26})$$

– indirect displacement control

$$\delta \mu^{(n,i)}(\eta) = \frac{\Delta l - \mathbf{c}^T \left( \Delta \mathbf{d}^{(n,i-1)} + \eta \delta \mathbf{d}_0^{(n,i)} \right)}{\mathbf{c}^T \delta \mathbf{d}_f^{(n,i)}}; \quad (\text{A.27})$$



- energy release control (Gutiérrez (2004))

$$\delta\mu^{(n,i)}(\eta) = \frac{2 \Delta\mathcal{G} - \left[ \mu^{(n-1)} \left( \Delta\mathbf{d}^{(n,i-1)} + \eta\delta\mathbf{d}_0^{(n,i)} \right) - \Delta\mu^{(n,i-1)} \mathbf{d}^{(n-1)} \right]^T \hat{\mathbf{f}}}{\left[ \mu^{(n-1)} \delta\mathbf{d}_f^{(n,i)} - \mathbf{d}^{(n-1)} \right]^T \hat{\mathbf{f}}}; \quad (\text{A.28})$$

- modified energy release control

$$\delta\mu^{(n,i+1)}(\eta) = \frac{\Delta\mathcal{G} + U_{inel}^{(n-1)} - U_{inel}^{(n,i-1)} - \eta \left[ \frac{\partial U_{inel}^{(n,i-1)}}{\partial \mathbf{d}} \right]^T \delta\mathbf{d}_0^{(n,i)}}{\left[ \frac{\partial U_{inel}^{(n,i-1)}}{\partial \mathbf{d}} \right]^T \delta\mathbf{d}_f^{(n,i)}}. \quad (\text{A.29})$$

The corresponding derivatives of the load factor correction  $\delta\mu$  with respect to the line search parameter  $\eta$  reads

- arc-length method

$$\frac{\partial \delta\mu^{(n,i)}}{\partial \eta}(\eta) = \frac{1}{a_1} \left( -\frac{\partial a_2}{\partial \eta} \pm \frac{2a_2 \frac{\partial a_2}{\partial \eta} - a_1 \frac{\partial a_3}{\partial \eta}}{2\sqrt{a_2^2 - a_1 a_3}} \right) \quad (\text{A.30})$$

with

$$\frac{\partial a_2}{\partial \eta} = \delta\mathbf{d}_f^{(n,i)T} \delta\mathbf{d}_0^{(n,i)} \quad (\text{A.31})$$

$$\frac{\partial a_3}{\partial \eta} = 2 \left( \Delta\mathbf{d}^{(n,i-1)} + \eta\delta\mathbf{d}_0^{(n,i)} \right)^T \delta\mathbf{d}_0^{(n,i)}; \quad (\text{A.32})$$

- indirect displacement control

$$\frac{\partial \delta\mu^{(n,i)}}{\partial \eta}(\eta) = -\frac{\mathbf{c}^T \delta\mathbf{d}_0^{(n,i)}}{\mathbf{c}^T \delta\mathbf{d}_f^{(n,i)}}; \quad (\text{A.33})$$

- energy release control (Gutiérrez (2004))

$$\frac{\partial \delta\mu^{(n,i)}}{\partial \eta}(\eta) = \frac{-\mu^{(n-1)} \delta\mathbf{d}_0^{(n,i)T} \hat{\mathbf{f}}}{\left[ \mu^{(n-1)} \delta\mathbf{d}_f^{(n,i)} - \mathbf{d}^{(n-1)} \right]^T \hat{\mathbf{f}}}; \quad (\text{A.34})$$

– modified energy release control

$$\frac{\partial \delta \mu^{(n,i)}}{\partial \eta}(\eta) = - \frac{\left[ \frac{\partial U_{inel}^{(n,i-1)}}{\partial \mathbf{d}} \right]^T \delta \mathbf{d}_0^{(n,i)}}{\left[ \frac{\partial U_{inel}^{(n,i-1)}}{\partial \mathbf{d}} \right]^T \delta \mathbf{d}_f^{(n,i)}}. \quad (\text{A.35})$$

## A.4 Microplane Damage Model

### A.4.1 Numerical Integration of the Inverse Integrity Tensor

In general, the implementation of microplane models involves the numerical integration of microplane quantities over the unit hemisphere. For the microplane-based damage model (MD), presented in Sect. 3.5, the evaluation of such an integral is required for the calculation of the inverse integrity tensor  $\boldsymbol{\psi}$ , Eq. (3.118). Using spherical coordinates this integral reads

$$\psi_{ij} = \frac{3}{2\pi} \int_0^{2\pi} \int_0^{\pi/2} \psi(\mathbf{n}) n_i n_j \sin \theta \, d\theta \, d\varphi, \quad (\text{A.36})$$

where  $\psi(\mathbf{n})$  is a scalar parameter characterizing the relative compliance on the microplane with normal vector  $\mathbf{n}$ ,  $\varphi$  is the azimuth angle and  $\theta$  the zenith angle. Furthermore, the orientation of the microplane, represented by the normal vector  $\mathbf{n}$ , can be expressed as function of these two angles

$$\mathbf{n}(\theta, \varphi) = \begin{bmatrix} \sin \theta \cos \varphi \\ \sin \theta \sin \varphi \\ \cos \theta \end{bmatrix}. \quad (\text{A.37})$$

By applying a numerical integration scheme, Eq. (A.36) can be written as

$$\psi_{ij} = \frac{3}{2\pi} \sum_{k=1}^{n_{IP}} w^k \psi(\mathbf{n}(\theta^k, \varphi^k)) n_i(\theta^k, \varphi^k) n_j(\theta^k, \varphi^k) \sin \theta^k, \quad (\text{A.38})$$

where  $n_{IP}$  is the number of integration points, the angles  $\theta^k$  and  $\varphi^k$  define the position of integration point  $k$  on the surface of the unit hemisphere, and  $w^k$  is the corresponding weight factor. Efficient numerical integration rules for the three-dimensional problem can be found in Bažant and Oh (1986); Badel and Leblond (2004).

For the two-dimensional model the integration domain is reduced to the boundary of the unit semicircle. Introducing polar coordinates the components of the inverse integrity

Table A.1: 13-point Gauss quadrature for the two-dimensional MD.

IP	$\varphi$	$n_1$	$n_2$	$w$
1	$\pm 0.0000000000$	$+1.0000000000000000$	$+0.0000000000000000$	0.23255155320
2	$-0.3620030763$	$+0.9351893144682923$	$-0.3541481979402486$	0.22628318040
3	$+0.3620030763$	$+0.9351893144682923$	$+0.3541481979402486$	0.22628318040
4	$-0.7044907660$	$+0.7619414539070705$	$-0.6476459069723050$	0.20781604800
5	$+0.7044907660$	$+0.7619414539070705$	$+0.6476459069723050$	0.20781604800
6	$-1.0089999830$	$+0.5327073016090508$	$-0.8462995514665028$	0.17814597340
7	$+1.0089999830$	$+0.5327073016090508$	$+0.8462995514665028$	0.17814597340
8	$-1.2591159210$	$+0.3066585122489681$	$-0.9518196031104053$	0.13887351030
9	$+1.2591159210$	$+0.3066585122489681$	$+0.9518196031104053$	0.13887351030
10	$-1.4413601950$	$+0.1290750118430869$	$-0.9916348326464268$	0.09212149896
11	$+1.4413601950$	$+0.1290750118430869$	$+0.9916348326464268$	0.09212149896
12	$-1.5459511280$	$+0.0248426435376009$	$-0.9996913739059989$	0.04048400460
13	$+1.5459511280$	$+0.0248426435376009$	$+0.9996913739059989$	0.04048400460

tensor can be written as

$$\psi_{ij} = \frac{2}{\pi} \int_{-\pi/2}^{\pi/2} \psi(\mathbf{n}) n_i n_j d\varphi, \quad (\text{A.39})$$

and the components of the microplane normal vector are defined as

$$\mathbf{n}(\varphi) = \begin{bmatrix} \cos \varphi \\ \sin \varphi \end{bmatrix}. \quad (\text{A.40})$$

In the present work, this integral is evaluated numerically using a 13-point Gauss quadrature rule. As a result, the components of the inverse integrity tensor are given by

$$\psi_{ij} = \sum_{k=1}^{13} w^k \psi(\mathbf{n}(\varphi^k)) n_i(\varphi^k) n_j(\varphi^k), \quad (\text{A.41})$$

where  $\varphi^k$  defines the position of integration point  $k$  on the boundary of the unit semicircle, and  $w^k$  is the corresponding weight factor. The position of the individual integration points characterized by the normal vector  $\mathbf{n}$  and the associated weight factors  $w$  are summarized in Table A.1.

## A.4.2 Derivation of the Damage Effect Tensor

The alternative derivation of the damage effect tensor presented in this section is based on Carol and Bažant (1997). In their paper the authors define the components of the microplane stress and strain vectors normal and tangential to the microplane. As a result,

the static constraint can be written as

$$s_N = \sigma_{ij} n_i n_j \quad (\text{A.42})$$

$$s_{T_r} = \sigma_{ri} n_i - s_N n_r = (\delta_{ri} - n_r n_i) n_j \sigma_{ij} \quad r = 1, 2, \quad (\text{A.43})$$

where subscript  $N$  denotes the normal component and subscript  $T$  identifies the two tangential components of the microplane stresses. Knowing that the stress tensor is symmetric, the tangential microplane stresses can be rewritten to

$$s_{T_r} = \frac{1}{2} (n_i \delta_{jr} + n_j \delta_{ir} - 2n_i n_j n_r) \sigma_{ij}. \quad (\text{A.44})$$

As presented in Sect. 3.5, scalar microplane damage law is introduced on the microplane. Consequently, the corresponding effective microplane stresses are given by

$$\tilde{s}_N = \psi s_N \quad (\text{A.45})$$

$$\tilde{s}_{T_r} = \psi s_{T_r}, \quad (\text{A.46})$$

where the scalar parameter  $\psi$  characterizes the relative compliance on that microplane. By applying the principle virtual work

$$\frac{4\pi}{3} \tilde{\sigma}_{ij} \delta \tilde{\varepsilon}_{ij} = 2 \int_{\Omega} \tilde{s}_N \delta \tilde{\varepsilon}_N + \tilde{s}_{T_r} \delta \tilde{\varepsilon}_{T_r} \, d\Omega, \quad (\text{A.47})$$

equilibrium between effective macro- and micro-stresses can be satisfied in a weak sense. Substituting the kinematic constraint, applied to the virtual effective strains

$$\delta \tilde{\varepsilon}_N = \delta \tilde{\varepsilon}_{ij} n_i n_j \quad (\text{A.48})$$

$$\delta \tilde{\varepsilon}_{T_r} = \frac{1}{2} (n_i \delta_{jr} + n_j \delta_{ir} - 2n_i n_j n_r) \delta \tilde{\varepsilon}_{ij}, \quad (\text{A.49})$$

into the principle of virtual work, Eq. (A.47), and considering that this equality must hold for an arbitrary virtual effective strain tensor, the effective stress tensor can be obtained

$$\tilde{\sigma}_{ij} = \frac{3}{2\pi} \int_{\Omega} \tilde{s}_N n_i n_j + \frac{1}{2} \tilde{s}_{T_r} (n_i \delta_{jr} + n_j \delta_{ir} - 2n_i n_j n_r) \, d\Omega. \quad (\text{A.50})$$

Note that Eq. (A.49) implies the symmetry of the virtual effective strain tensor. Substituting Eqs. (A.45) and (A.46) and Eqs. (A.42) and (A.44) into Eq. (A.50) yields

$$\begin{aligned} \tilde{\sigma}_{ij} &= \frac{3}{2\pi} \int_{\Omega} \psi n_i n_j n_k n_l \\ &\quad + \frac{\psi}{4} (n_i \delta_{jr} + n_j \delta_{ir} - 2n_i n_j n_r) (n_k \delta_{lr} + n_l \delta_{kr} - 2n_k n_l n_r) \, d\Omega \, \sigma_{kl} \end{aligned} \quad (\text{A.51})$$

$$= \frac{3}{2\pi} \int_{\Omega} \frac{\psi}{4} (n_i n_k \delta_{jl} + n_i n_l \delta_{jk} + n_j n_k \delta_{il} + n_j n_l \delta_{ik}) \, d\Omega \, \sigma_{kl}. \quad (\text{A.52})$$

Introducing the second-order inverse integrity tensor, Eq. (3.118), and considering the relationship between nominal and effective stress tensor, defined in Eq. (3.109), the components of the macroscopic damage effect tensor are given by

$$M_{ijkl} = \frac{1}{4} (\psi_{ik}\delta_{jl} + \psi_{il}\delta_{jk} + \psi_{jk}\delta_{il} + \psi_{jl}\delta_{ik}), \quad (\text{A.53})$$

which is equivalent to Eq. (3.120). This fourth order tensor exhibits not only minor but also major symmetries.

### A.4.3 Secant and Tangent Material Matrix (Plane Stress)

Using vectorial notation, the compliance form of the constitutive equations reads

$$\varepsilon_i = D_{ij}^s \sigma_j, \quad (\text{A.54})$$

where  $D_{ij}^s$  are the components of the damaged (secant) compliance matrix. In two-dimensional simulations the problem can be reduced and the corresponding stress and strain vectors are given by

$$\boldsymbol{\sigma}^T = [\sigma_{11}, \sigma_{22}, \sigma_{12}] \quad (\text{A.55})$$

$$\boldsymbol{\varepsilon}^T = [\varepsilon_{11}, \varepsilon_{22}, 2\varepsilon_{12}]. \quad (\text{A.56})$$

Assuming plane stress conditions, substituting Eq. (3.120) into Eq. (3.110) and considering the relationship between tensorial and vectorial notation of stresses and strains, the components of the damaged compliance matrix can be defined as

$$D_{11}^s = D_{1111}^s = \frac{1}{E}\psi_{11}^2 + \frac{1+\nu}{2E}\psi_{12}^2 \quad (\text{A.57})$$

$$D_{12}^s = D_{1122}^s = \frac{-\nu}{E}\psi_{11}\psi_{22} + \frac{1+\nu}{2E}\psi_{12}^2 \quad (\text{A.58})$$

$$D_{13}^s = D_{1112}^s + D_{1121}^s = \frac{3-\nu}{2E}\psi_{11}\psi_{12} + \frac{1+\nu}{2E}\psi_{22}\psi_{12} \quad (\text{A.59})$$

$$D_{22}^s = D_{2222}^s = \frac{1}{E}\psi_{22}^2 + \frac{1+\nu}{2E}\psi_{12}^2 \quad (\text{A.60})$$

$$D_{23}^s = D_{2212}^s + D_{2221}^s = \frac{3-\nu}{2E}\psi_{22}\psi_{12} + \frac{1+\nu}{2E}\psi_{11}\psi_{12} \quad (\text{A.61})$$

$$D_{33}^s = 2(D_{1212}^s + D_{1221}^s) = \frac{2-2\nu}{E}\psi_{12}^2 + \frac{1+\nu}{2E}(\psi_{11} + \psi_{22})^2, \quad (\text{A.62})$$

where  $\boldsymbol{\psi}$  is the inverse integrity tensor, which is defined by Eq. (3.118). It is to be noted that the secant compliance matrix has a symmetric shape ( $D_{21}^s = D_{12}^s$ ,  $D_{31}^s = D_{13}^s$ ,  $D_{32}^s = D_{23}^s$ ).

The tangent material matrix can be derived from the derivatives of the compliance form

of the constitutive relationship, Eqs. (A.54), with respect to the strains

$$\frac{\partial \varepsilon_i}{\partial \varepsilon_j} = \frac{\partial D_{ik}^s}{\partial \varepsilon_j} \sigma_k + D_{ik}^s \frac{\partial \sigma_k}{\partial \varepsilon_j}. \quad (\text{A.63})$$

By rewriting this system of equations and by multiplying with the secant material matrix  $\mathbf{C}^s = \mathbf{D}^{s^{-1}}$ , the tangent material matrix for the local formulation of the MD is obtained

$$\frac{\partial \sigma_i}{\partial \varepsilon_j} = C_{ik}^s \left( \delta_{kj} - \frac{\partial D_{kl}^s}{\partial \varepsilon_j} \sigma_l \right). \quad (\text{A.64})$$

The derivatives of the damaged compliance matrix are given by

$$\frac{\partial D_{11}^s}{\partial \varepsilon_i} = \frac{2}{E} \psi_{11} \frac{\partial \psi_{11}}{\partial \varepsilon_i} + \frac{1+\nu}{E} \psi_{12} \frac{\partial \psi_{12}}{\partial \varepsilon_i} \quad (\text{A.65})$$

$$\frac{\partial D_{12}^s}{\partial \varepsilon_i} = \frac{-\nu}{E} \left( \frac{\partial \psi_{11}}{\partial \varepsilon_i} \psi_{22} + \psi_{11} \frac{\partial \psi_{22}}{\partial \varepsilon_i} \right) + \frac{1+\nu}{E} \psi_{12} \frac{\partial \psi_{12}}{\partial \varepsilon_i} \quad (\text{A.66})$$

$$\frac{\partial D_{13}^s}{\partial \varepsilon_i} = \frac{3-\nu}{2E} \left( \frac{\partial \psi_{11}}{\partial \varepsilon_i} \psi_{12} + \psi_{11} \frac{\partial \psi_{12}}{\partial \varepsilon_i} \right) + \frac{1+\nu}{2E} \left( \frac{\partial \psi_{22}}{\partial \varepsilon_i} \psi_{12} + \psi_{22} \frac{\partial \psi_{12}}{\partial \varepsilon_i} \right) \quad (\text{A.67})$$

$$\frac{\partial D_{22}^s}{\partial \varepsilon_i} = \frac{2}{E} \psi_{22} \frac{\partial \psi_{11}}{\partial \varepsilon_i} + \frac{1+\nu}{E} \psi_{12} \frac{\partial \psi_{12}}{\partial \varepsilon_i} \quad (\text{A.68})$$

$$\frac{\partial D_{23}^s}{\partial \varepsilon_i} = \frac{3-\nu}{2E} \left( \frac{\partial \psi_{22}}{\partial \varepsilon_i} \psi_{12} + \psi_{22} \frac{\partial \psi_{12}}{\partial \varepsilon_i} \right) + \frac{1+\nu}{2E} \left( \frac{\partial \psi_{11}}{\partial \varepsilon_i} \psi_{12} + \psi_{11} \frac{\partial \psi_{12}}{\partial \varepsilon_i} \right) \quad (\text{A.69})$$

$$\frac{\partial D_{33}^s}{\partial \varepsilon_i} = \frac{4-4\nu}{E} \psi_{12} \frac{\partial \psi_{12}}{\partial \varepsilon_i} + \frac{1+\nu}{E} (\psi_{11} + \psi_{22}) \left( \frac{\partial \psi_{11}}{\partial \varepsilon_i} + \frac{\partial \psi_{22}}{\partial \varepsilon_i} \right), \quad (\text{A.70})$$

with

$$\frac{\partial \psi_{ij}}{\partial \varepsilon_k} = \frac{3}{2\pi} \int_{\Omega} \frac{\partial \psi}{\partial e_{eq}} \frac{\partial e_{eq}}{\partial \varepsilon_k} n_i n_j \, d\Omega. \quad (\text{A.71})$$

Using vectorial notation the equivalent microplane strain, given in Eq. (3.123), is rewritten as

$$e_{eq} = \frac{\varepsilon_1 n_1 n_1 + \varepsilon_2 n_2 n_2 + \varepsilon_3 n_1 n_2}{1 - \frac{m}{E e_0} (\sigma_1 + \sigma_2)} \quad (\text{A.72})$$

and the corresponding derivatives are given by

$$\frac{e_{eq}}{\varepsilon_1} = \frac{n_1 n_1}{1 - \frac{m}{E e_0} (\sigma_1 + \sigma_2)} \quad (\text{A.73})$$

$$\frac{e_{eq}}{\varepsilon_2} = \frac{n_2 n_2}{1 - \frac{m}{E e_0} (\sigma_1 + \sigma_2)} \quad (\text{A.74})$$

$$\frac{e_{eq}}{\varepsilon_3} = \frac{n_1 n_2}{1 - \frac{m}{E e_0} (\sigma_1 + \sigma_2)}. \quad (\text{A.75})$$

For increasing equivalent strain, which represents a loading situation on microplane level ( $e_{eq} = e_{eq,max}$ ), the derivative of the realtive compliance with respect to the equivalent strain reads

$$\frac{\partial \psi}{\partial e_{eq}} = \begin{cases} 0 & \text{if } e_{eq} \leq e_0 \\ \frac{e_f - e_0 + e_{eq}}{2\psi e_0(e_f - e_0)} \exp\left(\frac{e_{eq} - e_0}{e_f - e_0}\right) & \text{if } e_{eq} > e_0, \end{cases} \quad (\text{A.76})$$

Otherwise this derivative vanishes.

The advantage of the presented approach compared to the direct derivation of the stiffness form of the constitutive relationship is, that the derivative of the secant material matrix, which requires the derivation of the inversion process of the secant compliance matrix, is not needed. The tangential material matrix for the nonlocal formulation of the MD can be obtained in a similar way by considering the proposals given in Sect. 3.2.2.

## A.5 Interface Material Model - Tangential Material Matrix

In Sect. 3.6 the constitutive equations of the interface damage model are derived from a potential formulation. Consequently, the tangent material matrix, which is defined as the first derivative of the interface tractions with respect to the interface openings, can be written as the second derivative of the potential

$$\mathbf{C} = \begin{bmatrix} \frac{\partial T_N}{\partial \Delta u_N} & \frac{\partial T_N}{\partial \Delta u_{T,1}} & \frac{\partial T_N}{\partial \Delta u_{T,2}} \\ \frac{\partial T_{T,1}}{\partial \Delta u_N} & \frac{\partial T_{T,1}}{\partial \Delta u_{T,1}} & \frac{\partial T_{T,1}}{\partial \Delta u_{T,2}} \\ \frac{\partial T_{T,2}}{\partial \Delta u_N} & \frac{\partial T_{T,2}}{\partial \Delta u_{T,1}} & \frac{\partial T_{T,2}}{\partial \Delta u_{T,2}} \end{bmatrix} \quad (\text{A.77})$$

$$= \begin{bmatrix} \frac{\partial^2 \Phi}{\partial \Delta u_N^2} & \frac{\partial^2 \Phi}{\partial \Delta u_N \partial \Delta u_{T,1}} & \frac{\partial^2 \Phi}{\partial \Delta u_N \partial \Delta u_{T,2}} \\ \frac{\partial^2 \Phi}{\partial \Delta u_{T,1} \partial \Delta u_N} & \frac{\partial^2 \Phi}{\partial \Delta u_{T,1}^2} & \frac{\partial^2 \Phi}{\partial \Delta u_{T,1} \partial \Delta u_{T,2}} \\ \frac{\partial^2 \Phi}{\partial \Delta u_{T,2} \partial \Delta u_N} & \frac{\partial^2 \Phi}{\partial \Delta u_{T,2} \partial \Delta u_{T,1}} & \frac{\partial^2 \Phi}{\partial \Delta u_{T,2}^2} \end{bmatrix}. \quad (\text{A.78})$$

By applying the chain rule the components of this matrix can be rewritten as

$$\frac{\partial T_N}{\partial \Delta u_N} = \frac{\partial^2 \Phi}{\partial \Delta u_N^2} = \left[ \frac{\partial \sigma}{\partial \lambda} - \frac{\sigma}{\lambda} \right] \frac{\partial \lambda}{\partial \Delta u_N} \frac{\Delta u_N}{\lambda} + \frac{\sigma}{\lambda} \quad (\text{A.79})$$

$$\frac{\partial T_N}{\partial \Delta u_{T,i}} = \frac{\partial^2 \Phi}{\partial \Delta u_N \partial \Delta u_{T,i}} = \left[ \frac{\partial \sigma}{\partial \lambda} - \frac{\sigma}{\lambda} \right] \frac{\partial \lambda}{\partial \Delta u_{T,i}} \frac{\Delta u_N}{\lambda} \quad (\text{A.80})$$

$$\frac{\partial T_{T,i}}{\partial \Delta u_N} = \frac{\partial^2 \Phi}{\partial \Delta u_{T,i} \partial \Delta u_N} = \left[ \frac{\partial \sigma}{\partial \lambda} - \frac{\sigma}{\lambda} \right] \frac{\partial \lambda}{\partial \Delta u_N} \frac{\alpha^2 \Delta u_{T,i}}{\lambda} \quad (\text{A.81})$$

$$\frac{\partial T_{T,i}}{\partial \Delta u_{T,j}} = \frac{\partial^2 \Phi}{\partial \Delta u_{T,i} \partial \Delta u_{T,j}} = \left[ \frac{\partial \sigma}{\partial \lambda} - \frac{\sigma}{\lambda} \right] \frac{\partial \lambda}{\partial \Delta u_{T,j}} \frac{\alpha^2 \Delta u_{T,i}}{\lambda} + \delta_{ij} \frac{\alpha^2 \sigma}{\lambda}, \quad (\text{A.82})$$

where  $\lambda$  is the equivalent interface opening, Eq. (3.132), and  $\sigma$  is the equivalent interface traction, which is defined by the traction separation law, Eq. (3.133). The corresponding derivative of the equivalent interface traction with respect to the equivalent interface opening reads

$$\frac{\partial \sigma}{\partial \lambda} = \begin{cases} K_p & \lambda < \lambda_0 \\ -\frac{f_t^2}{G_f} \exp \frac{-f_t(\lambda - \lambda_0)}{G_f} & \text{otherwise} \end{cases} \quad (\text{A.83})$$

and the derivatives of the equivalent interface opening with respect to the relative displacements between the interface surfaces are given by

$$\frac{\partial \lambda}{\partial \Delta u_N} = \frac{\Delta u_N}{\lambda} \quad (\text{A.84})$$

$$\frac{\partial \lambda}{\partial \Delta u_{T,i}} = \frac{\alpha^2 \Delta u_{T,i}}{\lambda}. \quad (\text{A.85})$$

Equation (A.78) applies if the interface is in tension, that is a positive normal interface opening. In compression the tangent material matrix reads

$$\mathbf{C} = \begin{bmatrix} K_p & 0 & 0 \\ 0 & \frac{\partial T_{T,1}}{\partial \Delta u_{T,1}} & \frac{\partial T_{T,1}}{\partial \Delta u_{T,2}} \\ 0 & \frac{\partial T_{T,2}}{\partial \Delta u_{T,1}} & \frac{\partial T_{T,2}}{\partial \Delta u_{T,2}} \end{bmatrix}, \quad (\text{A.86})$$

in which the derivatives of the tangential interface tractions are given by Eq. (A.82).